Theoretical Insights into the Bonding in Thorium Organometallic Complexes: A Comparison with Group IV Transition Metal Chemistry

Thesis by

Mark John Brusich

In Partial Fulfillment of the Requirements

for the Degree of

Doctor of Philosophy

To my Mom and Dad and my Aunt Louise

In the beginning was the Word;

the Word was in God's presence,

and the Word was God.

He was present to God in the beginning.

Through Him all things came into being,

and apart from Him nothing came to be.

Whatever came to be in Him, found life,

life for the light of men.

No one has ever seen God.

It is God the only Son,

ever at the Father's side,

who has revealed Him.

John 1:1-4,18

Even when all possible
scientific questions
have been answered, the
problems of life remain
completely untouched.

Ludwig Wittgenstein 1921

I don't know. I don't know at all.
I think we're on some kind of spaceship.

Hitchhiker's Guide to the Galaxay
Douglas Adams

Acknowledgments

I would like to thank my research advisor, Bill Goddard, for his patient guidance and support. I also acknowledge the financial aid of Caltech.

I gratefully wish to thank the past and present members of the Goddard research group for their advice, their willingness to share knowledge, and most of all for their friendship. A Ph.D. dissertation can be likened to current events, full of new ideas but soundly based in history — in this work, Goddard group folklore is evident. In particular, I would like to thank Marvin Goodgame for introducing me, albeit carefully, to the rigors of electronic structure theory. His willingness to listen and help out a "wet behind the ears" first-year graduate student were most greatly appreciated! The many lively discussions with Chih-Mai Kao helped me immensely in putting together the contragradience story in Part II. Barbara Garrison, Sergei Shashkin, and Gilles Ohanessian, all visitors to the WAG group, were both friends and scientific sages! Thanks also go to Mark McAdon, Naoki Karasawa, Art Voter, Eugene Knight, Ann Miller, Terry Coley, Alan Mathiowetz, and Janet Allison for their many words of wisdom and encouragement.

The best thing that happened to me at Caltech was meeting so many wonderful friends. I have matured intellectually, personally, and spiritually since I first came here. The following people had a large part in promoting and encouraging that growth. Bill Finch was a great roommate and a tremendous friend. I've never met anyone who was as close to my "wavelength" as he is; he's always there to listen when I need to talk. Emily Carter has been a terrific friend — her support and encouragement both scientifically and emotionally have helped me to get through the stress that unfortunately is often a part of the Caltech existence.

Abstract

In this thesis a detailed ab initio theoretical study of organothorium chemistry is presented. The first part is devoted to examining both the bonding in and the reaction chemistry of various substituted thorium complexes. Using the chlorine ligand as a model for the usual cyclopentadienyl groups found in these systems, we examine the bonding of hydrogen and methyl ligands to thorium. Frequent comparisons with the experimental results on similar species are made. In addition, by contrasting the bonding in the thorium complexes with the bonding in the analogous Group IVB systems, a qualitative and quantitative picture of bonding, as the atomic number of the metal becomes larger, can be obtained. The reaction chemistry is studied via two different sets of processes. In the first, the deuterium (D_2) exchange reaction with a thorium-hydrogen bond is examined. Several studies have been done previously, both experimentally and theoretically, on the Group IVB exchange reactions. Hence, there is enough information to see trends and to make predicitions about relative reaction rates. Also, from our investigation the effect that different types of ligands have on the activation barrier to reaction can be ascertained.

In the second part of the thesis, the factors that go into stabilizing bond formation are discussed concerning both main group elements and transition metals, including actinides. In particular, the process of bond formation between hydrogen atom and the alkali metals is compared with the same process in the Group IVB-hydrogen and thorium-hydrogen saturated complexes. The main difference between the alkali metal and the transition metal bonds with hydrogen is the bond strength trends with increasing atomic number. For the alkali metals the bond energies decrease down the column, yet for the transition metals and

thorium it is the reverse. The conclusion is that the shape of the mostly d in character transition metal bonding orbitals is such that better overlap can be achieved with hydrogen as the orbitals become more diffuse. In the alkali metals the bonds can be described as s—s bonds whose overlap decreases with increasing diffuseness.

Table of Contents

Part I

Electronic Structure and Reactivity
of Organothorium Complexes

Abstract: Ab initio quantum mechanical calculations [generalized valence bond (GVB) and configuration interaction (CI)] have been used to study several thorium organometallic complexes. The experimentally observed systems often involve cyclopentadienyl (Cp) or pentamethylcyclopentadienyl (Cp*) groups, **1a**, but we find that the analogous systems with Cl ligands, **1b**,

$$(1)$$
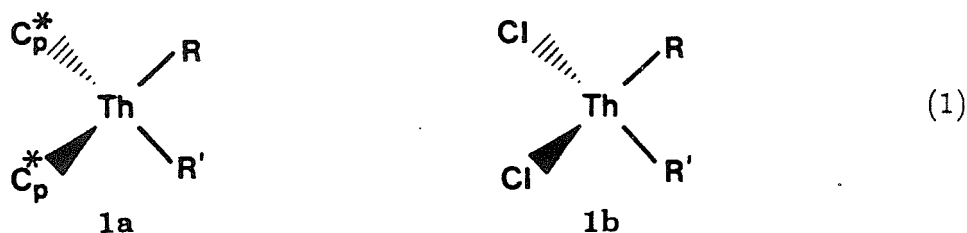
have very similar structure and properties.

Experimentally, compounds with $Th-CH_3$ bonds react readily with H_2

$$(2)$$
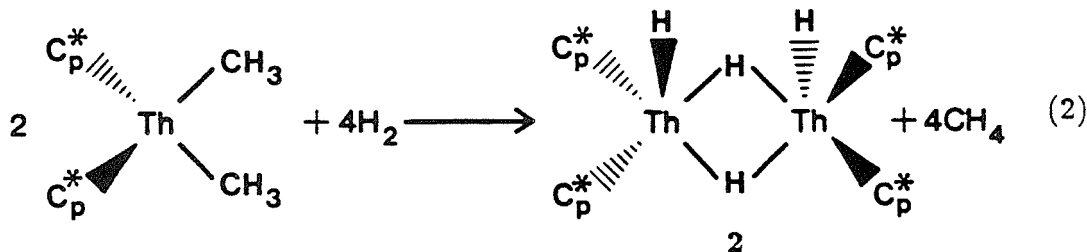
to form a dimer complex with both terminal and bridging $Th-H$ bonds. We have calculated the minimum energy structure of the dimer (with Cl's replacing the Cp* groups) and find excellent agreement with the neutron diffraction structure of **2**.

We believe that the reaction (2) involves a direct attack of H_2 on the $Th-CH_3$ bond, leading to a four-center transition state (2+2 addition). This is supported by the experimental studies of Anderson on analogous $Th-H$ systems [S. J. Simpson, H. W. Turner, and R. A. Andersen, J. Am. Chem. Soc.

101, 7728–7729 (1979)]. We have examined this process

$$M - H \atop D - D \quad \longrightarrow \quad \begin{pmatrix} M & \cdots & H \\ \vdots & & \vdots \\ D & \cdots & D \end{pmatrix}^{\ddagger} \quad \longrightarrow \quad \begin{matrix} M & H \\ | & | \\ D & D \end{matrix} \tag{3}$$
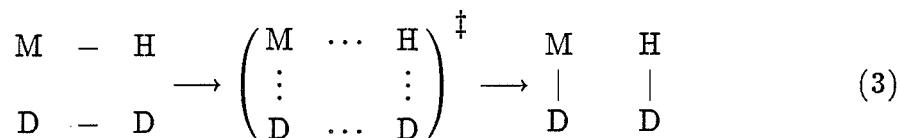
for $M = Cl_2Th^+$ and Cl_3Th where we find allowed reactions with relatively low energy barriers

$$Cl_2Th - H^+ + D_2 \quad \longrightarrow \quad Cl_2Th - D^+ + HD \quad \Delta E^{\ddagger} = 2 \text{ kcal mol}^{-1}$$

$$Cl_3Th - H + D_2 \quad \longrightarrow \quad Cl_2Th - D + HD \quad \Delta E^{\ddagger} = 19 \text{ kcal mol}^{-1}. \tag{4}$$
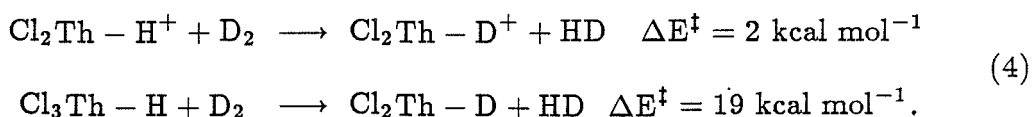
A comparison of the thorium reactions with the analogous Group IVB 2 + 2 additions reveals that the activation energies are smaller for the thorium complexes because of the increased polarity (metal-to-ligand charge transfer) of thorium's transition states. Attack on an ionic M−H bond via a concerted 2 + 2 pathway should lead to lower barriers than the similar reaction at a covalent M−H bond.

Bond energies are obtained for Th−H and Th−CH₃ bonds in saturated complexes [Cl_3Th-R, $Cl_2Th(R)(R')$], leading to $D(Cl_2(H)Th-H) = 77.8$ kcal mol^{-1}, $D(Cl_3Th-H) = 76.8$ kcal mol^{-1}, $D(Cl_2(H)Th-CH_3) = 73.0$ kcal mol^{-1}, and $D(Cl_3Th-CH_3) = 73.5$ kcal mol^{-1}. The magnitude of these bond energies is lower than the previous experimental estimates of bond strength, especially for $D(Th-H)$ ($D(Th-H) = 90\pm10$ and $D(Th-CH_3) = 77$-82 ± 10). In addition, the difference between the Th−H and Th−C dissociation energies is smaller than the experimental values predict. Studies on the similar complexes of the Group IVB column, $Cl_2M(R)(R')$, M = Ti, Zr, and Hf, R = R' = H, and R = H and R' = CH₃, indicate that M−C bonds are actually *stronger* than M−H bonds. Hence, the small difference in Th−H and Th−CH₃ bonds is not suprising.

The migratory insertion of carbon monoxide into Th−H and Th−CH₃ bonds has also been examined.

(5)

(6)
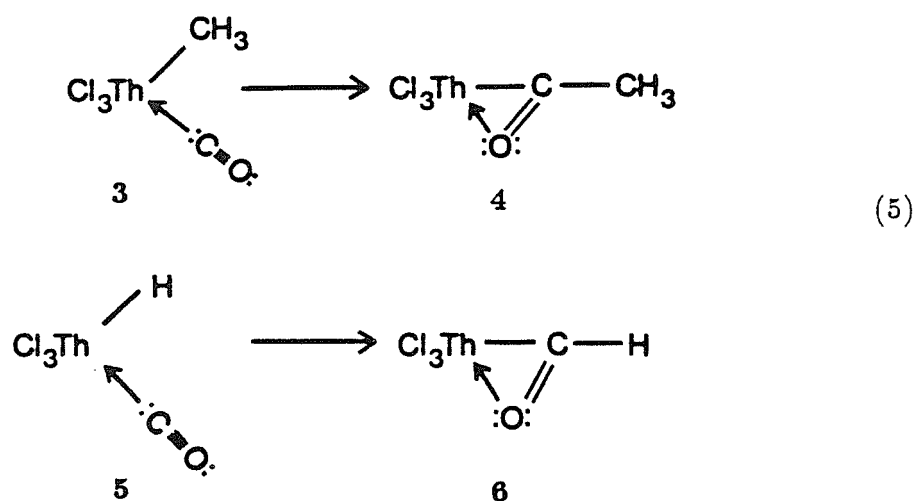
Formation of the coordinated CO species, **3** and **5**, is downhill by 10 and 8 kcal mol^{-1} for Th$-$H and Th$-$CH$_3$, respectively. The enthalpies of CO insertion are -2.4 for the hydride and -6.0 for the methyl complex. The reaction pathway for the Th$-$H insertion was studied using geometries obtained by scaling the bond distances between the reactants and products. The upper bound to the barrier was determined to be 60 kcal mol^{-1}. The reaction mechanism involves attack of the M$-$R bond on the C of the coordinated CO.
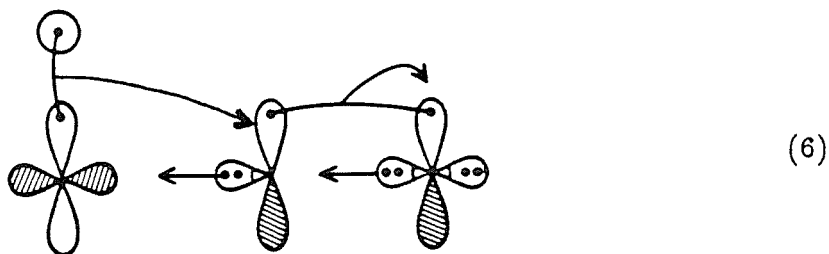
The in-plane polar (towards O) π bond moves over to become another O lone pair. The M$-$C and C$-$O σ dative bonds rehybridize to form covalent bonds.

1. Introduction

In recent years there has been marked progress in preparing organometallic compounds of nontransition metal systems, especially the lanthanides and actinides.[1a−h] This interest has been sparked by predictions that organometallic complexes of the f-block elements may have markedly different properties and reactivities than those of their transition metal (TM) cousins. Differences involve (1) the large size of the metal orbitals, which is expected to allow for an extended coordination sphere and (2) the intriguing possibilty of metal-ligand bonds using f orbitals. For the most part, however, the organometallic chemistry of the actinides and lanthanides has paralleled that of the tranisition metals. Nevertheless, certain systems [e.g., involving the elements Lu, Th, and U] enjoy (in our opinion) both a richer and more diverse metal-carbon chemistry than the TM — and in many cases similar reactions proceed faster at these centers than at TM. We shall discuss in later sections catalytic reactions that occur with Th and U but do not occur at TM.

A major obstacle in treating these systems computationally is the large number of electrons per atom (ninety for Th). Only with the development of effective core potentials (ECP) has this been possible. There are two difficulties. Because of limitations on computer time and space (memory, disk) full electron ab initio calculations on such systems rapidly become impractical. Even more important, however, is that relativistic effects are of essential importance for these elements and cannot be ignored for the actinides. Fortunately, relativistic core potentials have been developed for many of the lanthanide elements and Th. These potentials replace the core electrons with a (nonlocal) field that takes into account relativistic effects along with electrostatic and orthogonality

effects. This allows the molecule to be studied with explicit treatment of only the valence electrons. This ECP approximation is valid for situations in which the core orbitals do not change significantly. Thus, the ECP approach generally provides accurate results for chemical processes. More detailed information on this topic can be found in the Calculational Details section (2.).

This study is designed to assess both qualitatively and quantitatively the electronic structure of several organothorium model complexes. The motivation is to compare and contrast the chemistry of thorium with the TM in order to be able to make predictions about chemical reactivity and energetics. We begin with a discussion of the previous experimental work, examining the organometallic chemistry of the actinides.

1.1 Homogeneous Organoactinide Reaction Chemistry

Only the first four elements of the actinide series (Ac, Th, Pa, U) are naturally occurring, with Th and U exhibiting large abundances.[2] The other elements are made during nuclear collisions in reactors and have comparatively short half-lives. Thus the experimental study of actinide organometallic chemistry has been limited almost exclusively to Th and U. The ground state of Th atom has an electronic configuration of $[Rn]7s^26d^2$. Hence, its valence electronic configuration is similar to the Group IVB transition metals (Ti, Zr, Hf), which also possess s^2d^2 ground states. However, Th has low-lying f orbitals so that the ground state of Th^{2+} has a d^1f^1 configuration (Ti^{2+}, Zr^{2+}, Hf^{2+} have a d^2 configuration). The principal *formal* oxidation state of Th is +4. From these electronic configurations, we might expect Th reaction chemistry to parallel that of the Group IVB metals, with the possibility of f orbitals playing a role for the +2 oxidation state.

On the other hand, uranium has a ground electronic configuration of

$[Rn]7s^2 6d^1 5f^3$. Its principal *formal* oxidation states are +3, +4, +5, and +6, with the latter most stable. Thus U reaction chemistry is expected to be more exotic than Th due to the existence of several oxidation states and the presence of occupied f orbitals. In reality, the organometallic chemistries of Th and U are both similar to group IVa transition metal chemistry. For example, the following compounds can be synthesized via the same routes for both Th and U.[1a,3a-l]

$$C^*_{p_3}MX + RLi(\text{or } RMgX) \rightarrow C^*_p \cdots M - R + LiCl \ (\text{or } MgCl_2) \tag{7}$$

$$C^*_p MCl_3 \cdot 2S \quad \text{(8)}$$

$$C^*_{p_2} MCl_2 \quad \text{(9)}$$
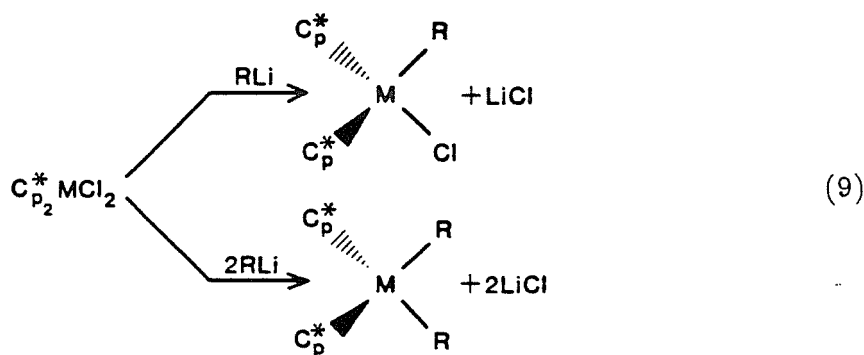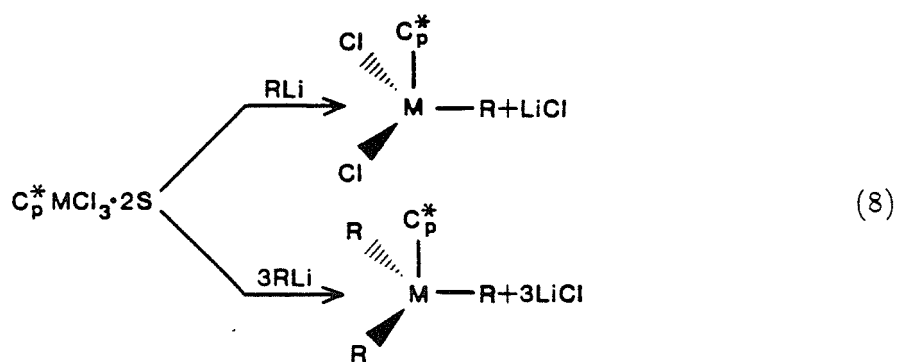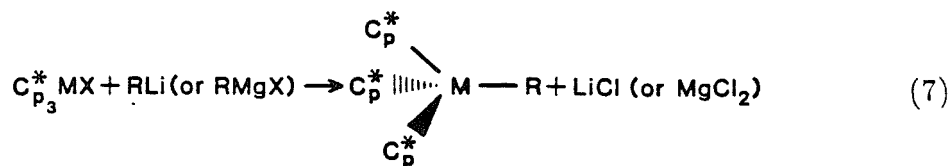
M = Th, U
X = Cl, Br, I
R = alkyl, aryl, alkenyl, alkynyl

These Cp [Cp $\equiv \eta^5$-C_5H_5] and Cp* [Cp* $\equiv \eta^5$-$C_5(CH_3)_5$] halide complexes are precursors of organometallic compounds for both Th and U. For Th, these are "saturated" complexes, with four ligands to match with its four valence electrons. The Cp and Cp* ligands are generally believed to remove charge from the metal.[4] If one electron was ionized from the metal by each ligand (thereby creating an aromatic Cp$^-$ group), the overall charge on the metal would be $+2$. Since the ground state of the dication of thorium has occupied f orbitals, we might expect that the f's may influence thorium chemistry greatly, possibly in a different direction than the TM.

The major difference between U and Th chemistry is that U can have an expanded coordination sphere. For example, the U complexes below have been synthesized,[5a,b] whereas the analogous Th compounds have not.

$$(10)$$
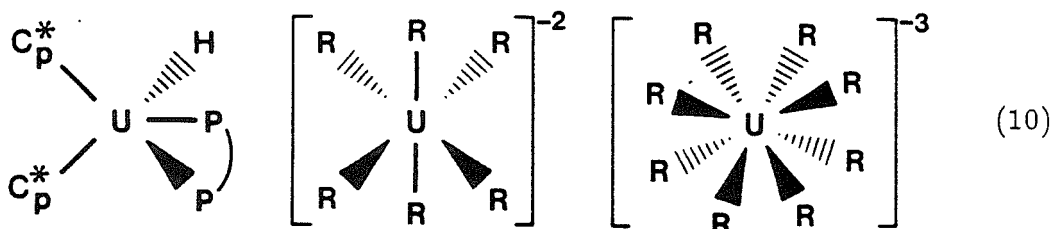
However, most U compounds of interest have the same number of ligands (four) as the saturated Th complexes. Even though U has much more energetically accessible f orbitals than Th, the chemistry is similar. In contrast to the oxidation state arguments above, this implies that the effect of f orbitals may be small in both Th and U complexes.

The chemistry of the actinide-carbon bonds is extremely diverse. Typical reactions involve C−H activation, cyclometallation (models for metathesis), CO migratory insertion, and metal-carbon, metal-oxygen, and metal-hydrogen bond

formation. All of these reactions involve rearrangements and transformations of hydrocarbons and hence are of critical interest to the petroleum industry. In general, the reactivity of the Th complexes is greater than that of the analogous U compounds.[1a,3j] Examples of these reactions follow.

$$C_p^* \diagdown Th \diagup CH_2C(CH_3)_3 \diagdown CH_2C(CH_3)_3 \longrightarrow \quad \text{(Ref. 7) (11)}$$

(Ref. 7) (11)

(Ref. 3j,8) (12)

$$+ 2ROH \longrightarrow \quad + 2CH_4 \qquad \text{(Ref. 3j) (13)}$$

$$+ 2CH_3\overset{O}{\underset{\|}{C}}CH_3 \longrightarrow \quad \text{(Ref. 3j) (14)}$$

$$+ CO \longrightarrow \quad \text{(Refs. 9a–d) (15)}$$
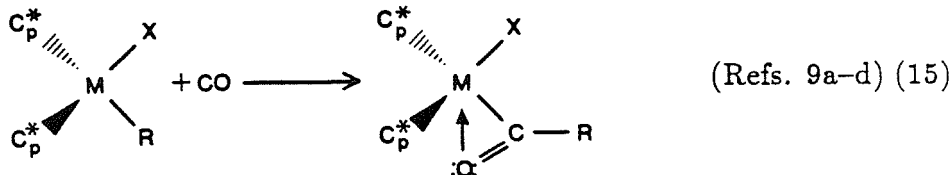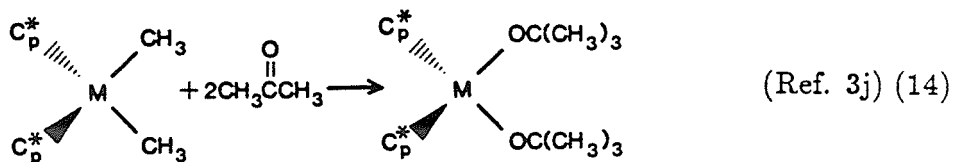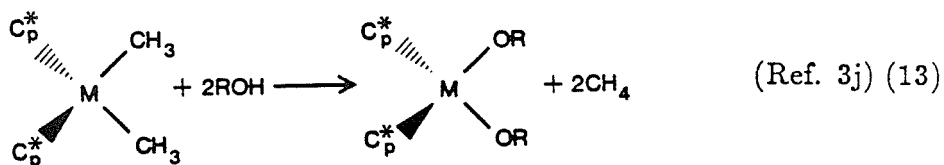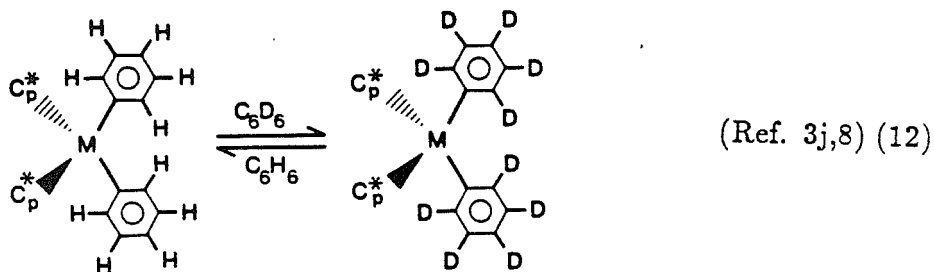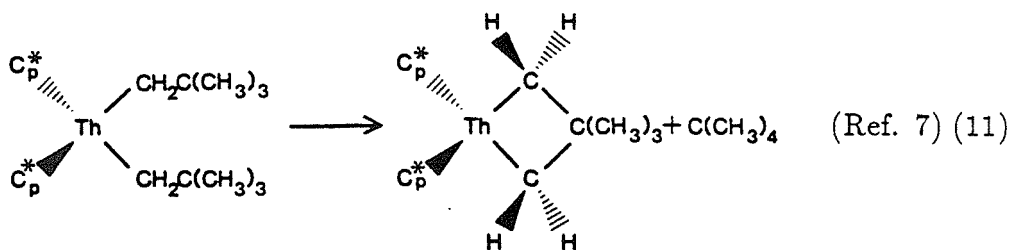
m = Th,U

x = Cl

R = hydrocarbyl

Actinide-hydrogen bonds can be formed easily from the reaction of $Cp_2^*M(CH_3)_2$ (M = Th, U) with hydrogen.[3j]

$$2 \quad \begin{array}{c} C_p^* \\ \diagdown \\ C_p^* \end{array} M \begin{array}{c} CH_3 \\ \diagup \\ CH_3 \end{array} + 4H_2 \longrightarrow \begin{array}{c} C_p^* \\ \diagdown \\ C_p^* \end{array} M \begin{array}{c} H \\ H \\ H \end{array} M \begin{array}{c} C_p^* \\ \diagup \\ C_p^* \end{array} + 4CH_4 \quad (16)$$
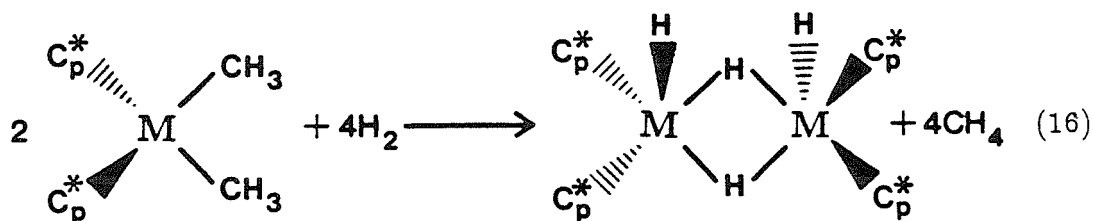
Neutron diffraction studies[9] of the crystalline form of the dimeric thorium hydride species indicate that the structure of the dimer involves two bridging and two terminal hydrogens with an overall molecular symmetry of C_2. In solution, NMR evidence indicates that there is rapid interchange of the terminal and bridging hydrogen atoms.[10] This suggests that there could be some amount of the monomer present in equilibrium with the more stable dimer.

The Th−H and U−H bonds rapidly exchange deuterium, much faster than the Ti and Zr analogs.[11a,b] In addition, they react quantitatively with methyl chloride to produce methane.[10]

$$\{Cp_2^*M(\mu - H)H\}_2 + 4CH_3Cl \longrightarrow 2Cp_2^*MCl_2 + 4CH_4$$

$$(17)$$

$$M = Th, U$$
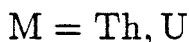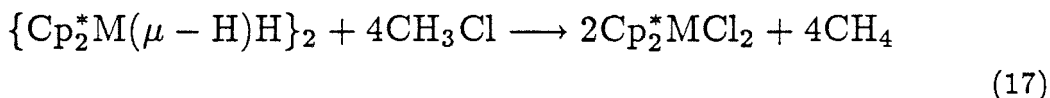
Oxidative addition and reductive elimination steps are ruled out as mechanisms because of the degree of saturation at the metal center (no valence electrons are available to participate in such mechanistic steps). Similar concerted reaction mechanisms are also implicated in the hydrocarbyl reactions [see Eqs. (11)-(15)].[1a] Ab initio calculations on the model exchange reaction of Cl_3ThH with H_2 will probe the chemistry of these systems and help to explain via a concerted "2+2" mechanism why these processes occur.

The hydrides are reactive with many types of ligands. Some of the first

unambiguous evidence for CO insertion into a metal-hydrogen bond involved the carbonylation of a thorium hydride complex at low temperatures.[12a,b]

$$
\begin{array}{c}
Cp^* \\
\diagdown \\
Th \\
\diagup \quad \diagdown \\
Cp^* \quad OR
\end{array}
\begin{array}{c} H \end{array}
+ CO \rightleftharpoons
\begin{array}{c}
Cp^* \\
\diagdown \quad :O: \\
Th \text{---} C \text{---} H \\
\diagup \quad \diagdown \\
Cp^* \quad OR
\end{array}
\qquad (18)
$$
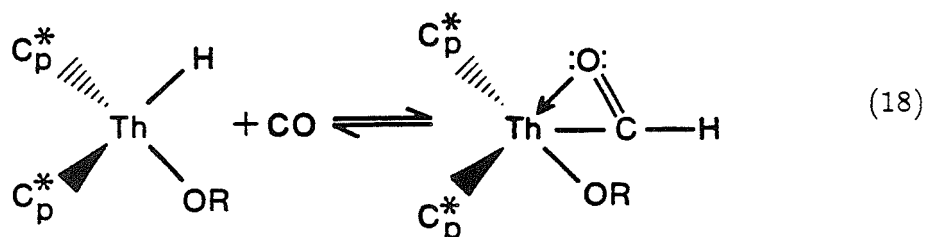
Thorium hydrides also act catalytically to hydrogenate terminal olefins.[3j].

$$
\begin{array}{c}
\diagup\diagup \\
R
\end{array}
+ H_2 \xrightarrow{[M(Cp^*)_2(u\text{-}H)H]_2}
\begin{array}{c}
H \qquad\qquad H \\
\diagdown\diagup\diagdown\diagup \\
R
\end{array}
\qquad (19)
$$
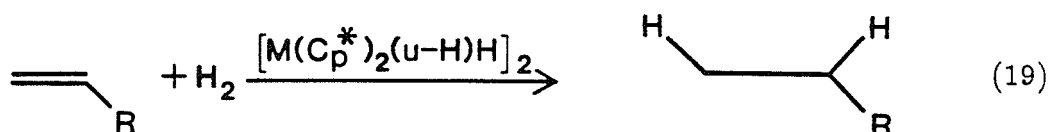
In summary, the homogeneous organometallic reaction chemistry of Th and U is very similar. The chemistry is diverse, and because of saturation at the metal centers, concerted processes (rather than oxidation and reduction mechanisms) seem likely as the major pathways for reaction. Many of the reactions of Th and U have parallels in Group IVB transition metal chemistry, with the actinide reactions generally proceeding faster (and often catalytically).

1.2 Heterogeneous Organoactinide Reaction Chemistry

Marks and co-workers discovered that certain organometallic complexes of uranium and thorium exhibit catalytic activity towards olefin hydrogenation and polymerization when supported on alumina.[13a-e] For example, propylene is hydrogenated at a turnover frequency, N_t, of ≈ 0.5 s^{-1} by alumina-supported $Cp_2^* M(CH_3)_2$, M = Th, U.[13e] These supported organoactinides are about ten times more active as catalysts for propylene hydrogenation than supported Pt systems (Pt/SiO_2) under similar reaction conditions.[13e,14] However, little or no catalytic activity is observed for the same unsupported complexes in solution. For

instance, the hydride complexes $\{Cp_2^*M(\mu_2\text{-}H)H\}_2$ (M = Th, U) have only small hydrogenation turnover frequencies of $\approx 1.5 \times 10^{-4}$ s^{-1} for Th and $\approx 1.9 \times 10^{-2}$ s^{-1} for U under homogeneous conditions.[13a,c,15] Furthermore, the homogeneous complexes are only slightly active (U) or inactive (Th) for ethylene polymerization. On the other hand, the above supported organoactinide complexes will continue to adsorb ethylene even after 45 pulses (100% initial adsorption, levelling off to 30% adsorption by the forty-fifth pulse).[11e] Hence, the interaction between the alumina and the organoactinide complex determines the catalytic reactivity of these systems.

1.2.1 Hydroxylation of Alumina Surface

An investigation of the dependence of the catalytic activity upon the degree of hydroxylation of the alumina surface led to an unexpected result. Catalytic hydrogenation was only observed on an alumina surface that was totally dehydroxylated (DA) prior to reaction with the organoactinide complexes. Partially dehydroxylated alumina (PDA) adsorbed the complexes but further reaction with alkenes and hydrogen was not observed. The speculation was that two different types of bonds had been formed to the alumina surface due to the presence of Al-OH bonds. For the PDA surface, the reaction of Th-CH$_3$ bonds with the surface was envisioned to take place at the hydroxyl groups producing methane and Th-O-surface bonds as shown below.

$$\text{(20)}$$
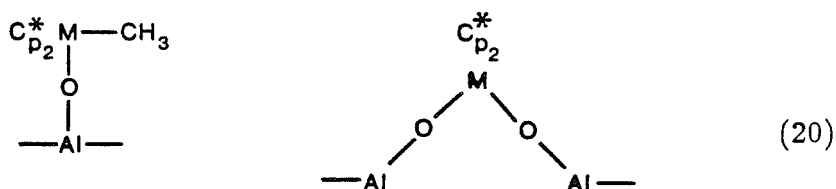
This type of reaction is very common in solution chemistry of organoactinide complexes (see Section 1.1) and hence a high probability exists that it occurs readily on the PDA surface. On the DA surface, reaction of Th-CH$_3$ groups with the surface must occur through another mechanism since there are no Al-OH linkages. This mechanism has been speculated upon by Marks and his coworkers, but it is much less certain what the entire processes entails.

From ^{15}C NMR studies of thorium-methyl complexes on the PDA surface, it was found that there was an upfield shift in the CH$_3$ peak — similar to that observed in neat Cp*Th(CH$_3$)X complexes, where X is an electron-withdrawing ligand (e.g., Cl or O). Hence, the possible species in (20) seem to be likely candidates. Similar NMR studies on DA indicate that Al-CH$_3$ species are very likely to be present on the surface. Possible surface moieties, involving either complete or partial methyl transfer to the surface from Th, include:

$$\tag{21}$$
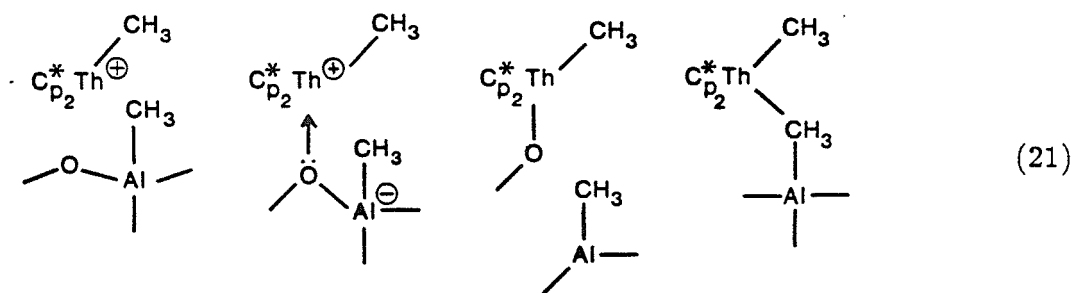
1.2.2 Carbon Monoxide Poisoning

Carbon monoxide was injected over the Cp$_2^*$M(CH$_3$)$_2$/DA catalysts in both He and H$_2$ streams.[13e] After CO adsorption, N$_t$ values were less than 10% of their usual values, with no increase in turnover rates with time. Analysis of the effluent gases showed that only 0.025 molecule of CO per metal atom had been adsorbed by the alumina. This indicates that the percentage of sites active for catalysis must be small. However, when the catalysts were then subjected to a

stream of hydrogen and propylene at -63°C, catalytic activity was slowly regained for the catalysts saturated with CO in He, but not for the cases saturated with CO in the presence of H_2. Thus two different CO species may be present on the surface. No CO (within the limits of experimental accuracy) was adsorbed by the $Cp_2^*M(CH_3)_2$/PDA catalysts and no CO was adsorbed on the bare surfaces of DA or PDA. Marks has speculated that the CO may insert into actinide-carbon bonds. In homogeneous reaction chemistry, such insertions occur readily for various Th and U complexes (see   Section 1.1). These homogeneous results found for CO are in agreement with observations on DA and PDA. With PDA, most of the CH_3 groups are gone from the surface; hence, there are few alkyl groups for the CO to react with. On the other hand, on DA, the presence of CH_3 groups allows the CO to react with the surface. The removal of Th-C bonds then leads to a drop in the catalytic activity.

1.2.3 Ligand Effects

Marks and co-workers also investigated the effect of hydrocarbyl ligand upon the rate of hydrogenation of propylene.[13e] They did experiments with the following compounds on DA: $Cp_3^*U(CH_3)$, $Cp_2^*U(CH_3)Cl$, $Cp_3^*Th(n-C_4H_9)$, $\{Cp_2^*Th(\mu-H)H\}_2$, $Cp_2^*Th[CH_2C(CH_3)_3]_2$, and $Cp^*Th(CH_2C_6H_5)_3$. The $Cp_3^*UCH_3$ and $Cp_2^*U(CH_3)Cl$ complexes were found to be inactive for propylene hydrogenation. Although $Cp_3^*Th(n-C_4H_9)$ is inactive at 100°C, its activity towards hydrogenation increases at higher temperatures ($N_t = 0.40$ s^{-1} at T = 250°C). The hydride complex is about as active as the dimethyl Th complex ($N_t = 0.66$ s^{-1} at T = 100°C). Lastly, the neopentyl and benzyl ligand complexes were more reactive than the dimethyl, with $N_t > 3.0$ s^{-1} at 130°C for the benzyl complex. These results show that the effect of ancillary electron-withdrawing ligands, such as Cl

and Cp*, is to depress the catalytic activity. Electron-donating ligands increase the activity. The effect of steric interactions is not as clear-cut. For example, the complexes with three bulky Cp* ligands were not good catalytic agents, whereas the complex with three bulky benzyl ligands was the best catalyst in the entire study! Thus, we can conclude that catalytic activity depends primarily on electronic rather than steric effects. Of course, other ligands must be studied to fully ascertain the magnitude of steric versus electronic effects.

1.3 Previous Theoretical Work

The previous theoretical work on the actinides has been very sparse. A few semiempirical calculations have been reported on small U and Th systems. For example, UO_2^+ and $U-CH_3$ have been examined with extended Hückel techniques by Hoffmann et al.[16a,b] Ab initio studies are even sparser. The uranium fluorides, UF_6 and UF_5, have been examined by Hay et al.[17] at Los Alamos using the first U relativistic effective core potential (RECP). Subsequently, an RECP was developed for Th by Wadt and the electron and molecular structure of ThO_2 and UO_2^{2+} was examined.[18] To date there have been no ab initio calculations reported on thorium or uranium organometallic complexes.

1.4 Motivation

The motivation behind this work is to obtain fundamental knowledge of the nature of the bonding of an actinide, thorium, to various ligands, especially carbon and hydrogen, since these are involved in much of the interesting organometallic reaction chemistry. From the first two sections of the introduction, it can be seen that thorium organometallic chemistry has a very promising future for the production and manipulation of hydrocarbon feedstocks. The

catalytic activity of organothorium and organouranium complexes supported on alumina is of much importance in the commercialization of alkene hydrogenation processes. However, even with this rich chemistry, there is little knowledge of the qualitative and quantitative description of the electron structure in these complexes. We feel that this knowledge would help greatly in addressing unanswered questions from the known chemistry and in predicting the future of this chemistry.

Questions we would like to answer include:

(1) How do Cp ligands bond to Th? What is the oxidation state of the metal after two Cp ligands are bound? Can we mimic the effect of a Cp ligand with a more computationally efficient (smaller) ligand?

(2) What is the nature of the Th-ligand bonding interaction? Is it covalent or ionic? What is the hybridization? Do f orbitals play any role?

(3) How do Th-ligand bonds compare to Group IVB-ligand bonds? Do these differences and/or similarities manifest themselves in the reaction chemstry?

(4) What is the reaction pathway of substitution reactions at Th? Is there a change of oxidation state at the metal center?

(5) What are the energetics of these reactions? What are the barrier heights? What does the transition state look like? Do these energetics depend on the degree of saturation at the metal center or on the oxidation state of the metal? What effect does metal-ligand bond ionicity have on the activation energies?

(6) What are typical bond dissociation energies of Th-C, Th−H, and Th−O bonds? How does the theory compare with the experimental bond energies? What are the implications, in terms of complex reactivity, of differences in metal-ligand bond strengths from one ligand to another? Does this mean

that certain reaction pathways may be shut off if there are strong metal-ligand interactions?

(7) What is the nature of CO insertion reactions at Th? What happens to the orbitals at the transition state? What implications does this have for the CO poisoning reactions on organoactinide-treated DA?

Before describing the results, we outline the computational aspects of the methods used to examine the Th ligand complexes.

2. Calculational Details

2.1 Relativistic Effective Core Potentials (RECP) and Basis Sets

Thorium has 90 electrons, all of which must be carried along at every step of an ab initio calculation on Th-containing molecules. However, of these 90 electrons, only the four valence electrons change significantly as bonds are formed and broken. The other 86 electrons retain almost exactly the same shape and mainly play the role of ensuring that the valence electrons do not collapse into the core. Fortunately, methods have been developed for replacing these 86 core electrons with an effective potential such that the remaining four valence electrons are described in the same way as if the core electrons were present. The basic ideas were developed by Kahn, Melius, and Goddard,[19] expanded to include relativistic effects by Kahn, Hay, and Cowan,[20] with the modern programs developed by Kahn and Melius.[21] With well-optimized ECP's, accuracies of better than a kcal mol^{-1} are possible. Since the computational time for ab initio calculations scales as N^4 (where N is the number of contracted basis functions), it is clear that ECP's are essential for studies of actinide complexes.

A problem peculiar to "heavy" atoms, such as the third-row transition metals, the lanthanides, and the actinides, is the relatively large influence of rela-

tivistic effects on electronic structure.[22] These effects result from the decreased kinetic energy associated with rapidly changing potential and become very large for systems having nuclear charge over fifty-seven (La). Because of this decrease in kinetic energy, the orbitals contract towards the nucleus to further decrease the potential energy. This orbital contraction is largest for the orbitals closest to the nucleus (largest potential gradient). Hence, the 1s orbital is stabilized the most by the relativistic effects. This contraction of the 1s leads to additional contraction of the other ns orbitals (because of changes in the orthogonality and shielding). The 2p orbitals (and therefore the other np orbitals) also are somewhat stabilized (contracted), but orbitals with higher principal quantum number contract little and may expand (due to the higher shielding of the nucleus by the contracted s and p electrons). These changes lead to significant shifts in the orbital energy levels with the s and p orbitals (atomic orbitals) stabilized (lower orbital energy) and the d and f orbitals destabilized. In addition to energetics, the molecular structure properties are also affected by relativistic effects. Bonds involving s and p orbitals will be shorter and bonds using d and f orbitals will be longer (than expected from a nonrelativistic description).

For Th, the relativistic effects are particularly large and, hence, the effective core potential must include terms to mimic the core and core-valence relativistic interactions. Such an RECP with only the outer ten electrons ($6p^6 7s^2 6d^2$) treated explicitly was developed for Th by Wadt at Los Alamos.[18] We used this RECP, along with a modification of the valence level gaussian basis set originally developed by Wadt. The original basis (LA), given in Table I, consists of 3s, 3p, 4d, and 4f gaussian basis functions contracted to 3s, 3p, 2d, and 2f functions [denoted as (3s3p4d4f/3s3p2d2f)]. We found that the d orbitals are well described with just two *uncontracted* d functions (see Table II); however, we could not

adequately describe the f space with only two primitive functions. Hence, our final Th basis set (3s3p2d4f/3s3p2d2f) (named TH1) consists of 44 contracted basis functions. A truncated basis without f functions (TH2 - 24 functions) was found to give results in excellent agreement with experimental geometries (see, for example, Section 3.5) and was employed in all geometry optimizations.

The spin-orbit coupling is very large for Th, and it would be important to include these coupling effects for valence open-shell (non-singlet) configurations (e.g., the ground state of Th). However, all the organometallic systems in this study are saturated (singlet-paired), so that spin-orbit correlations have not been included in our calculations.

All electrons on the ligands were treated explicitly except for Cl, for which an ECP[23a] was used to replace the $1s^2 2s^2 2p^6$ core electrons. In addition, we used a valence minimal basis on the Cl, with the contraction optimized for $TiCl_4$.[23b] Two different sets of basis functions were used for H atom. When the H was bound to the metal, the unscaled triple-ζ contraction of the six-gaussian basis of Huzinaga[24] with the unscaled p function ($\zeta = 1.0$) of Bair and Goddard[25] was used. When the H was bound to a carbon or oxygen, the scaled (scale factor 1.2) double-ζ contraction of the four-gaussian basis of Huzinaga was used. One exception was the study of CO migratory insertion into a Th−H bond. For the $Cl_2Th(CO)(H)$ and Cl_2ThCOH complexes, the unscaled s and p basis sets were used so that the energetics of the two species could be compared. For C, O, and N, we used the Dunning[26] double-ζ contractions (3s2p) of the Huzinaga (9s5p) primitive bases and one set of d polarization functions[25] ($\zeta_C^d = 0.64, \zeta_N^d = 0.76, \zeta_O^d = 0.95$). For S we used the Dunning double-ζ contraction of the Huzinaga (11s7p) basis and one set of d polarization functions[25] ($\zeta_S^d = 0.532$).

All electrons of Ti and Zr were considered explicitly. The bases for Ti and

Zr were developed by Rappé and Goddard[27] using the same methodology. In all cases a double-ζ valence contraction was used. A set of 5d primitives was employed on Ti.[28] The RECP developed at Los Alamos by Hay and Wadt[29] was used to replace the inner core electrons of Hf [Nd]. The outer 12 electrons of Hf ($5s^2 5p^6 6s^2 5d^2$) were then treated explicitly using the double-ζ valence contraction of the associated Los Alamos Hf basis set (5s5p3d/3s3p2d).[29]

2.2 Wavefunctions

2.2.1 SCF

The simplest ab initio wavefunction is the restricted Hartree-Fock (HF) wavefunction. For an N electron system with total spin S = j/2 the wavefuction is a Slater determinant with j singly occupied orbitals and n = (N - j)/2 doubly occupied orbitals.

$$\Psi = \widehat{\mathcal{A}}[(\phi_1 \phi_1 \alpha\beta) \cdots (\phi_2 \phi_2 \alpha\beta)(\phi_n \phi_n \alpha\beta)(\phi_{n+1} \cdots \alpha \phi_{n+j} \alpha)], \qquad (22)$$

where $\widehat{\mathcal{A}}$ is the antisymmetrizer, n is the number of closed-shell orbitals, and j is the number of open-shell high-spin coupled orbitals. All the orbitals are then determined self-consistently. For all gradient geometry optimizations except for the CO insertion processes, HF wavefunctions were used. It was found (see Section 3.5) that this level of wavefunction gives excellent geometries.

We also used several higher order wavefunctions that include the effects of electron correlation. The simplest wavefunction including electron correlation is the Generalized Valence Bond (GVB) method.[30] In this wavefunction, each electron in a bond pair is allowed to have its own orbital, which is then optimized self-consistently to obtain the best possible shape while allowing the two orbitals

of the pair to overlap.[31] Thus, one doubly occupied orbital, say, $(\phi_n \phi_n \alpha\beta)$ of (22), is replaced by

$$[\phi_l(1)\phi_r(2) + \phi_r(1)\phi_l(2)](\alpha\beta - \beta\alpha). \tag{23}$$

Generally, the optimum GVB orbitals localize on one or two atoms whereas the HF wavefunction leads to delocalized doubly occupied orbitals. Thus the GVB wavefunction of Cl_2ThH_2 leads to two orbitals per Th−H bond pair, with one electron localized on the Th and one on the H in each bond (see Fig. 3d). We find that correlation of the electrons included in the Th core and on the Cl are less important and consequently these electrons are described with doubly-occupied orbitals (they are optimized self-consistently). The wavefunction in which just two-electron pairs are GVB correlated (with a total of four electrons) is denoted GVB(2/4).

The two GVB orbitals for a covalent bond will generally have one centered on each of the atoms in the bond. Thus, as above for the dihydride, each metal-hydrogen bond has one orbital centered on the metal and the other centered on the H atom. (This is called left-right correlation: when one electron 1 is on the right, electron 2 is more likely to be on the left, and vice versa.) The degree of ionicity in a bond can be evaluated by the amount of character that the GVB orbital has on the opposite atom. For a totally ionic system or for a system with a lone pair, both GVB orbitals are centered on the same atom.

In general, only the electrons that change during a chemical process are correlated. The remaining electrons are left in doubly occupied orbitals. Thus, in the dihydride example above, the Th 6p electrons and the Cl electrons are treated as doubly occupied, just as in HF. Our approach is first to optimize the geometry of a molecule at the HF level and then to correlate all the important

valence electrons at the GVB level. Tests were conducted to determine whether a higher level of wavefunction would markedly change the optimized HF geometry (see Section 3.4); only small geometry changes occurred. In all GVB calculations, all Th-ligand bonds (except for Th−Cl) were correlated. In addition, appropriate intraligand bonds were correlated. For example, for cases with a CH_3 group bound to the metal, the Th−C bond was correlated but not the C−H bonds. However, CO is not well described at the HF level so that when a CO was bound to the metal, it was necessary to correlate not only the Th−C bonds but also the three bond pairs comprising the triple bond in CO and, in addition, the O 2s and $2p_z$ lone pairs (since the O lone pairs may interact with the metal).

The GVB wavefunction described above involved only one spin-coupling or VB bonding structure. (Hence, it is often referred to as the perfect-pairing or GVB-PP wavefunction.) This is often a good qualitative approximation, but for most systems, particularly metals, additional electron correlation and spin couplings are required for an accurate description of the bonding. The electron correlation missing from the GVB-PP wavefunction is called dynamic correlation since it involves correlation between bonds (as opposed to the static correlation of GVB-PP which is mainly intrabond pair correlation). The additional spin coupling configurations would include other resonance bonding configurations and, in the case of transition metals with high spin coupled electrons, intra-atomic exchange interactions. These possibilities are implicit in the totaly generalized form of the GVB wavefunction [termed a multiconfigurational self-consistent field (MCSCF) GVB calculation]. However, the calculations are considerably faster, and, for most systems, adequately accurate, when a single spin-coupling is used (perfect-pairing) as in (23). Consequently, the procedure used in these calculations was to optimize the orbitals for the restricted GVB-PP wavefunction and

then to include the effects of other spin couplings with a limited interaction (CI) calculation.

2.2.2 CI

In a configuration interaction (CI) wavefunction, we consider a linear combination of n-orbital wavefunctions

$$\Phi^{CI} = \sum_i C_i \Phi_i, \tag{24}$$

where each wavefunction Φ_i involves a set of doubly and singly occupied orbitals. The orbitals in Φ_i are selected from the occupied and empty (virtual) orbitals of the SCF wavefunction. For each occupation of these orbitals (spatial configurations), all possible spin pairings of the electrons (spin eigenfunctions) are included. The spatial orbitals used from the SCF calculation (HF or GVB) are transformed from the original atomic (AO) basis to the final set of orbitals from the SCF calculation [molecular orbital (MO) basis]. If all possible Φ_i are used (i.e., all excitations of electrons to all the orbitals of the basis) then the wavefunction is termed a full CI. In practice, only a small fraction of the full CI is possible. Various procedures have been developed to select an appropriate subset of configurations to describe, say, the correlation involved in bond rupture. Two important points of relevance for a bond dissociaton CI wavefunction are:

1) the configurations selected should be a dissociation consistent wavefunction; i.e., the wavefunction should be able to go smoothly from describing the molecule at equilibrium to the same level of description of the appropriate molecular fragments at infinite separation, and

2) the wavefunction should effectively include the major electron correlation that changes upon dissociation of the bond pair(s) of interest.

In most calculations, it is an energy difference which we need — a bond energy or excitation energy. Since the GVB orbitals are localized, it has been possible to develop a general approach to include the configurations missing from the GVB wavefunctions that affect a specific energy difference and thereby to obtain accurate energy differences from relatively simple and interpretable CI wavefunctions.

These procedures were first developed by Bair and Goddard[32] (dissociation-consistent CI) and later simplified and extended by Carter and Goddard[33] (correlation-consistent CI). The starting point is the GVB-PP wavefunction. The orbital space is divided into three parts: the active, the semi-active, and the core. The active space consists of orbitals involved in the bonds being changed in the process of interest. The semi-active space consists of any other orbitals that interact with the atoms of the bond. The core orbitals are other orbitals that change little during the process. These core orbitals can be incorporated as a nonlocal field during the integral transformation that proceeds the CI and hence are completely eliminated from the CI. One can describe a large number of dissociation-consistent CI's with successive inclusion of additional molecular correlation.

The simplest extension beyond the GVB-PP wavefunction used to determine the orbitals is to allow the two electrons of each GVB pair to occupy the two orbitals of the pair in all three ways. For a system with eight GVB pairs, this *restricted configuration iteraction* or RCI would lead to 3^8 configurations. The RCI includes the spin-coupling terms ignored in the simple GVB-PP.

The highest level wavefunction for a given set of occupied orbitals (called a GVB-CI) consists of a full CI within the active and semi-active orbital space. The GVB-RCI and GVB-CI are useful in comparing the energetics along a reaction

pathway (activation barriers) and for comparing energetics of product and reactant molecules. However, for accurate bond energies, higher order correlation-consistent CI's are necessary.

In this work we carried out a full CI (excluding the core orbitals — often referred to as a full valence CI) whenever the number of valence electrons was three or less. For more valence electrons, either an RCI*S_{val} or CCCI (correlation-consistent CI) was used. The RCI*S_{val} allows all single excitations from the RCI reference configurations to all the virtual orbitals. The CCCI allows all the RCI*S_{val} configurations plus all single and double excitations from each bond pair individually (not simultaneously). The CCCI allows for full correlation of the bond pairs (RCI*SD) and readjustment of the other orbitals (RCI*S) and is dissociation consistent (as is all the other CI's based on GVB orbitals previously described). In some cases, because of calculational size, a slightly truncated version of the CCCI was used where all single and double excitations were allowed only from the bond breaking plus the usual RCI*S_{val} from the rest of the active and semi-active space. This will be noted in the appropriate table or figure.

As an example, for the determination of the Th−H bond energy in the complex Cl_2ThH_2, the molecule was first treated at the GVB(2/4) level with each Th−H bond correlated with two orbitals one per each electron. The wavefunction was transformed to the basis of GVB natural orbitals with all the other occupied orbitals treated as a fixed field. The following CI's were then used on the complex: RCI(2/4), GVB-CI(2/4), RCI(2/4)*S_{val}, and a CCCI.

In order to determine the bond dissociation energy, the energy of the molecular fragments at infinite separation (Cl_2ThH and H·) must be calculated at consistent levels. For all the above CI wavefunctions, the limiting wavefunction of H is just the normal wavefunction for H·. For Cl_2ThH, the RCI(2/4) separates

to an RCI(1/2), the GVB-CI separates to a GVB-CI in the remaining GVB pair orbitals and the high spin orbital, the RCI*S separates to a RCI(1/2)*S_{val}, and the CCCI separates to all singles out of the high-spin orbital simultaneous with singles out of the GVB-RCI configurations of the GVB pair plus doubles from the bond pair (effectively a CCCI on the fragment).

2.3 Gradient Optimizations

The following singlet ground state molecules were optimized with the closed-shell gradient optimization programs of Low and Goddard[34] at the Hartree-Fock (HF) level: Cl_2ThH_2, Cl_2ThH^+, Cl_3ThH, $\{Cl_2Th(\mu\text{-}H)H\}_2$, and Cl_3ThCH_3. Certain symmetry restrictions were maintained. For Cl_2ThH_2, both the Th−H bond distances and both the Th-Cl bond distances were made equivalent, keeping C2$_v$ symmetry. The Cl_3ThH molecule was restricted to be C$_s$. The Th dimeric complex, $\{Cl_2Th(\mu\text{-}H)H\}_2$, was assumed to be of C$_2$ symmetry as per the neutron diffraction crystal structure (see Section 3.5). C$_s$ symmetry was maintained in the Cl_3ThCH_3 complex with one of the methyl protons in one of the Cl-Th-C planes and with the other protons symmetric with respect to this plane - an eclipsed geometry with the Cl's. No symmetry restrictions were imposed on Cl_2ThH^+, but it s optimimum geometry is C$_{2v}$ (see Section 3.6).

The ground states (symmetry and spin) of the open-shell molecules Cl_2Th and Cl_3Th were first determined using bond distances and angles obtained from the gradient optimized geometry of Cl_2ThH_2. Then, the optimum geometries were determined at the HF level using the open-shell gradient programs of Low and Goddard with no symmetry restrictions.

The transition states formed via reaction of H_2 with Cl_3ThH and with Cl_2ThH^+ were found by symmetry restricting the geometries of Cl_3ThH_3 and

$Cl_2ThH_3^+$ to be C_{2v} and C_s, respectively, and then optimizing the geometry as a ground state with the closed-shell gradient programs at the HF level. The plane of symmetry chosen for Cl_3ThH_3 was that which contained the three H's and one of the Cl's (see Section 3.6.2). For the cationic species, the C_{2v} geometry traps the molecule such that it cannot fall apart to the lower energy structures, $Cl_2ThH^+ + H_2$. The C_s restriction for Cl_3ThH_3 does not prevent the molecule from decomposing to $Cl_3ThH + H_2$; however, a local stationary state was found. The other possible plane of symmetry for Cl_3ThH_3 (90° from the other plane) was investigated using the gradient package of Rappé[35] at the HF level.

For the Th$-$H CO insertion process, the η^2-acyl complex, Cl_2ThCOH, and the CO coordinated complex, $Cl_2Th(CO)(H)$, were optimized with the gradient programs of Rappé using a GVB(6/12) wavefunction. The Th, C, O, and H atoms were restricted to lie in one plane with the Cl's bisecting the plane equidistantly (C_s). All of the valence electrons of Th, H, C, and O were correlated. The Th 6p, the C 1s and the O 1s orbitals, and all the electrons on the Cl's were treated as doubly-occupied orbitals. The complexes of the Th-CH$_3$ CO insertion process, the η^2-acyl, $Cl_2ThCOCH_3$, and the CO coordinated, $Cl_2Th(CO)(CH_3)$ were likewise gradient optimized at the GVB(6/12) level. Here, the Th, C, O, and one of the methyl H's were restricted to be in a plane with the other two methyl H's and the Cl's bisecting the plane equidistantly (C_s). Only the geometry where the methyl H's were staggered with respect to the CO was examined. As with the Th$-$H CO insertion, all the valence electrons of Th, C, and O were correlated. However, the C$-$H bonds were left HF.

Other molecules optimized with the Rappé codes included Cl_3ThOH at the GVB(3/6) level and the metal-hydride and metal-methyl complexes, Cl_2MH_2 and $Cl_2M(H)CH_3$, M = Ti, Zr, Hf, and Th, at the GVB(2/4) level.

3. Results and Discussion

3.1 Thorium Atomic Wavefunctions

We use the generalized *valence bond* model for describing bond formation. In this approach, we start with the ground state of the atoms or molecular fragments and spin pair orbitals to form the optimum bonds. Hence, in order to understand the nature of bonding in thorium comlexes, it is necessary first to consider the atomic states of both Th atom and its cations.

Experimental determinations of Th and Th cations atomic excited states have been somewhat limited due to the complications involved in interpreting levels that involve strong LS coupling.[36] Although many lines have been observed in the spectra of Th atom, relatively few of the low-lying states have been identified. In Table III we list the well-established Th atomic state splittings, averaged over J states.[37] The ground state is ^3F (s^2d^2) and the corresponding ^3P state is only ≈ 560 cm^{-1} up. The first state with a configuration different than s^2d^2 is the ^5F ($6d^37s$) state 5168 cm^{-1} above the ground state. The first f configuration, ^3H ($5f6d7s^2$), is at 8500 cm^{-1}.

For Th$^+$ and Th^{++}, the situation is even more complex. Because of strong spin orbital coupling, the lowest lying state of Th$^+$ cannot be assigned to a specific state configuration.[38] The calculations of Minsky[39] (which include a spin operator in the Hamiltonian) indicate that this eigenstate can be described as 43% $^4F_{3/2}$ (s^1d^2) and 27% $^2D_{3/2}$ (s^2d^1). Since there is no dominant component (>50 % character), we have listed this state in Table IV as $(s+d)^3$. Many excited levels also include strong mixing from adjacent levels and are also listed in this way. For this reason, no attempt has been made to average over J states in Table IV. The states of Th$^+$ corresponding to ^4F (s^1d^2), ^2D (s^2d^1), and ^4F (d^3)

are all very close in energy. The lowest lying f states are $^2F_{5/2}$ ($5f7s^2$), and $^4H_{7/2}$ ($5f6d7s$), at 4490 and 6168 cm^{-1}, respectively, above the ground state. The ground state of Th^{2+} has been the subject of some controversy. Originally, Klinkenberg et al.[40] had experimentally measured two distinct sets of Th lines, each with about 40 configurations. However, relative energetics between the two sets of configurations could not be determined. The $^3F_2$ (d^2) was the lowest term in one set; the $^3H_4$ (df) was the lowest term in the other. Klinkenberg determined that one line was an intersystem combination which gave the d^2 term as the ground state 809.9 cm^{-1} below the df state. A later experiment by Litzén[41] discovered ten Th^{+2} lines that were identified as intersystem levels. These firmly established that the difference between the two sets of terms was only 63.2 cm^{-1}. This new analysis leads to the conclusion that the df state is the ground state with the d^2 state the first excited level, 63.2 cm^{-1} above the ground level. In addition, this enables a complete ordering of the levels for Th^{2+}, as shown in Table V. When the levels are averaged over J states, the ^3F ($6d^2$) level is now the ground state with the ^3H ($5f6d$) level 651.0 cm^{-1} higher. There are several states within 1500 cm^{-1} of the ground level. The lowest level with occupied f orbitals is not the 5f6d, but rather the ^3F ($5f7s$), only 135.3 cm^{-1} above the 6d^2 level. Lastly, the known spectrum of Th^{3+} (averaged over J states) is shown in Table VI.[42] The ^2F (5f) state is the lowest state with the ^2D (6d) almost 10000 cm^{-1} above it.

From examining the experimental spectra of Th and its oxidized species, we find definite trends in the relative stability of the s, d, and f orbitals. For example, the relative energy of states involving f electrons is stabilized as the metal is oxidized. Starting with Th atom, the nearest f electron state is over 8500 cm^{-1} above the ground level. As we move to Th$^+$ and Th^{2+} that gap between the

ground state and the nearest f level decreases to ≈ 4490 cm^{-1} and 135.3 cm^{-1}, respectively. For Th^{3+}, the 5f^1 state is the ground state by ≈ 10000 cm^{-1}. In contrast, the stability of the 7s orbital decreases with increasing oxidation of the metal. When Th is oxidized, the electron removed comes preferentially from the 7s orbital as the leading component of the $(6d+7s)^3$ ground state of Th$^+$ is the ^{4}F (7s6d^2) state. However, as alluded to above, there is very strong coupling of this state with the ^{2}D (7s^{2}6d) state. Thus the 7s and 6d orbitals are very close in energy. When a second electron is removed from Th, it definitely comes from the 7s orbital — leaving no electrons in the s orbital. The ^{1}S (7s^2) level is 7792.0 cm^{-1} above the ground state. Finally, when a third electron is removed from Th, the ^{2}S (s^1) state is more than 20,000 cm^{-1} above the ^{2}F and ^{2}D states. The energetics of the s, d, and f orbitals thus depend strongly on the degree of oxidation of the metal atom. When ligands are brought up to the metal, they will change its oxidation state. Hence, it is very important, in describing the bonding of ligands to a metal, to understand what the stability of the orbitals is in the atomic system and what the oxidation state of the metal is, and how the orbital stability changes, when ligands are bound to it.

There has been little previously published in the way of energies for Th atom using the basis sets and potentials from Los Alamos described in the Calculational Details section. Thus we carried out an extensive and comprehensive study of the atomic states of Th, Th$^+$, Th^{2+}, Th^{3+}, and Th^{4+} for both the Los Alamos basis set, LA, and our basis set, TH1. The only difference between the two bases is the d functions. TH1 has two uncontracted d functions whereas LA has three primitive d's with the *outer* two functions contracted together. This rather unusual contraction scheme was based on the total energy of ThO$_2$.[18]

A comparison (see Table VII) of the LA and TH1 basis sets using HF wave-

functions for Th through Th^{+4} reveals that LA gives a lower energy than the TH1 basis for the three low- lying states of Th neutral. However, the TH1 basis correctly predicts the right ordering of the states, whereas LA basis predicts that the ^{5}F (s^{1}d^3) state is lower than the ^{3}F (s^{2}d^2) state by 543.6 cm^{-1}. Experimentally, from Table III, we see that the actual splitting is 5167.8 cm^{-1} in favor of the s^{1}d^3. HF would be expected to bias the calculations for the high spin ^{5}F state. For the ionized species, an interesting trend in the total energies with the LA and TH1 bases is observed. The LA basis results in higher total energies for all the states with occupied d orbitals [except the ^{4}F (d^3) state of Th$^+$] and the difference in energies between LA and TH1 increases as the atom is further ionized. This implies that the LA basis of Wadt is not tight enough to describe the electrons in the cationic species as compared to the TH2 basis. As seen in Tables I and II, the exponents of the inner d gaussians in the LA basis are only very slightly tighter than the two d exponents for the TH1 basis. This suggests that the exponents and/or contraction scheme employed for the TH1 basis are not correct inasmuch as the three primitive d basis should obtain lower total energies than the two primitive basis especially if they were optimized for ThO$_2$, which would be expected to have an oxidized Th atom.

Our results for HF wavefunctions of Th neutral through Th^{4+} species are shown in Table VII. In all cases we have solved only for those eigenstates that are true combinations of real orbitals. The calculated states for Th atom lie very close to the state splittings obtained experimentally, with the ^{3}F (s^{2}d^2) state predicted to be the ground level, 1832 cm^{-1} lower than the ^{5}F (s^{1}d^3) configuration — the experimental splitting from Table III, averaged over j states, is 5168 cm^{-1}. The splitting is smaller than expected because the HF favors the quintet state due to the greater correlation error present in the triplet. For Th$^+$, the ground

level is found to be the ^4F ($7s^16d^2$) state. The next level up is the ^2D ($7s^26d^1$) level. Again, HF will favor the higher spin state. Hence, we would expect that increasing correlation will lead to a decrease in the splitting. For Th^{2+}, we can compare two states with the same spin that have occupied d and s orbitals, namely, the ^3F ($6d^2$) and the ^3D ($6d^17s^1$) states. The d^2 is the ground state both experimentally and with HF, but the splitting to the higher sd state is smaller for HF (1260 cm^{-1}) than that found experimentally (3793 cm^{-1}). This implies that the basis set and/or the HF calculation is biased in favor of the s orbitals versus the d orbitals at least at this oxidation state. There may be more freedom in the s space, since it is treated triple-ζ (see Tables I and II). The enhanced stabilization for the s orbitals (or destabilization of the d's) is also apparent in the splitting between the ^2S and ^2D states of Th^{3+}. The experimental splitting is 20659 cm^{-1} whereas the HF value is only 10966 cm^{-1}. We can also compare the relative stability of the d versus f orbitals for Th^{3+}. The $5f^1$ state is the experimental ground state, but HF gives the ^2D ($6d^1$) level lower by 3502 cm^{-1}. Hence, it appears that the f orbitals are destabilized somewhat with this basis or calculation.

To investigate these orbital stability affects further, full valence level CI calculations ($6p^6$ electrons were cored) were performed on all the Th species. The full CI calculations, since they include all correlations, enable us to separate out the effects of basis set deficiencies from correlation deficiencies. However, since most of our molecular calculations do not include these atomic correlations, the HF results are indicative of the atomic states at the metal when we have ligands.

In Table VIII, the full CI results for Th are presented. They agree very well with the experimental Th spectrum in Table III. The ^3P and ^3F (s^2d^2) states are essentially isoenergetic whereas experimentally the ^3F is slightly lower, 559

cm^{-1}. The ^5F (s^{1}d^3) level is 5877 cm^{-1} above the ^3F state with the full CI and this is very close to the experimental splitting of 5048 cm^{-1}. Since the ^3H (5f^{1}6d^{1}7s^2) is 8500 cm^{-1} above the ground state experimentally but 12738 cm^{-1} above it with full CI, there is a deficiency in the f basis functions. The full CI results for Th$^+$ in Table IX indicate that the ground state is, like the experimental ground level, a mixture of configurations with no term dominant (> 50 %). In our calculations, the Hamiltonian does not permit the mixing of states with different total spin; therefore, the configurations contributing to the ground state are only those corresponding to doublet spin. The breakdown of components was 44 % ^2D (6d^{1}7s^2) and 28 % ^2D (6d^{2}7s^1). The next highest state is the ^4F (7s6d^2) state 2325 cm^{-1} up. Thus the s and d orbitals are very close in energy after the removal of one electron. Further comparisons between theory and experiment are difficult because we cannot average the experimental levels over j states. The Th^{2+} ion full CI spectrum in Table X yields a rather puzzling result for the ground level — the ^1D (6d^2) state falls below the ^3F (6d^2) state by 1092 cm^{-1}. This preference for low spin states in CI calculations on atoms with effective potentials has been observed previously.[43] The explanation for this phenomenon is not known. Although in this case the expermental splitting is quite small, the ^1D level is only 507 cm^{-1} above the ground level. There is a marked preference for d states as opposed to f states. The closest f state is the ^3H (5f^{1}6d^1), which is 7267 cm^{-1} above the ground state whereas actually it is only 1410 cm^{-1} up. As noted above, there also seems to be a small stabilization of the s orbitals. The ^1S 7s^2 level (lowest-lying with s electrons) is 7792 cm^{-1} above the ground level, but for the full CI it is only 6022 cm^{-1} up.

The experimental ionization potentials (IP) and the IP's calculated using the HF and full CI methods are shown in Table XI. Only the 1st and 4th IP's have

been obtained experimentally.[44a,b] The full CI method gives larger IP's than HF since the correlation error is larger for the systems with more electrons (reduced). Both theoretical methods give IP's lower than the actual values because of basis set deficiencies. (These, like correlation error, would lower the energy of the species with more electrons; hence, the IP would be larger.) The implication of this is that it will be slightly easier to ionize the metal, possibly leading to more ionic bonds.

The HF and full CI results show that there is a small stabilization of the s orbitals relative to the d orbitals and that there is a significant destabilization of the f orbitals relative to the s and d's. Both of these effects increase as Th is oxidized. The s stabilization possibly results from the triple-ζ basis used for the s functions as opposed to the double-ζ d and f functions. Having double-ζ f functions is not adequate to fully describe the f space at higher oxidation states. This can be visualized by considering the small radial extent of the f orbitals relative to their d counterparts. Since the f's involved here have principal quantum number one less than the d's, the f's are actually interior to the d orbitals. With higher oxidation state, the f's will be drawn in even tighter. Hence, the conclusion is that in order to treat high oxidation states correctly the f basis must include functions with tighter exponents — probably, triple-ζ is needed. Unfortunately, since each primitive f function added increases the number of basis functions by ten, the total number of functions may well become calculationally impractical. As long as the oxidation state of the metal is sufficiently low, the current basis should be fine for our purposes.

3.2 Cl versus Cp ligands

Almost all of the organothorium complexes have either one, two (most common), or three Cp groups bonded to them in addition to other ligands (see Section 1). The theoretical treatment of these groups is somewhat difficult since even a minimum basis set description would result in needing thirty basis functions per Cp. Hence, it is computationally efficient to develop a replacement ligand that will be smaller than the Cp group, yet have the same electronic effect on the metal. Rappé and Goddard[45] have found such a ligand in Cl. Cl's core electrons are replaced with an EP and the valence electrons are minimum basis. Based on the molecular results obtained, this ligand has been successfully used as a substitute for Cp groups in calculations involving Ti[46] and Ru[47] as well as several other transition metals, although owing to the calculational size of the Cp ligand complexes few if any direct comparisons have been made.

In order to test whether Cl will correctly mimic the electronic behaviour of Cp for Th complexes, we have compared the complexes CpThCl and Cl_2Th using both HF and CI methods (see Tables XII and XIII). The Th-Cp distance used, 2.56 Å, was obtained from the neutron diffraction structure[9] of $\{ Cp_2^*$ $ThH(\mu - H)\}_2$; the Th-Cl distance, 2.73 Å, was obtained from the HF gradient optimized geometry of Cl_2ThH_2. Qualitatively, since the Cp groups are much more electronegative than the transition metals and thorium, the bond between a metal atom and the Cp can be viewed as a complete transference of an electron from the metal to the Cp. Hence for CpThCl and ClThCl (assuming the effect of Cl is similar to Cp), there would be two electrons left on the Th in d orbitals, since the s electrons are easier to ionize (see Section 3.1).

The HF orbital energies, from an average field calculation on the $6d^2$ triplet

state, for the d_σ, d_π, and d_δ orbitals, are listed in Table XII. For both the dichloro and the Cpchloro complexes the ordering of the orbitals is the same — σ lowest followed by δ and π. The σ-δ gap is the same for both molecules to within 0.1 electron-volt (eV). There is a much larger difference in the orbital energy of the π orbitals, however. This difference arises from the ability of the Cp ligand to back-donate electrons to the empty metal orbitals; thus, destabilizing the metal d_π orbitals which point at the filled π symmetry Cp orbitals. Cl likewise has filled π orbitals, $2p_x^2$ and $2p_y^2$, but they are much tighter than for Cp, so they do not back-donate very much. One possible modification to correct for this would be to add a set of diffuse p functions to the basis on the Cl atom.

A full valence CI calculation within the average field d^2 triplet space was also performed. From Table XIII, we see that again the same ordering of states occurs for both complexes. The first excited state, $\delta\bar\delta$, is 1.148 eV and 1.323 eV above the ground state, $\sigma\delta$, for the CpThCl and ClThCl complexes, respectively. All states involving π orbitals are more destabilized with Cp than without it. The $\pi\bar\pi$ state is 5.471 eV up from the ground state for CpThCl, but only 3.926 eV above for ClThCl. As with the HF orbital energies, the destabilization of the π states is due to the lack of Cl backbonding to the Th.

Using Mulliken population analysis (see Table XIV), we compare the electronic charges on the Th, Cp, and Cl's in both complexes, and find that the Cp and Cl ligands pull off, to within $\approx$ .01 electron, the same amount of charge from the Th, approximately 0.5 electrons. Thus the Th in both complexes is left with a charge of +1. Our conclusion is that Cl is an excellent substitute ligand for Cp because Cl and Cp both have the same effect on the overall electronic state of the metal, i.e., charge transferred, and because both give the same ordering of resultant metal electronic states. However, if one is interested in looking at

cases which involve only metal-Cp bonds like ferrocene (Cp_2Fe), or cases in which the metal is highly unsaturated (unbonded electrons on the metal, or low-lying unoccupied orbitals), there will be difficulties with this approach because the Cl ligand does not mimic the backbonding capabilites of Cp. For our cases, in which we are interested in describing metal-ligand bonds in saturated systems, Cl should have the same affect on the other metal-ligand bonds as Cp has.

3.3 Cl_2Th — The Starting Point

The starting point for all the complexes which we are going to model theoretically is Cl_2Th. As discussed in the previous section (3.2), when two Cl ligands are brought up to the bare metal atom two ionic bonds are formed. Initially, the thorium atom will be in the ground, s^2d^2 configuration. Since the s electrons are easier to ionize than the d electrons, most of the charge transferred would come from the s orbitals on the thorium. Electrostatic considerations would thus favor formation of a linear molecule with two electrons remaining ($\sigma\delta$, triplet spin state) in orbitals which are predominantly d in character.

A gradient optimization was carried out on Cl_2Th at the HF level with only s, p, and d functions on the thorium. A local mode optimization was performed which included f functions (HF-f) on thorium. In both cases the optimum geometry obtained is nonlinear (see Table XV). The potential energy surface for the Cl-Th-Cl bending mode is extremely flat; the energy difference (HF-f) between the linear restricted geometry and the fully optimized structure (Cl-Th-Cl = 174.17°) is only 13 microhartrees!

The analogous Cl_2Ti complex is linear. This implies that for Th there are other effects besides electrostatics that contribute to the bonding. The Mulliken populations (see Table XVI) indicate that approximately 0.45 electron is trans-

ferred from the thorium to each Cl. The magnitude of the charge transferred from titanium to Cl is somewhat smaller, 0.41 electron. Thus the Th-Cl bond is more ionic than the Ti-Cl bond which, of course, would favor the linear geometry over the bent in contradiction to the results we find. The bonds to Cl are not totally ionic, however, as shown by the lack of complete charge transfer to the Cl. The electronic population over basis functions, shown in Table XVII, indicates that for both Ti and Th there is backbonding (0.14 electron transferred back from Cl to Ti and Th) from the doubly occupied Cl $2p_x$ and $2p_y$ functions to the metal. The population of the Cl $2p_z$ basis function shows that the metal-Cl bonds are approximately 80% ionic and 20% covalent (ca. 0.2 electron short of complete charge transfer). Since the bond is partly covalent, we must take into account what effects this would have on the geometry.

If we were to make two covalent bonds to the two metal s electrons we would expect the geometry to be linear to minimize steric repulsions (similar to the bonding in BeH_2). Covalent bonds to d orbitals are a different story. It has been shown[46] that the best covalent bonds to d orbitals result in d_σ orbitals which are either 54.7° or 125.3° apart. Thus if the two Cl's were covalently bonded to the two d electrons on the metal we would expect a bent geometry. Is there any reason to expect the Th-Cl bonds to have more metal d character than Ti-Cl bonds? For Ti we know that the d orbitals are quite small because of orthogonality effects (first-row transition metal 3d orbitals have no lower principal quantum number d's), whereas the 4s orbitals are quite diffuse. This leads to a fairly large dichotomy in the stability of the s and d orbitals. Ionization of an s electron from the ground state of Ti (^3F s^2d^2) costs 6.84 eV (^3F s^1d^2) whereas ionization of a d electron requires 9.95 eV (^2D s^2d^1)[48]. For Th, however, the s and d orbitals are much closer energetically (see Tables III-VI). Hence, the covalent character

of the bonds in Cl_2Ti should be almost entirely metal 4s and for Cl_2Th we would expect a mixture of 6s and 7d character in the Th-Cl bonds. There is then a driving force for bending the Cl-Th-Cl angle from linear.

The Mulliken population analysis bears this out (see Table XVII). For Cl_2Ti there is only 0.4 electron remaining in the Ti 4s orbital, with actually over two electrons, 2.35, in the 3d orbitals (due to backbonding). This means that the s electrons are almost entirely ionized when the Cl's are brought up to Ti. The population of the two high spin orbitals left on Ti are entirely 3d electrons (see Table XVIII) and there is essentially only metal s character left in the symmetric Cl-Th-Cl bonding orbital. For Cl_2Th, on the other hand, there is double the amount of s electrons remaining, 0.8, and less than two d electrons left on the metal, 1.88. If we look at the population in the two high spin orbitals left on Th, we see that the δ orbital is all d (by symmetry), but the σ orbital has more s character than d, 0.71 s electron and 0.29 d electron. The character of these high-spin orbitals can be graphically seen in the orbital plots in Figure 1 for Ti and Figure 2 for Th. The high spin orbitals on Ti are d_{xy} and d_{z^2} orbitals which are quite tight; whereas the orbitals on Th are d_{xy} and a very diffuse s-like orbital with some d_{z^2} character mixed in. Finally, the Th character left in the symmetric Th-Cl bonding orbital is almost all due to the d functions. Hence, the remaining, albeit small, covalent part of the Th-Cl bond, unlike Ti-Cl, is mostly d and its slightly bent geometry arises because of this.

Our qualitative picture of Cl_2Th is thus different than for Cl_2Ti. For Th we see that bonding two Cl's results in the tying up of one s electron and one d electron. The remaining two electrons on the metal are an s and a d electron in orbitals that can be described as a $\sigma\delta$ symmetry configuration. The extent to which there is covalent Th d character in the Th-Cl bonds causes the equi-

librium geometry to be bent. Using Mulliken population analysis, there are 1.3 electrons with d character and 0.7 electron with s character in the high spin orbitals on Th. Thus, assuming covalent bonds and no rehybridization effects from geometry changes, the resultant Th-ligand bonds to these orbitals should have approximately 65% d character and 35% s character from the metal. Our prediction would thus be that, because of the closeness in energy of the 7s and 6d levels in Th, bonds to Cl_2Th should contain much more s character than the analogous 1st row transition metals would. This difference will thus be one of the major factors contributing to the uniqueness of Th organometallic chemistry.

What is the effect of the inclusion of f functions? The population analysis in Tables XVII and XVIII shows that the f's are used mainly for increasing the backbonding to the Cl orbitals. This can also be seen by comparing the metal-chlorine orbitals in Figs. 1b and 2b. The f's mix in with this bonding orbital fairly strongly for Th; whereas for Ti, with only low-lying p basis functions having the the proper symmetry to mix, there is less metal-chlorine interaction. A comparison of the geometries calculated with and without f functions (Table XV) indicates that the equilibrium geometry with f's is less bent (174.16° as opposed to 170.78° without f's). Wadt has found that the effect of f's in ThO_2 and UO_2 is mainly in increasing the backbonding from the O to the metal and that the f's prefer linear geometries in this case[18]. The bonding of additional ligands to the high-spin orbitals of Cl_2Th should cause the f's to be used for polarization of these bonds.

3.4 Thorium Hydride Complexes

3.4.1 Cl_2ThH_2

Starting with our Cl_2Th fragment, which has two unpaired electrons in Th orbitals, we can make two bonds to a ligand(s). The first ligand we chose was hydrogen, both for its simplicity and its relevance to the complexes made by Marks. Experimently, thorium forms Th−H bonds readily by the reaction of Th-C bonds with H_2 (see Introduction). In Eq. 16, $Cp_2^*Th(CH_3)_2$ reacts with hydrogen to form a dimeric product, $\{Cp_2^*ThH(\mu\text{-H})\}_2$. The monomer, $Cp_2^*ThH_2$, cannot be isolated — it has been speculated to exist in an equilibrium with the dimer in solution and to play a role in the reaction chemistry of the Th−H bond.[7,10]

Theoretically, we have solved for the optimum structure of our model complex, Cl_2ThH_2, at the HF and GVB levels without f functions (using analytic gradients) and at the GVB level with f functions (using local mode optimization). Our GVB wavefunction includes correlation of both Th−H bond pairs [GVB(2/4)]. The structural parameters and total energies are presented in Table XIX. There are no significant differences between the geometries predicted at the HF and GVB(2/4) levels without f functions — all angles are within 1° and all bond lengths are within 0.05Å. In general, the GVB wavefunction predicts longer equilibrium bond distances than HF as is the case here (Th−H and Th−Cl 0.026Å and 0.002Å longer, respectively, for GVB). When f functions are added to the system, we see that the optimized structure does not change significantly. Comparing geometries obtained with the GVB(2/4) wavefunctions, the effect of f functions is to decrease all the bond distances slightly. The Th−H bond length is shortened by 0.029Å and the Th−Cl distance is reduced by 0.060Å. F functions

help polarize the bond, increasing its directionality. Since the f's are actually smaller than the d orbitals, this tightens the atom-atom distances. The effect on bond angle is not as clear-cut. The H—Th—H angle is smaller with f's, while the Cl—Th—Cl is about the same. In any case, the differences between the HF optimized structure without f's and the GVB(2/4) with f's is very small. Only the Th-Cl bond distance is slightly different, by 0.058Å. However, since we are not examining the Cl interactions (they are left uncorrelated), this need not be a matter of concern. Therefore, we conclude that geometry optimizations at the HF level without f functions on Th will give sufficiently good molecular structures and that additional correlation and basis set effects produce only small geometrical changes.

The Mulliken populations obtained from the wavefunctions for each of the optimized geometries are listed in Table XX. There are significant changes in the charge distribution with increasing electron correlation [HF to GVB(2/4)] and with increasing basis set size (f functions). The Th charge changes from +1.80 to +1.68 to +1.41 on going from HF to GVB(2/4) to GVB(2/4) with f's. Increasing correlation decreases the amount of charge transferred from the thorium to the H ligands (the Th-Cl interactions are basically unchanged since those bonds are treated as doubly occupied orbitals as in HF). Allowing each electron to have its own orbital allows the electrons to be left-right correlated; thus providing a much better description of the covalent bond than with a single doubly occupied orbital as in HF. Hence, HF overestimates the amount of ionic character in the bond. F functions further decrease the amount of thorium to ligand charge transfer by providing increased polarization within the bond. The effect of f's on the ionicity of the thorium-ligand bonds is actually greater than electron correlation effects at this level of wavefunction. Although we found the

effects of increased electron correlation and additional polarization functions (f functions) to be small on molecular structures, it will be necessary to consider these effects when examining both the qualitative and quantitative features of the bonding.

In Figure 3d, the two correlated Th−H bond pairs from the GVB(2/4) calculation are plotted. Each orbital is a one electron orbital. By symmetry, the two Th−H GVB pairs are equivalent. The orbitals on the left side of the figure are predominantly on the Th - qualitatively appearing like metal d_σ orbitals, while those on the right side are predominately centered on the H atoms—looking like H 1s orbitals. Thus the Th−H bonds are covalent bonds. Another perspective of the bonding is obtained by examining the amplitude of the GVB bonding orbital (1st natural orbital) along a line connecting the Th and H nuclei (see Fig. 4d). At first glance the orbital appears to be centered almost exclusively on the H atom. In reality, the bulk of the thorium-bonding orbital is centered right under the H atom as shown by the overlap of the fragment orbitals in Fig. 4d.

Quantitatively, the percent of ionicity can be calculated for each one electron orbital using Mulliken population analysis (see Table XXI). The results show that for the orbitals on the right-hand side of Figure 1 94% of the electron density resides on the H; for the left-hand side orbitals 68% is on the Th and 32% is on the H. The bonds are covalent, but there are significant polarizations towards the H. The net number of electrons transferred in each Th−H bond pair is 0.26 electrons; hence, the bond is 26% ionic. Using Pauling's scale of electronegativities, we find that for a bond between Th (electronegativity of 1.3) and H (electronegativity of 2.2) the percent ionic character should be approximately 19%.[49a,b] Since the Th is bound to two even more electron withdrawing ligands, Cl's, one would expect that the Th would be much more electropositve and hence the ionicity would

be less than 19% using Pauling's scheme. There are two reasons why this is not the case. First, as shown in Table XI, the HF wavefunction underestimates the ionization potential for Th by approximately 1.5 eV. It is easier to remove an electron from the HF calculated Th atom than from the real system. Thus an increase in ionicity would be observed for the calculated complexes. Second, the Mulliken analysis is suspect when it comes to computing the electron populations of orbitals that overlap strongly as in this case. Since much of the thorium character in the bonding orbital is at the H nucleus, the population analysis will overestimate the amount of charge transfer. From the electronegativity scale we would expect Th to behave similarly to Hf (also electronegativity of 1.3). However, Th does have lower 1st and 2nd ionization potentials than Hf [Hf: 7 and 14.9 eV (Table XXII); Th 6.1 and 11.8 eV (Table XI)]. In any event, the Th—H bond can be described as a polar covalent bond.

If we compare the degree of ionicity in Th—H bonds with that in similar transition metal hydrogen bonds, we see that there are very few transition metals that will have as polar a metal-hydrogen interaction as Th. The first and second ionization potentials of Th are lower than almost all of the corresponding transition metal IPs (compare the Th IPs in Table XI with the transition metal IPs in Table XXII).[48] In general then, the bonds between thorium and a ligand will be more polar than for transition metal ligand bonds.

3.4.2 Comparison of Cl_2ThH_2 with Group IVB Cl_2MH_2 Complexes

The bonding in the analogous Group IVB tranisition metal-hydrogen complexes, Cl_2TiH_2 and Cl_2ZrH_2, has been examined by Rappé and Goddard[46,50], and Steigerwald and Goddard[51]. Using their optimized geometries we have carried out GVB(2/4) calculations on those systems. In addition, we have optimized the geometry of Cl_2HfH_2, the last member of the Group IVB triad, at the GVB(2/4) level using the RECP of Wadt and Hay.[29] The appropriate structural parameters used are shown in Table XXIII. Two important points are evident in this table. One is that, except for Hf, the hydrogen and chlorine bond angles with the metal become closer to the tetrahedral angle ($\approx 109°$) as the atomic size of the metal increases. This is a direct result of the s and d orbitals becoming closer in energy. If all the orbitals could mix equally, then the best orbitals would be oriented tetrahedrally to minimize electronic and steric repulsions.

Interestingly, the Hf complex, a third row metal, has shorter bond lengths to the H and Cl ligands than Zr does — both the Hf−H and Hf−Cl bond distances are approximately 0.05 Å shorter than the Zr−H and Zr−Cl bonds. In the bulk metals[52], the Hf−Hf bond length is 3.127 Å (hexagonal close packed, hcp) and the Zr−Zr is 3.179 Å (hcp); again, a difference of $\approx$0.05 Å. The reason for this bond shortening is the "lanthanide contraction" resulting from the filling of the 4f orbitals by the lanthanide elements. The first shell of f orbitals, just like the first d shell (3d), is very tight spatially. They shield the nucleus very well and allow the ligands to approach closer to the metal (less effective nuclear repulsion). The contraction of bond lengths also helps to explain why the H−Hf−H angle is wider than for Th. Since the Hf−H distances are shorter, the angle opens up to reduce the steric repulsion interaction between the hydrogens. This anomalous behavior

of Hf leads to several interesting similarities and differences in its chemistry compared to Th's which we will develop   further in later sections.

Two-dimensional orbital plots of the metal-hydrogen bonds for the Ti, Zr, and Hf systems are shown in Figs. 3a–c, respectively. The orbital amplitudes are all plotted on the same scale for Ti through Th for ease of comparison. Qualitatively, all the metal-hydrogen bonds are essentially covalent. Each metal-hydrogen bond pair consists of an sd hybrid orbital from the metal (on the righthand side of the plot) and an s orbital from hydrogen (on the lefthand side). The metal orbitals become more polarized towards the hydrogen as we go from 1st to 3rd row transition metal and then to the actinide. The maximum contour shifts from being essentially centered on Ti to being roughly 3/4 of the way towards the H ligand in Cl_2ThH_2. An atomic Mulliken population analysis for these complexes, shown in Table XXIV, indicates that the net charge residing on the metal varies considerably from Cl_2TiH_2 to Cl_2ThH_2, with Ti having an approximate charge of $+\frac{1}{2}$, Zr and Hf having a charge of $\approx+1$, and Th having a charge of $\approx+\frac{3}{2}$.

Breaking down the charge density further by examining only the M−H GVB pairs (Table XXI), we can see several trends corresponding with metal size. First, the amount of charge transferred from metal to hydrogen ligand increases going down the periodic table. For Ti, the H atom is actually positively charged — in contradistinction to the formal oxidation state assignment of −1 to a metal bound H atom. The Zr and Hf species have similar ionicities in their metal-hydrogen bonds, $\approx$0.1 electron transferred from the metal to hydrogen. Cl_2ThH_2 possesses a considerably more ionic bond, ca. 2.5X more ionic than in the Hf case, although, as discussed above, the population analysis for the Th−H bond is definitely overestimating the degree of ionicity.

Secondly, the percentage s and d character in each of the metal orbitals varies considerably from the 1st row metal Ti to the actinide Th. As nuclear charge increases the amount of d character in the bond decreases from 84% for Ti to 59% for Th. The amount of s character increases on going down the column in Group IVB as the s and d orbitals become closer in energy. For Th, however, the amount of s and p character decreases from the values for Hf. An indicator of the relative energetic stability of the s and d orbitals is the relative state splittings for the s^1d^2 and s^2d^1 states of the +1 metal ions, which are shown in Table XXV.[48] For Ti and Zr the ground state of the ion is ^4F (s^1d^2) with the splitting between that state and the ^2D (s^2d^1) diminishing from Ti to Zr. On the other hand, for Hf the ^2D state is the ground state of the monocation with the ^4F 0.53 eV higher in energy. Because of the lanthanide contraction, the energy of the s and p orbitals, which are closer to the nucleus relative to the d orbitals and hence less screened by the tight, filled 4f orbitals, should decrease with respect to the d orbitals. Hence, the s^2d^1 is more stable than the s^1d^2. This would cause a higher percentage of s and p character in the bonds relative to Zr and Th.

As predicted above in the dichloride section, the character of the two high-spin orbitals on Cl_2Ti and Cl_2Th determine the character of the metal bonding orbitals. The unbonded (high-spin) metal electrons of Cl_2Th are essentially s^1d^1 while those of Cl_2Ti are d^2; and the Th–H bonds have considerably more s character and less d character than the Ti–H bonds in the Cl_2MH_2 series. The ionicity of the M–H bonds (more character taken out of the metal s orbitals since they are slightly easier to ionize) and rehybridizaion effects (mixing in p character and f character) change the percentages of s and d character from their predicted values of 35% s and 65% d for Th, but the overall trend of decreasing d character is still the same.

We have calculated the diabatic (Table XXVI) and adiabatic (Table XXVII) bond energies for breaking a M−H bond in the Cl_2MH_2 complexes using both full CI and CCCI methods.[53] The diabatic or snap bond energy is the energy to break a bond with no changes to the geometry of the fragment molecules. It can be referred to as an intrinsic M−H bond energy since it is the bond energy before the fragments are allowed to relax. As shown in Tables XXVI and XXVII, the bond energies increase with atomic size, i.e., Ti−H < Zr−H < Hf−H ≈ Th−H. This trend is the exact opposite of that observed for the main group elements. For example, alkali metal-hydrogen bond strengths decrease down the column[54] (D^0 values in kcal mol^{-1}): Li−H, 56.0; Na−H, 43.4; K−H, 42.9; and Cs−H, 41.7 (Rb−H unknown). Likewise, in the oxygen series,[54] we find that $D^0_{OH} = 4.39$, $D^0_{SH} = 3.55$, and $D^0_{SeH} = 3.2$.

What causes this reversal in the M−H bond energy versus atomic size trend between the transition metals and the main group elements and what implications does this have on the chemistry that we observe in these systems? To answer these questions a detailed study has been carried out on the nature of the chemical bond in both the alkali metal-hydrogen series and the Group IVB and thorium metal-hydrogen bond complexes. The results are presented in Part II of this thesis and are summarized in the following paragraphs.

The one key calculatable property that can tell us much about what is occurring in the bond formation process is the overlap. For the Cl_2MH_2 series, the overlap of the GVB one-electron orbitals in the M−H bond pair increases with increasing atomic number. If we examine Figs. 3a-d, the GVB orbitals for Ti, Zr, Hf, and Th, respectively, we see that this is graphically depicted in the overlayed one-electron orbitals shown in subplot iii (bottom plots). The H "1s-like" orbitals are contained increasingly within the metal orbitals' contours

as one goes from Ti to Th. Ti—H orbital overlap is very low, only 0.61; Zr is intermediate, at 0.74; and Hf and Th are essentially the same at 0.79 (see Table XXI). On the other hand, for the alkali metal-hydrogen bonds, overlap decreases with atomic size.

The overlap is related to two factors: 1) the ability of the two orbitals to penetrate each other; and 2) the amount of charge transfer in the bond. Cl_2ThH_2 has a more polarized bond than all the rest of the complexes. In order to investigate what influence charge transfer and the presence of f polarization functions have on the overlap, we calculated GVB(2/4) wavefunctions for Cl_2ThH_2 excluding those effects. Without f functions the overlap in the Th—H bond dropped to 0.771. We were able to eliminate the ionic character in the Th—H bond by using as our wavefunction the orbitals from Cl_2ThH and the 1s orbital of H atom. The natural orbitals for the Th—H bond pair of interest were constructed from a linear combination of the H 1s orbital and the Cl_2TiH singly occupied orbital. The orbitals were then frozen except for orthogonalization. The overlap of the Th—H orbitals dropped to 0.770. Using the same frozen wavefunction approach without f polarization functions led to an overlap of 0.748. Therefore the effects appear to be cumulative. Even with both of these effects excluded from the wavefunction the overlap is still higher than that of the Zr complex. Hence, the conclusion is that charge transfer is only playing a small role in increasing the overlap of the metal-hydrogen bonds from Ti to Th. Charge transfer would play a role in the alkali hydrides. However, we eliminated the effect of charge transfer entirely in both the alkali metals and transition metals by examining frozen wavefunctions in which the fragment orbitals were not allowed to change shape (except for orthogonalization) as the internuclear separation was decreased. We find the same trends in bond energy and overlap as for the fully relaxed wavefunctions.

What, then, is the cause for the differences in overlap between the two different groups? The sizes and directionality of the metal orbitals are the key in determining the magnitude of the metal-hydrogen overlap. For the first row metal Ti, the orbital used in the bonding is much tighter than the metal bonding orbitals of Ti's cogeners (see Table XXVIII). The hydrogen atom can not approach close enough, because of electron-electron and nuclear repulsions, to make as good an overlap with Ti's orbitals as it can with the larger metals. The situation is made even worse by the character of the Ti metal orbital, almost all d. The d orbitals in Ti, because of the lack of orthogonality constraints (3d is the first set of d orbitals), are much tighter than the 4s orbitals. This tightness leads to a large gap in the 3d versus 4s orbital energies precluding any hybridization. In summary, the large increase in the overlap from Ti to Zr is caused by two factors: 1) the valence orbital size of Zr (1.402Å) is much larger than for Ti (0.942Å), and 2) the Zr bonding orbital contains more s (Ti: 12.1%, Zr: 20.5%) and less d (Ti: 83.5%, Zr: 70.4%) character than the Ti orbital. From Zr to Th the d orbitals become more diffuse. Nonetheless, the directionality of the d orbital actually leads to a better overlap with the incoming H atom. This is best demonstrated by comparing the overlap of the two high-spin fragment orbitals (Cl_2(H)M· and H·) as shown in Figs. 4a–d. We see that for Ti and Zr, the peak of the metal orbital is still observable on the amplitude plot. For Th—H, the peak of the Th orbital is very close to the H orbital and appears only as a broad shoulder in the molecular orbital. If there were no lanthanide contraction, we would predict Hf—H to have a bond energy in between that of Zr—H and Th—H. The contraction enables the H atom to move closer to the Hf and obtain a better overlap.

As a reflection of the size and shape of the orbitals, the metal-hydrogen snap

bond energies can be correlated with overlap, S, and the distance between the nuclei, R. It can be shown that bond energy is proportional to

$$\frac{S^2}{R}.\tag{25}$$

However, this holds only within a particular set of orbitals. For orbitals of different sizes, a scaled R value, R_s was developed that relates the radial extent of the fragment orbitals (using the quantity $< \phi|r^2|\phi >^{1/2}$), R_M and R_H, to the final equilibrium internuclear separation, r_e,

$$R_s^{MH} = \frac{r_e}{R_M + R_H}.\tag{26}$$

Basing the proportionality relation on the largest bond strength of the series, Th$-$H, the bond energy of M$-$H, E_{MH}, is

$$E_{MH} = \frac{R_s^{ThH}}{R_s^{MH}}\frac{S_{MH}}{S_{H_2}}E_{Th},\tag{27}$$

where S is the overlap between the GVB pair, one-electron orbitals. Table XXVIII presents the predicted snap bond energies of Ti, Zr, and Hf using the proportionality relation based on the CCCI bond energy and GVB(2/4) overlap of Th$-$H. Excellent agreement is found between the actual binding energies and those obtained via the proportionality relationship with R_s.

For the alkali metals, the size of the orbitals, of course, increases down the column, but the directionality of the bonding orbitals is essentially zero because the bond is the overlap of a H 1s orbital with a spherical metal s orbital. Thus the overlap of the orbitals gets smaller with atomic size and the bond energy follows the same trend.

Finally, hybridization helps out the transition metal-hydrogen bonds by directionalizing the bonding orbitals. Since the s and d orbitals of the Zr, Hf, and

Th are quite close in energy there is little promotional energy cost. However, for the alkali metals and Ti the energy gap between the s, p, and d orbitals is large and hence hybridization effects are small, which further hinders any attempt to increase the directionality of the bonding orbitals.

In summary, the unique shape of the d orbital (i.e., it is pointy) enables the overlap of the transition metal (and actinides) bonding orbitals with the incoming ligand orbital to increase even though the metal orbitals are becoming more diffuse. The spherical nature of the s orbital (i.e., it is round) causes the overlap of the alkali metal orbitals with hydrogen to decrease with overlap. Hence, the trends in the bond energy with atomic size are reverse for these two groups. The p orbital is apparently still not directional enough to reverse the bond energy trend of oxygen and its cogeners with hydrogen. The implications of this are that it is the shape of the d orbital and the isoenergetic nature of transition metal and actinide s and d orbitals that enable these complexes to undergo very different chemical reactions and have markedly different chemical properties from the associated main group complexes.

3.5 The Dimeric Species, $\{Cl_2Th(\mu\text{-}H)H\}_2$

Calculations were carried out on the dimeric thorium hydride species with chlorine ligands replacing the Cp* groups. As a test for the accuracy of our gradient optimization techniques, the structure of $\{Cl_2Th(\mu\text{-}H)H\}_2$ was determined in C_2 symmetry (same as in the Cp* complex but not including the symmetry of the ring carbons and hydrogens) using a HF wavefunction without f functions. The relevant bond distances and angles are presented in both Fig. 5 and Table XXIX. The agreement between the neutron diffraction crystal structure data on the dimer and our results on the model complex is extremely good. For the

bridging H (b-H) ligands, bond distances to thorium are within 0.05 Å of the experimental values. The Th−Th distance is very close, 4.04 Å for the model versus 4.01 Å in the crystal structure. All bond angles in the bridge region are to within 3° of the actual angles with most to within 1°. The only structural parameters which are farther off are the terminal Th−H (t-H) bond distances, which are 0.1 Å too long. Note, however, that these angles are consistent with the R(Th−H) obtained in the Cl_2ThH_2 complexes. It is possible that the use of the chlorine ligands and/or the lack of f functions has caused this inflation of the bond distance. However, since good results are obtained for the bridging hydrogens and since similar "long" bond distances were found for the Cl_2ThH_2 case with f functions, it is most likely that this effect is caused by the RCEP.

The effect of electron correlation was investigated on the bridging and terminal Th−H bonds. Because of the large size of the system, all GVB calculations were performed with the TH3 basis set without f functions on the thorium atoms. Since both bridging bonds are delocalized, the GVB description of these bonds is somewhat different from the straightforward left-right correlation of the t-H bonds. In effect, the bridge can be visualized as three resonance structures

$$
\begin{array}{ccc}
\text{Th}\diagup\!\!\!\overset{\text{H}}{\diagdown}\text{Th} & \longleftrightarrow & \text{Th}\overset{\text{H}}{\diagdown}\text{Th} & \longleftrightarrow & \text{Th}^{\oplus} \quad {}^{\ominus}\text{Th} \\
\end{array}
\qquad (28)
$$
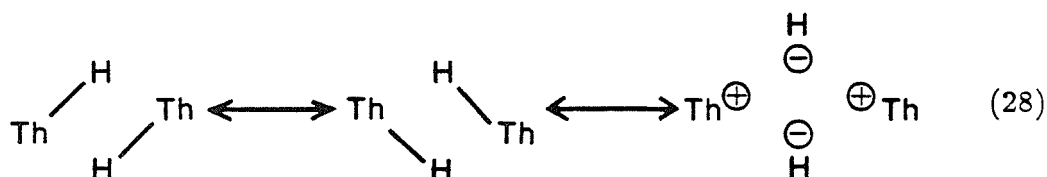
There is essentially no metal-metal interaction so the contribution of another resonance structure,

$$
\text{Th}\!-\!\!\!\overset{\displaystyle \text{H}}{\underset{\displaystyle \text{H}}{\rule{0pt}{1em}|}}\!\!\!-\!\text{Th}
\qquad (29)
$$

should be very small. The GVB wavefunction can describe this type of resonance

adequately by allowing three orbitals per electron pair [GVB(1/3)] instead of the usual two. The three natural orbitals for both of the b-H atoms are shown in Fig. 6 along with the percentage that each contributes to the wavefunction. It is interesting that the natural orbital with two nodes contributes more towards the lowering of the energy than the single-node orbital.

An easier way to visualize the type of correlation inherent in the second and third natural orbitals is to combine them pairwise (using the GVB orbitals coefficients) with the dominant orbital as in Fig. 7. The top two sets of orbitals (Fig. 7a) are combinations of the first and second natural orbitals. One orbital is very tightly centered on the H; the other orbital is spread diffusely over all three centers. These orbitals show the ionic character present in the third resonance structure above (Eq. 28). The bottom sets of orbitals (Fig. 7b) are combinations of the first and third natural orbitals. The first orbital of each set has electron density primarily between the left thorium atom and the H atom; the second orbital is mostly centered between the right thorium and H. Thus this combination represents the first and second covalent resonance structures (Eq. 28). Of course, the perfect pairing orbitals are only a first-order description of these resonance structures because of the strong orthogonality and spin-coupling restrictions imposed.

RCI and GVB-CI calculations were carried out starting with the GVB(4/10) wavefunction for the metal dimer (two t-H bonds each correlated 1/2; two b-H bonds each correlated 1/3) in order to relax both the spin-coupling and orthogonality restraints imposed by the perfect pairing wavefunction. The RCI and GVB-CI energies are only slightly lower (< 2 millihartrees) than the GVB(4/10) (see Table XXX). Thus the contributions of spin and orthogonality relaxation effects are minimal, and the GVB-PP gives a good description of the bridge

bonding.

The ionic resonance structure in Eq. 28 has a significant contribution to the ground state. A Mulliken population analysis of the HF and GVB(4/10) wavefunctions, Table XXXI, shows that there is indeed more charge transfered to a b-H than to a t-H. Generally, the atomic populations are similar to those for the monomer, Cl_2ThH_2.

The energetics of formation of the dimer from two monomer units,

$$2Cl_2ThH_2 \longrightarrow \{Cl_2Th(\mu-H)H\}_2 \qquad (30)$$
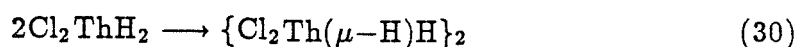
$$\Delta H_{rxn}^{HF} = -27.2 \text{ kcal mol}^{-1}$$

$$\Delta H_{rxn}^{GVB} = -31.1 \text{ kcal mol}^{-1}$$

indicate that the dimer is energetically favored. At both the HF and GVB(4/10) levels of calculation it is found that the energy of the dimer is approximately 30 kcal mol^{-1} lower in energy than the monomer complexes. Hence, no monomers would be present in the crystalized state. In solution, these results provide us with a lower bound to the barrier to dissociation (at 0K). The size of the barrier is large enough such that dissociation should be slow at room temperature.[55]

A possible mechanism of association of two monomer units into the dimer complex could involve a $2_s + 2_s$ concerted reaction in which the interchange of the Th$-$H bonds is stopped in the middle, yielding the dimer:

$$
\begin{array}{ccc}
\text{Th} \!-\! \text{H} & & \text{Th} \!-\! \text{H} \\
& \rightleftharpoons & | \quad | \\
\text{H} \!-\! \text{Th} & & \text{H} \!-\! \text{Th}
\end{array}
\qquad (31)
$$
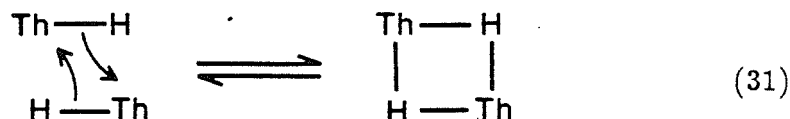
The exchange of b-H and t-H in the NMR would then be explained by the reverse of Eq. 31 with Th$-$H$-$Th cleavage, and then reassociation of the monomer with the previously terminal Th$-$H bonds becoming the bridging ligands. In the next

section, model 2 + 2 reactions at Th—H bonds will be discussed and it will be shown that this type of mechanism both fits the experimental observations and proceeds with a low activation barrier.

3.6 [2 + 2] Reactions at Th—H Bonds

Many of the observed reactions of thorium-alkyl and thorium-hydrogen bonds involve exchange of ligands at a saturated thorium center (for example, in Eqs. 11–14 there are several such reactions). In general, these reactions occur rapidly in solution. Since oxidative addition/reductive elimination reactions proceed via the gain/loss of ligands, this type of mechanism must be ruled out as a possible pathway for these ligand exchange reactions. A very plausible reaction mechanism would be a concerted 2 + 2 addition in which the bond pair electrons of a Th—L bond are interchanged with another bond pair, L'—L'',

$$
\begin{matrix} M & - & L \\ \\ L' & - & L'' \end{matrix} \longrightarrow \begin{pmatrix} Th & \cdots & L \\ \vdots & & \vdots \\ L' & \cdots & L'' \end{pmatrix}^{\ddagger} \longrightarrow \begin{matrix} Th & & L \\ | & & | \\ L' & & L'' \end{matrix} \tag{32}
$$
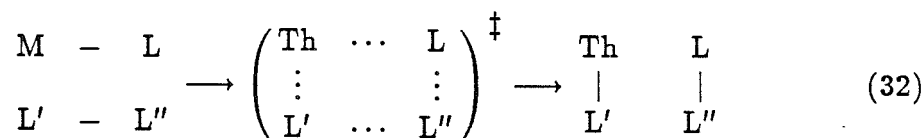
The problem with the above mechanism is that it is known that the simplest version of a $2_s + 2_s$ addition, $H_2 + D_2$, is a forbidden reaction with a large barrier estimated to be over 100 kcal.[56a,b] A schematic view of the orbitals at the transition state,

$$ \tag{33} $$
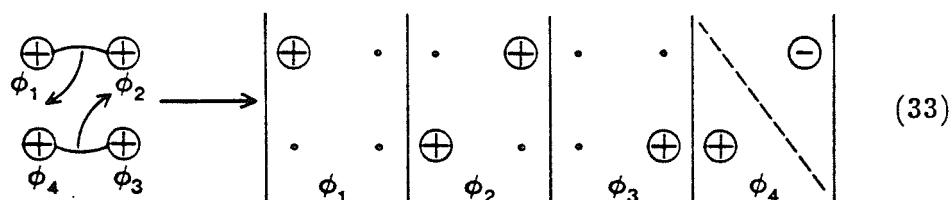
illustrates that the large barrier is due to the presence of the node in orbital four. H does not have low-lying orbitals of the proper symmetry to maintain overlap during the reaction. The nodal surface means that at the transition state an H−H bond has been broken leading to an activation energy approximately equal to the bond strength of H_2. Steigerwald and Goddard[57a,b] found for the transition metals Sc, Ti, and Zr that the concerted exchange reaction of M−H + D_2 had a *low* barrier (< 25 kcal mol^{-1}). The predominant character of the metal orbital bonded to the H is d. This orbital has the proper symmetry to maintain the overlap of the bond pairs during the reaction,

$$\tag{34}$$
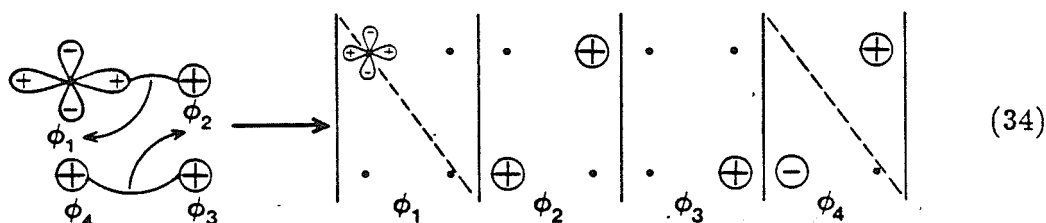
and hence, it proceeds with a small activation energy.

3.6.1 The Exchange Reaction of D_2 with Cl_2ThH^+

In the case of thorium, two different model complexes were used to study deuterium exchange reactions with the thorium-hydrogen bond. The first system we looked at was the positively charged complex, Cl_2ThH^+. The geometry of the reactant was fully optimized(HF gradient — no f functions on Th) and is shown in Table XXXII. The geometry of the saddle point of the reaction (Table XXXIII) was calculated, using gradient optimization techniques at the HF level without f functions, by restricting the complex to C_{2v} symmetry.

$$\tag{35}$$

F basis functions and electron correlation were then included, starting with a GVB(2/4) wavefunction, and continuing to the RCI, RCI*S_{val}, and CCCI wavefunctions.

The perfect pairing orbitals for the reactants, the transition state, and the products are shown in Fig. 8. The Th−H bond in the reactant has, at the transition state, delocalized into a three center bond over both the H and D atoms adjacent to the Th. The D−D bond also has become a three center bond over the H and D atoms. Within the perfect pairing restriction, both three center bonds are orthogonal. The symmetry of the Th orbital allows it to overlap both the H and D atoms at the transition state and to transform smoothly from a bond to H in the reactants to a bond to D in the products. The GVB pair overlaps in Table XXXIV indicate that indeed overlap is maintained from reactants to products. For the $H_2 + D_2$ reaction, this is not possible because the H−H bonds involve mainly s orbitals.

The barrier heights in Table XXXV manifest that the activation energy for the exchange reaction is low. The GVB(2/4) wavefunction increases the activation energy. At the transition state, the bonds are half-way between Th−H and H−H bonds. The perfect pairingwavefunctiondescribes the localized reactant much better than the delocalized three–center bonds at the transition state. As correlation is increased the barrier decreases, except for the highest level of correlation employed, CCCI. This CI includes double excitations from the GVB pair orbitals and these excitations could lead to greater correlation in the localized reactant orbitals. The presence of f functions also lowers the barrier (at the HF level). As with correlation, increasing the amount of polarization stabilizes the partial bonds at the transition state with respect to the reactant bonds.

The Mulliken populations in Table XXXVI reveal that the metal at the

transition state is slightly less cationic than in the reactants. Likewise, the terminal hydrogens are less anionic at the transition state. The bridging H atom is positively charged. A more detailed look at the character of the orbitals for the saddle point in Table XXXVII proves that the transition state is essentially nonpolar, since there is almost exacltly one electron from thorium and three electrons from the hydrogens involved in total for both GVB pairs. There is a slight polarization of the electrons between the terminal and bridging hydrogens, with each terminal H being slightly anionic, -0.05, and the bridging H being cationic, $+0.12$.

As pointed out by Steigerwald and Goddard[57a,b] concerning this type of nonpolar transition state, since the H$-$Th$-$D three-center bond must have no s character at the transition state, the hybridization of the M$-$H bond in the reactant is very important in determining the barrier height. The more s character present in the metal bonding orbital, the higher the barrier, because the orbitals must pay a higher energetic cost to rehybridize at the transition state. The character of the metal orbital in the reactant, shown in Table XXXVIII, is almost the same as in Cl_2ThH_2 (Table XXI), with the salient feature being a slight increase in the contribution of f functions (probably due to the smaller bond distance).

3.6.2 The Exchange Reaction of D_2 with Cl_3ThH

The second complex we investigated was Cl_3ThH — a model for saturated thorium exchange reactions. For the saddle point of this molecule, two possible orientations of the incoming D_2 with respect to the Cl ligands are possible.

$$(36)$$
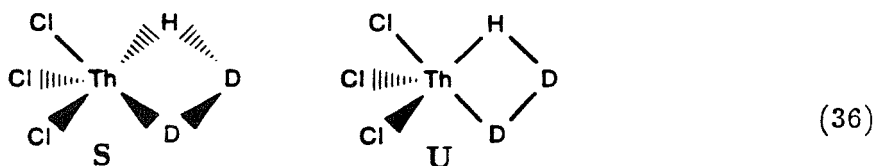
In either case, the geometries possess C_s symmetry. Both of these isomers have been investigated. The first structure can be trapped using symmetry; however, the second structure could fall apart to reactants during the gradient optimization procedure. Fortunately, we were able to find the second saddle point as a local minimum.

The geometry of the reactant molecule, Cl_3ThH, in Table XXXII, is very similar to that found for Cl_2ThH_2 (Table XIX). The optimized geometries in Table XXXIII indicate that the transition state geometries are almost identically the same for both isomers. The thorium-terminal hydrogen bond lengths are slightly longer for these species (2.25-2.27 Å) than for the cationic transition state, $Cl_2ThH_3^+$ (2.215 Å), resulting from the additional ligand in the neutral cases. $R(H-D)$, $\theta(H-D-D)$, and $\theta(H-Th-D)$ are almost the same for both the neutral and cationic saddle points. Hence, geometrically, the $2 + 2$ D_2 exchange reactions at the neutral saturated thorium are occurring in a similar fashion to those in the cationic complex.

The orbitals from the GVB(2/4) wavefunction for the transition states of both neutral isomers are shown in Fig. 9. For the symmetric first isomer, the orbitals are very similar to those obtained for $Cl_2ThH_3^+$ (Fig. 8). There are two three-electron bonds, $D-Th-H$ and $D-D-H$, pictured. However, for the second isomer the orbitals look somewhat different from the other two cases. In Fig. 9b, the top GVB pair consists of one orbital with density on the terminal H (closest to the in-plane Cl) and the other with most of its density on the bridging D and considerable character on the Th. This pair can be described qualitatively as an $H-D$ bond that is delocalized onto the thorium. The bottom GVB pair is made up of one orbtial with density on the terminal D (farthest from the in-plane Cl) and one orbital with most of its density on the Th but

with considerable delocalization onto the bridging D. Thus these orbitals can be pictured as a Th—D bond which is delocalized onto the bridging D. For the second isomer, we can say that there are two three electron bonds, Th—H—D and D—D—Th.

The difference between this transition state and the other two is brought about by the presence of the Cl ligand in the plane of the ThHD$_2$ group. The angle between the Cl and the terminal H closest to it is only 83°. The Th—Cl bond would be too close to make a very good Th—H bond and therefore, instead of seeing a transition state with evenly balanced H—D—D and D—Th—H three electron bonds, the bonds shift to having a good H—D interaction near the Cl and a good Th—D interaction away from the Cl.

Is the reaction allowed or forbidden? The orbitals clearly show that in both isomers the orbitals on the thorium metal are such that overlap is maintained at the transition state. For the symmetric transition state with the orbitals similar to the cationic complex above, the Th d orbital can overlap both terminal hydrogens simultaneously. In Table XXXIV, the GVB pair overlaps show that overlap is maintained with respect to the reactant bonds and the reaction is allowed. For the unsymmetric case, the thorium d orbital is able to be involved in both delocalization of the H—D bond (Fig. 9a) and in bonding to the terminal D (Fig. 9b) at the same time. Hence, overlap is maintained (see Table XXXIV) at the transition state. As the reaction moves along, the d orbital will be able to switch character from one terminal to the other so as to form one M—H bond while breaking the other. Bond breakage is concomitant with bond formation and so a low barrier to exchange would be expected.

The barrier heights shown in Table XXXV point out that low activation energies are achieved for these transition states. After correlation, the barriers are

approximately 20 kcal mol^{-1}. The barriers for both isomers are approximately the same for all levels of wavefunction. In general, similar trends as in $Cl_2ThH_3^+$ are observed upon adding additional electron correlation and f functions.

A Mulliken population analysis of these systems and the reactant molecule in Table XXXVI indicates that the charge on the metal is unchanged from reactants to the transition state. Both isomers have similar populations on the H and D atoms as well. On comparison with $Cl_2ThH_3^+$, it is seen that each terminal hydrogen has about 0.1 electron more in the neutral transition states but the bridging one is similarly charged. The reason for this is the greater polarization in a Th—H bond caused by the greater electron density at the neutral Th atom. A detailed summary of the Mulliken populations in the GVB pairs orbitals in Table XXXVII shows that there is much more charge transfer from the Th atom to the hydrogens in the Cl_3ThH_3 transition states as opposed to $Cl_2ThH_3^+$. There is only 0.8 electron on the Th but 1.12 and 1.19 electrons on the two terminal hydrogens. The hydrogen away from the in-plane Cl has a higher charge because it had a greater interaction with the thorium. The bridging hydrogen possesses about the same amount of charge as in $Cl_2ThH_3^+$. Therefore the transition states in Cl_2ThH_3 are polar with the metal cationic, the terminal hydrogens anionic, and the bridging hydrogen cationic.

3.6.3 Comparison with Other Transition Metal Systems:
M—H + D$_2$ ⟶ M—D + H—D
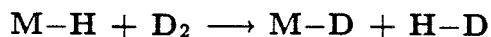
Steigerwald and Goddard[57a,b] have found the transition state geometries and activation barriers for several transition metal-hydrogen exchange reactions with D$_2$. The percentage s, p, and d character for the orbitals at the various transition states and the barrier heights that they obtained for the reaction of

$Cl_2MH + D_2$, M = Ti, Sc, and Zr, and for the reaction of $Cl_2TiH^+ + D_2$, are listed in Table XXXIX.

The cation, Cl_2ThH^+, has the same barrier to exchange, ca. 2 kcal mol^{-1}, as the analogous Ti complex, Cl_2TiH^+. The amount of d character in the reactant M$-$H bond decreases markedly from Ti to Th. For Ti[51a], the Ti$-$H bond is 83% d; for Th (see Table XXXVIII), the Th$-$H bond is 59% d. As discussed above, since the overlapping antisymmetric orbital at the transition state must have an antisymmetric and hence, predominantly d in character, metal orbital to maintain overlap with the hydrogens, the more d character the reactant M$-$H bond has, the less rehybridization is necessary at the transition state and the lower the barrier. The above results obviously disagree with this conclusion.

A second possibility brought out by Steigerwald and Goddard is that the M$-$H bond strength in the reactant molecule will influence the barrier height to reaction. For example, Cl_2TiH^+ has a lower barrier than Cl_2ScH. On comparison of the overlaps of the M$-$H orbitals of the reactants versus the transition state, they concluded that the Ti$-$H bond in Cl_2TiH^+ is significantly weaker than the Cl_2Sc-H bond. A weaker bond in the reactant would imply a less energetic cost to delocalize that electron pair and hence, a lower activation energy. However, in the case of the cationic Ti and Th reactants, we know from the discussion in Section 3.4.2, that Th$-$H bonds are considerably stronger than Ti$-$H bonds and yet the barriers for reaction are similar for the two species.

The explanation for the relative heights of the barriers being approximately the same for Cl_2TiH^+ and Cl_2ThH^+ involves the polarity of the transition state. In the Ti complex, the terminal hydrogens are cationic and, in fact, are more positively charged than the bridging hydrogen (see Table XXXIX). This means that the Ti is anionic. As discussed above, in the Th complex the opposite

situation prevails, with Th being cationic and the terminal hydrogens being anionic. In their work[57b] on the exchange reactions of D_2 with the main group hydrides (M−H), Steigerwald and Goddard found that allowed reactions occurred where there was charge transfer from M to the H_3 unit at the transition state,

$$\overset{+}{M}-\overset{-}{H} \quad \longrightarrow \quad \left[\overset{+}{M}\cdots\overset{-}{H}\cdots\overset{+}{D}\right]^{\ddagger} \quad \longrightarrow \quad \overset{+}{M} + \overset{}{H} \qquad (37)$$
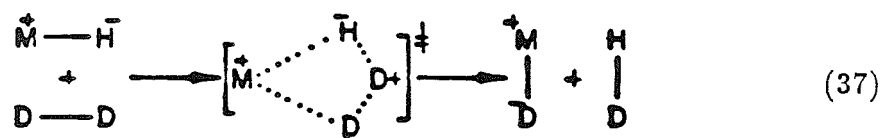
In other words, hydride transfer reactions go with low activation energy. Therefore, for Cl_2ThH^+, the transition state has more hydridic character than for Cl_2TiH^+, and we would predict a lowering of the barrier for Th relative to Ti. The more the exchange reaction takes on the characteristics of a hydride transfer reaction the lower the barrier will be.

Both cationic reactants have much lower barriers than the overall neutral reactants. One explanation for this effect is that when an electron is removed from the metal it generally comes from the s orbital. Thus the cationic reactants will have less s and more d character in the M−H bond. However, comparing the amount of d character in the Th−H bond of Cl_2ThH^+ with that of Cl_3ThH in Table XXXVIII, we see that the neutral complex has more d and more s character. So it is not a clear-cut line of reasoning. Another explanation is that the effect of the additional radical electron (in Cl_2MH) or the other bond pair (in Cl_3ThH) increases the amount of electron-electron repulsions at the transition state. One may also say that the involvement of the d functions in the non-reacting orbitals increases the energetic cost of rehybridization at the transition state. (Note, however, the barrier for Cl_2ScH is in the same ballpark as the other neutral complexes, yet it has no additional "interfering" electrons or bond pairs)

The ordering of the barrier heights among the neutral complexes is Ti > Th

> Sc, Zr (barriers determined at the RCI*S level). The amount of d character in the reactant metal—H bond is: Ti—H, 65%; Th—H, 60%; Zr—H, 56%; and Sc—H, 56%.[51a,b] Using the amount of d character explanation, we would expect the ordering of the barrier heights to be just the reverse of the actual results. The bond strengths for M—H bonds (using those for Cl_2MH_2 in Table XXI) are: Ti—H, 40; Zr—H, 65; and Th—H, 80 (in kcal mol^{-1}). As detailed above, this would predict that the ordering of barrier heights should be Th > Zr > Ti. For both Cl_2ZrH and Cl_2TiH there is a radical electron acting as a spectator to the exchange reaction; for Cl_3ThH there is an extra Th—Cl bond; and in Cl_2ScH there are no extra interfering electrons or bonds. This suggests that the order of activation energies should be Th > Ti, Zr > Sc. Finally, the hydridic character of the transition state, as indicated by Table XXXVI for Th and Table XXXIX for the rest, increases with atomic number for the isovalent Ti, Zr, and Th metals. The Sc transition state is very close in polarity to Zr's (Sc terminal H, 1.00 electrons, Zr terminal H 1.02 electrons). This suggests the ordering of barrier heights, based on the trends in the main group metal-hydrides[57b], as Ti > Zr, Sc > Th.

As can be seen, none of these explanations by itself offers a complete picture of what is occuring at the transition state of these exchange reactions. It is the interplay of all four of the above trends (as well as possibly other factors) that determine the relative barrier heights in these systems. It can be said, however, that the d character argument seems to have the least influence on the barrier heights for these systems since it predicts the opposite trend. We believe that it is the ionicity of the transition state that has the most influence on the relative barrier heights. The Th complex has a higher barrier than Zr and Sc because in the Th case there is the extra Th—Cl bond for the transition state to become

orthogonal to. If the analogous Cl_3TiH and Cl_3ZrH complexes were computed, we would predict from this analysis that the barriers should be higher than the Th complex. Hence, it is believed that the M−H bond polarity can play a strong role in reaction energetics, even though it does not appear to contribute much to the bond energy (see Part II).

Finally, we must consider how close these models are to the real systems. Only the Cl_3ThH and Cl_2ScH complexes are saturated with all valence metal electrons involved in bond pairs. Steigerwald and Goddard[57b] mention that the radical electron in the Cl_2MH, M = Ti, Zr, systems takes on much more d character than in the M−H bond. With a H ligand bound to the metal electron the two bonds would then have equivalent character before reaction. Presumably, this would impact the magnitude of the activation barriers significantly. These results would predict that the reactivity of the M−H bonds would go in the order Sc−H > Th−H > Zr−H > Ti−H, given saturated complexes with the same ligands.

3.7 Thorium-Carbon and Transition Metal-Carbon Bonds

We examined the nature of the metal-carbon bond for Th, Ti, Zr, and Hf. The complexes studied were analogous to the hydride series in Section 3.4.2, with a methyl group replacing one of the hydrogens, $Cl_2MH(CH_3)$. The gradient optimized geometries [GVB(2/4)] for these systems and the associated relaxed fragment molecules (Cl_2MH) are shown in Tables XL and XLI, respectively. In all cases, the hydrogens attached to the carbon were orientated such that the overall molecular symmetry was C_s and the in-plane methyl hydrogen was anti with respect to the M−H bond,

$$\begin{array}{c}
\text{Cl} \diagdown \text{Th} \diagup \text{H} \\
\text{Cl} \diagup \quad \diagdown \text{C} \text{—H} \\
\text{H}
\end{array} \qquad (38)$$
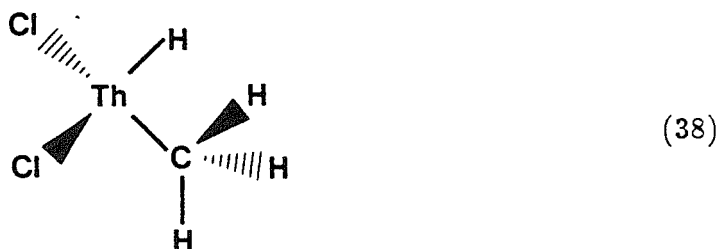
Steric repulsions should be at a minimum for this configuration; therefore, we believe this to be the lowest energy orientation of the methyl group.

The geometry changes from the metal dihydride complexes (see Table XXIII) are small. R(M—C) is significantly longer than R(M—H), about 0.4Å. The angle between the H and methyl ligands is much larger than the associated θ(H—M—H) for Ti, but for the other metals it actually is smaller. This occurs because the larger coordination sphere from Zr when coupled with the larger R(M—C) means that the steric repulsion is lessened relative to a narrowing of θ(H—M—H). The decreasing θ(Cl—M—Cl) with increasing atomic number is similar to that observed for the dihydrides. (There are changes in both the Cl angles and M—Cl bond distances from Cl_2MH_2, but because of the extreme flatness of the potential energy surface for these modes, it is not very significant.) Finally, there is a very minor trend in both the C—H bond distances and angles: R(C—H) decreases slightly while θ(H—C—H) increases slightly with increasing atomic number of the metal. Again, this is probably due to the increased coordination sphere of the larger metals.

The GVB(2/4) perfect pairing orbitals for these molecules are presented in Figs. 10a–d. The qualitative picture that these orbitals present to us is one of covalent bonding between the metal and the methyl group. The orbitals on the left-hand side of each plot are predominantly centered on the metal; the orbitals on the right-hand side are primarily about the carbon atom. The degree of ionicity present in these bonds can be quantitatively determined using Mulliken

population analysis. The results in Tables XLII and XLIII show that the metal center becomes increasingly cationic from Ti to Th. The same trend is observed in the dihydride complexes but it is accentuated with the methyl ligand. The GVB pair Mulliken population data indicate that the Ti−C bond is nonpolar, but from Zr to Th the M−C bond becomes increasingly polarized. This polarization of electron density towards carbon is greater in magnitude than in a M−H bond (see Table XXI). The electron affinity of CH_3 is higher than that of H (24.8 and 18.4 kcal mol^{-1}, respectively[58]), and the ionization potential of methyl is lower than that of H's (227 and 314 kcal mol^{-1}, respectively[58]). The electronegativity of methyl versus hydrogen atom supports our findings.

The amount of d character in the M−C bond is significantly higher and the amount of s character is lower than in the hydrides. A qualitative argument for this would be that as the methyl bonding orbital is sp in character it would be more directed than a H 1s orbital. Hence, the metal orbital would become more directed to maintain good overlap. By mixing in more d character (and less s) the metal bonding orbital can become more pointy.

The diabatic and adiabatic bond energies(D_e^{diab} and D_e^{adiab}, respectively) for cleavage of the methyl group from the above complexes have been calculated and are shown in Tables XLIV and XLV. A full valence CI has too many spin eigenfunctions. Therefore the CCCI wavefunction and a CCCI in which single excitations were allowed from the C−H bond pairs [CCCI(CH*S)] were used. As seen in the table, the extra correlation provided by the single excitations from the CH pairs is necessary for an accurate description of the M−C bond. These excitations provide for the relaxation of the C−H bonds as the M−C bond is allowed to have more correlation.

The trend of increasing bond energy with increasing atomic number holds for

the M−C bonds as it did for the M−H bonds. For all the metals, the diabatic or intrinsic metal-carbon bond energies [CCCI(CH*S)] are significantly greater than the metal-hydrogen diabatic bond energies (full CI, see Table XXVI). The adiabatic or relaxed metal-carbon bond energies are, except for Th, slightly greater than the adiabatic metal-hydrogen bond strengths (full CI, see Table XXVII). (The difference from diabatic to adiabatic energies is the relaxation of the methyl group.) This is contrary to much of the conventional wisdom that M−H bonds are stronger than M−C bonds in transition metals. Recent investigations of H and C bonds to naked transition metal atoms support our results.[59] There are very few experimentally determined bond energies on saturated metal complexes (see Section 3.9 for a further discussion of thorium bond energies).

As with the M−H bonds (see Eqs. 25−27), we can develop a proportionality relationship for the M−C bond strengths based upon the overlap and radial extent of the GVB one electron orbitals. Basing our bond strengths on that of Hf−C (the largest M−C), we see in Table LXVI that neither overlap nor overlap weighted by R_s account for $D_e(Th−C)$. The distance weighted overlap relation gives very good agreement with $D_e(Zr−C)$ but not with $D_e(Ti−C)$. Overlap alone gives good agreement for Ti but not for Zr. These irregularities are probably explained by hybridization differences at the metal center. Hf and Zr are the most alike and hence, the full propotionality relation holds well for comparing their bond energies. It is very interesting to note that in spite of the significant changes in hybridization from M−H to M−C bonds the bond strengths and trends among the different metals stay essentially the same. This implies that the energy cost of rehybridization must not vary much from one metal to the next.

How would we expect the nature of the M−C bond to impact upon its

reaction chemistry? $2_s + 2_s$ reactions at a M—C bond as opposed to at a M--H bond will be influenced by five factors: 1) the strength of the metal-carbon is slightly more than the metal-hydrogen, this should increase the barrier; 2) the increased directionality of the metal-carbon bond will make rehybridization of the orbitals more difficult, and thus also raise the barrier; 3) on the other hand, the increased amount of d character from the metal should decrease the amount of rehybridization required for that orbital, and the barrier will decrease; 4) the "extra" hydrogens on the methyl group will have to become orthogonal to the transition state orbitals, and will drive up the activation barrier; and 5) the polarity of the transition state, with the methyl group much more anionic than H, will decrease the barrier. There is not enough information to predict which of these four quantities will dominate. However, from the evidence presented for the M—H 2 + 2 reactions, factors 1 and 3 should be of minimal importance, whilst factor 5 will be of greater significance.

Experimentally, thorium-alkyl bonds, though of high thermal stability, are quite reactive. For example, in reaction (16) thorium-methyl bonds are rapidly hydrolyzed by H_2, very probably involving a concerted 2 + 2 process, to form thorium-hydrogen bonds. This implies that the carbon bonds are more reactive than the hydrogen bonds. Also, in reaction (17), CH_3Cl is found to react with Th—H bonds such that Th—Cl bonds and CH_4 are produced. Although there are undoubtedly thermodynamic forces driving these reactions (see Section 3.9 concerning bond energies), the results imply that more ionic ligands (like Cl) enjoy an increased reactivity along this concerted pathway. In addition, the metal-carbon bonds are quite susceptible to cleavage by protic reagents.[60] For example,

$$2Cp_2Zr(Cl)CH_3 + H_2O \longrightarrow [Cp_2ZrCl]_2O + 2CH_4 \qquad (39)$$

$$Cp_2Zr(CH_3)_2 + H_2O \longrightarrow [Cp_2ZrCH_3]_2O \longrightarrow [Cp_2ZrO]_n. \qquad (40)$$
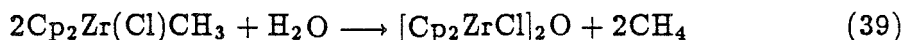
It is the anionic character of the methyl ligands which brings about this reactivity. The catalytic hydrogenation of propylene with alumina-supported thorium and uranium complexes indicates that the reactivity decreases sharply if electron-withdrawing spectator ligands (like Cl or Cp*) are present in the complexes.[13e] Electron-withdrawing groups decrease the anionic nature of the M−C and M−H bonds undergoing the reaction and therefore lessen the rate. Marks and co-workers have examined the reactivity of thorium and uranium alkyls with molecules that are good probes of bond polarity (i.e., ketones, alcohols, and carbon dioxide). Their results indicate extremely rapid rates of reaction with Th > U and highly polar M−C bonds with Th−H more polar than U−H.[1a,3j] For the first row transition metal Sc, the trend in reactivity for 2 + 2 σ bond metathesis reactions of Sc−R + R′−H is R = R′ = H ≫ R = alkyl, R′ = H ≫ R = alkyl, R′ = alkyl.[61] For nonpolar transition states, the key is the amount of rehybridization that the orbitals have to do at the transition state. The H s orbital being spherical has less energy cost to do this than the directed alkyl "sp" bonding orbitals.

As with the M−H bonds above, we would predict that the reactivity of the systems towards concerted addition processes would increase as the anionicity of the methyl group increases. This would indicate that for similar complexes, Th−CH₃ > Hf−CH₃ > Zr−CH₃ > Ti−CH₃. Note, however, that the trend in thermal stability of the methyl bonds increases down the periodic table. Since thermal stability predicts the opposite trend in reaction rates, it would be the interaction of these two factors which would determine what the rate would be. This may explain why in general the reactivity of Group IVB metals is relatively ordered as Ti > Zr, Hf.[62]

3.8 CO Insertion into Th–H and Th–CH$_3$ Bonds

We have investigated the insertion of CO into Th–H and Th–CH$_3$ bonds,

$$Cl_3Th - H + CO \longrightarrow Cl_3Th(H)CO \longrightarrow Cl_3Th[\eta^2 - OCH] \qquad (41)$$

$$Cl_3Th - CH_3 + CO \longrightarrow Cl_3Th(CH_3)CO \longrightarrow Cl_3Th[\eta^2 - OCCH_3] \qquad (42)$$
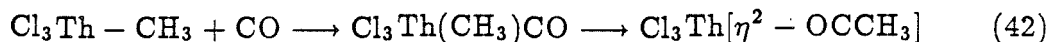
Experimentally, Marks et al. have found that migratory insertion of CO into a Th–H bond occurs rapidly and reversibly, yielding η^2-formyls, as in reaction (18).[12a,b] The ΔH for this reaction has been estimated by van't Hoff measurements to be approximately −5 kcal mol^{-1}. Similarly, CO insertion into thorium-alkyl[8a−e] and thorium-amide[63] bonds have been observed.

$$
\begin{array}{c}
\text{Th–R + CO} \rightleftharpoons \text{Th–R} \rightleftharpoons \text{Th–C–R} \\
 \underset{\displaystyle \overset{\displaystyle C}{O}}{\uparrow} \underset{\displaystyle \overset{\displaystyle O}{\nwarrow //}}{} \\[2em]
\text{Th–NR}_2 \text{ + CO} \rightleftharpoons \text{Th–NR}_2 \rightleftharpoons \text{Th–C–NR}_2 \qquad (43) \\
 \underset{\displaystyle \overset{\displaystyle C}{O}}{\uparrow} \underset{\displaystyle \overset{\displaystyle O}{\nwarrow //}}{} \\[2em]
\text{R = H, alkyl}
\end{array}
$$
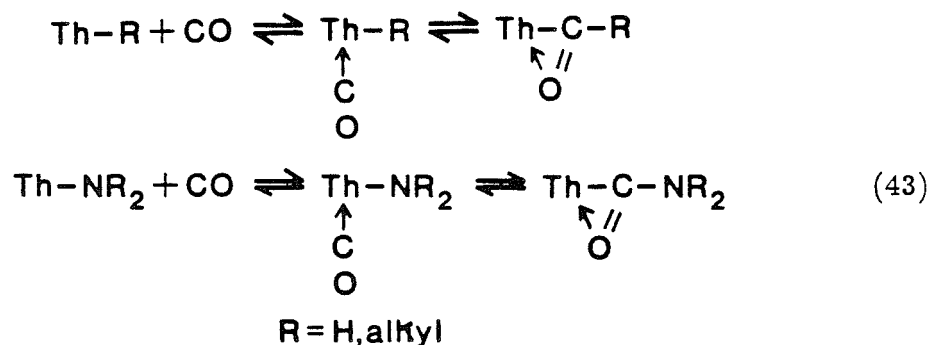
Based on the thermochemistry of Th–H and Th–C bonds (presented in Section 3.9), Marks and co-workers have calculated that the enthalpy of reaction of Th–C should be approximately −15 kcal mol^{-1} [D(Th–H) > D(Th–C) by ca. 10 kcal mol^{-1}]. These reactions are very significant in that they present one of the first pieces of unambiguous evidence for formyl formation via CO insertion.[12a,b] In addition, there are relatively few η^2-formyls and acyls known[64], yet in thorium this is the preferred orientation of binding.

In our calculations, we have examined the CO coordinated reactant as well as the inserted product for both Cl$_3$Th-–H and Cl$_3$Th–CH$_3$. For the Th–H bond

we also have investigated a reaction pathway for the intramolecular "migratory insertion" of the CO into the metal-hydride bond. In all the complexes, the valence electrons on Th, H (attached to the metal or CO), C, and O were correlated explicitly. The C−H bonds of the methyl group were not correlated. Optimum geometries of the coordinated CO and inserted CO complexes were obtained from gradient optimizations using the correlated wavefunctions [GVB(6/12)] without f functions on the Th. The scaled reaction coordinate was obtained with and without f functions at the GVB(6/12) level.

We first evaluated the energy of CO coordination. The optimum geometries for Cl_3Th-H and Cl_3Th-CH_3 are reported in Table X. The bonding in CO is predominately described by the structure shown below.[65]

(44)

Since the CO would be a fifth ligand about the already saturated metal center and since the bond to the metal involves a dative interaction from C, coordination must occur at a site that is both sterically unhindered and electron deficient. The best site for this is underneath the plane formed by two of the chlorines and the H/CH_3.

(45)
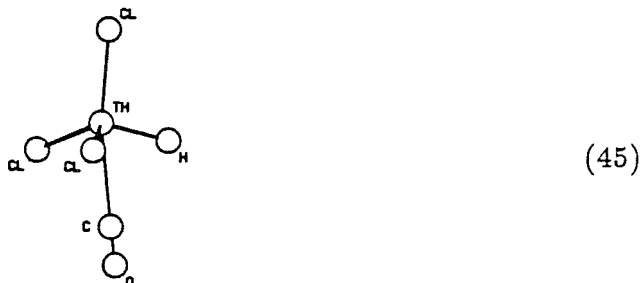
The resulting structure can be described as a pseudo-trigonal bipyramid. The optimum geometries for $Cl_3Th(H)CO$ and $Cl_3Th(CH_3)CO$ are shown in Tables XLVII and XLVIII, respectively. The Th−C distance is very long, greater

than 3Å, indicative of the weak dative bonding interaction (Th−C covalent bonds are about 2.5 Å long). The energetics of coordination as shown in Table XLIX indicate that $\Delta H = -9.5$ kcal mol^{-1} for Th−H and $\Delta H = -7.8$ for Th−CH$_3$, in favor of CO binding. It is interesting to note that in spite of the increased polarity of the Th−C and hence, the increased electron deficiency of the metal, the CO prefers to bind to the complex with the H ancillary ligand. Apparently, the greater steric repulsions of the methyl group outweigh any benefits from a slightly better dative bond on the methyl complex. For comparison, Rappé[64] found a binding energy of 16.4 kcal mol^{-1} between CO and Cl$_2$Sc using a CI wavefunction. We might expect a stronger binding energy to Th since the larger metal atom is less sterically hindered and more electropositive. Most probably a higher order wavefunction would recoup the energetic differences seen.

The optimum geometries of the inserted product species are shown in Table XLVII for Cl$_3$Th[η^2-OCH] and Table XLVIII for Cl$_3$Th[η^2-OCH$_3$]. As might be expected, the bond distances and angles change little from Th−H to Th−CH$_3$ complexes. In both molecules, the O is bent towards the Th at a fairly acute angle, about 74°. Hence, the η^2 structure is more stable than the η^1.

$$Cl_3Th - C \overset{\displaystyle H}{\underset{\displaystyle O}{\diagup\diagdown}} \qquad \eta' \qquad (46)$$

In fact, we could not find a stationary state corresponding to η^1. Marks and co-workers have obtained an X-ray crystal structure for the complex Cp$_2^*$[η^2-COCH$_2$C(CH$_3$)$_3$]Cl.[8e] It is also an η^2 coordinated acyl and its structural parameters in Table L compare well with our molecules. In particular, the Th−C−O angle is found to be at 73° ± 1 in the experimental structure, while we obtain 74.1° for the formyl and 73.2° for the acyl.

The enthalpies of the CO insertion reactions tell of the importance of f functions in thorium reaction chemistry. For without f functions on the metal both reactions are slightly endothermic. With f functions, the enthalpies of CO insertion are -2.4 and -6.0 for Th$-$H and Th$-$CH$_3$, respectively (see Table XLI). The reaction is more exothermic for insertion into a Th$-$CH$_3$ bond but the energy gap between hydride and alkyl insertion is smaller than that predicted by Marks et al. For the first-row transition metal Sc, Rappé[64] found that CO insertion into the Sc$-$H bond of Cl$_2$Sc$-$H was downhill 6.1 kcal mol^{-1} (CI wavefunction), in general agreement with our results.

In order to study in more detail the reaction pathway for insertion into a Th$-$H bond, we attempted to find the transition state for the reaction using analytic gradient techniques.[35] However, we were unsuccessful at obtaining a geometry at which the gradient was zero with one negative eigenvalue in the force constant matrix. Instead, we used for the reaction pathway a series of scaled geometries between the reactant and product. The coordinates of each point along the pathway were obtained by scaling the following atom-atom distances as they change from reactant to product: all R(Th$-$Cl), R(Th$-$H), R(Th$-$C), R(C$-$O), R(C$-$H), R(O$-$H), and all R(C$-$Cl). For example, the geometry for the first point along the reaction path was determined by taking the differences of the product and reactant atom-atom distances listed above and multiplying that difference by the scale factor 0.1. The scaled difference was then added to the appropriate R of the reactant geometry. This point is labeled as 10% since it is 10% of the way to the product geometry. Although the above distances are sufficient to describe the geometry change between reactant and product (restricting the symmetry to be C$_s$), they are not unique as we may just as well have used R(Th$-$O) instead of R(O$-$H).

The scaled geometry energy pathway is shown in Figure 11 both with and without f functions on Th. The transition state occurs between 60% to 70% of the way to the product geometry. The barrier heights are listed in Table LII. Unlike the energetics of CO coordination, f functions appear to have little influence on the barrier height, at least with the GVB(6/12) wavefunction, as $\Delta E^{\ddagger} = 62.8$ and 59.7 kcal mol^{-1}, sans f's and with f's, respectively. This activation energy serves as an upper bound to the true barrier for insertion. Rappé[64] found a barrier of 23.7 kcal mol^{-1} for CO migratory insertion into a Sc$-$H bond using a CI wavefunction and at a transition state found via gradient techniques. Using the same level of calculation as us, GVB(6/12), his activation energy is approximately 34 kcal mol^{-1}.

By evaluating the changes in the orbitals from reactant to product along the reaction coordinate we can ascertain a mechanism for the insertion process. In Figure 12a–f, we show the progression of the valence orbitals from reactants to products. The 12 valence electrons are correlated using a GVB(6/12) wavefunction. For the coordinated CO reactant the orbitals are almost unperturbed from Cl$_3$Th$-$H and CO. The dative interaction is weak and is essentially still the 2s orbital on C. The Th$-$H bond appears as the other hydride bonds we have examined previously. The CO σ bond is a strong dative interaction from O to C. Both the out-of-plane, π_x, and in-plane, π_y, bonds are polarized towards O. The O lone pair is mainly of 2s character.

The next set of plots is for the geometry 40% of the way along the reaction coordinate at about half the height of the barrier. The geometry is shown in Table LIII. There is little change in the dative bond. The other orbitals of CO look much the same as in the reactant. However, the Th$-$H bond has started to delocalize towards the C. There is a node in the orbital along the Th$-$C axis.

The character on the C and O in this GVB pair looks like that of a π^* orbital.

At 60% of the reaction pathway we are very close to the transition state. The dative bond continues to be centered mainly on C, but there is more character now on the thorium. The Th—H bond is very delocalized onto the carbon atom, with the π^* CO character. The C—O σ bond pair is now quite distorted. The O lone pair and the C—O out of plane π bond are essentially unchanged. The 70% geometry is just past the transition state. The dative Th—C bond is slowly converting into a covalent bond. The Th—H bond appears to be more like a C—H bond with some delocalization onto the metal. There is still a node through the thorium-carbon axis. The C—O σ bond is undistorted and the O lone pair has delocalized slightly towards the forming C—H bond. The in-plane π bond is disappearing with much more character on the O atom pointed away from the C—H interaction; i.e., it is becoming another O lone pair.

The 90% point is half-way down the other side of the barrier towards the product. The reaction coordinate drops at a faster rate after the transition state is passed. This geometry looks much like an η^1- formyl (see Table LIII), with $\theta(\text{Th—C—O}) = 116.7°$. There are now full-fledged covalent Th—C and C-–H bonds. There are two lone pairs on the O and the C—O bond is becoming more covalent. Finally, we reach the product orbitals. At this point the O is bent over to form the η^2 interaction with the metal.

The above analysis of the changes in the orbitals along the scaled reaction pathway suggests that the mechanism of reaction involves attack of the Th—H bond upon the C.

(47)
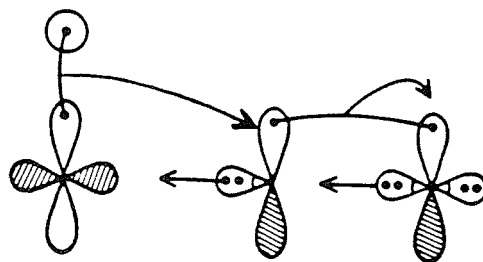
The in-plane π bond moves out of the way to become an oxygen lone pair, which eventually is involved in the η^2 dative bond to Th. The dative M$-$C interaction becomes the M$-$C covalent bond via rehybridization and charge flow from carbon to thorium. The other CO orbitals stay virtually unchanged, except for the C$-$O σ bond which must rehybridize at the transition state, from an O doubly occupied sp orbital donating into an empty C p orbital to a covalent bond with a C sp^2 orbital. This rehybridization causes the bond to distort since the orbital on C involved in the in-plane π bond must become an sp^2 orbital to bond to H. The distortion would certainly increase the barrier height. Since the π^* orbital appears to be accessible energy-wise, the reaction should be considered allowed. However, in CO the dipole moment is pointed towards the C. The less electron deficient the carbon is the greater the barrier would be. This along with the distortion of the C$-$O bond may be the reason for the relatively high activation energy. We would expect that a CI calculation on the transition state, allowing relaxation of spin coupling and orbital shapes, would lower the barrier significantly.

Rappé has suggested a different mechanism for the CO insertion reaction involving a sort of 2 + 2 reaction,

$$\text{(48)}$$
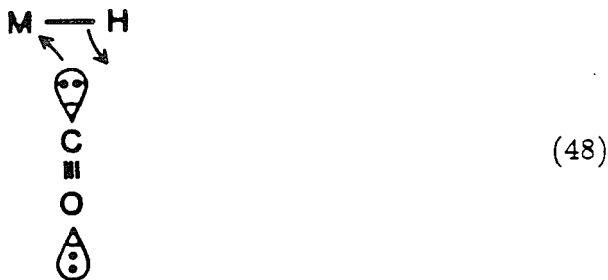
in which the 2s lone pair on the carbon and the metal-hydrogen bond trade

places. The transition state that he finds is close to the η^1-formyl. However, it appears to be well past the point where the M$-$H bond should be delocalizing. In this transition state, the C$-$H bond is already well-formed and the in-plane π bond is already strictly an O lone pair. Even though our reaction coordinate is not the actual one, we believe that C$-$H bond formation and π bond migration to become a lone pair are the keys to this reaction and that the transition state should reflect this.

What would be the effect of replacing the hydrogen with a methyl group? There would be several changes, most of which echo the earlier arguments concerning the 2 + 2 transition states (Section 3.7). Steric considerations and the directed nature of the carbon-bonding orbital would increase the barrier for methyl relative to hydrogen. However, since the Th$-$CH$_3$ bond is more ionic than Th$-$H, the CH$_3$ group should be a stronger electrophile and the ease with which it moves over to the carbon atom should be greater. Since ionic effects seem to play a large role for the 2 + 2 reactions, we may expect them to be predominant here as well; in which case, insertion into the Th$-$CH$_3$ bond would have a lower barrier. Marks was able to see both species, CO coordinated and CO inserted, for the Th$-$H complex, but only the CO inserted product has been isolated for thorium-alkyl bonds. Perhaps this observation is not just a thermodynamic effect, but is also related to the activation energies.

There are strong implications in this CO insertion process concerning the CO poisoning seen on organoactinide-doped alumina surfaces. Since CO insertion is favorable with respect to both H and alkyl ligands, one would expect it to happen readily at the Th$-$R groups supported on the surface. Once the inserted product is formed, it would probably kill off any further reactivity of the metal center since it is a thermodynamic sink. The η^2-O interaction helps to alleviate the

electropositiveness of the metal which we showed earlier (Section 3.6) to be a major factor in thorium's enhanced reactivity with respect to the Group IVB metals.

3.9 Thorium-Ligand Bond Energies: Theory and Experiment

There have been very few measurements of metal-ligand bond dissociation energies for the transition metals or actinides. Marks and co-workers have determined bond disruption enthalpies for a wide variety of ligands bonded to Cp_2^*Th and Cp_3Th fragments.[66] Their results for $D(Th-CH_3)$ and $D(Th-H)$ in the gas phase are shown in Table LIV. They found that ligands attached to the Cp_3Th fragment have bond energies that are significantly larger (by about 5–6 kcal mol^{-1}) than those same ligands on the Cp_2^*Th fragment. On the other hand, there is some evidence that an extra Cl ligand (Cp_2^*ClTh) has the opposite, although somewhat weaker [$D(Th-C_2H_5)$ decreased by about 2 kcal mol^{-1}], effect on metal-ligand bond energies, decreasing the binding energy. Lastly, it was seen that alkoxy groups [$Cp_2^*(OR)Th$] strengthen Th—R bonds. Their conclusion was that the more electron withdrawing the ancillary ligands are, the greater the higher oxidation states of the metal will be stabilized, and that this increases the Th—R bond energies. For Cp and Cp*, they speculated that several effects could be occurring, including π donation from the Cp rings back to the metal, overlap differences in the Th—R bonds, and electronic effects.

In order to evaluate the effect of anionic ancillary ligands on $D(Th-H)$ and $D(Th-CH_3)$, we have calculated these bond energies in the complexes Cl_2MH_2, Cl_3MH, $Cl_2Th(H)CH_3$, and Cl_3ThCH_3. In Table LIV, our results show that there is little or no effect on the bond energy from the extra electron-withdrawing Cl. $D(Th-H)$ in the Cl_3ThH complex is lower than in the Cl_2ThH_2, while $D(Th-C)$

in the trichloride is slightly higher than in the dichloride. Since we have shown that the EP Cl acts electronically as a Cp ligand (see Section 3.3), there is not a large differential electronic effect of an extra Cp ligand on the Th−R bond strength. There are two distinctions between the Cl and Cp ligands, however. Of course, the Cl ligand does not have the same steric bulk as the Cp, but steric repulsions should act to decrease the overlap in the bond by increasing R(Th−R) and thus weaken the bond. The other difference is, as pointed out in Section 3.3, that the Cp group destabilizes the π orbitals on the metal (in Cp−Th−Cl) significantly more than the Cl (in Cl−Th−Cl). In other words, charge is pulled off from the metal by the Cp group via the σ system, but is put back on the metal via the π system. Hence, though the overall charge may remain the same on the metal, the orbitals in which the charge resides may differ. For the saturated complexes discussed here, the Cp ligands may redistribute the charge on the metal such that there is more available to the R group — generally the more anionic the ligands are the stronger the bond is. An example of this is the very large bond energy of the Th−O bond in Cl_3ThOH. As can be seen from the orbitals in Fig. 13, there is almost complete charge transfer to the p_y orbital of the O which leads to a linear Th−O−H geometry.

The relative ordering of the bond strengths (gas phase) in Marks' study on the di-Cp complexes (ThR_2) is C_6H_5 > CH_3 > CH_2CH_3. For the tri-Cp comlexes, CH_3 > $CH(CH_3)_3$ > CH_2C_6. Thus the results parallel each other in showing that the more electronegative R groups have stronger bond energies. However, D(Th−H) is found to be larger than D(Th−C) by 13.3 kcal mol^{-1}, even though CH_3 is more electronegative than H. Our theoretical bond energies show that the Th−C bond energy is closer to that of Th−H, the difference being only approximately 5 kcal mol^{-1}. This follows from our results on D(M−H) versus

D(M−C) for M = Ti, Zr, and Hf, where we found that metal-carbon bonds are slightly stronger than metal-hydrogen bonds. Apparently there are other factors besides electronegativity which effect the relative ordering of H versus CH_3 bond strengths. Possibilities include overlap of the bonding orbitals (neglecting charge transfer) and steric interactions, which are decidely worse for methyl. In any event, our conclusion is that the experimental Th−H bond energies may be too large.

There are several factors which could account for the differences between the magnitudes of the ab initio bond energies and the experimentally determined ones. First, in Marks' study several assumptions are made in the thermodynamic analysis of the data. The bond energies are determined by measuring the heat of reaction, ΔH_{rxn}, of the alcoholysis of a Th−R bond in solution,

$$L_n Th - R + R'OH \longrightarrow L_n Th - OR' + RH. \tag{49}$$
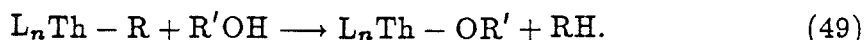
The enthalpy of reaction is related to the bond strength as follows,

$$D(Th - R)_{soln} = \Delta H_{rxn} + D(Th - O)_{soln} + D(R - H)_{soln} - D(O - H)_{soln}. \tag{50}$$

The enthalpies in solution of some of the RH species and OH are not known. Estimates are made for the unknown RH species, and the D(O−H) of ethanol is used (the actual alcohol used is F_3CCH_2OH). These enthalpies are stated to be reasonable approximations to the actual values. Of greater concern is the value of D(Th−O) which is not measured directly in this study. This is estimated from mean bond energies obtained by Lappert et al. on $M(OR)_4$, M = Ti, Zr, and Hf (R = i-C_3H_7).[67] The value used is 124 kcal mol^{-1}. Marks' best guess is that the error in this value is approximately 10 kcal. Theoretically, we obtain 131.5 kcal mol^{-1} for D(Th−OH).

To obtain gas phase bond energies, the enthalpies of solution, vaporation, and sublimation must be known for the various species,

$$\Delta H^\circ_{gas} = \Delta H_{rxn} + \Delta H^\circ_{sub}(L_n ThOR) + \Delta H_{vap}(RH)$$

$$- \Delta H^\circ_{sub}(L_n ThR) - \Delta H^\circ_{vap}(ROH) - \Delta H^\circ_{soln}(L_n ThOR) \quad (51)$$

$$- \Delta H^\circ_{sub}(RH) + \Delta H^\circ_{soln}(L_n ThR) + \Delta H^\circ_{soln}(ROH).$$

The heats of solution for ThR and ROH were measured by Marks and co-workers. The heats of vaporization for RH and ROH, and heat of solution of RH were all obtained from previous experimental determinations. The remaining quantities, $\Delta H^\circ_{sub}(L_n ThOR)$, $\Delta H^\circ_{sub}(L_n ThR)$, and $\Delta H^\circ_{soln}(L_n ThOR)$, are unknown. They made the assumption that the sublimation energies of ThOR and ThR were equivalent and thus cancel in Eq. 50. Likewise, the heat of solution of ThOR was equivalenced with $\Delta H^\circ_{soln}(ThR)$. Thus there are possibly some inaccuracies in the way the bond energy was derived from the heat of reaction and it is estimated that the bond energies could be systematically in error by up to 10 kcal.

Secondly, the complexes studied experimentally differed from our theoretical systems. Besides the obvious steric differences between Cp and Cl, they studied the bridging dimeric hydrogen complex, while our D(Th−H) came from the monomer. We examined $Cl_2 Th(H)CH_3$, but the experimental complex was $Cp^*_2 Th(CH_3)_2$. We would not expect these changes to have a major effect on the magnitude of the bond energies. As previously discussed (Section 3.5), there is strong evidence for the monomer existing in equilibrium with the dimer. Also, H and CH_3 are very similar ligands as evidenced by their nearly equal bond energies.

Finally, the level of wavefunction used could affect the bond energies. For all cases, bond energies were obtained with CI wavefunctions that included

the highest amount of correlation computationally possible, while maintaining a dissociation-consistent limit at infinite internuclear separation. For the Th–H bonds, the bond energies are from a full valence CI calculation (for Cl_2ThH_2 the full CI is estimated from the CCCI). For the Th–C bonds, the highest level of correlation used was CCCI within the active space (both Th–C and adjoining Th–H ligand in $Cl_2Th(H)CH_3$), which included single excitations from the semi-active space (C–H HF bond pairs) times the RCI configurations. There may be some additional correlation present in the CH bond pairs, but this would only help to lower the gap between D(Th–H) and D(Th–C).

In order to further assess electronegativity effects on bond strengths, we investigated the molecules Cl_2ThO, Cl_2ThS, and Cl_2ThNH (linear Th–N–H only). In all these systems, the ligands form a triple bond (two polar π bonds and one donor σ bond) with the thorium, rather than a double bond,

$$\text{Th} \equiv \text{O}$$
$$\text{or}$$
$$\text{Th} \equiv \text{S}$$

$$\text{Th} \equiv \text{N-H}$$

(52)
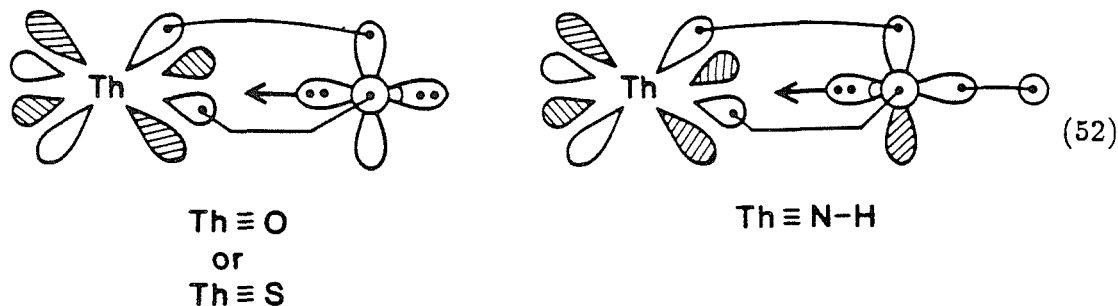
as would be suggested by the two unpaired electrons remaining on the O, S, and N atoms. Similar triple bonds have been found theoretically for Ti–O and Ti–NH species.[68] Interestingly, this also occurs for Th–S, even though S, as a second-row element, is not noted for making good π bonds.

The optimum geometries for these systems are shown in Table LV and a Mulliken population analysis is shown in Table LVI. The size of the Th–O bond energy in Table LVII shows that the Th ligand is extremely oxophilic. In com-

parison, for Cl_2TiO, $D_e(Th-O) = 140$ kcal mol^{-1}.[68] Since Th is much more electronegative than Ti, the amount of metal-to-ligand charge transfer is the predominant force increasing the bond energy from Ti to Th. Note, however, that in comparing the O, S, and NH ligands, a simple charge transfer argument does not explain fully the binding energies obtained. For example, even though the bond energies follow the trend in electronegativities of the ligands (O > NH > S), the Mulliken populations show that the NH and O ligands pull off about the same amount of charge from the metal. The difference between the NH ligand and the O ligand is the N$-$H bond. This bond and the M$-$N bond must be orthogonal to each other. This requires rehybridization of the orbitals. And each bond can be described as an sp hybrid. With O, no such rehybridization is required, and it can bond to the metal with a doubly-occupied p orbital. Since the p orbital has less s character than the sp hybrid, it is higher in energy and has a greater radial extent. Both of these qualities facilitate bonding into the empty orbital on the metal. There is a synergistic relationship between charge transfer into the π bonds and into the σ bond. Hence, for Th$-$NH, charge flows into the π system, but not as much flows back to the metal through the σ space as with Th$-$O. That is probably the reason why Th$-$NH appears to have the same amount of charge transfer as Th$-$O. The overlaps of the σ bonding orbitals support this conclusion. For NH, the overlap is 0.896, while for O it is 0.834. The doubly occupied orbital on the NH ligand pointed at the metal is much tighter than the O σ orbital. The bond energy of NH to Cl_2Ti is 102 kcal mol^{-1} and thus the difference between O and NH bond strengths between Ti and Th is the same, about 40 kcal mol $^{-1}$. This indicates that the same line of reasoning as above applies to the first row metal.

4. Summary

In this first chapter of the thesis, we have discussed in considerable detail the bonding and reaction chemistry of thorium organometallic compounds, and have compared and contrasted the actinide's chemistry to its isovalent neighbors, the Group IVB elements, Ti, Zr, and Hf. There are two major trends that occur as the atomic number increases in this series of elements. First, the shape and radial extent of the d orbital enables the overlap of a metal bonding orbital with an incoming ligand orbital to be larger with increasing principal quantum number. The upshot of this is that bond energies increase down the column from Ti to Th in marked contrast to the main group-ligand bond strengths, which generally decrease with increasing atomic and orbital size. Second, the amount of charge transferred from metal to ligand increases from Ti to Th, as a consequence of the increasing electropositiveness of the metal. The ionicity of the metal-ligand bonds has profound impact on the activation energies of concerted $[2 + 2]$ reactions at $M-H$ and $M-C$ bonds.

The reaction chemistry of Th is not radically different from that of its isovalent cogeners but rather an evolution from their chemistry. In the $2 + 2$ addition reactions, the increasing polarity of the transition state from Ti to Th has a great bearing on decreasing the activation barrier. In comparison with the main group metals, as the reaction becomes more like a hydride transfer, the barrier decreases. From this alone we would predict that Th would be more reactive along the concerted pathway. The ligand bound to the metal, of course, also has a great effect on the activation energy. Since transition metal-L bonds are generally of greater strength with increasing atomic size, we would expect that it would be harder to distort the stronger bonds at the transition state, which

would lead to a higher barrier. This may be why the general reactivity of the Group IVB metals goes as Ti $\gg$ Zr > Hf. The anionicity of the ligand is also very important in determining the activation energy. From our studies, M$-$C bonds are more polar (with the C more anionic than H) than M$-$H bonds, but their relative bond energies are virtually the same. On this basis we would predict that for a polar 2 + 2 transition state like Th, e.g., Th$-$R + D_2 $\rightarrow$ Th$-$D + R$-$D, R = methyl would have a lower barrier than R = H. For a nonpolar transition state like Ti or Sc, the increased directionality of the M-alkyl bond along with steric effects would reverse the above trend with the M$-$H bond being more reactive. Finally, another factor which one may consider to have a large impact on the relative stability of the tranistion state is the amount of s versus d character in the metal-L bonds. However, our conclusion is that the relative character of the orbitals is of only minor importance. It is only important to note that the major portion of the character in a M$-$L bond must be d for a low 2 + 2 barrier. For example, M$-$C bonds appear to have significantly more d character from the metal than M$-$H bonds, yet the realative reactivity in Ti through Th metals seems not to follow this trend. From Ti to Th the s and d orbitals become more equivalent in energy and hence, the amount of d character in the M$-$L bonds drops. However, the Th complexes we studied are more reactive.

References

(1) See, for example, a) T. J. Marks, Science, **217**, 989–997 (1982); b) T. J. Marks and R. D. Ernst, in *Comprehensive Organometallic Chemistry*, G. Wilkinson, F. G. A. Stone, and E. W. Abel, Eds. (Pergamon, Oxford, 1982); c) K. N. Raymond and C. W. Eigenbrot, Jr., Acc. Chem. Res. **13**, 276 (1980); d) T. J. Marks, Prog. Inorg. Chem. **24**, 52 (1978); e) *ibid.* **25**, 224 (1979); f) S. A. Cotton, J. Organomet. Chem. Libr. **3**, 189 (1977); g) *Organometallics of the f-Elements*, T. J. Marks and R. D. Fischer, Eds. (Reidel, Dordrecht, 1979); h) T. J. Marks, Acc. Chem. Res. **9**, 223–230 (1976).

(2) F. A. Cotton and G. Wilkinson, *Advanced Inorganic Chemistry* (Wiley & Sons, New York, 1980 [4th Ed.]), p. 1005 ff.

(3) a) K. N. Raymond and C. W. Eigenbrot, Jr., Acc. Chem. Res. **13**, 276 (1980); b) T. J. Marks, Prog. Inorg. Chem. **24**, 52 (1978); c) *ibid.* **25**, 224 (1979); d) S. A. Cotton, J. Organomet. Chem. Libr. **3**, 189 (1977); e) T. J. Marks, A. M. Seyam, and J. R. Kolb, J. Am. Chem. Soc. **95**, 5529 (1973); f) T. J. Marks and W. A. Wachter, *ibid.* **98**, 803 (1976); g) T. J. Marks, Acc. Chem. Res. **9**, 223 (1976); h) G. Brandi, M. Brunelli, G. Lugli, and A. Mazzei, Inorg. Chim. Acta. **7**, 319 (1973); i) M. Tsutsui, N. Ely, and R. Dubois, Acc. Chem. Res. **9**, 217 (1976); j) P. J. Fagan, J. M. Manriquez, E. A. Maatta, A. M. Seyam, and T. J. Marks, J. Am. Chem. Soc. **103**, 6650 (1981); k) P. J. Fagan, J. M. Manriquez, and T. J. Marks in *Organometallics of the f-Elements* (Reidel, Dordrecht, 1979), Chap. 4; l) E. A. Mintz and T. J. Marks, Abstr. Am. Chem. Soc. Natl. Meet., Atlanta (March 1981), INOR 224;

(4) J. P. Colman and L. S. Hegedus, *Principles and Applications of Organotran-*

sition Metal Chemistry (University Science Books, Mill Valley, California, 1980), p. 119 ff.

(5) a) E. R. Sigurdson and G. Wilkinson, J. Chem. Soc. Dalton Trans. (1977), 812; b) P. G. Edwards, R. A. Andersen, and A. Zalkin, J. Am. Chem. Soc. **103**, 7792 (1981).

(6) J. W. Bruno and T. J. Marks, J. Am. Chem. Soc. **104**, 7357–7360 (1982).

(7) P. J. Fagan, E. A. Maatta, J. M. Manriquez, K. G. Moloy, A. M. Seyam, and T. J. Marks, Actinides Perspect., Proc. Actinides Conf., 433–452 (1982).

(8) a) P. J. Fagan, E. A. Maatta, and T. J. Marks, ACS Symp. Ser. **152**, 52 (1981); b) T. J. Marks, J. M. Manriquez, P. J. Fagan, V. W. Day, C. S. Day, and S. H. Vollmer, *ibid.* **131**, 1 (1980); c) P. J. Fagan, J. M. Manriquez, S. H. Vollmer, C. S. Day, V. W. Day, and T. J. Marks, J. Am. Chem. Soc. **103**, 4063 (1981); d) E. A. Maatta and T. J. Marks, J. Am. Chem. Soc. **103**, 3576 (1981). e) P. J. Fagan, J. M. Manriquez, T. J. Marks, V. W. Day, S. H. Vollmer, and C. S. Day, J. Am. Chem. Soc. **102**, 5396–5398 (1980).

(9) R. W. Broach, A. J. Schultz, J. M. Williams, G. M. Brown, J. M. Manriquez, P. J. Fagan, T. J. Marks, Science **203**, 172 (1979).

(10) J. M. Manriquez, P. J. Fagan, and T. J. Marks, J. Am. Chem. Soc. **100**, 3939 (1978).

(11) a) J. M. Manriquez, D. R. McAlister, R. D. Sanner, and J. E. Bercaw, J. Am. Chem. Soc. **100**, 2716-2724 (1978); b) S. J. Simpson, H. W. Turner, and R. A. Andersen, J. Am. Chem. Soc. **101**, 7728-7729 (1979).

(12) a) P. J. Fagan, K. G. Moloy, and T. J. Marks, J. Am. Chem. Soc. **103**, 6959 (1981); b) D. A. Katahira, K. G. Moloy, and T. J. Marks, Organometallics **1**, 1723-1726 (1982).

(13) a) R. G. Bowman, R. Nakamura, P. J. Fagan, R. L. Burwell, Jr., and T. J.

Marks, J. Chem. Soc., Chem. Commun. 257-258 (1981); b) M.-Y. He, R. L. Burwell, Jr., and T. J. Marks, Organometallics **2**, 566-569 (1983); c) R. L. Burwell, Jr., J. Catal. **86**, 301-314 (1984); d) R. L. Burwell, Jr. and T. J. Marks, Chem. Ind. (Dekker), Catal. Org. **22**, 207-224 (1985); e) M.-Y. He, G. Xiong, P. J. Toscano, R. L. Burwell, Jr., and T. J. Marks, J. Am. Chem. Soc. **107**, 641-652 (1985).

(14) P. H. Otero-Schipper, W. A. Wachter, J. B. Butt, R. L. Burwell, Jr., and J. B. Cohen, J. Catal. **50**, 494-507 (1977).

(15) P. J. Fagan, E. A. Maatta, A. M. Seyam, and T. J. Marks, Rare Earth Mod. Sci. Technol. **3**, 77-84 (1982).

(16) a) K. Tatsumi and R. Hoffmann, Inorg. Chem. **19**, 2656 (1980); b) K. Tatsumi and R. Hoffmann, Inorg. Chem. **23**, 1633 (1984).

(17) a) P. J. Hay, W. R. Wadt, L. R. Kahn, R. C. Raffenetti, and D. C. Phillips, J. Chem. Phys. **71**, 1767 (1979); b) W. R. Wadt and P. J. Hay, J. Am. Chem. Soc. **101**, 5198 (1979).

(18) W. R. Wadt, J. Am. Chem. Soc. **103**, 6053 (1981).

(19) a) L. R. Kahn and W. A. Goddard III, Phys. Rev. **180**, 747 (1969); b) *ibid.*, J. Chem. Phys. **56**, 2685 (1972); c) C. F. Melius, W. A. Goddard III, and L. R. Kahn, J. Chem. Phys. **56**, 3342 (1972); d) C. F. Melius and W. A. Goddard III, Phys. Rev. A **10**, 1528 (1974).

(20) a) L. R. Kahn, P. J. Hay, and R. D. Cowan, J. Chem. Phys. **68**, 2386 (1978); b) L. R. Kahn, Int. J. Quant. Chem. **25**, 149–183 (1984).

(21) The effective potential portion of the Caltech one-electron integrals program, ONEHON, was modified by C. F. Melius, based on the earlier work of L. R. Kahn, to correctly do relativistic core potentials of high angular momemtum.

(22) R. M. Eisberg, *Fundamentals of Modern Physics* (Wiley, New York, 1961),

pp. 353-355.

(23) a) A. K. Rappé, T. A. Smedley, and W. A. Goddard III, J. Chem. Phys. **85**, 1662 (1981); b) A. K. Rappé and W. A. Goddard III, unpublished results.

(24) S. Huzinaga, J. Chem. Phys. **42**, 1293 (1966).

(25) R. A. Bair and W. A. Goddard III, unpublished results.

(26) T. H. Dunning, J. Phys. Chem. **85**, 2607 (1981).

(27) A. K. Rappé and W. A. Goddard III, unpublised results.

(28) A. K. Rappé, T. A. Smedley, and W. A. Goddard III, J. Phys. Chem. **85**, 2607 (1981).

(29) P. J. Hay and W. R. Wadt, J. Chem. Phys. **82**, 299-310 (1985).

(30) a) W. A. Goddard III, T. H. Dunning, W. J. Hunt, and P. J. Hay, Accts. Chem. Res. **6**, 368 (1973); b) W. A. Goddard III and L. B. Harding, Ann. Rev. Phys. Chem. **29**, 363 (1978).

(31) In actual practice, the GVB orbitals are calculated in terms of natural orbitals, plus and minus combinations of the one-electron orbitals. The natural orbitals for a left-right correlated bond pair consist of one orbital which is a bonding combination of functions on both atoms and one orbital that is antibonding with a node bisecting the internuclear axis. For ease of interpretation, most of the orbital plots in this work are of one-electron orbitals (except Fig. 6).

(32) a) R. A. Bair and W. A. Goddard, submitted for publication; b) R. A. Bair, Ph. D. thesis, California Institue of Technology, 1981.

(33) E. A. Carter and W. A. Goddard III, J. Chem. Phys., in press.

(34) J. J. Low and W. A. Goddard III, unpublished results.

(35) A. K. Rappé, unpublished results.

(36) For a general compilation of the ground levels and ionization potentials of

lanthanide and actinide atoms and ions, see W. C. Martin, L. Hagan, J. Reader, and J. Sugar, J. Phys. Chem. Ref. Data **3** 771–779 (1974).

(37) R. Zalubas, J. Opt. Soc. Amer. **58**, 1195–1199 (1968).

(38) R. Zalubas and C. H. Corliss, J. Res. Nat. Bur. Stand. A. **78A**, 163–179 (1974).

(39) N. Minsky, Ph. D. thesis, Hebrew Univ. Jerusalem, 1969.

(40) a) T. L. de Bruin, P. F. A. Klinkenberg, and P. H. Shuurmans, Z. Phys. **118**, 58 (1941); b) P. F. A. Klinkenberg, Physica **16**, 618 (1950).

(41) U. Litzén, Phys. Scr. **10**, 100 (1974).

(42) P. F. A. Klinkenberg and R. J. Lang, Physica **15**, 774–791 (1949).

(43) Private communication with M. H. McAdon.

(44) J. Sugar, J. Chem. Phys. **59**, 788 (1973); b) *ibid.* **60**, 4103 (1974).

(45) A. K. Rappé, Ph. D. thesis, California Institute of Technology, p. 73, 1981.

(46) A. K. Rappé and W. A. Goddard III, J. Am. Chem. Soc. **104**, 297–299 (1982).

(47) E. A. Carter and W. A. Goddard III, Organometallics, in press.

(48) C. E. Moore, *Atomic Energy Levels* (National Bureau of Standards, Washingtion, D. C., 1971).

(49) a) T. L. Brown and H. E. LeMay, Jr., *Chemistry the Central Science* (Prentice-Hall, Englewood Cliffs, New Jersey, 1977), p. 224; b) *Table of Periodic Properties of the Elements* (Sargent-Welch, Skokie, Illinois, 1968).

(50) A. K. Rappé, Ph. D. thesis, California Institute of Technology, p. 56 ff, 1981.

(51) M. L. Steigerwald, Ph. D. thesis, California Institute of Technology, p. 161, 1984.

(52) *CRC Handbook of Chemistry and Physics*, R. C. Weast and M. J. Astle,

Eds. (CRC Press, West Palm Beach, Florida, 1978 [59th Ed.]), p. F-216.

(53) We have estimated the full valence CI energy of the molecule, Cl_2ThH_2, from the full valence CI and CCCI energies of Cl_2ZrH, Cl_2ZrH_2, and Cl_2ThH and from the CCCI energy of Cl_2THH_2. The difference in energy between the full CI and CCCI wavefunctions for both Zr complexes and for the Th fragment is obtained. We then take the ratio of these energy differences for Cl_2ZrH and Cl_2ThH, and *assuming* that this ratio holds for Cl_2MH_2, M = Zr and Th, we can predict the full valence CI energy for the Th dihydride. We did not use the values for Ti and Hf since both have unique properties (Ti is a first-row metal; Hf has a small atomic radius due to the "lanthanide" contraction).

(54) K. P. Huber and G. Herzberg, *Molecular Spectra and Molecular Structure, IV. Constants of Diatomic Molecules* (Van Nostrand Reinhold, New York, 1979).

(55) P. W. Atkins, *Physical Chemistry* (W. H. Freeman San Francisco, 1978), p. 884.

(56) a) C. W. Wilson, Jr., and W. A. Goddard III, J. Chem. Phys. **51**, 716 (1969); b) *ibid.* **56**, 5913 (1972).

(57) a) M. L. Steigerwald and W. A. Goddard III, J. Am. Chem. Soc. **106**, 308 (1984); b) M. L. Steigerwald and W. A. Goddard III, unpublished results.

(58) *CRC Handbook of Chemistry and Physics*, R. C. Weast and M. J. Astle, Eds. (CRC Press, West Palm Beach, Florida, 1978 [59th Ed.]), pp. E-67,E-68,E-74.

(59) P. B. Armentrout, L. F. Halle, and J. L. Beauchamp, J. Am. Chem. Soc. **103**, 6501 (1981).

(60) P. C. Wailes, R. S. P. Coutts, and H. Weigold, *Organometallic Chemistry of*

Titanium, Zirconium, and Hafnium (Academic Press, New York, 1974), p. 151.

(61) M. E. Thompson, S. M. Baxter, A. R. Bulls, B. J. Burger, M. C. Nolan, B. D. Santarsiero, W. P. Schaefer, and J. E. Bercaw, J. Am. Chem. Soc. **109**, 203-219 (1987).

(62) *Comprehensive Organometallic Chemistry*, G. Wilkinson, F. G. A. Stone, and E. W. Abel, Eds. (Pergamon Press, Oxford, 1982), Vol. 3, p. 550 ff.

(63) P. J. Fagan, J. M. Manriquez, S. H. Vollmer, C. S. Day, V. W. Day, and T. J. Marks, J. Am. Chem. Soc. **103**, 2206–2220 (1981).

(64) A. K. Rappé, J. Am. Chem. Soc. **109**, 5605 (1987) and references therein.

(65) a) S. P. Walch and W. A. Goddard III, J. Am. Chem. Soc. **98**, 7908–7917 (1976); b) W. A. Goddard III, *The Nature of the Chemical Bond* (California Institute of Technology, Pasadena, California, 1983), p. 8.13.1 ff.

(66) a) J. W. Bruno, T. J. Marks, and L. R. Morss, J. Am. Chem. Soc. **105**, 6824–6832 (1983); b) D. C. Sonnenberger, L. R. Morss, and T. J. Marks, Organometallics 4, 352–355 (1985).

(67) M. F. Lappert, D. S. Patil, and J. B. Pedley, J. Chem. Soc., Chem. Commun. 830–831 (1975).

(68) A. K. Rappé, Ph. D. thesis, California Institute of Technology, p. 86 ff, 1981.

Table I. The Los Alamos (LA) Basis Set (Ref. 18) for Thorium: Cartesian Gaussian Functions with Exponents (α_i) and Contraction Coefficients (C_i).

type	α_i	C_i
s	0.1628	1.000000
s	0.09045	1.000000
s	0.02721	1.000000
p	1.163	−0.293240
p	0.5092	0.867030
p	0.187	1.000000
p	0.07	1.000000
d	0.3244	1.000000
d	0.1185	0.489490
d	0.04389	0.186990
f	3.336	0.222601
f	1.209	0.475920
f	0.3969	0.450580
f	0.1105	0.225200

Table II. The Set of d Functions Used in the TH1 and TH2 Basis Sets for Thorium (replacing the three d primitives in Table I): Cartesian Gaussian Functions with Exponents (α_i) and Contraction Coefficients (C_i).

type	α_i	C_i
d	0.3169	1.000000
d	0.1157	1.000000

Table III. Experimental Spectrum[a] (< 9000 cm^{-1}) of Thorium Atom Averaged over J States.

Configuration	Designation	Energies[b] (cm^{-1})
$6d^2 7s^2$	^3F	0.000
$6d^2 7s^2$	^3P	558.756
$6d^2 7s^2$	^1D	4217.280
$6d^2 7s^2$	^1G	5048.161
$6d^3 7s^1$	^5F	5167.800
$5f^1 6d^1 7s^1$	^3H	8500.453
$5f^1 6d^1 7s^1$	^3F	8735.835

a) Ref. 37. b) Energies relative to the ground state (averaged over J states), $6d^2 7s^2$ ^3F.

Table IV. Experimental Spectrum[a] (< 8000 cm^{-1}) of Th$^+$.

Configuration	Designation	J	Energies[b] (cm^{-1})
$(6d+7s)^3$	—	1 1/2	0.000
$6d^2 7s^1$	^4F	2 1/2	1521.893
$(6d+7s)^3$	—	1 1/2	1859.936
$(6d+7s)^3$	—	2 1/2	4113.356
$6d^2 7s^1$	^4F	3 1/2	4146.575
$5f^1 7s^2$	^2F	2 1/2	4490.256
$5f^1 6d^1 7s^1$	^4H	3 1/2	6168.351
$6d^2 7s^1$	^4F	4 1/2	6213.488
$6d^2 7s^1$	^4P	1/2	6244.294
$5f^1 6d^1 7s^1$	^4F	1 1/2	6691.386
$(5f+6d+7s)^3$	—	4 1/2	6700.183
$(6d+7s)^3$	—	1 1/2	7001.425
$5f^1 6d^1 7s^1$	^4F	2 1/2	7331.485
$(6d+7s)^3$	—	1/2	7828.526

a) Ref. 38. b) Energies relative to the ground state, $(7s+6d)^3$.

Table V. Experimental Spectrum[a] (lowest two levels for each configuration) of Th^{2+} Averaged over J States.

Configuration	Designation	Energies[b] (cm^{-1})
$6d^2$	^3F	0.0
$5f^1 7s^1$	^3F	135.3
$6d^2$	^1D	507.4
$5f^1 6d^1$	^3H	651.0
$5f^1 6d^1$	^3F	1410.2
$5f^1 7s^1$	^1F	3331.4
$6d^1 7s^1$	^3D	3792.9
$7s^2$	^1S	7792.0
$6d^1 7s^1$	^1D	11868.5
$5f^2$	^3H	14107.3
$5f^2$	^3F	16605.0

a) Ref. 40b. b) Energies relative to the ground state (averaged over J states), $6d^2$ ^3F.

Table VI. Experimental Spectrum[a] (involving 5f, 6d, and 7s orbitals) of Th^{3+}.

Configuration	Designation	Energies[b] (cm^{-1})
$5f^1$	^2F	0.00
$6d^1$	^2D	9897.07
$7s^1$	^2S	20658.55

a) Ref. 42. b) Energies relative to the ground state (averaged over J states), $5f^1$ ^2F.

Table VII. Hartree-Fock Total Energies of Th, Th$^+$, Th^{2+}, Th^{3+}, and Th^{4+} Atomic States Using the TH1 and LA Basis Sets.

Configuration[a]	Designation	TH1 Basis		LA Basis	
		Total Energies (hartrees)	Relative Energies[b] (cm^{-1})	Total Energies (hartrees)	Relative Energies[b] (cm^{-1})
		Th			
$6d^27s^2$	^3F	−22.507635	0.00	−22.514541	543.64
$6d^37s^1$	^5F	−22.499288	1831.96	−22.517018	0.00
$6d^4$	^5D	−22.392638	25238.93	−22.425524	20080.62
		Th$^+$			
$6d^27s^1$	^4F	−22.339088	0.00	−22.338782	0.00
$6d^17s^2$	^2D	−22.307584	6914.33	−22.306882	7001.24
$6d^3$	^4F	−22.286773	11481.82	−22.290835	10523.15
		Th^{2+}			
$6d^2$	^3F	−21.915268	0.00	−21.908932	0.00
$6d^17s^1$	^3D	−21.909528	1259.78	−21.905915	1259.78
$7s^2$	^1S	−21.859609	12215.74	−21.859609	10825.15
		Th^{3+}			
$6d^1$	^2D	−21.257786	0.00	−21.252948	0.00
$5f^1$	^2F	−21.241789	3501.94	−21.241789	2449.12
$7s^1$	^2S	−21.207821	10966.05	−21.207821	9904.23
		Th^{4+}			
$[6p^6]$	^1S	−20.313342	0.00	−20.313342	0.00

a) Each state includes $6p^6$ core. b) Energies relative to the HF ground state.

Table VIII. Full CI Total Energies[a] for Thorium Atom.

Configuration	Designation	Total Energies (hartrees)	Relative Energies[b] (cm^{-1})
$6d^2 7s^2$	^3P	-22.562808	0.00
$6d^2 7s^2$	^3F	-22.562256	121.15
$6d^2 7s^2$	^1D	-22.557639	1134.46
$6d^3 7s^1$	^5F	-22.535478	5998.24
$6d^2 7s^2$	^1G	-22.532094	6740.95
$6d^3 7s^1$	^5P	-22.513027	10925.67
$5f^1 6d^1 7s^2$	^3H	-22.504768	12738.31
$6d^1 7s^2 7p^1$	^1D	-22.504139	12876.36
$6d^2 7s^2$	^1S	-22.502256	13289.63
$5f^1 6d^1 7s^2$	^1G	-22.501666	13419.12

a) Using the TH1 basis set. b) Energies relative to the lowest state, $6d^2$ ^3P.

Table IX. Full CI Total Energies[a] for Th^+.

Configuration	Designation	Total Energies (hartrees)	Relative Energies[b] (cm^{-1})
$(6d+7s)^3$	^2D	-22.362804	0.00
$6d^2 7s^1$	^4F	-22.352212	2324.68
$(6d+7s)^3$	^2P	-22.337020	5658.94
$6d^2 7s^1$	^4P	-22.332807	6583.58
$6d^3$	^4F	-22.316089	10252.76
$6d^2 7s^1$	^2F	-22.315373	10409.90
$6d^2 7s^1$	^2F	-22.312687	10999.41
$(6d+7s)^3$	^2P	-22.309922	11606.26
$5f^1 7s^2$	^2F	-22.303974	12911.70
$5f^1 6d^1 7s^1$	^4H	-22.299742	13840.51

a) Using the TH1 basis set. b) Energies relative to the lowest state, $(6d+7s)^3$ ^2D.

Table X. Full CI Total Energies[a] for Th^{2+}.

Configuration	Designation	Total Energies (hartrees)	Relative Energies[b] (cm^{-1})
$6d^2$	^1D	-21.927750	0.00
$6d^2$	^3F	-21.922775	1091.89
$6d^2$	^3P	-21.907048	4543.57
$6d^17s^1$	^3D	-21.904698	5059.33
$7s^2$	^1S	-21.900311	6022.17
$5f^16d^1$	^3H	-21.894641	7266.59
$5f^16d^1$	^1G	-21.894213	7360.52
$5f^16d^1$	^3F	-21.887273	8883.68
$\vdots$	$\vdots$	$\vdots$	$\vdots$
$5f^17s^1$	^3F	-21.865317	13702.46
$\vdots$	$\vdots$	$\vdots$	$\vdots$
$5f^2$	^3H	-21.732851	42775.40

a) Using the TH1 basis set. b) Energies relative to the lowest state, $6d^2$ ^1D.

Table XI. Experimental[a] and Theoretical Ionization Potentials (IP).[b]

Transition	Experiment	Theory	
		HF	Full CI
Th $\longrightarrow$ Th$^+$	6.08$\pm$.12	4.59	5.43
Th$^+$ $\longrightarrow$ Th^{2+}	—	11.53	11.84
Th^{2+} $\longrightarrow$ Th^{3+}	—	17.89	18.23
Th^{3+} $\longrightarrow$ Th^{4+}	28.75$\pm$.12	25.70	25.70

a) Ref. 44b. b) All IP's are in electron volts.

Table XII. HF^a Orbital Energies for CpThCl and Cl$_2$Th.

Orbitals	Cp-Th-Cl		Cl-Th-Cl	
	Orbital Energy (hartrees)	Relative^b Energy (eV)	Orbital Energy (hartrees)	Relative^b Energy (eV)
d$_\pi$	-0.139050		-0.203201	
		2.350		1.437
d$_\delta$	-0.225400		-0.256016	
		0.535		0.618
d$_\sigma$	-0.245077		-0.278711	

a) Average field calculation with two electrons in d orbitals. b) Energies relative to the next lower state.

Table XIII. Valence Full CI^a Energies for CpThCl and Cl$_2$Th.

d States	Cp-Th-Cl		Cl-Th-Cl	
	Relative^b Energy (eV)	Relative^c Energy (eV)	Relative^b Energy (eV)	Relative^c Energy (eV)
$\pi\bar{\pi}$	5.471		3.926	
		2.284		1.353
$\pi\delta$	3.187		2.573	
		0.359		0.403
$\pi\delta$	2.828		2.170	
		0.429		0.567
$\sigma\pi$	2.399		1.603	
		0.251		0.280
$\delta\bar{\delta}$	1.148		1.323	
		1.148		1.323
$\sigma\delta$	0.000		0.000	

a) Using the HF average field orbitals, with two electrons in d orbitals. b) Energies relative to the $\sigma\delta$ ground state. c) Energies relative to the next lower state.

Table XIV. Mulliken Population Analysis of the HF[a] Valence Orbitals for CpThCl and Cl_2Th.

	Cp–Th–Cl		Cl–Th–Cl	
Atom/Group	Charge	Atom	Charge
Th	+1.057	Th	+1.090
Cp	−0.524	Cl	−0.545
Cl	−0.532	Cl	−0.545

a) Average field calculation with two electrons in d orbitals.

Table XV. Geometries[a] and Total Energies of Cl_2Ti and Cl_2Th.

Geometry[b]	Cl_2Ti	Cl_2Th	
		TH2 Basis[c]	TH1 Basis[d]
$r(M-Cl)$	2.382	2.770	2.690
$\theta(Cl-M-Cl)$	180.0°	170.78°	174.16°
Total Energy	−1766.566414	−941.664298	−941.695104

a) Cl_2Ti and Cl_2Th with f functions were optimized at the HF level using local mode optimization; Cl_2Th without f functions was optimized using analytic gradients at the HF level. *b*) r is in Å; θ is in degrees. *c*) (3s4p2d/3s2p2d) *d*) (3s4p2d4f/3s3p2d2f)

Table XVI. Atomic Mulliken Population Analysis for the HF Ground State Wavefunctions of Cl_2Ti and Cl_2Th.

Cl_2Ti		Cl_2Th	
Atom	Charge	Atom	Charge
Ti	+0.821	Th	+0.906
Cl	−0.411	Cl	−0.453
Cl	−0.411	Cl	−0.453

Table XVII. Mulliken Population Analysis over Valence[a] Atomic Basis Functions for the HF ground state wavefunctions of Cl_2Ti and Cl_2Th.

Type	Cl_2Ti		Cl_2Th	
	Populations			
	Cl	Ti	Cl	Th
s	1.9380	0.4006	1.9449	0.8067
p_x	1.8562	0.1099	1.8602	0.0564
p_y	1.8562	0.1099	1.8602	0.0566
p_z	1.7601	0.2115	1.7875	0.0380
d	—	2.3467	—	1.8787
f	—	—	—	0.1900

a) The following basis functions are included: for Ti, 4s, 4p, 3d; for Th, 7s, 7p, 6d, 5f; for Cl, 3s, 3p;

Table XVIII. Mulliken Population Analysis over Valence Orbitals[a] for the HF ground state wavefunctions of Cl_2Ti and Cl_2Th.

| | | Cl₂Ti | | | | | Cl₂Th | | | | | |
| | | Cl | | Ti | | | Cl | | Th | | | |
Orbital	Symmetry[b]	s	p	s	p	d	s	p	s	p	d	f
Cl1s + Cl1s	A₁	1.872	0.016	0.059	0.000	0.043	1.889	0.008	0.030	0.004	0.061	0.000
Cl1s − Cl1s	B₂	1.911	0.010	0.000	0.079	0.000	1.532	0.000	0.000	0.455	0.000	0.013
Clpx + Clpx	B₁	0.000	1.892	0.000	0.108	0.000	0.000	1.889	0.000	0.058	0.000	0.053
Clpx − Clpx	A₂	0.000	1.820	0.000	0.000	0.180	0.000	1.829	0.000	0.000	0.171	0.000
Clpy + Clpy	A₁	0.000	1.892	0.000	0.108	0.000	0.000	1.889	0.000	0.058	0.001	0.052
Clpy − Clpy	B₂	0.000	1.820	0.000	0.000	0.180	0.000	1.828	0.000	0.000	0.172	0.000
Clpz + Clpz	B₂	0.029	1.816	0.000	0.155	0.000	0.017	1.807	0.000	0.112	0.001	0.063
Clpz − Clpz	A₁	0.056	1.659	0.188	0.000	0.097	0.051	1.696	0.067	0.000	0.186	0.000
M d_z²,s	A₁	0.000	0.008	0.155	0.000	0.837	0.000	0.000	0.711	0.001	0.288	0.000
M d_xy	B₁	0.000	0.000	0.000	0.000	1.000	0.000	0.000	0.000	0.001	0.999	0.000

a) The core orbitals, Th 6p$_x$, 6p$_y$, 6p$_z$, are not included. *b*) C$_{2v}$ symmetry was used for both the linear and bent geometries. C$_1$ symmetry was tried but gave the same energy as C$_{2v}$.

Table XIX. Geometries[a] and Total Energies of Cl_2ThH_2 optimized with HF and GVB(2/4) wavefunctions.

Basis Sets	TH3 (No f's)		TH2 (Inc. f's)
Geometry[b]	HF	GVB(2/4)	GVB(2/4)
r(M-H)	2.133	2.159	2.130
r(M-Cl)	2.733	2.735	2.675
θ(H-M-H)	106.6	105.0	104.2
θ(Cl-M-Cl)	119.2	119.1	119.2
Total Energy	−942.834222	−942.866596	−942.913652

a) Cl_2Th optimized with f functions using using local mode optimization; Cl_2Th without f functions was optimized using analytic gradients at the HF level. b) r is in Å; θ is in degrees.

Table XX. Atomic Mulliken Population Analysis for the HF, GVB(2/4), and CCCI Ground State Wavefunctions of Cl_2ThH_2.

Basis Sets	TH3 (No f's)		TH2 (Inc. f's)	
	Atomic Charges			
Atom[b]	HF	GVB(2/4)	GVB(2/4)	CCCI
Th	+1.797	+1.677	+1.406	+1.464
H	−0.414	−0.350	−0.277	−0.306
Cl	−0.485	−0.488	−0.426	−0.426

Table XXI. Mulliken Population Analysis and Overlaps[a] for the M-H GVB[b] pairs in Cl_2MH_2, M = Ti, Zr, Hf, Th.

M-H	Electron Population[c]		Overlap	% Character[d]			
	M	H		s	p	d	f
Ti-H	1.081	0.901	0.608	12.09	4.34	83.57	—
Zr-H	0.929	1.070	0.739	20.56	9.03	70.40	—
Hf-H	0.888	1.099	0.788	24.55	14.91	60.54	—
Th-H	0.743	1.260	0.794	22.58	11.93	59.32	6.17

a) The one electron GVB orbitals were used in calculating the Mulliken populations and in determining the overlaps. *b*) The wavefunction used in all cases was a GVB(2/4) with both Th-H bond pairs correlated. *c*) Electron population is per GVB pair. The populations may not add up to 2 electrons because of small populations (both positive and negative) on the other atoms in the molecule. *d*) % Character is calculated from the one electron orbital of the GVB pair centered on the metal.

Table XXII. First and Second Ionization Potentials[a] of 1st, 2nd, and 3rd Row Transition Metals.

Atom	First IP (eV)	Second IP (eV)	Average IP (eV)
Sc	6.54	12.8	9.68
Ti	6.82	13.57	10.20
V	6.74	14.65	10.70
Cr	6.76	16.49	11.63
Mn	7.43	15.64	11.54
Fe	7.87	16.18	12.03
Co	7.86	17.05	12.46
Ni	7.63	18.15	12.89
Cu	7.72	20.29	14.01
Sr	5.69	11.03	8.36
Y	6.38	12.23	9.31
Zr	6.84	13.13	9.99
Nb	6.88	14.32	10.60
Mo	7.10	16.15	11.63
Tc	7.28	15.26	11.27
Ru	7.36	16.76	12.06
Rh	7.46	18.07	12.77
Pd	8.33	19.42	13.88
Ag	7.57	21.48	14.53
La	5.61	11.43	8.52
Hf	7.	14.9	11.0
Ta	7.88	16.2	12.04
W	7.98	17.7	12.84
Re	7.87	16.6	12.24
Os	8.5	17.	12.8
Ir	9.	—	—
Pt	9.0	18.56	13.78
Au	9.22	20.5	14.86

a) Ref. 48.

Table XXIII. Cl_2MH_2, M = Ti, Zr, Hf, and Th, Geometries[a].

Molecule	r(M−H)	r(M−Cl)	θ(H−M−H)	θ(Cl−M−Cl)
$Cl_2TiH_2^b$	1.70	2.328	74.9	142.
$Cl_2ZrH_2^b$	1.86	2.450	102.1	127.2
$Cl_2HfH_2^c$	1.817	2.393	104.9	121.8
$Cl_2ThH_2^d$	2.130	2.675	104.2	119.2

a) r is in Å; θ is in degrees. b) Refs. 50,51. c) The Hf complex was optimized at the GVB(2/4) level using analytic gradients. d) The Th complex was optimized at the GVB(2/4) level (including f functions) using local mode optimization (see Table XIX).

Table XXIV. Atomic Mulliken Population Analysis for the GVB(2/4) Ground State Wavefunctions of Cl_2MH_2, M = Ti, Zr, Hf, and Th.

Molecules	Cl_2TiH_2	Cl_2ZrH_2	Cl_2HfH_2	Cl_2ThH_2
Atom	Atomic Charges			
M	+0.587	+0.940	+1.008	+1.406
H	+0.070	−0.100	−0.130	−0.277
Cl	−0.363	−0.370	−0.374	−0.426

Table XXV. M^+, M = Ti, Zr, and Hf; Experimental Splittings[a] for the ^4F (s^1d^2), the ^4F (d^3), and the ^2D (s^2d^1) States, Averaged Over J States.

Metal	Relative Energies[b] (eV)		
	$^4F\ s^1d^2$	$^4F\ d^3$	$^2D\ s^2d^1$
Ti$^+$	0.00	0.10	3.11
Zr$^+$	0.00	0.31	1.73
Hf$^+$	0.53	2.41	0.00

a) Ref. 48. b) Energies relative to the lowest state for each atom.

Table XXVI. Diabatic (Snap) Bond Energies of M-H bonds in Cl_2MH_2, M = Ti, Zr, Hf, and Th, complexes.

| Molecule | Snap Bond Energies[a] (kcal) | | Total Energies (hartrees)[b] | | | |
| | | | Cl_2MH_2 | | Cl_2MH | |
	Full CI[c]	CCCI	Full CI[c]	CCCI	Full CI	CCCI
Cl_2TiH_2	40.31	40.03	-1767.687612	-1767.685191	-1767.123438	-1767.121463
Cl_2ZrH_2	64.88	65.05	-4455.964632	-4455.962551	-4455.361300	-4455.358943
Cl_2HfH_2	79.11	79.43	-968.669102	-968.667238	-968.043088	-968.040713
Cl_2ThH_2	(79.77)	80.29	(-942.947995)	-942.945056	-942.320931	-942.317602

a) The full CI and CCCI wavefunctions for Cl_2MH_2 dissociate consistently to HF H atom and the full CI and CCCI wavefunctions for Cl_2MH, respectively. b) The total energy of H atom is 0.499940 hartrees. c) The values in parentheses indicate that the full CI energies for Th-H were estimated from the full CI energy of the fragment, Cl_2ThH, relative to the full CI numbers for the other molecules. See Ref. 53 for a more extensive explanation.

Table XXVII. Adiabatic (Relaxed) Bond Energies of M—H bonds in Cl_2MH_2, M = Ti, Zr, Hf, and Th, complexes.

Molecule	$D_e^{adiab\ a}$ (kcal mol^{-1})		Total Energies (hartrees)[b] Cl_2MH	
	Full CI[c]	CCCI	Full CI	CCCI
Cl_2TiH_2	39.33	38.95	−1767.124996	−1767.123186
Cl_2ZrH_2	61.46	61.66	−4455.366750	−4455.364349
Cl_2HfH_2	74.88	75.17	− 968.049826	− 968.047500
Cl_2ThH_2	(77.81)	78.98	− 942.324053	− 942.319258

a) The full CI and CCCI wavefunctions for Cl_2MH_2 dissociate consistently to HF H atom and the full CI and CCCI wavefunctions for Cl_2MH, respectively. b) The total energies for the Cl_2MH_2 molecules are the same as in Table XXVI. The total energy of H atom is 0.499940 hartrees. c) The value in parentheses indicates that the full CI bond energy for Th-H was estimated. See Table XXVI and Ref. 53 for more information.

Table XXVIII. The Radial Extent of the Bonding Orbitals, as Measured By $\langle\phi|r^2|\phi\rangle^{1/2}$, their Overlap, and Projected Bond Strengths Based on Overlap and Distance for the Cl_2MH_2, M = Ti, Zr, Hf, and Th, Complexes.

Molecule	R_M [a]	R_s^{MH} [b]	S [c]	$D_e^{diab} \propto (S^2)_{Th-H}$ [d]	$D_e^{diab} \propto (\frac{S^2}{R_s})_{Th-H}$ [e]	D_e^{diab}
Cl_2TiH_2	0.942	0.915	0.608	47.1	37.8	40.0
Cl_2ZrH_2	1.402	0.802	0.739	69.6	63.0	65.1
Cl_2HfH_2	1.552	0.736	0.788	79.1	78.1	79.4
Cl_2ThH_2	2.012	0.727	0.794	—	—	80.3

a) R_M is the radius of the high spin fragment orbital of Cl_2MH in Å. The radius is measured using the expectation value $\langle\phi|r^2|\phi\rangle^{1/2}$. $R_H = 0.916$Å. b) $R_s^{MH} = \frac{r_e}{R_M + R_H}$. c) S is the overlap of the two bonding orbitals at r_e. d) The projected bond energies in kcal mol^{-1} for Cl_2HM-H determined using the ratio of the square of the overlaps in M$-$H and Th$-$H (see Eqs. 25$-$27). e) The projected bond energies in kcal mol^{-1} for Cl_2HM-H computed using the ratio of the square of the overlaps in M$-$H and Th$-$H and the inverse ratio of the scaled R parameters, R_s, for M$-$H and Th$-$H (see Eqs. 25$-$27).

Table XXIX. The Optimized Geometry[a] of $Cl_2Th(\mu\text{-}H)H_2$ and the Neutron Diffraction Structure[b] of $Cp_2^*Th(\mu\text{-}H)H_2$.

Geometry[c,d]	$Cl_2Th(\mu\text{-}H)H_2$	$Cp_2^*Th(\mu\text{-}H)H_2$
r(Th−t-H)	2.13	2.03
r(Th−b-H)[e]	2.30	2.29
	2.34	—
r(Th−Th)	4.04	4.01
r(Th−Cl)[e]	2.74	—
	2.73	—
r(Th−Cp*)	—	2.57
θ(b-H−Th−b-H)	59.1	58.
θ(Th−b-H−Th)[e]	122.8	122.
	119.	—
θ(Cl−Th−Cl)	112.4	—
θ(Cp*−Th−Cp*)	—	130.

a) $Cl_2Th(\mu\text{-}H)H_2$ optimized without f functions using using analytic gradient optimization at the HF level; C_s symmetry was imposed. b) Ref. X; c) r is in Å; θ is in degrees. d) t-H refers to the terminal hydrogens; b-H refers to the bridging hydrogens. e) The symmetry of the wavefunction allows for inequivalency of the two bridging hydrogen atoms and of the two chlorines attached to each thorium.

Table XXX. Total Energies[a] for the HF, GVB(4/10), RCI, and GVB-CI Wavefunctions of the Dimeric Dihydride, $Cl_2Th(\mu\text{-}H)H_2$.

Wavefunction	Total Energies (hartrees)
HF	−1885.711822
GVB(4/10)	−1885.782180
RCI(4/10)	−1885.782996
GVB-CI(4/10)	−1885.783606

a) The gradient optimized geometry, without f functions, was used.

Table XXXI. Mulliken Population Analysis for the HF and GVB(4/10) Wavefunctions[a] of The Dimeric Dihydride, $Cl_2Th(\mu\text{-}H)H_2$.

Atom	Atomic Charge	
	HF	GVB(4/10)
Th	+1.78	+1.70
t-H	−0.40	−0.34
b-H[b]	−0.44	−0.41
Cl[b]	−0.47	−0.47

a) The gradient-optimized geometry, without f functions, was used.
b) The Mulliken populations for the inequivalent bridging hydrogens and chlorines were averaged.

Table XXXII. The Reactant Geometries[a-c], Cl_2ThH^+ and Cl_3ThH.

Molecule	r(Th−H)	r(Th−Cl)	θ(Cl−Th−Cl)
Cl_2ThH^+	2.088	2.683	129.1
Cl_3ThH	2.115	2.722	113.4

a) r is in Å; θ is in degrees. b) Cl_2ThH^+ was optimized at the HF level without f functions using analytic gradients. Both planar and nonplanar structures were investigated, and the planar geometry is lowest in energy(C_{2v}). c) Cl_3THH was optimized at the HF level without f functions using analytic gradients; C_{3v} symmetry was imposed.

Table XXXIII. The Transition State Geometries^{a,b}, $Cl_2Th(H)(D)_2^+$ and $Cl_3Th(H)(D)_3$ (Both Isomers).

Molecule	r(Th–t-H)	r(Th–Cl)	r(t-H–D)^c	θ(t-H–Th–t-D)	θ(H–D–D)	θ(Cl–Th–Cl)
$Cl_2Th(H)(D)_2^+$	2.215	2.685	1.034	53.5	149.6	124.4
$Cl_3Th(H)(D)_3$ (S)^d	2.257	2.725	1.034	52.9	153.2	114.3
		2.738				103.4
$Cl_3Th(H)(D)_3$ (U)^e	2.268	2.734	1.018	52.9	153.5	108.1
	2.249	2.750	1.049			110.9

a) r is in Å; θ is in degrees. b) Both $Cl_2Th(H)(D)_2^+$ and $Cl_3Th(H)(D)_3$ (S and U) were optimized at the HF level without f functions using analytic gradients. The former was restricted to C_{2v} symmetry; both isomers of the latter to C_s. c) r(t-H–D) is the distance between the terminal hydrogen and the middle deuterium. d) For the S isomer there are two different chlorines (by symmetry). Consequently, there are two sets of Th–Cl bond lengths and two sets of Cl–Th–Cl angles. Those geometrical parameters involving the Cl in the plane of symmetry which includes the Th and the middle D are listed as the top values; those involving the other two chlorines are the bottom values. e) The same situation holds for the U isomer. However, since the inequivalent chlorines are not equivalent to the Th–t-H and t-H–D Cl is in the H–D–D plane, the Th–t-D and D–D distances are not equivalent to the Th–t-H and t-H–D distances. Those distances involving only deuterium are listed on top; those involving the t-H are listed on the bottom.

Table XXXIV. GVB(2/4) One Electron Orbital Overlaps in the Active Bonds of the Reactants and the Transition States.

Complex	Reactants		Transition State	
	M−H	H−H	H···Th···D[a]	H···D···D[b]
Cl_2ThH^+	0.784	0.802	0.825	0.841
Cl_3ThH (S)	0.790	0.802	0.844	0.847
Cl_3ThH (U)	0.790	0.802	0.823	0.821

a) For **U**, this corresponds to Th···H···D. *b*) For **U**, this corresponds to D···D···Th.

Table XXXV. Barrier Heights for the Reaction:
$Cl_nThH + D_2 \rightarrow Cl_nTh(H)(D)_2 \rightarrow Cl_nThD + H−D$.

Reactant	Wavefunctions					
	HF (no f's)	HF (f's)	GVB(2/4)	RCI	RCI*S_{val}	CCCI
Cl_2ThH^+	8.5	5.4	·15.1	10.9	2.2	5.5
Cl_3ThH (S)	25.3	20.7	31.0	27.4	18.7	21.4
Cl_3ThH (U)	25.5	21.0	25.9	24.8	18.6	18.3

Table XXXVI. Atomic Mulliken Population Analysis for the GVB-PP Wavefunctions of the Reactants and Transition States.

Complex	Atomic Charge[a]			
	Th	t-H	b-H	Cl
Cl_2ThH^+	+1.77	−0.12	—	−0.32
$Cl_2Th(H)(D)_2^+$	+1.68	−0.09	+0.16	−0.33
Cl_3ThH	+1.49	−0.24	—	−0.42
$Cl_2Th(H)(D)_2$ (**S**)	+1.48	−0.18	+0.14	−0.42
$Cl_2Th(H)(D)_2$ (**U**)	+1.48	−0.17	+0.13	−0.43

a) The Mulliken populations for the inequivalent H and D atoms of **U** and for the inequivalent chlorines of both **S** and **U** were averaged.

Table XXXXVII. Mulliken Population Analysis of the GVB(2/4) Pair Orbitals at the Transition States.

Atom[a]	H···Th···D					H···D···D					Grand Total Pop.
	s	p	d	f	Total[b] Pop.	s	p	d	f	Total[b] Pop.	
					$Cl_2Th(H)(D)_2^+$						
Th	0.000	0.049	0.530	0.130	0.712	0.073	0.081	0.127	0.021	0.303	1.015
t-H	0.618	0.007	—	—	0.624	0.413	0.015	—	—	0.429	1.053
b-D	0.000	0.039	—	—	0.039	0.833	0.005	—	—	0.838	0.877
					$Cl_3Th(H)(D)_2$ (S)						
Th	0.000	0.052	0.386	0.125	0.563	0.056	0.064	0.124	0.020	0.264	0.827
t-H	0.689	0.006	—	—	0.695	0.419	0.015	—	—	0.434	1.129
b-D	0.000	0.034	—	—	0.034	0.863	0.004	—	—	0.867	0.901
					$Cl_3Th(H)(D)_2$ (U)						
Th	0.011	0.018	0.042	0.011	0.082	0.031	0.062	0.296	0.085	0.473	0.811
t-H	1.127	0.013	—	—	1.141	-0.021	0.010	—	—	-0.020	1.121
t-D	-0.059	0.003	—	—	-0.056	1.230	0.012	—	—	1.242	1.186
b-D	0.557	0.017	—	—	0.573	0.273	0.024	—	—	0.298	0.871

a) The t-H and t-D atoms are equivalent for $Cl_2Th(H)(D)_2^+$ and $Cl_2Th(H)(D)_2$ (S) transition states. *b*) The populations may not add up to two electrons per GVB pair because of both round-off error and a very small contribution due to the chlorines.

Table XXXVIII. Mulliken Population Analysis for the M$-$H GVB[a,b] pair in Cl_2ThH^+ and Cl_3ThH.

Complex	Electron Population[c]		% Character[d]			
	Th	H	s	p	d	f
Cl_2ThH^+	0.886	1.112	19.2	11.5	58.8	10.4
Cl_3ThH	0.784	1.215	21.7	10.8	59.7	7.8

a) The one-electron GVB orbitals were used in calculating the Mulliken populations. *b*) The wavefunction used in all cases was a GVB(1/2) with the Th-H bond pair correlated. *c*) Electron population is per GVB pair. The populations may not add up to 2 electrons because of small populations (both positive and negative) on the other atoms in the molecule. *d*) % Character is calculated from the one-electron orbital of the GVB pair centered on the metal.

Table XXXIX. Barrier Heights[a] and Mulliken Populations for the Reaction: $Cl_2MH + D_2 \rightarrow Cl_2M(H)(D)_2 \rightarrow Cl_2MD + H-D.$[b]

Reactant	$\Delta E^{\ddagger}$	Mulliken Populations				
		Transition State D···M···H Bond			Total on Hydrogen in MH$_3$ Unit	
	(kcal mol^{-1})	s	p	d	t-H	b-D
Cl_2ScH	17.4	0.00	0.13	0.61	1.00	0.80
Cl_2TiH^+	2[c]	0.00	0.06	1.09	0.70	0.82
Cl_2TiH	21.7	0.00	0.11	0.72	0.93	0.82
Cl_2ZrH	17.4	0.00	0.12	0.60	1.02	0.86

a) Obtained at the RCI*S$_{val}$ level. b) See Ref. 57a,b for the details of these calculations. c) An upper bound for the activation barrier using a GVB(2/4) geometry optimized via a point-by-point search.

Table XL. Cl$_2$M(H)(CH$_3$), M = Ti, Zr, Hf, and Th, Geometries.[a,b]

Molecule	r(M–C)	r(M–H)	r(M–Cl)	r(C–H)[c]	θ(H–M–C)	θ(Cl–M–Cl)	θ(H–C–H)[c]
Cl$_2$Ti(H)(CH$_3$)	2.100	1.673	2.287	1.086/1.085	94.7	134.9	112.2/112.9
Cl$_2$Zr(H)(CH$_3$)	2.209	1.802	2.461	1.089/1.090	100.9	124.3	109.9/110.0
Cl$_2$Hf(H)(CH$_3$)	2.198	1.826	2.408	1.091/1.093	101.8	122.0	108.0/108.1
Cl$_2$Th(H)(CH$_3$)	2.563	2.165	2.743	1.092/1.093	101.7	121.1	109.2/109.3

a) r is in Å; θ is in degrees. *b*) All complexes were optimized at the GVB(2/4) level. The Th complex was optimized without f functions. *c*) For both r(C–H) and θ(H–C–H) there are two values presented. The first involves the H on C that is in the same plane as the M–H and M–C bonds. The second involves the two H's on the C that are out of the plane.

Table XLI. Cl_2MH, M = Ti, Zr, Hf, and Th, Geometries.[a,b]

Molecule	r(M−H)	r(M−Cl)	θ(Cl−M−Cl)
Cl_2TiH	1.692	2.328	146.3
Cl_2ZrH	2.47	1.82	132.7
Cl_2HfH	2.406	1.832	132.5
Cl_2ThH	2.130	2.743	115.4

a) r is in Å; θ is in degrees. *b*) The Ti and Hf complexes were optimized at the GVB(1/2) level using analytic gradients. The Zr complex was optimized using local mode optimization at the GVB(1/2) level. The Th complex was optimized with f functions at the GVB(1/2) level via local mode optimization. All geometries are planar.

Table XLII. Atomic Mulliken Population Analysis for the GVB(2/4) Ground State Wavefunctions of $Cl_2M(H)(CH_3)$, $M = Ti$, Zr, Hf, and Th.

Molecules / Atom	$Cl_2Ti(H)(CH_3)$	$Cl_2Zr(H)(CH_3)$	$Cl_2Hf(H)(CH_3)$	$Cl_2Th(H)(CH_3)$
		Atomic Charges		
M	+0.736	+1.071	+1.187	+1.532
H	+0.024	−0.126	−0.106	−0.282
C	−0.828	−0.957	−1.109	−1.067
H_{ci}^a	+0.266	+0.263	+0.265	+0.234
H_{co}^a	+0.274	+0.260	+0.258	+0.233
Cl	−0.373	−0.385	−0.376	−0.441

a) H_{ci} is the in-plane H attached to C. H_{co} are the out-of-plane H's attached to C.

Table XLIII. Mulliken Population Analysis and Overlaps[a] for the M$-$CH$_3$ GVB[b] pairs in Cl$_2$M(H)(CH$_3$), M = Ti, Zr, Hf, and Th.

M-H	Electron Population[c]		Overlap	% Character[d]			
	M	H		s	p	d	f
Ti-CH$_3$	0.994	0.961	0.556	7.2	0.5	92.2	—
Zr-CH$_3$	0.853	1.166	0.741	15.8	4.7	79.5	—
Hf-CH$_3$	0.704	1.325	0.790	19.0	7.3	73.7	—
Th-CH$_3$	0.628	1.409	0.791	19.5	6.8	66.3	7.4

a) The one-electron GVB orbitals were used in calculating the Mulliken populations and in determining the overlaps. b) The wavefunction used in all cases was a GVB(2/4) with both M$-$H and M$-$CH$_3$ bond pairs correlated. c) Electron population is per GVB pair. The populations may not add up to 2 electrons because of small populations (both positive and negative) on the other atoms in the molecule. d) % Character is calculated from the one-electron orbital of the GVB pair centered on the metal.

Table XLIV. Diabatic (Snap) Bond Energies of $M-CH_3$ bonds in $Cl_2M(H)(CH_3)$, $M = Ti$, Zr, Hf, and Th, complexes.

M	Snap Bond Energies[a] (kcal mol⁻¹)		Total Energies (hartrees)[b]				
			$Cl_2M(H)(CH_3)$		Cl_2MH	CH_3	
	CCCI(CH*S)	CCCI	CCCI(CH*S)	CCCI	CCCI	HF*S(CH*S)	HF
Ti	46.20	39.15	−1806.756898	−1806.738705	−1767.119221	−39.564046	−39.557100
Zr	72.60	62.28	−4495.033961	−4495.011250	−4455.359446	−39.558827	−39.552555
Hf	88.74	78.46	−1007.737699	−1007.715296	−968.040860	−39.555417	−39.549402
Th	85.46	75.06	−982.004966	−981.982479	−942.315069	−39.553709	−39.547793

a) The CCCI(CH*S) wavefunction for $Cl_2M(H)(CH_3)$ dissociates to CCCI on Cl_2MH and HF*S(CH*S), i.e, singles from HF out of the high spin orbital and CH bonds, on CH_3. The CCCI wavefunction for $Cl_2M(H)(CH_3)$ dissociates to CCCI on Cl_2MH and HF on CH_3.

Table XLV. Adiabatic (Relaxed) Bond Energies of $M-CH_3$ bonds in $Cl_2M(H)(CH_3)$, M = Ti, Zr, Hf, and Th, complexes.

Molecule	$D_e^{adiab\ a}$ (kcal mol^{-1})		Total Energies (hartrees)^b Cl_2MH
	CCCI(CH*S)	CCCI	CCCI
$Cl_2Ti(H)(CH_3)$	40.32	34.61	-1767.123186
$Cl_2Zr(H)(CH_3)$	62.85	54.30	-4455.364349
$Cl_2Hf(H)(CH_3)$	75.77	67.41	$- 968.047500$
$Cl_2Th(H)(CH_3)$	72.95	64.54	$- 942.319258$

a) The CCCI(CH*S) wavefunction for $Cl_2M(H)(CH_3)$ dissociates to CCCI on Cl_2MH and HF*S(CH*S) on methyl radical. The CCCI wavefunction dissociates to CCCI on Cl_2MH and HF on methyl radical. *b*) The total energies for the $Cl_2M(H)(CH_3)$ molecules are the same as in Table XLIV. The relaxed total energies of methyl radical are -39.560367 for HF and -39.569459 for HF*S(CH*S).

Table XLVI. The Radial Extent of the Bonding Orbitals, as Measured By $<\phi|r^2|\phi>^{1/2}$, their Overlap, and Projected Bond Strengths Based on Overlap and Distance for the M−CH$_3$ Bonds in Cl$_2$M(H)(CH$_3$), M = Ti, Zr, Hf, and Th, Complexes.

Molecule	R_M [a]	R_{CH_3} [b]	$R_s^{MCH_3}$ [c]	S^d	$D_e^{diab} \propto (S^2)_{Hf-CH_3}^d$	$D_e^{diab} \propto (\frac{S^2}{R_s})_{Hf-CH_3}^e$	D_e^{diab}
Cl$_2$(H)Ti−CH$_3$	0.948	1.085	1.033	0.556	44.0	34.9	46.2
Cl$_2$(H)Zr−CH$_3$	1.406	1.075	0.890	0.741	78.1	71.9	72.6
Cl$_2$(H)Hf−CH$_3$	1.611	1.071	0.820	0.790	—	—	88.7
Cl$_2$(H)Th−CH$_3$	1.980	1.068	0.841	0.791	89.0	86.7	85.5

a) R_M is the radius of the high-spin fragment orbital of Cl$_2$MH (snap geometry) in Å. The radius is measured using the expectation value $<\phi|r^2|\phi>^{1/2}$. b) R_{CH_3} is the radius of the high spin fragment orbital of methyl radical (snap geometry) in Å. c) $R_s^{MCH_3} = \frac{r_s}{R_M + R_{CH_3}}$. c) S is the overlap of the two GVB one-electron bonding orbitals at r_e. d) The projected bond energies in kcal mol^{-1} for Cl$_2$(H)M−CH$_3$ determined using the ratio of the square of the overlaps in M−CH$_3$ and Hf−CH$_3$ (see Eqs. 25-27). e) The projected bond energies in kcal mol^{-1} for Cl$_2$(H)M−CH$_3$ computed using the ratio of the square of the overlaps in M−CH$_3$ and Hf−CH$_3$ and the inverse ratio of the scaled R parameters, R_s, for M−CH$_3$ and Hf−CH$_3$ (see Eqs. 25-27).

Table XLVII. Optimized Geometries of the CO Coordinate, $Cl_3Th(H)CO$, and the Inserted Product, $Cl_3Th[\eta^2\text{-}OCH]$, Complexes.

Geometry[a,b]	$Cl_3Th(H)CO$[c]	$Cl_3Th[\eta^2\text{-}OCH]$[c]
r(Th−C)	3.035	2.534
r(Th−H)	2.145	—
r(Th−O)	—	2.501
r(C−H)	—	1.110
r(C−O)	1.123	1.256
r(Th−Cl)[d]	2.729	2.737
	2.742	2.732
θ(H−Th−C)	70.6	—
θ(Th−C−O)	178.6	74.1
θ(H−C−O)	—	115.7
θ(Cl−Th−H)[e]	99.0	—
θ(Cl−Th−C)[e]	—	104.3
θ(Cl−Th−Cl)[d]	108.7	107.1
	120.4	118.9

a) r is in Å; θ is in degrees. *b*) For bond distances, only those atoms that are bonded to each other (including dative interactions) are reported. *c*) Both complexes were optimized at the GVB(6/12) level without f functions on the Th. *d*) For both r(Th−Cl) and θ(Cl−Th−Cl) there are two values presented. The top involves the Cl that is in the same plane as the Th, C, H, and O atoms. The bottom involves only the two Cl's that are out of the plane of the above four atoms. *e*) The Cl in this angle is the in-plane Cl.

Table XLVIII. Optimized Geometries of the CO Coordinate, $Cl_3Th(CH_3)CO$, and the Inserted Product, $Cl_3Th[\eta^2\text{-}OCCH_3]$, Complexes.

Geometry[a,b]	$Cl_3Th(CH_3)CO$[c]	$Cl_3Th[\eta^2\text{-}OCCH_3]$[c]
r(Th–CO)	3.051	2.532
r(Th–CH$_3$)	2.566	—
r(Th–O)	—	2.482
r(C–O)	1.124	1.260
r(OC–CH$_3$)	—	1.520
r(H–CH$_2$)	1.094	1.083
	1.092	1.088
r(Th–Cl)[d]	2.729	2.741
	2.754	2.735
θ(OC–Th–CH$_3$)	79.0	—
θ(Th–C–O)	177.6	73.2
θ(O–C–CH$_3$)	—	118.3
θ(Cl–Th–CH$_3$)[e]	95.5	—
θ(Cl–Th–CO)[e]	—	103.3
θ(Cl–Th–Cl)[d]	107.8	107.1
	122.1	119.2
θ(H–C–H)	106.7	109.8
	107.7	108.4

a) r is in Å; θ is in degrees. b) For bond distances, only those atoms that are bonded to each other (including dative interactions) are reported. c) Both complexes were optimized at the GVB(6/12) level without f functions on the Th. d) For r(Th–Cl), r(H–CH$_2$), θ(Cl–Th–Cl), and θ(H–C–H) there are two values presented. The top involves the Cl or H that is in the same plane as the Th, C, H, and O atoms. The bottom involves only the two Cl's or H's that are out of the plane of the above four atoms. e) The Cl in this angle is the in-plane Cl.

Table XLIX. CO Coordination Energetics:[a]
$Cl_3ThR + CO \longrightarrow Cl_3Th(R)CO$, R = H and CH_3.

R	ΔH	Total Energy (hartrees)	
		$Cl_3Th(R)CO$	Cl_3ThR
H	−9.51	−1514.735718	−1401.889784
CH_3	−7.55	−1553.780956	−1440.938150

a) The geometries of the CO coordinate and the inserted product were optimized at the GVB(6/12) level without f functions on the Th. All energies reported here are with f functions. Cl_3ThH and Cl_3ThCH_3 were optimized at the GVB(1/2) level. The experimental geometry was used for CO; the GVB(5/10) total energy is −112.830778.

Table L. Experimental Geometry of $Cp_2^*Th[\eta^2\text{-}OCCH_2C(CH_3)_3]Cl.$[a]

Geometry[b]	$Cp_3^*Th[\eta^2\text{-}OCCH_2C(CH_3)_3]$
$r(Th-CO)$	2.44
$r(Th-O)$	2.37
$r(C-O)$	1.18
$r(OC-CH_2)$	1.55
$r(Th-Cl)$	2.672
$\theta(Th-C-O)$	73
$\theta(O-C-CH_2)$	118

a) Ref. 8e. *b*) r is in Å; θ is in degrees.

Table LI. CO Insertion Energetics:[a] $Cl_3Th(R)CO \longrightarrow Cl_3Th[\eta^2\text{-OCR}]$, R = H and CH$_3$.

| R | ΔH | | Total Energy (hartrees) | | | |
| | | | $Cl_3Th(R)CO$ | | $Cl_3Th[\eta^2\text{-OCR}]$ | |
	f's	No f's	f's	No f's	f's	No f's
H	−2.45	+3.74	−1514.735718	−1514.681198	−1514.739621	−1514.675240
CH$_3$	−6.04	+0.06	−1553.780956	−1553.726908	−1553.790587	−1553.726806

a) The geometries of all complexes were optimized at the GVB(6/12) level without f functions on the Th.

Table LII. Barrier Heights, $\Delta E^{\ddagger}$, for CO Insertion:[a] $Cl_3Th(H)CO \longrightarrow Cl_3Th[\eta^2\text{-}OCH]$.

	$\Delta E^{\ddagger}$ (kcal mol^{-1})	Transition State[b]	Reaction Coordinate Total Energies (hartrees)			
			40%	60%	70%	90%
f's	59.74	63.42%	-1514.678775	-1514.641848	-1514.645187	-1514.695808
No f's	62.82	63.50%	-1514.623243	-1514.582643	-1514.586158	-1514.638478

a) The geometries of all complexes were optimized at the GVB(6/12) level without f functions on the Th. All energies are for the GVB(6/12) wavefunction. b) As a percentage of the reaction coordinate.

Table LIII. Geometries of the 40%, 60%, 70%, and 90% Points Along the Reaction Coordinate.

Geometry[a,b]	40%	60%	70%	90%
$r(Th-C)$	2.835	2.734	2.684	2.584
$r(Th-H)$	2.740	3.038	3.187	3.484
$r(Th-O)$	3.983	3.845	3.742	3.333
$r(C-H)$	2.291	1.897	1.700	1.307
$r(C-O)$	1.176	1.203	1.216	1.243
$r(Th-Cl)^c$	2.732	2.734	2.735	2.736
	2.738	2.736	2.735	2.733
$\theta(H-Th-C)$	48.5	37.9	32.2	18.2
$\theta(Th-C-O)$	165.3	153.0	144.6	116.7
$\theta(H-C-O)$	131.1	127.3	125.1	119.5
$\theta(Cl-Th-H)^d$	84.7	84.5	85.4	90.3
$\theta(Cl-Th-C)^d$	133.2	122.5	117.6	108.5
$\theta(Cl-Th-Cl)^c$	113.3	112.6	111.9	109.3
	119.8	119.5	119.3	119.0

a) r is in Å; θ is in degrees. *b*) All geometries were optimized at the GVB(6/12) level without f functions on the Th. *c*) For both r(Th−Cl) and θ(Cl−Th−Cl) there are two values presented. The top involves the Cl that is in the same plane as the Th, C, H, and O atoms. The bottom involves only the two Cl's that are out of the plane of the above four atoms. *d*) The Cl in this angle is the in-plane Cl.

Table LIV. Adiabatic Bond Energies, D_e^{adiab}, from Theory and Bond Disruption Energies, D, from Experiment.[a]

Theory		Experiment	
Molecule	D_e^{adiab}(Th$-$R) (kcal mol^{-1})	Molecule	D(Th$-$R)$_{gas}$ (kcal mol^{-1})
Cl$_2$(H)Th$-$H[b]	76.93	[Cp$_2^*$(H)Thμ-H]$_2$	90.5
Cl$_3$(H)Th$-$H[c]	76.78		
Cl$_2$(H)Th$-$CH$_3$[d]	72.95	Cp$_2^*$(CH$_3$)Th$-$CH$_3$	77.2
Cl$_3$(H)Th$-$CH$_3$[e]	73.54	Cp$_3$Th$-$CH$_3$	82.7
Cl$_3$(H)Th$-$OH[f]	131.45	Th$-$OR	124[g]

a) Ref. X. b) The bond energy for this complex was determined by an estimated valence full CI (see Table XXVI). c) The bond energy for this complex was determined using a valence full CI. The total energies of the complex and the fragments are: Cl$_3$ThH$_2$, $-$1401.904947; Cl$_3$Th, $-$1401.282652 (HF); and H, $-$0.499940 (HF). d) The bond energy for this complex was determined using the CCCI(CH*S) wavefunction (see Table XLV). e) The bond energy for this complex was found using the CCCI(CH*S) wavefunction. The total energies are: Cl$_3$Th(CH$_3$), $-$1440.969301; Cl$_3$Th, same as above; and CH$_3$, $-$30.569459 [HF*S(CH*S)]. f) The bond energy for this complex was determined with the CCCI method (Th$-$O, O$-$H, and O p$_x^2$ orbital were all correlated and in the active space). The total energies are: Cl$_3$ThOH, $-$1476.969569; Cl$_3$Th, same as above; and OH, $-$75.477440 (CCCI). g) Estimated, *vide infra*.

Table LV. Optimized Geometries[a] of Cl_2ThX, X = O, S, and N−H.

Geometry[b]	Molecules		
	Cl_2ThO	Cl_2ThS	Cl_2ThNH
r(M-X)	1.91	2.43	2.05
r(M-Cl)	2.74	2.72	2.74
θ(Cl-M-Cl)	127.2	128.9	123.9
r(N−H)	—	—	1.031

a) The O and S complexes were optimized with the GVB-CI(3/6) wavefunction (all M−X bonds correlated) and f functions. The NH complex was optimized with the GVB-CI(4/8) wavefunction (all M−X bonds plus N−H bond were correlated) and f functions. *b*) r is in Å; θ is in degrees.

Table LVI. Atomic Mulliken Population Analysis for the GVB-PP Wavefunctions[a] of Cl_2ThX, X = O, S, and N−H.

	Atomic Charges		
	Molecules		
Atom	Cl_2ThO	Cl_2ThS	Cl_2ThNH
Th	+1.565	+1.290	+1.543
X[b]	−0.627	−0.397	−0.613
Cl	−0.469	−0.447	−0.465
H	—	—	+0.275

a) GVB(3/6) for O and S; GVB(4/8) for NH. *b*) X includes sum of N and H.

Table LVII. Adiabatic Bond Energies for $Cl_2Th{\equiv}X$, X = O, S, and NH.

Molecule	D_e^{adiab} (kcal mol^{-1})	Total Energy (hartrees)
$Cl_2Th{\equiv}O^a$	177.65	-1016.812311
$Cl_2Th{\equiv}S^a$	128.56	-1339.393986
$Cl_2Th{\equiv}NH^b$	137.19	$-\ 996.912975$

a) The CCCI wavefunction was used with the triple bond as the active space. The energy of the fragments are: Cl_2Th, -941.695104 (HF); O, -74.834104 (CCCI using the O $2p^4$ electrons as the active space); and S, -397.494001 (CCCI, S $3p^4$ electrons). b) The CCCI(NH*S) was used with the triple bond and the dominant configuration of the NH pair in the GVB(4/8) wavefunction as the active space. The energy of the NH fragment is -54.999242 [CCCI(NH*S) from the GVB(2/4) wavefunction; singles from the dominant configuration of the NH GVB pair, full CCCI in the $2s^2$ pair and high spin $2p^3$ electrons]. The experimental geometry was used for NH (X).

Figure 1. The HF symmetric (g) and antisymetric (u) Cl–Ti–Cl bonding orbitals and the triplet high-spin orbitals for linear Cl_2Ti.

a) Cl–Ti–Cl (g)

Cl   Ti   Cl

b) Cl–Ti–Cl (u)

Cl   Ti   Cl

c) d_{s^2}

Cl   Ti   Cl

d) d_{xy}

Ti
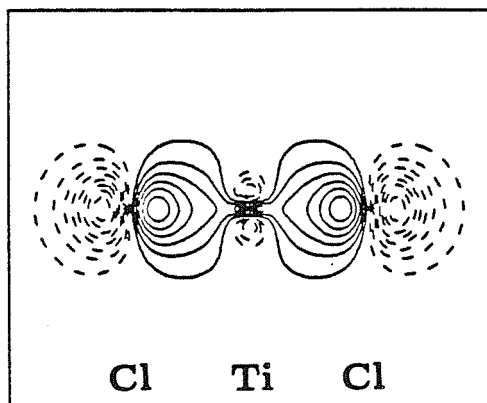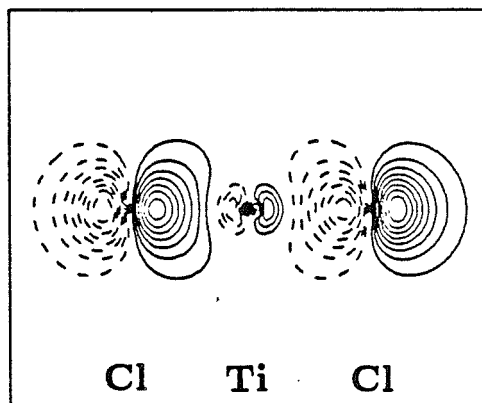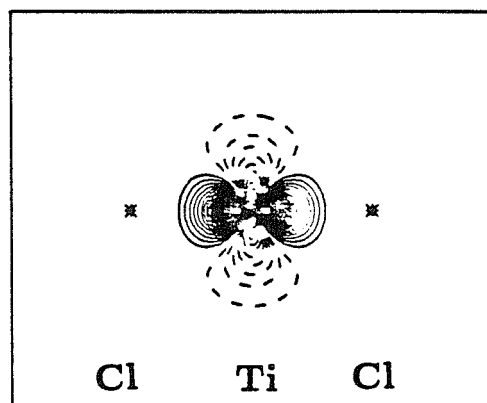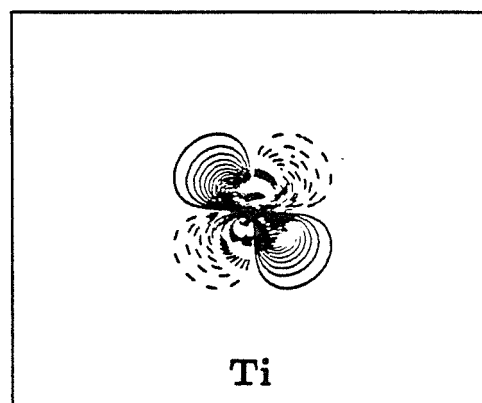
Figure 2. The HF symmetric (g) and antisymetric (u) Cl$-$Th$-$Cl bonding orbitals and the triplet high-spin orbitals for slightly bent Cl$_2$Th (174°).

a) Cl$-$Th$-$Cl (g)
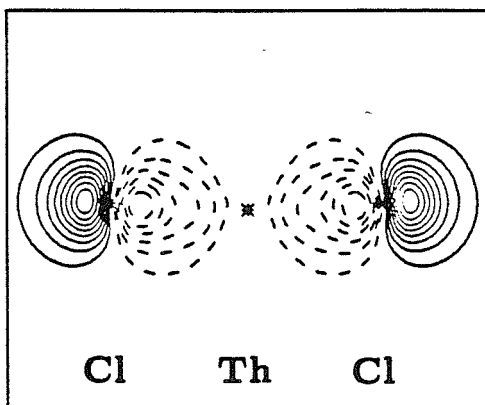
b) Cl$-$Th$-$Cl (u)
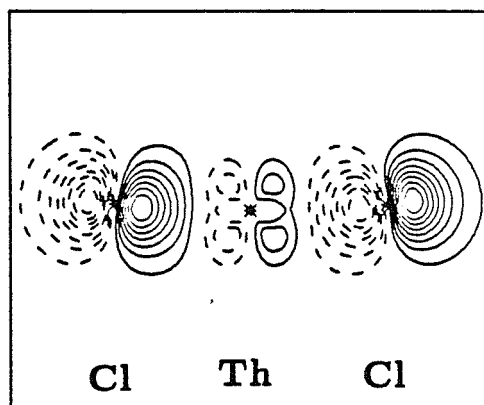
c) s, d$_{z^2}$
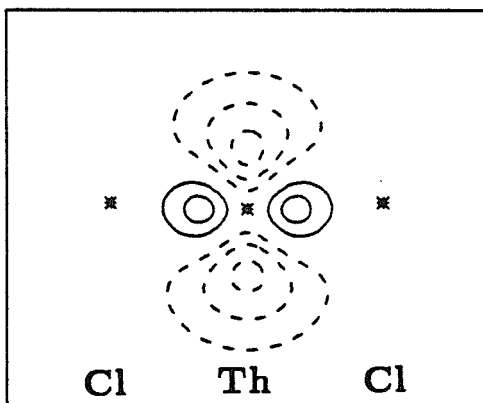
d) d$_{xy}$
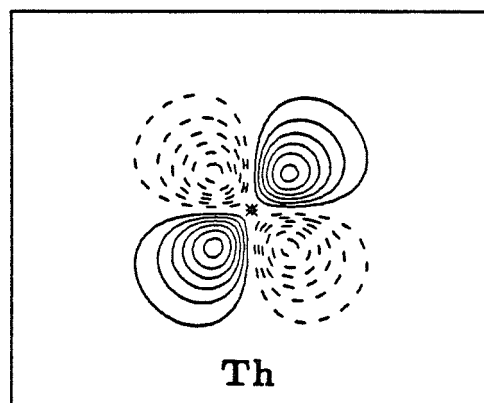
Figure 3a. The GVB(2/4) one-electron orbitals of the Ti$-$H Bonds in Cl_2TiH_2.
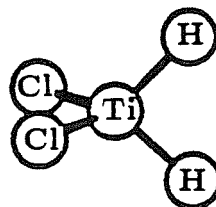
i) GVB pair for a Ti$-$H bond.
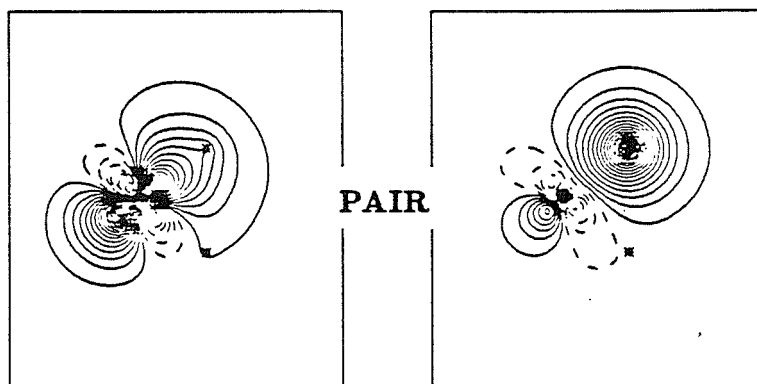
PAIR

ii) GVB pair for the other Ti$-$H bond.
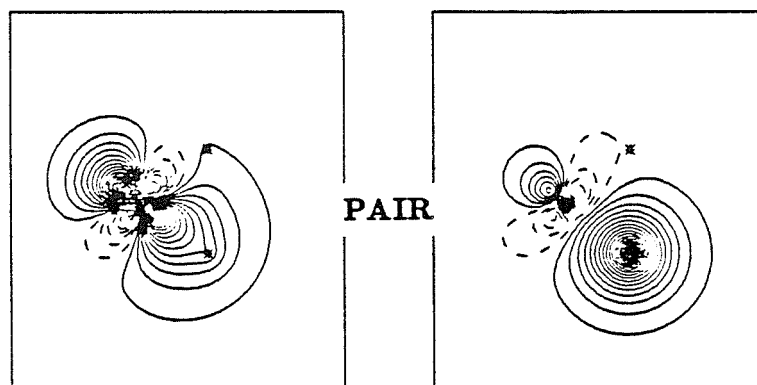
PAIR

iii) Overlap of the one electron orbitals centered on Ti and H.
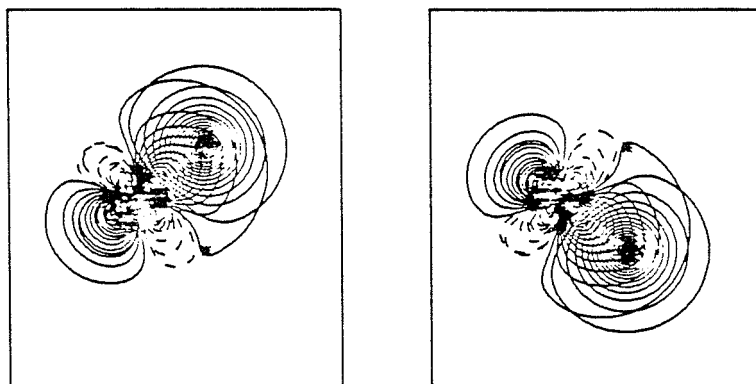
Figure 3b. The GVB(2/4) one-electron orbitals of the Zr—H Bonds in Cl_2ZrH_2.
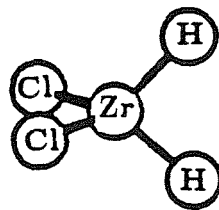
i) GVB pair for a Zr—H bond.
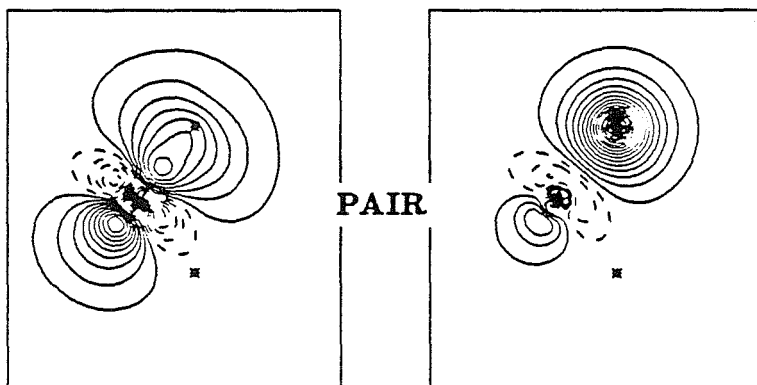
PAIR

ii) GVB pair for the other Zr—H bond.
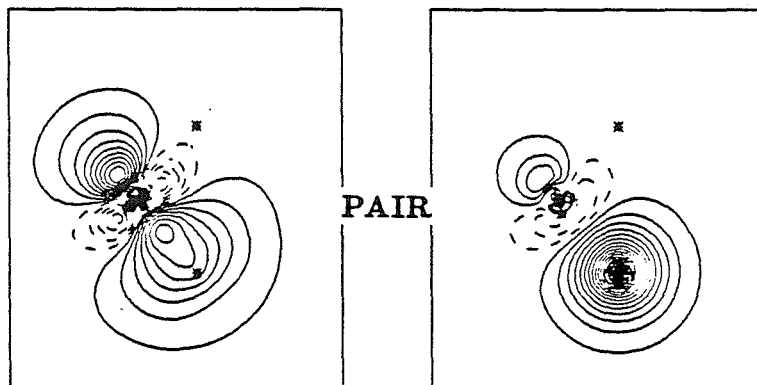
PAIR

iii) Overlap of the one electron orbitals centered on Zr and H.
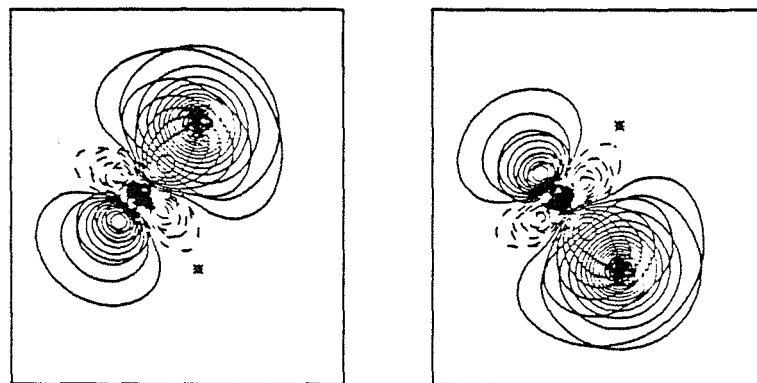
Figure 3c. The GVB(2/4) one-electron orbitals of the Hf—H Bonds in Cl_2HfH_2.
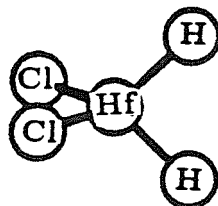
i) GVB pair for a Hf—H bond.
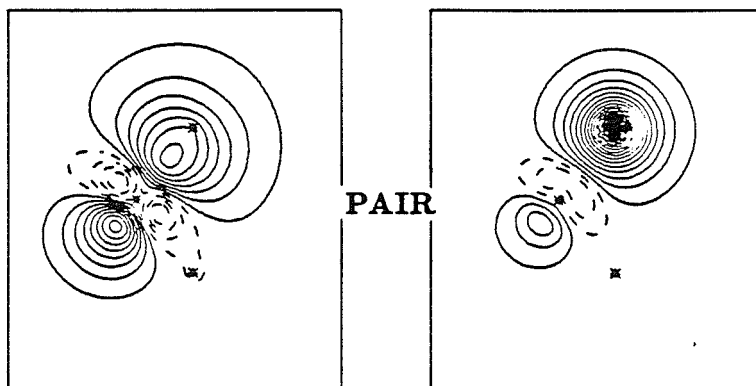
PAIR

ii) GVB pair for the other Hf—H bond.
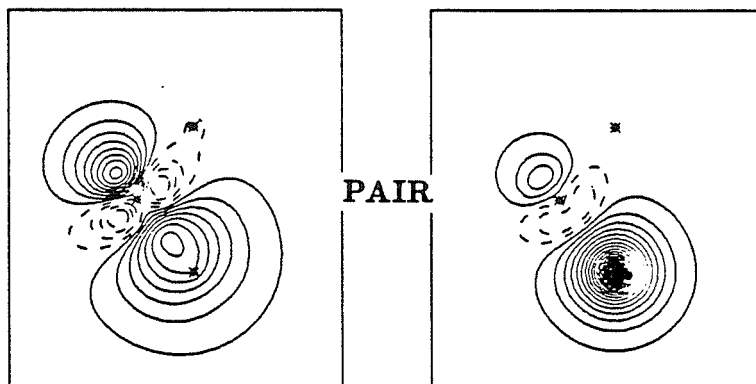
PAIR

iii) Overlap of the one electron orbitals centered on Hf and H.
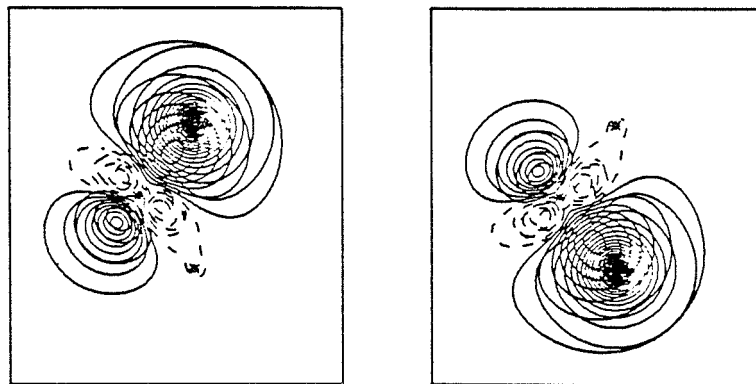
Figure 3d. The GVB(2/4) one-electron orbitals of the Th−H Bonds in Cl_2ThH_2.
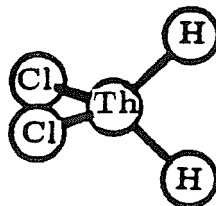
i) GVB pair for a Th−H bond.
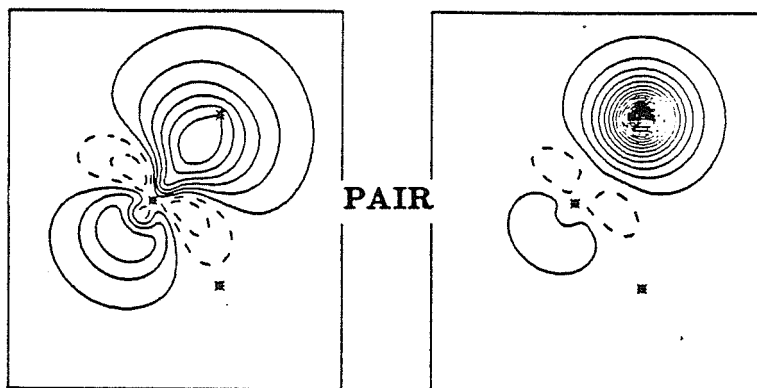
PAIR

ii) GVB pair for the other Th−H bond.
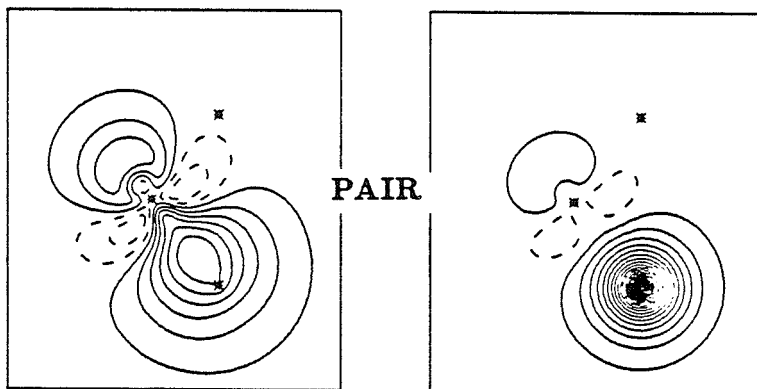
PAIR

iii) Overlap of the one electron orbitals centered on Th and H.
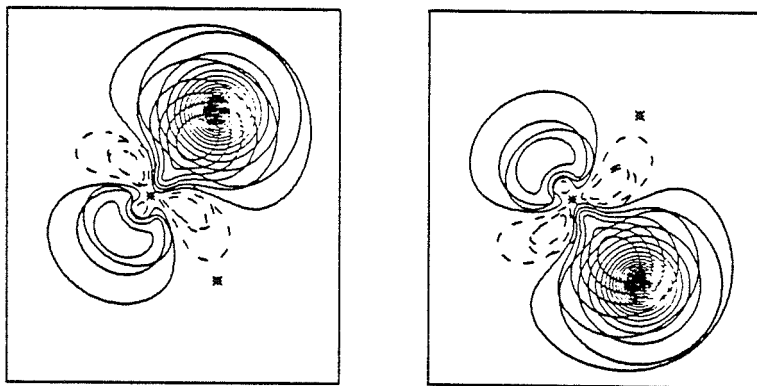
Figure 4a. The amplitudes of the overlapping $Cl_2(H)Ti$ and H fragment orbitals (dotted lines) and of the bonding orbital [first natural, Ti–H GVB(1/2) pair] of $Cl_2(H)Ti$–H (solid line).
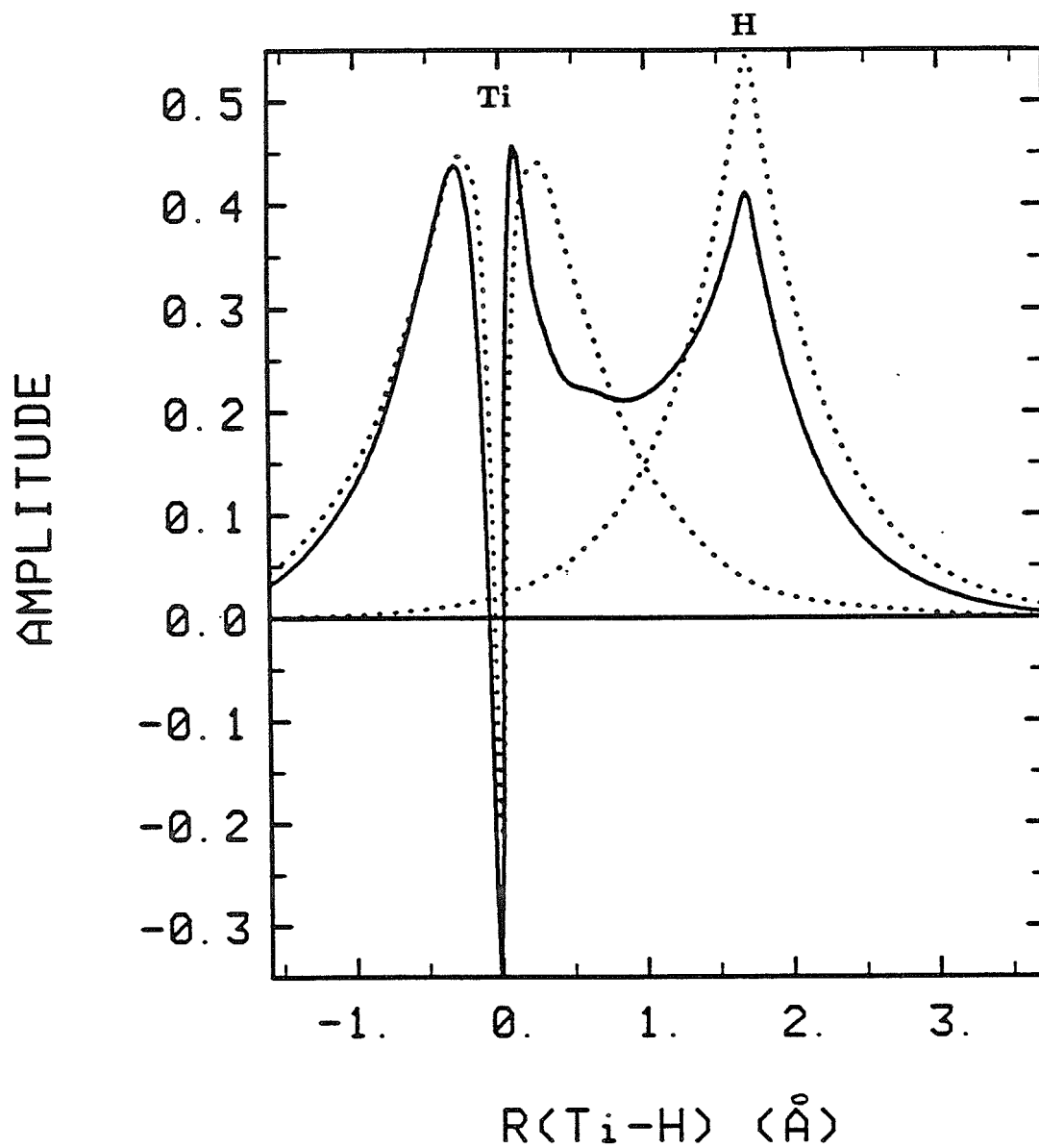
Figure 4b. The amplitudes of the overlapping $Cl_2(H)Zr$ and H fragment orbitals (dotted lines) and of the bonding orbital [first natural, $Zr-H$ GVB(1/2) pair] of $Cl_2(H)Zr-H$ (solid line).
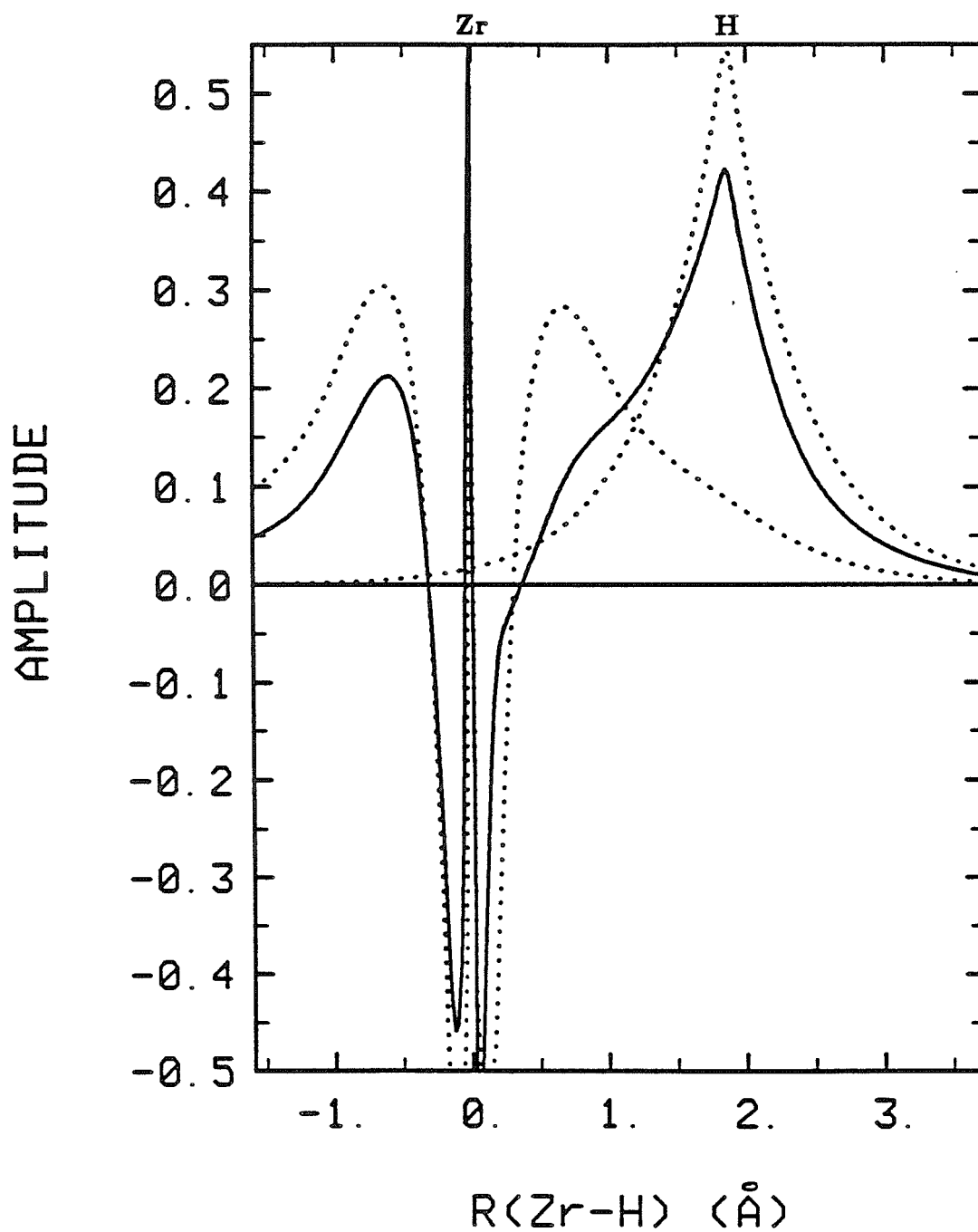
Figure 4c. The amplitudes of the overlapping $Cl_2(H)Hf$ and H fragment orbitals (dotted lines) and of the bonding orbital [first natural, Hf–H GVB(1/2) pair] of $Cl_2(H)Hf$–H (solid line).
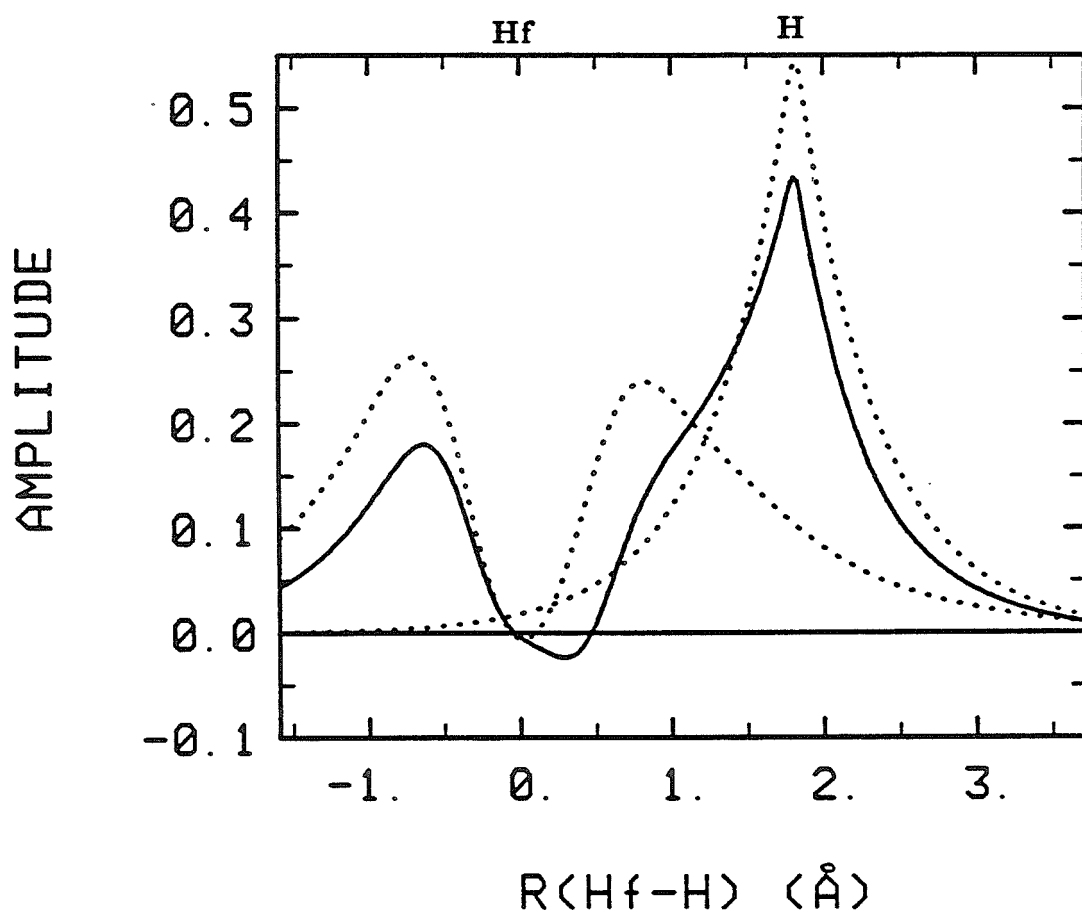
Figure 4d. The amplitudes of the overlapping $Cl_2(H)Th$ and H fragment orbitals (dotted lines) and of the bonding orbital [first natural, Th−H GVB(1/2) pair] of $Cl_2(H)Th−H$ (solid line).
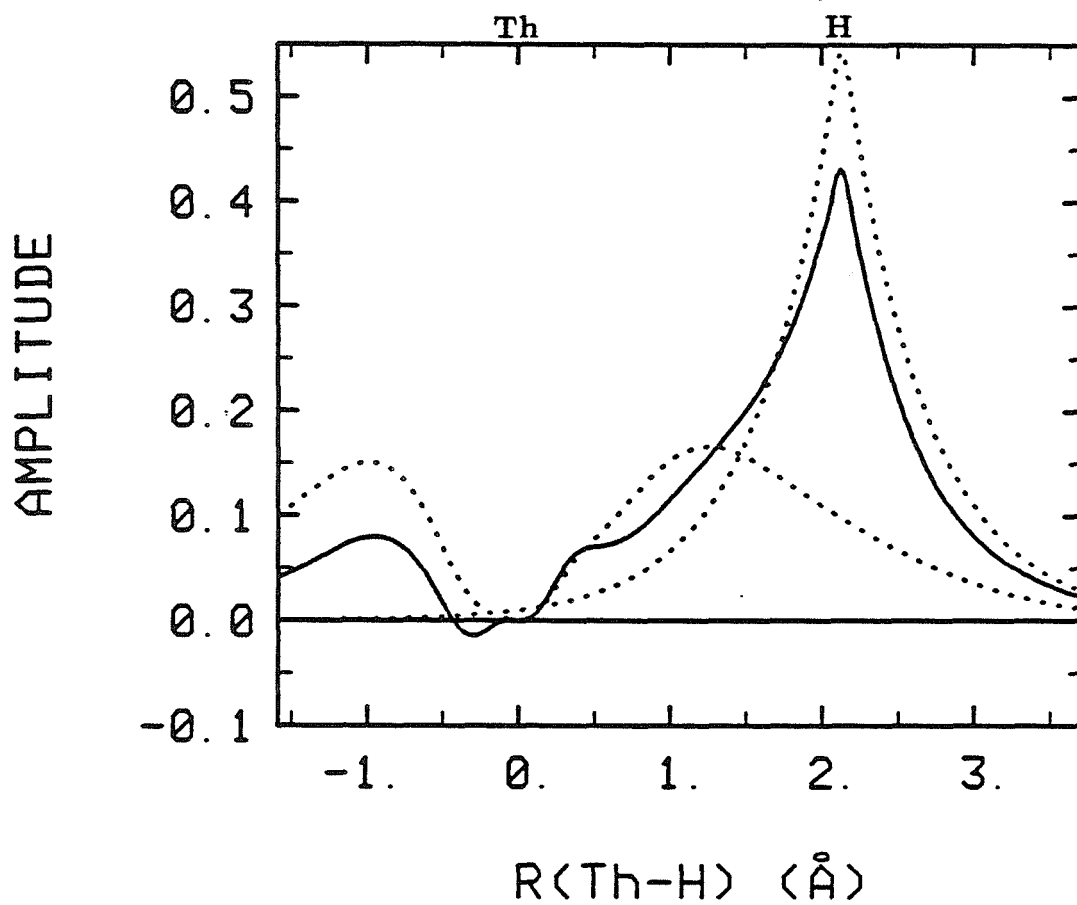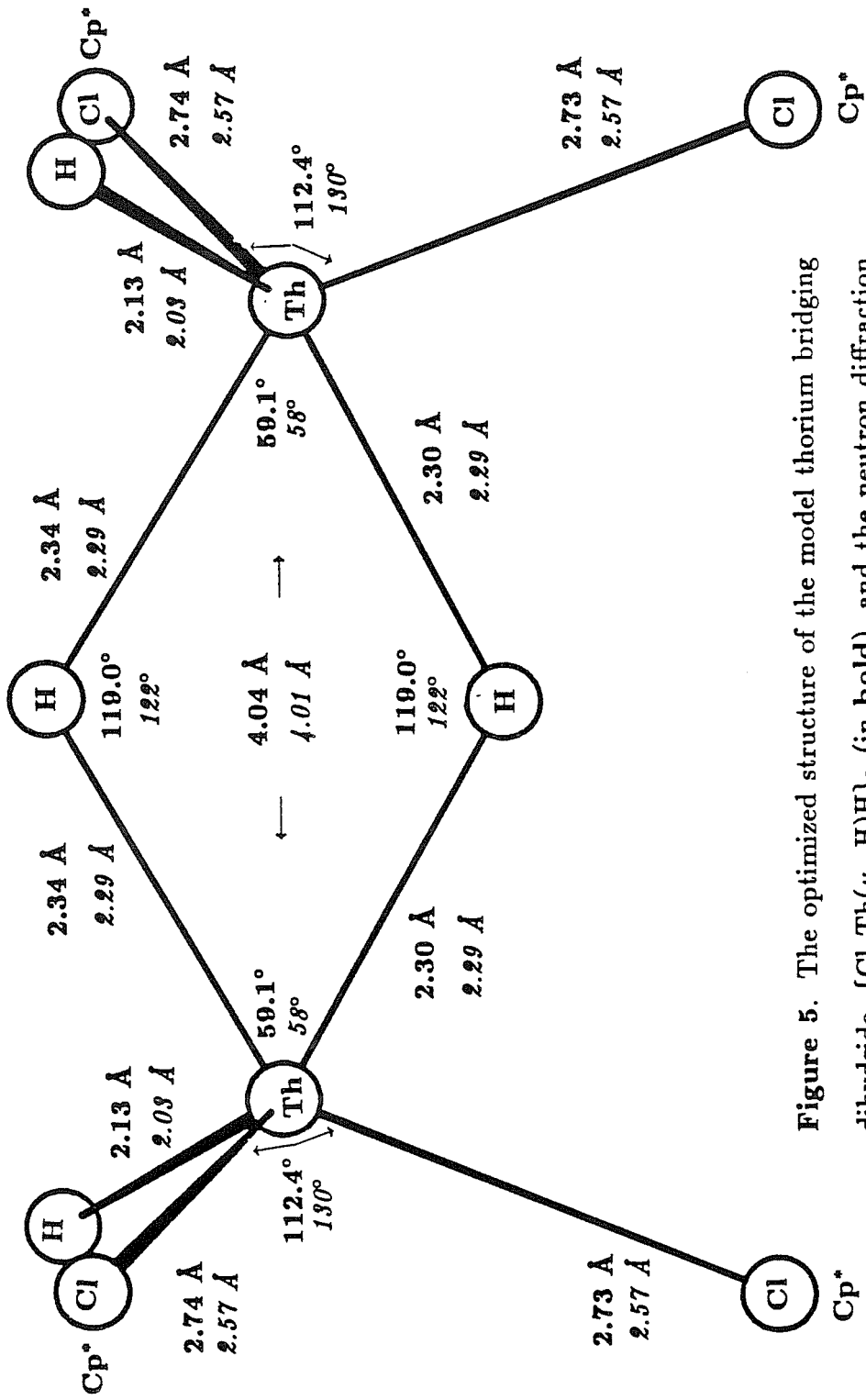
Figure 5. The optimized structure of the model thorium bridging dihydride, {Cl$_2$Th(μ-H)H}$_2$ (in bold), and the neutron diffraction structure of {Cp$_2^*$Th(μ-H)H}$_2$ (in italics).

Figure 6. The GVB(2/6) natural orbitals of the bridging Th−H−Th bonds in $\{Cl_2Th(\mu\text{-}H)H\}_2$.

first

98.68%

second

0.85%

third

0.46%

first

98.68%

second

0.85%

third

0.46%
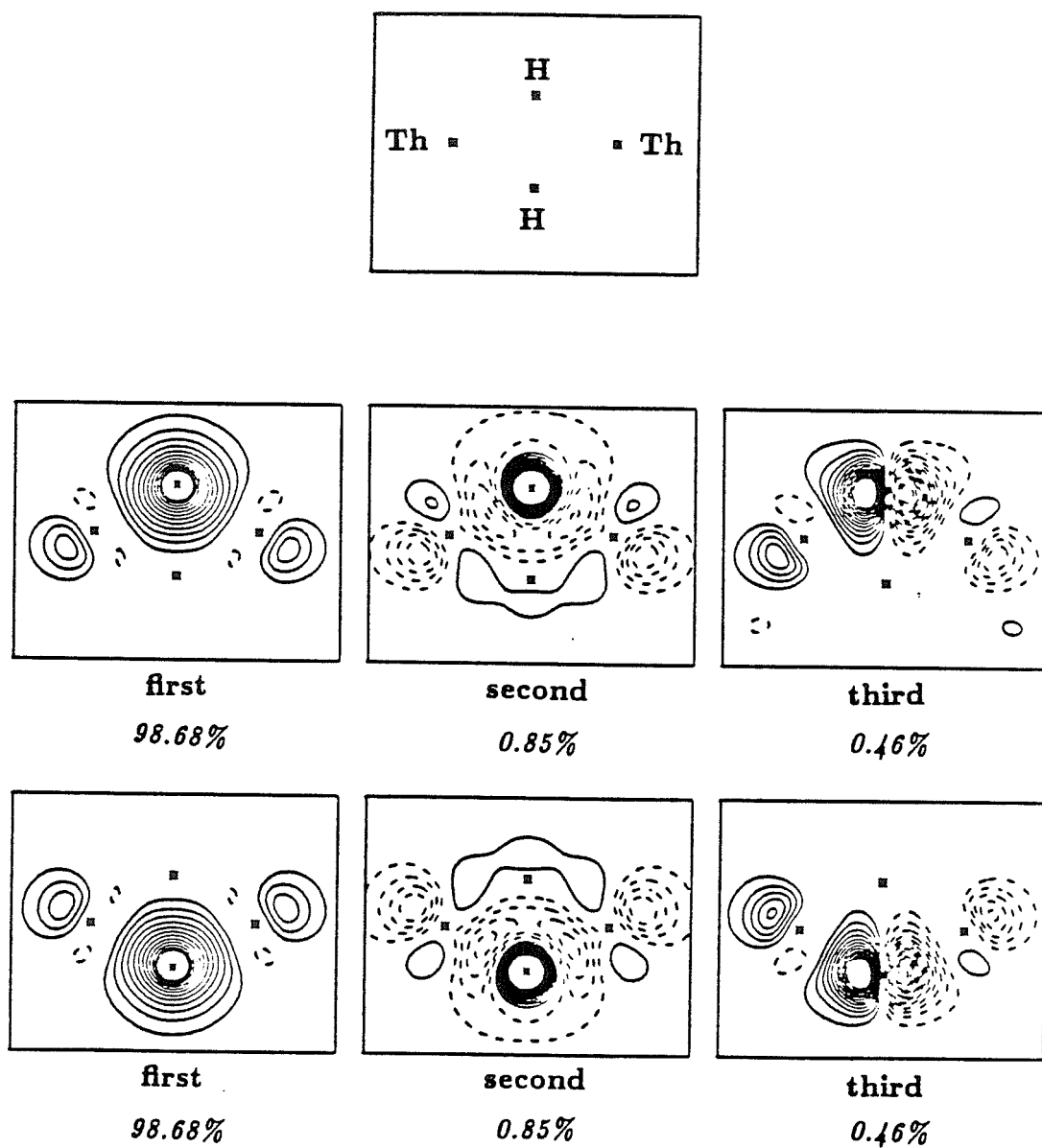
Figure 7. The GVB(2/6) orbitals of the bridging Th$-$H$-$Th bonds in $\{Cl_2Th(\mu\text{-}H)H\}_2$.

a) Linear combinations of the first and second natural orbitals for both bridging bonds (weighted by CI coefficients).

in-out
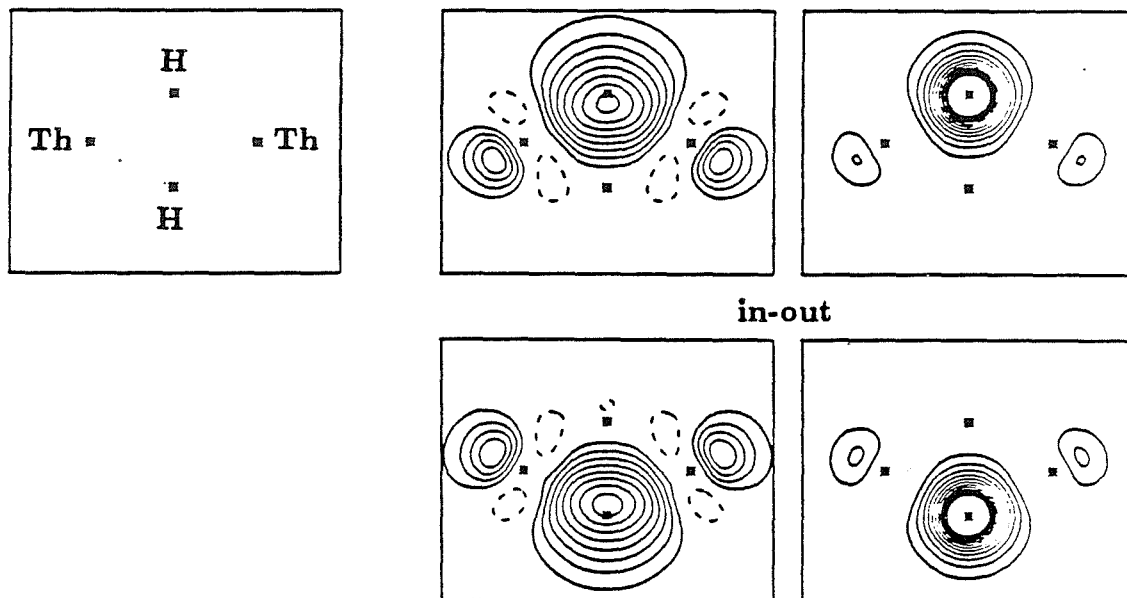
b) Linear combinations of the first and third natural orbitals for both bridging bonds (weighted by CI coefficients).

left-right
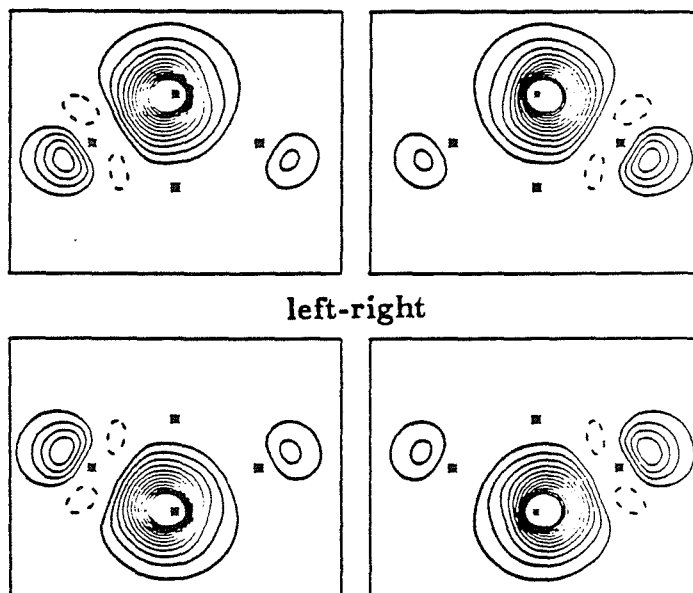
Figure 8a. The GVB-PP orbitals of the reactants for the reaction:
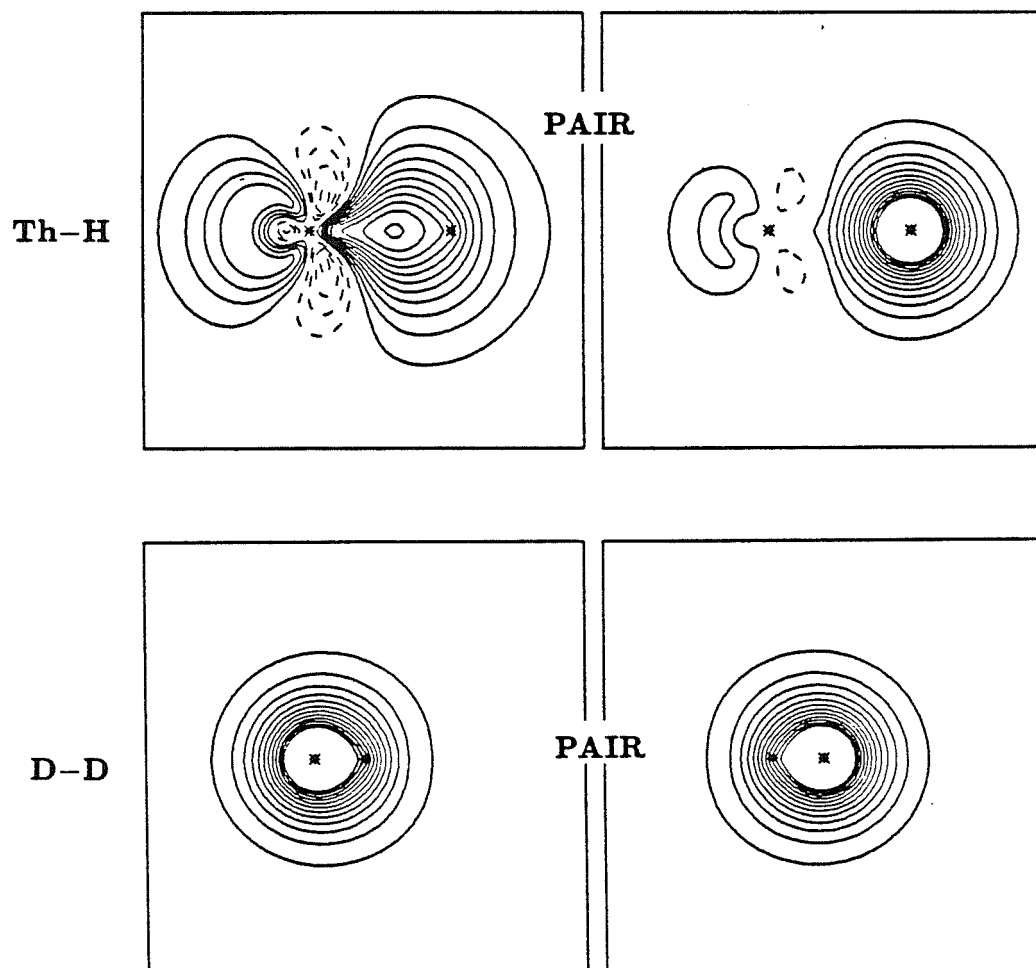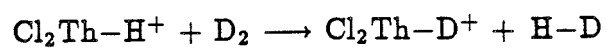
$Cl_2 Th-H^+ + D_2 \longrightarrow Cl_2 Th-D^+ + H-D$

Figure 8b. The GVB-PP orbitals at the transition state for the reaction: $Cl_2Th-H^+ + D_2 \longrightarrow Cl_2Th-D^+ + H-D$
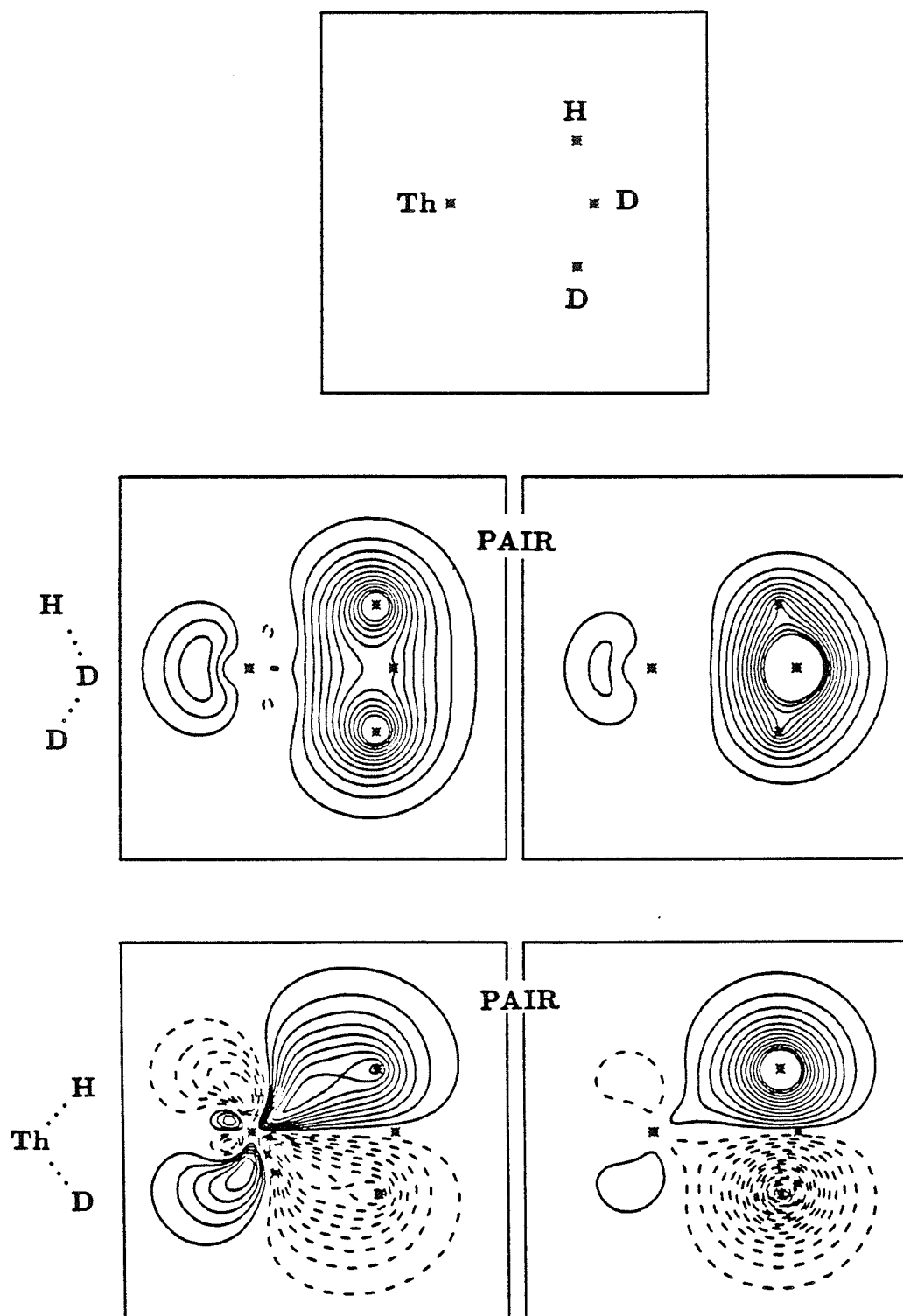
Figure 8c. The GVB-PP orbitals of the products for the reaction:

$Cl_2Th-H^+ + D_2 \longrightarrow Cl_2Th-D^+ + H-D$

Th
|
D

H
|
D

PAIR

PAIR
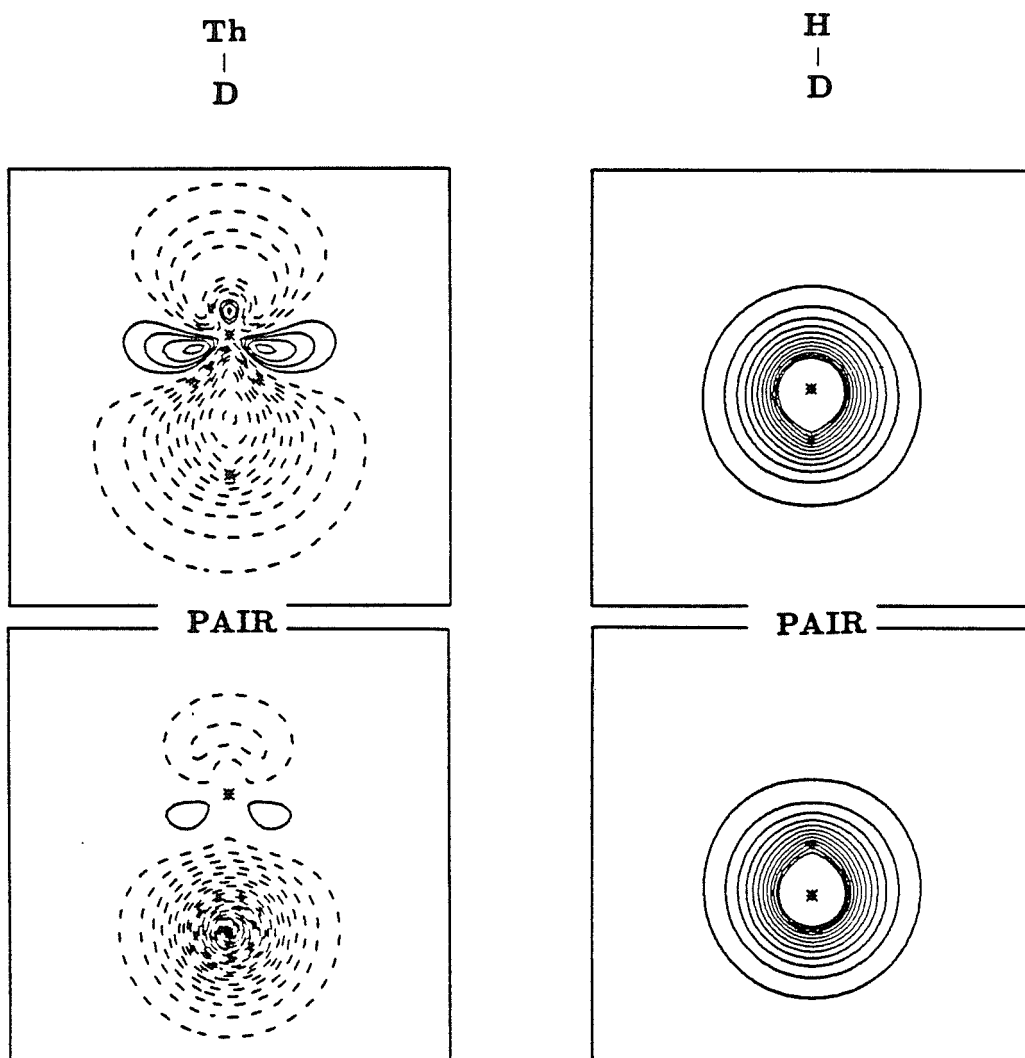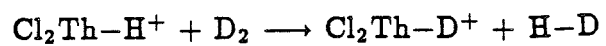
Figure 9a. The GVB-PP orbitals at the transition state (S) for the reaction: $Cl_3Th-H + D_2 \longrightarrow Cl_3Th-D + H-D$
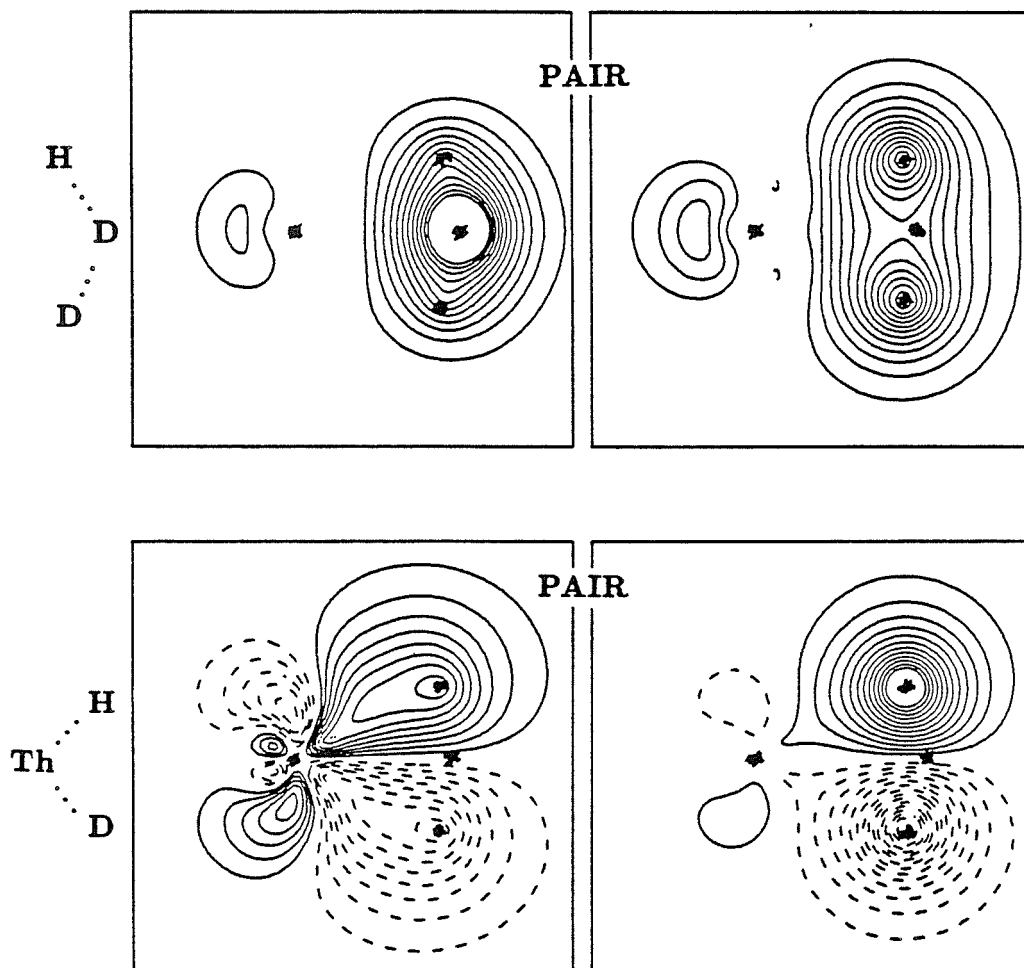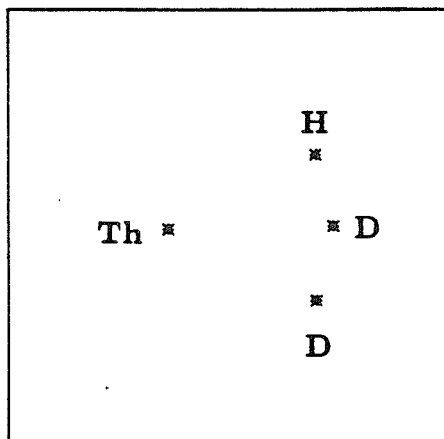
Figure 9b. The GVB-PP orbitals at the transition state (U) for the

reaction: $Cl_3Th-H + D_2 \longrightarrow Cl_3Th-D + H-D$
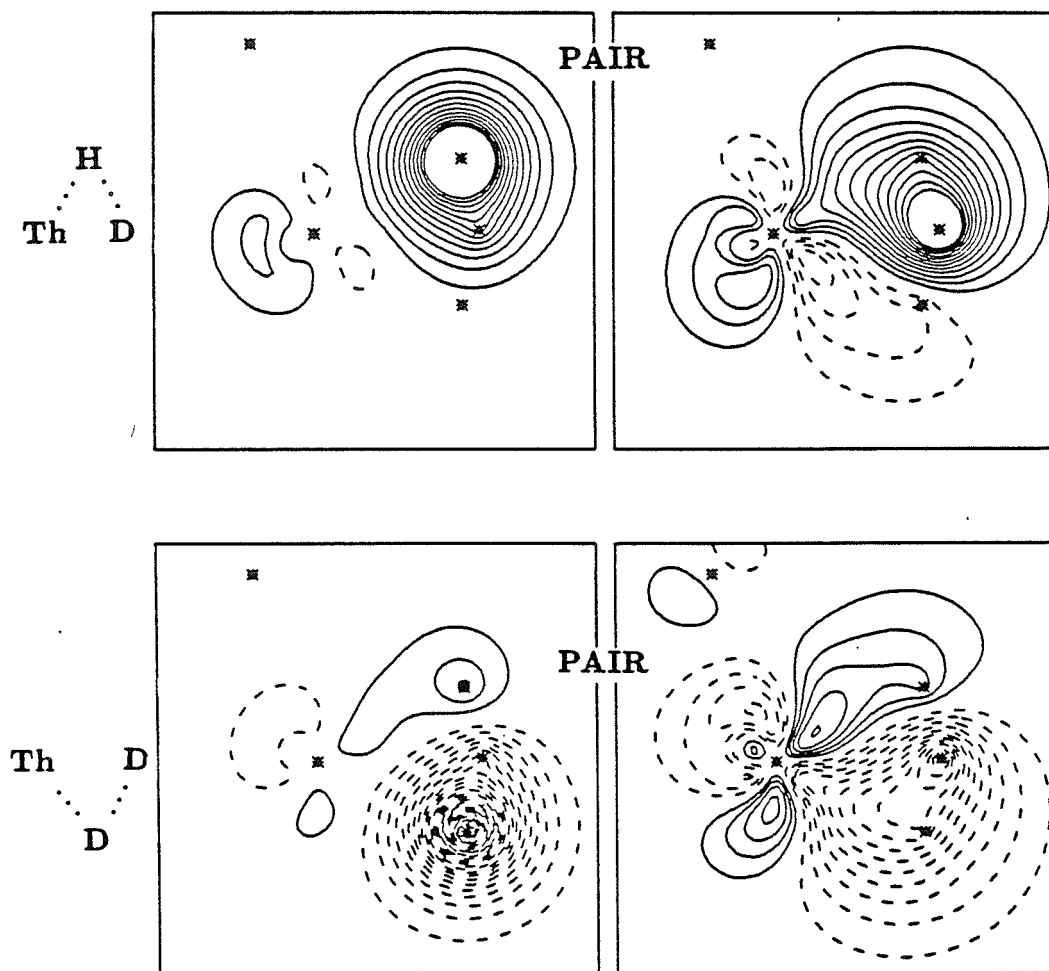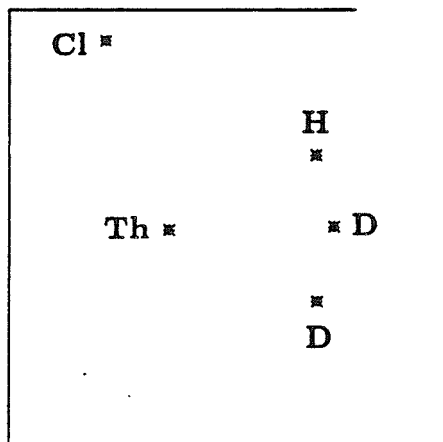
Figure 10a. The GVB(2/4) one-electron orbitals of the Ti—H and Ti—CH$_3$ bonds in Cl$_2$Ti(H)CH$_3$.
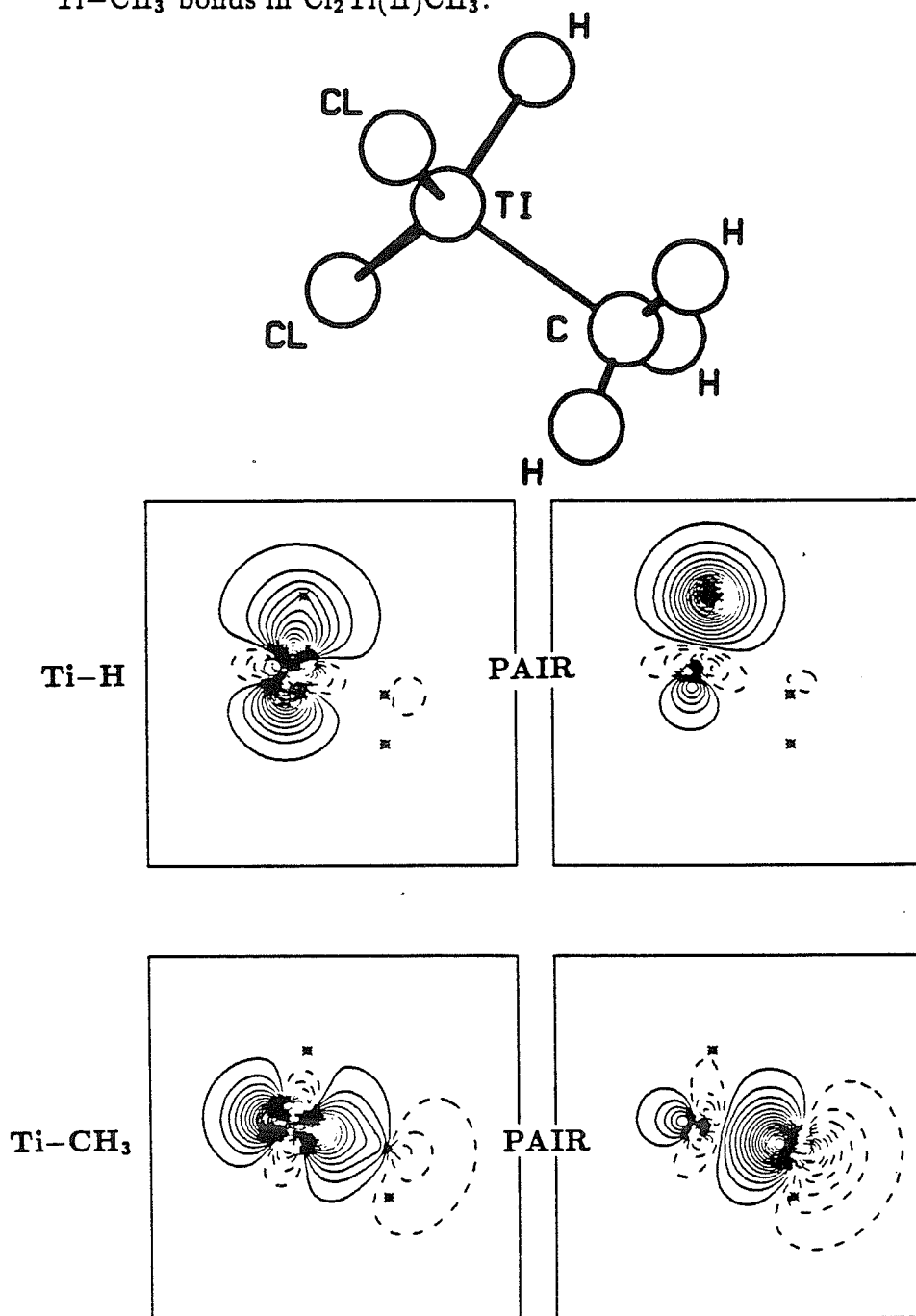
Figure 10b. The GVB(2/4) one-electron orbitals of the Zr—H and Zr—CH$_3$ bonds in Cl$_2$Zr(H)CH$_3$.
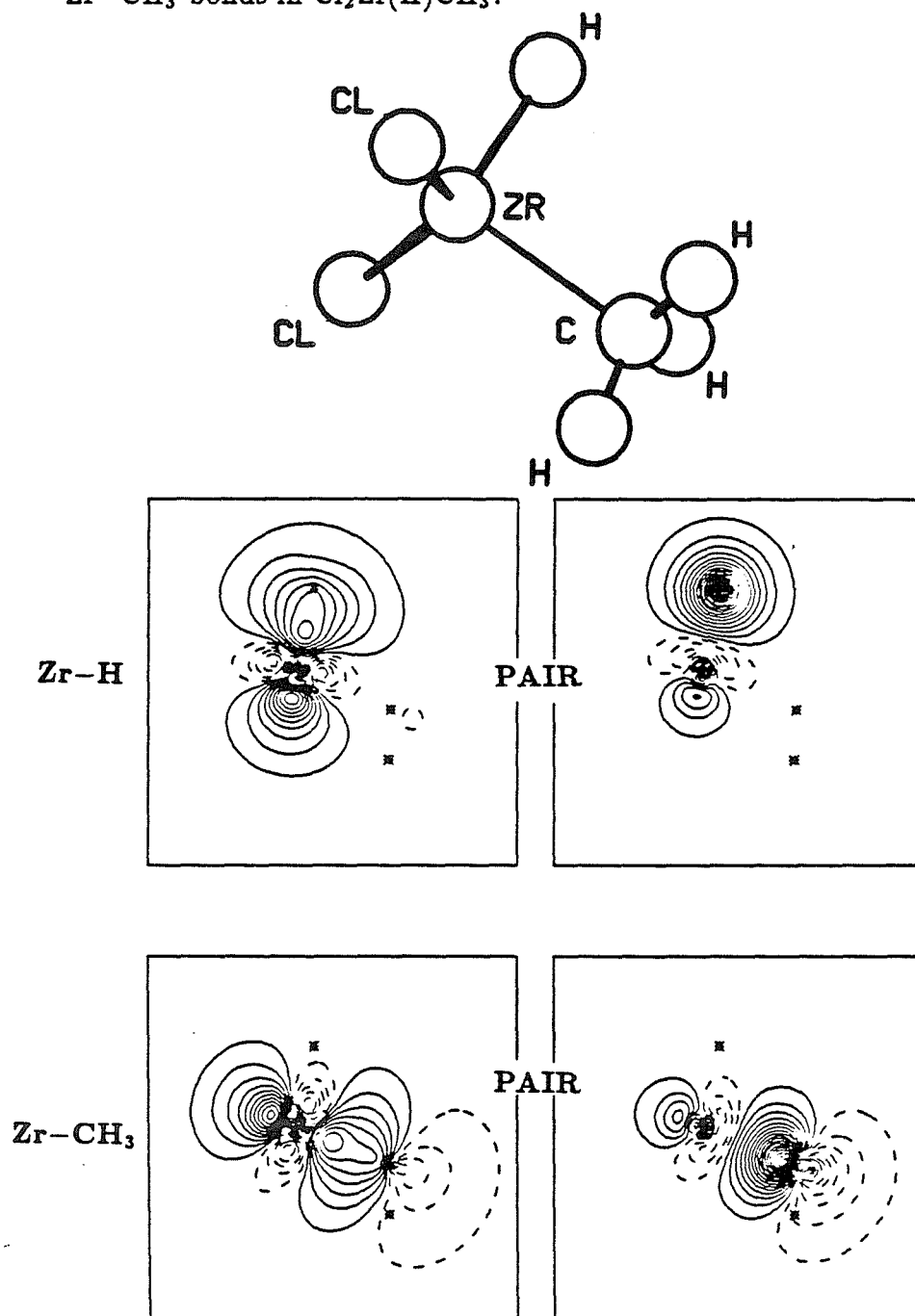
Figure 10c. The GVB(2/4) one-electron orbitals of the Hf—H and Hf—CH$_3$ bonds in Cl$_2$Hf(H)CH$_3$.
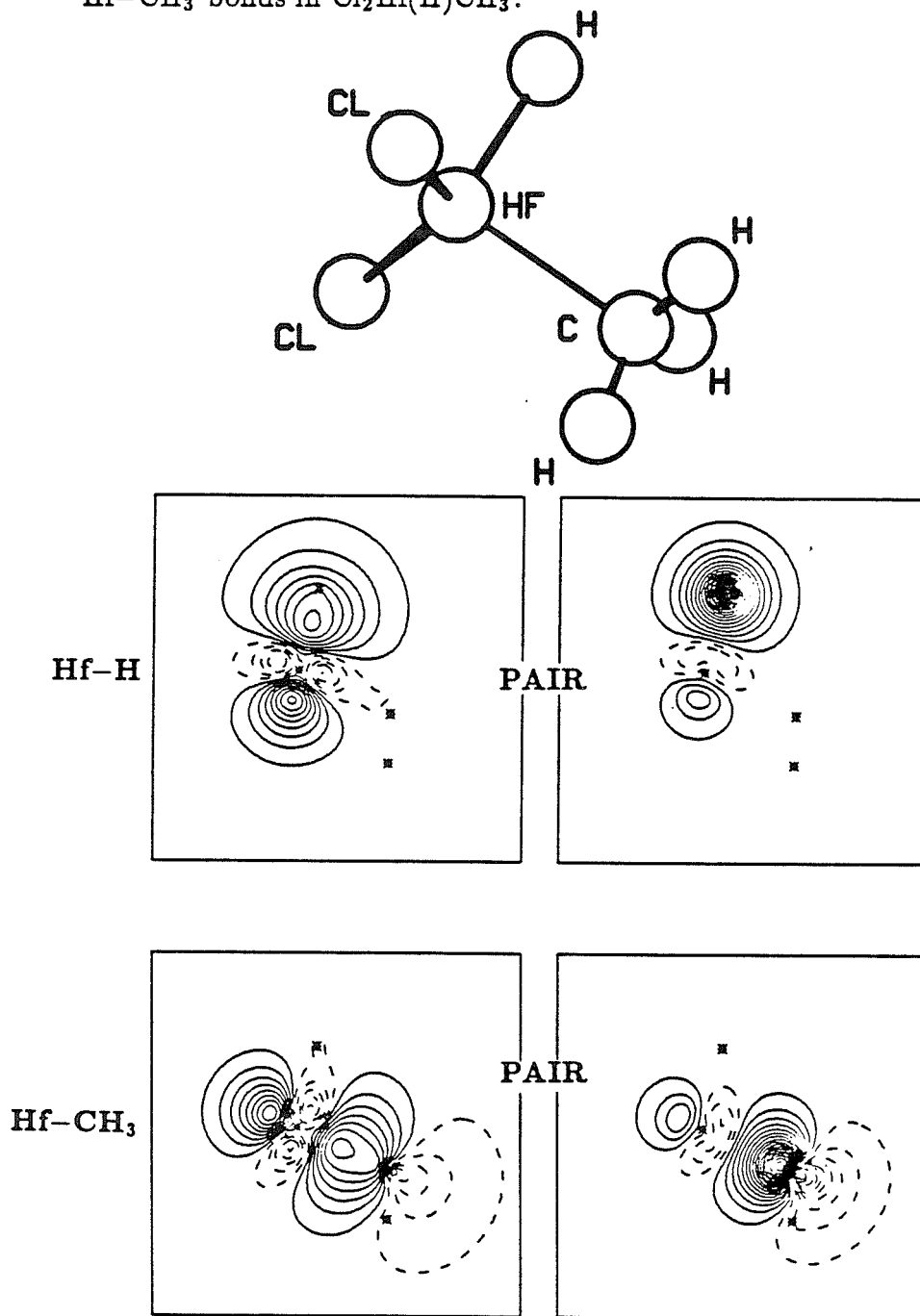
Figure 10d. The GVB(2/4) one-electron orbitals of the Th$-$H and Th$-$CH$_3$ bonds in Cl$_2$Th(H)CH$_3$.
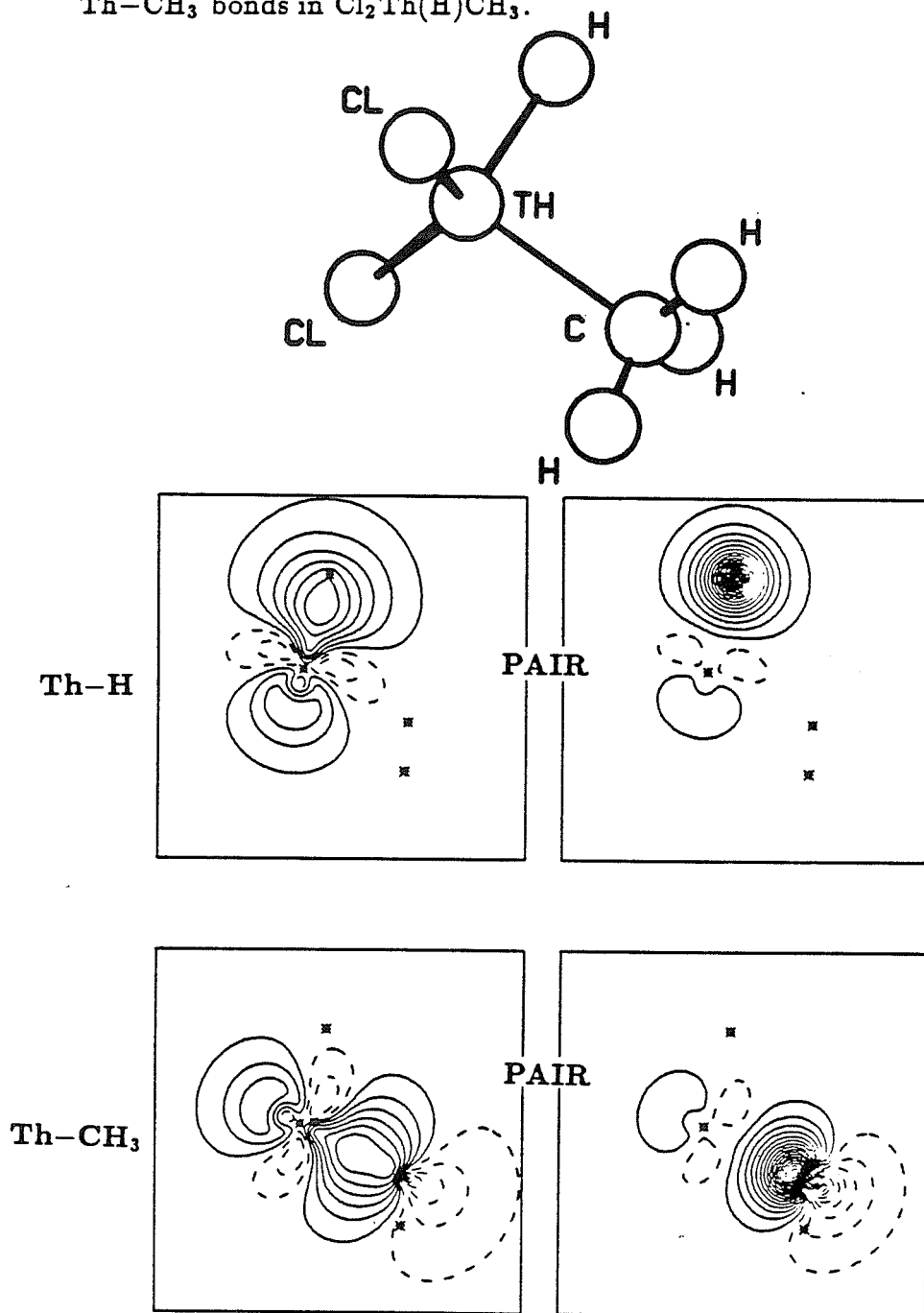
Figure 11. The scaled reaction coordinate for CO insertion:

$Cl_3Th(H)CO \longrightarrow Cl_3Th[\eta^2\text{-}OCH]$,
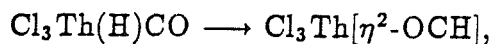
shown for the GVB(6/12) wavefunction both with f functions (solid line) and without f functions (dotted line) on Th. 0% corresponds to the CO coordinate reactant, 100% to the formyl product.
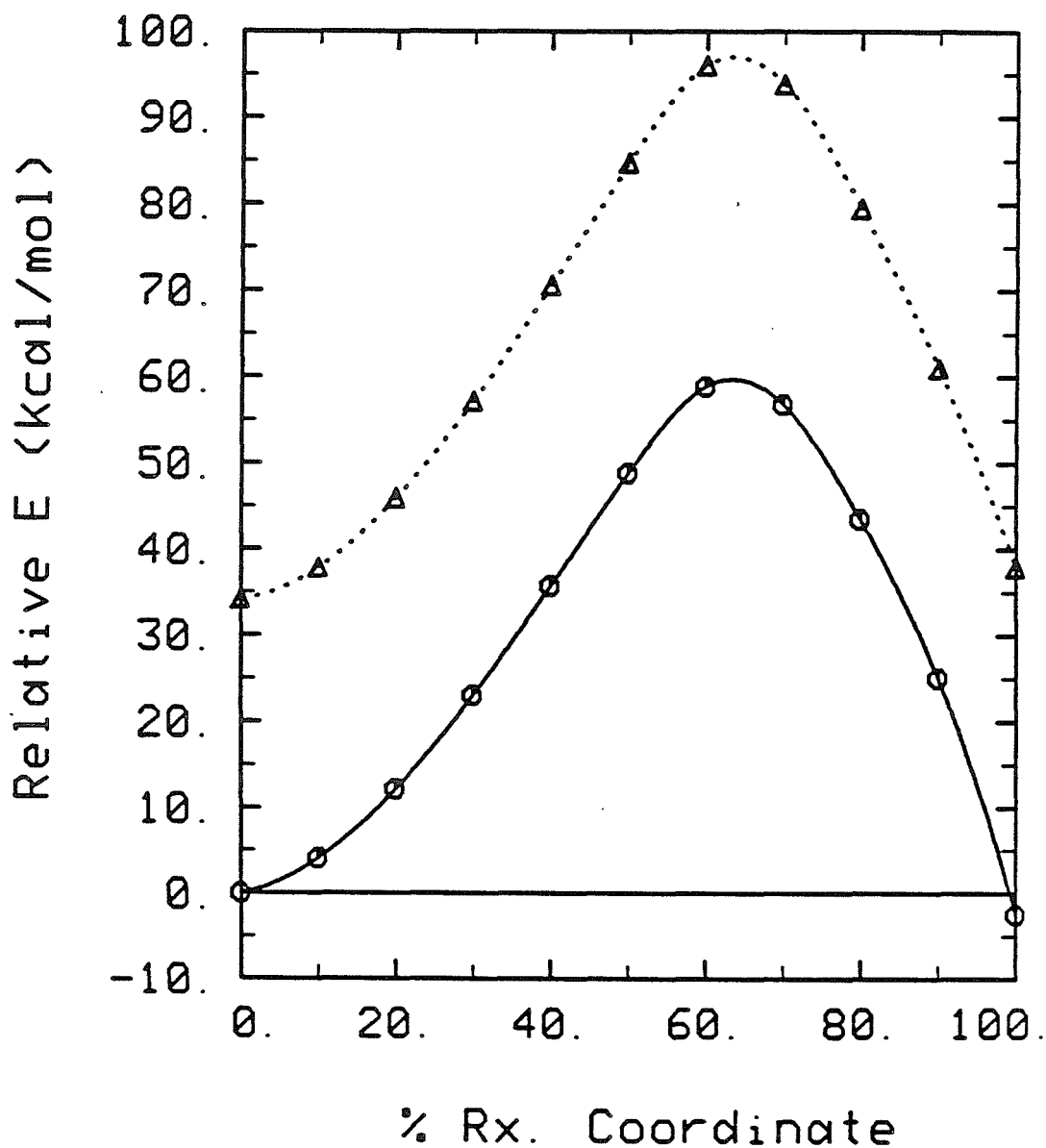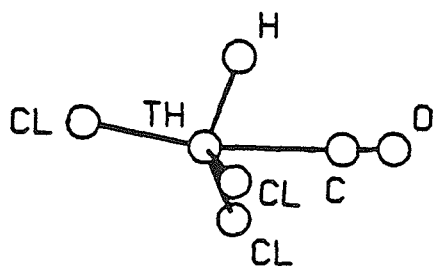
Figure 12a. The GVB(6/12) orbitals for the CO coordinate reactant complex, $Cl_2Th(H)CO$.

Th–H σ bond

C–O in-plane π bond

Th–C dative bond

C–O σ bond
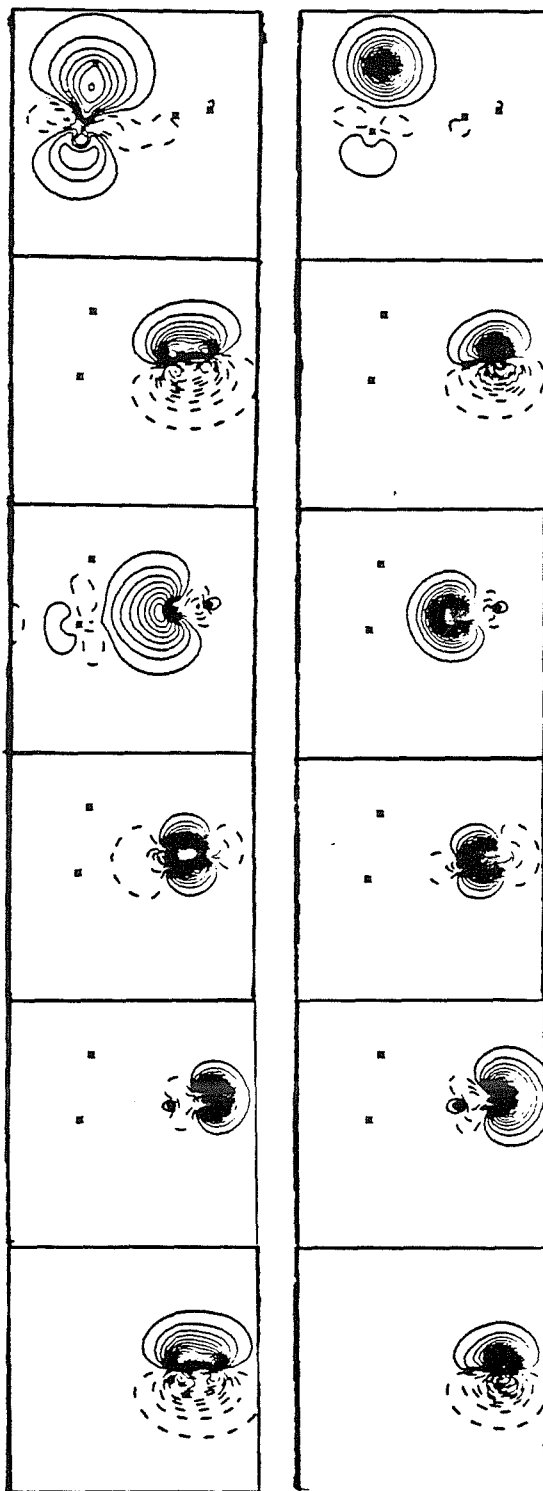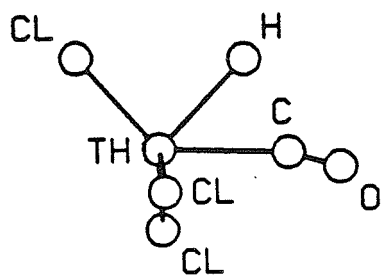
O lone pair

C–O out-of-plane π bond

Figure 12b. The GVB(6/12) orbitals for the 40% (along the scaled reaction coordinate) geometry.

Th–H σ bond

C–O in-plane π bond

Th–C dative bond

C–O σ bond

O lone pair

C–O out-of-plane π bond
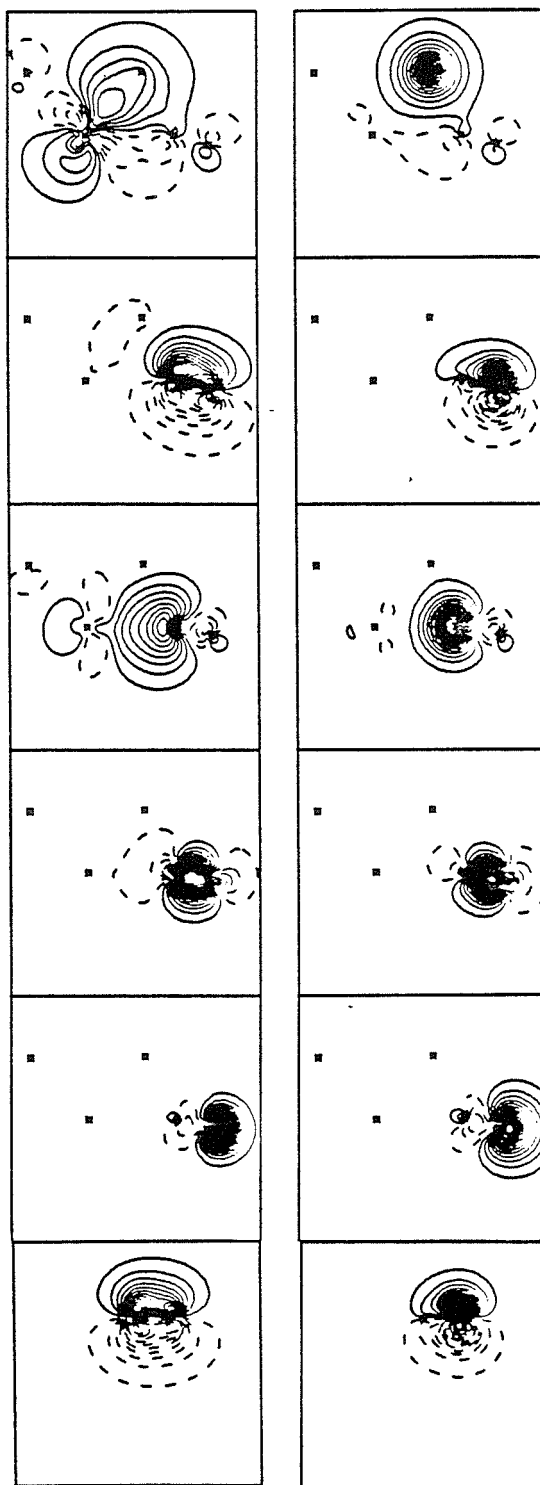
Figure 12c. The GVB(6/12) orbitals for the 60% (along the scaled reaction coordinate) geometry.
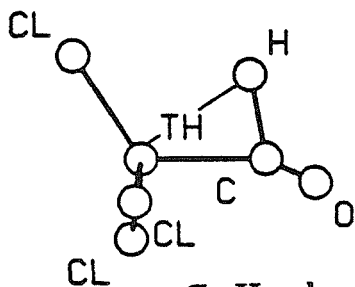
C−H σ bond/
Th−H σ bond

O lone pair/
C−O in-plane π bond

Th−C σ bond/
Th−C dative bond

C−O σ bond

O lone pair

C−O out-of-plane π bond
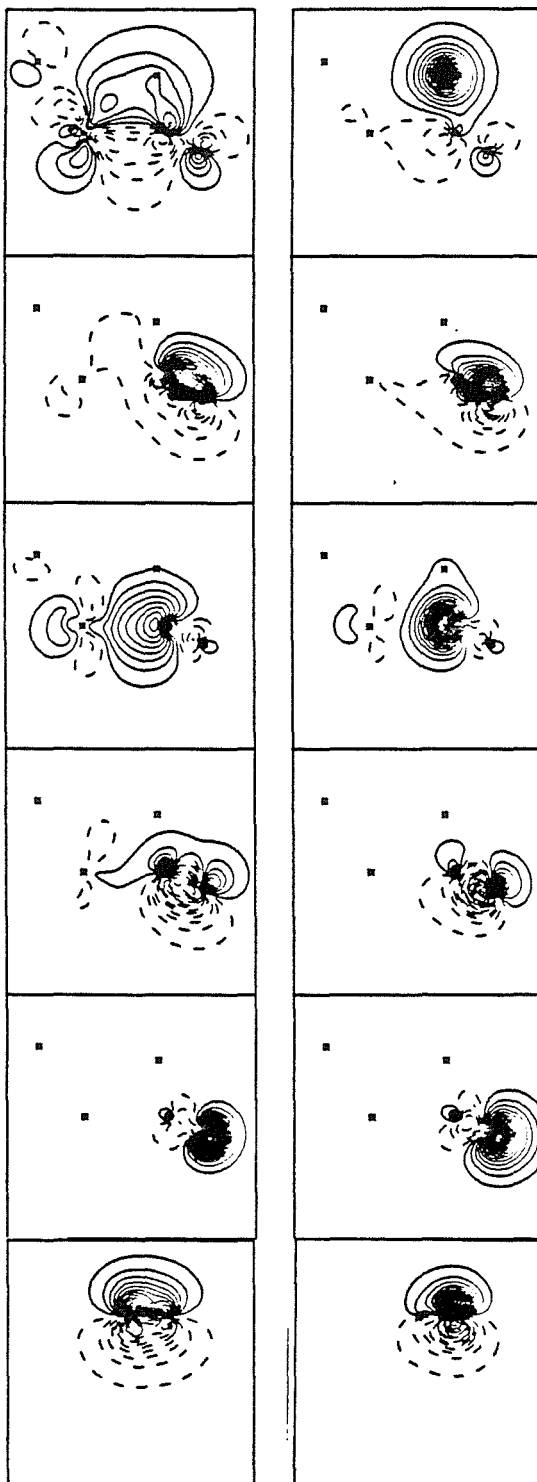
Figure 12d. The GVB(6/12) orbitals for the 70% (along the scaled reaction coordinate) geometry.

C–H σ bond

O lone pair

Th–C σ bond

C–O σ bond

O lone pair

C–O out-of-plane π bond
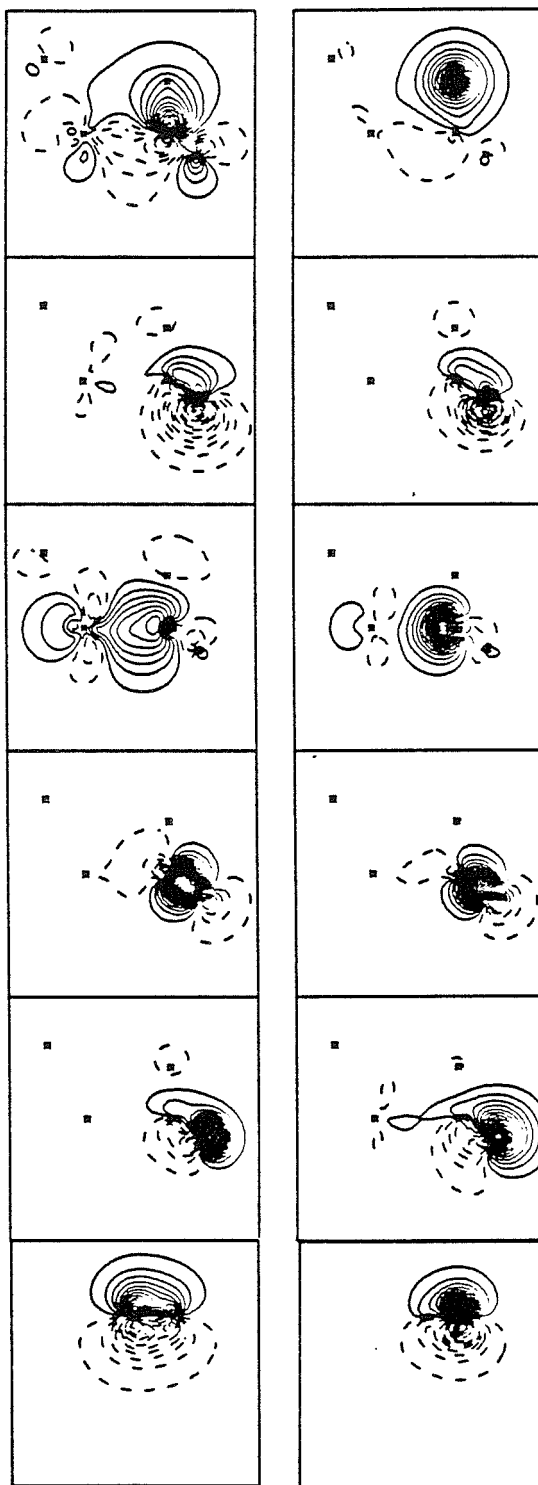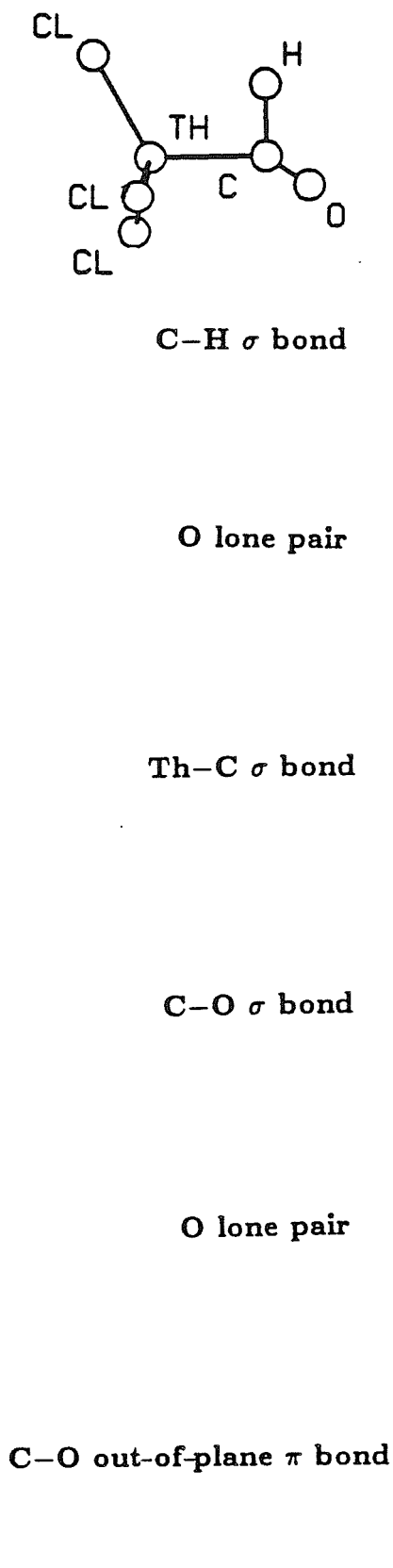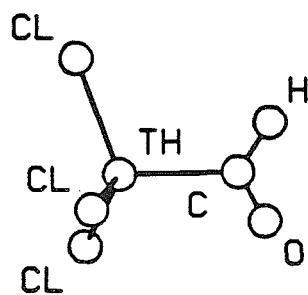
Figure 12e. The GVB(6/12) orbitals for the 90% (along the scaled reaction coordinate) geometry.

C–H σ bond

O lone pair

Th–C σ bond

C–O σ bond
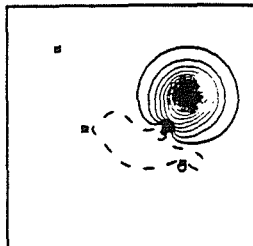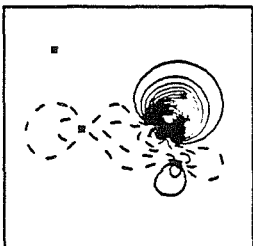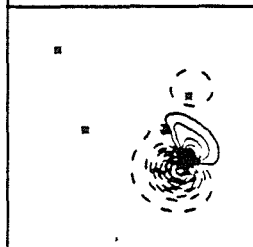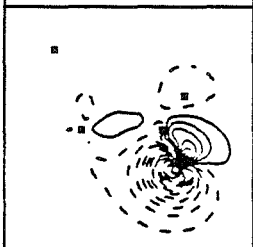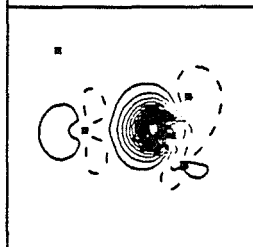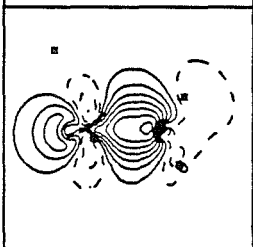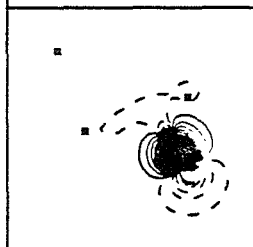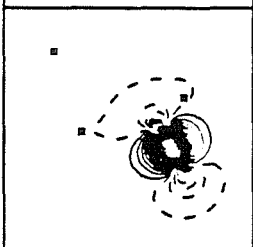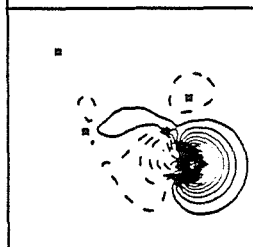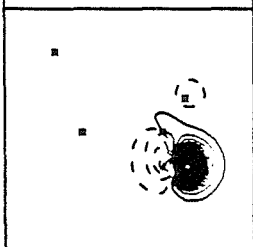
O lone pair

C–O out-of-plane π bond
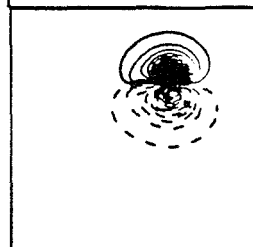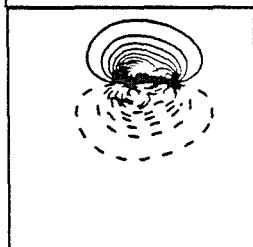
Figure 12f. The GVB(6/12) orbitals for the inserted product, $Cl_3Th[\eta^2\text{-}OCH]$.

C–H σ bond
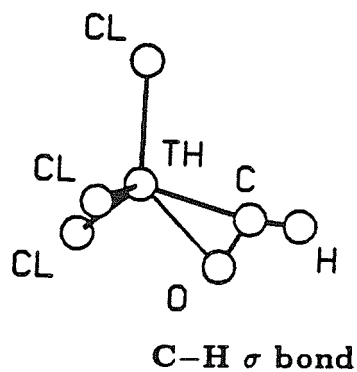
Th–O dative bond

Th–C σ bond

C–O σ bond

O lone pair

C–O out-of-plane π bond
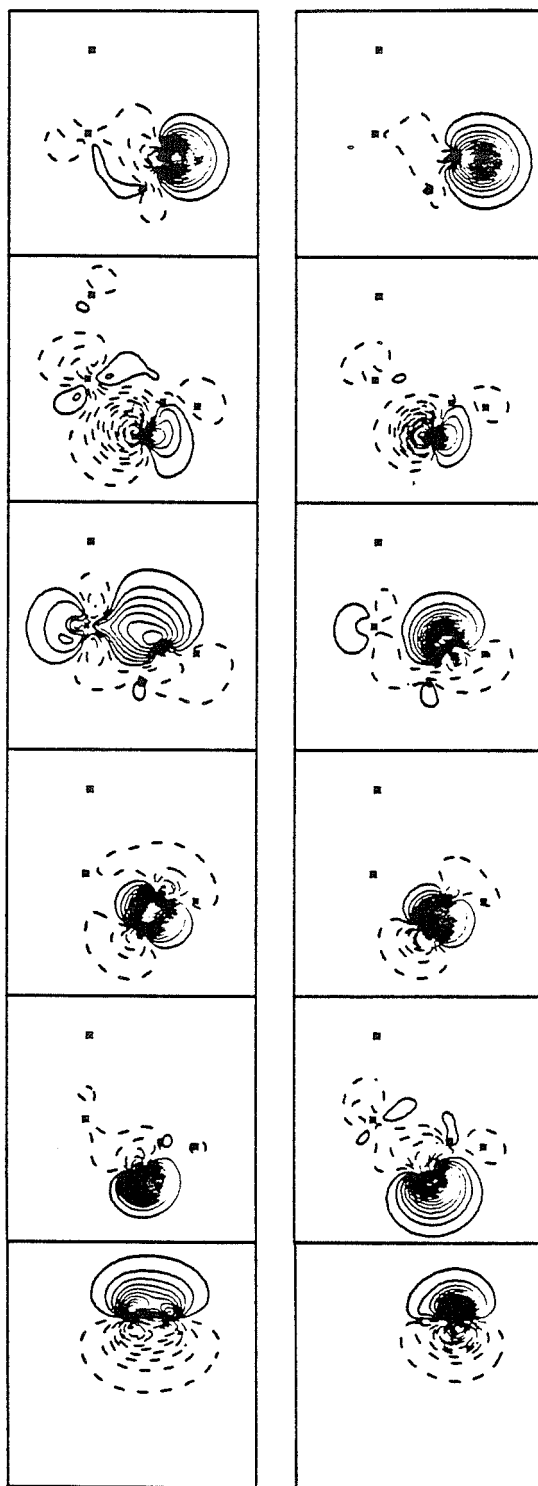
Figure 13. The GVB(3/6) orbitals for Cl_3ThOH, including the Th to O p_y charge transfer, the O—H bond, and the O p_x lone pair.
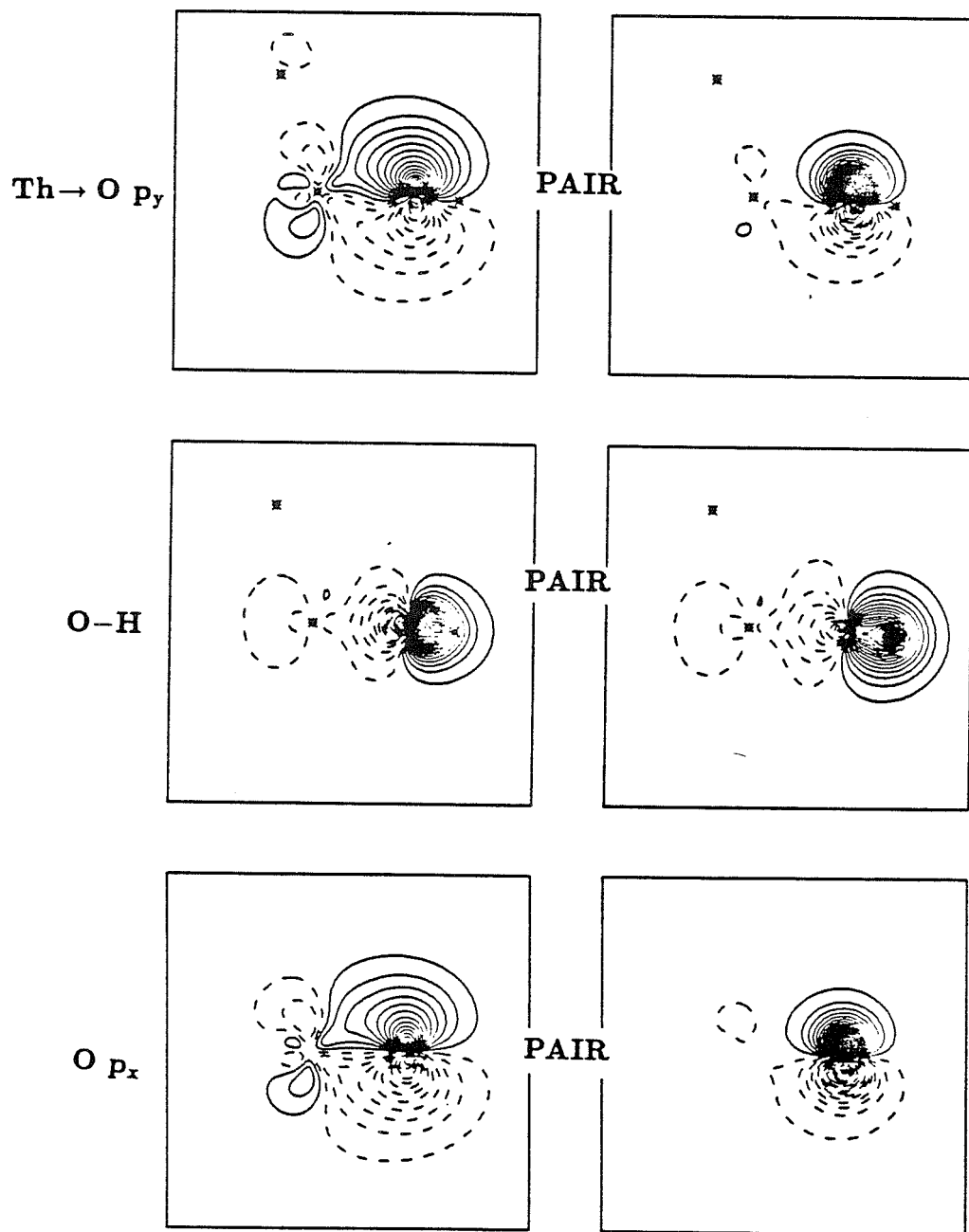
There is no subject, however complex,
which, if studied with patience and
intelligence, will not become more complex.

Siddarth Dasgupta (from Gaussian86!)

Part II

Metal Hydrogen Bond Formation Energetics

Abstract: The process of metal hydrogen bond formation is investigated using the series of molecules Cl_2MH_2, M = Ti, Zr, Hf, and Th, and the series M−H, M = H, Li, Na, K, Rb, and Cs. The metal-hydrogen bond strengths for Group IVB and thorium increase with increasing atomic number. In contrast, the bond strengths of the alkali metal-hydrogen bonds decrease down the column. By analyzing in detail the energy components of the generalized valence bond (GVB) wavefunctions (M−H bonds correlated) for both these groups, a complete picture of chemical binding is obtained. It is found that the different ordering of M−H bond dissociation energies arises from the unique characteristics of actinide and transition metal d orbitals and that the *exchange kinetic energy*, T^x, is responsible for chemical bond formation.

1. Introduction

From previous studies[1-15] on the forces involved in covalent bond formation three different interpretations have arisen. The earliest notions were that chemical binding arose from a decrease of potential energy associated with placing an electron in between two nuclei.[16] The electron would then be attracted to two nuclei instead of one, overriding the repulsive nuclear-nuclear interaction. However, it has been shown conclusively that in H_2^+ the internuclear zone is a region of higher potential energy[17]. Hence, a build-up of electron density between atoms does not cause a drop in potential energy and this cannot be the driving force for bonding. (Nonetheless, this argument is still seen in many physical chemistry textbooks.[18]) The second explanation of bonding, an elaboration on the above electrostatic potential energy argument, is that the atomic orbitals on each atom contract during bond formation, thus lowering the potential energy of the system. This line of reasoning is also found in many textbooks.[19]

Finally, the third explanation of chemical bonding is that the cause of binding is due to a decrease in the kinetic energy. This idea was proposed by Hellman[11] and was later refined and investigated by Ruedenberg[12]. Wilson and Goddard[17] analyzed in detail the energy components of the binding energy in H_2 and H_2^+. By decomposing the binding energy into exchange kinetic energy and exchange potential energy, they found that the only part of the binding energy that decreased (relative to the infinitely separated fragments) during bond formation was the exchange kinetic energy term. They were further able to demonstrate that the exchange kinetic energy was dominated by the contragradience of the orbitals. The contragradience is the smoothing of the slopes of the orbitals in the bonding region. This leads to a a larger box for the electrons to

move within and the kinetic energy is reduced. Wilson and Goddard also note that the electron density between the nuclei does increase, but that this increase is a consequence of the kinetic energy term.

In this study our goal was twofold. We first wanted to be able to show what the driving force is in chemical binding over a wide range of systems including transition metals and actinides, that is, whether kinetic or potential energy was the dominant term leading to bonding. Secondly, we wanted to address the question of why transition metal bond strengths increase with increasing atomic number while the bond strength trends in main group chemistry are the opposite. To assess both these questions, we choose to evaluate the energy components of metal-hydrogen bond formation for two series of molecules, one a main group series, the alkali metal-hydrogen systems, the other, a transition metal series, Cl_2MH_2, M = Ti, Zr, Hf, and Th complexes. Within both series the valence ground electronic state of the metal atoms is the same, s^1 for the alkalies, and s^2d^2 for the transition metals and thorium. Thus, in both set of molecules all valence electrons are involved in bonding.

2. Calculational Details

2.1 Basis Sets and Effective Core Potentials

The relativistic effective core potentials (RECP) developed at Los Alamos by Wadt[20a,b] and Hay[20b] were used to replace the inner core electrons of Cs [Pd], Hf [Nd], and Th [Hg]. A double-ζ valence contraction[20b] (5s5p/3s3p) for Cs's remaining $5s^25p^66s^1$ electrons was used, augmented by two d polarization functions ($\zeta = 0.0279$ and 0.0113). The outer 12 electrons of Hf ($5s^25p^66s^25d^2$) were then treated explicitly using the double-ζ valence contraction of the associated

Los Alamos Hf basis set (5s5p3d/3s3p2d).[20b] For the outer 10 electrons of Th ($6p^6 7s^2 6d^2$) the Wadt basis set[20a] (3s3p4d4f/3s3p2d2f) was modified such that in the d space there were two uncontracted functions; the rest of the functions were left unchanged from above (3s3p2d4f/3s3p2d2f). The reader is referred to Part I, Section 2.1 for more information on RECP's and a detailed discussion of the Th basis.

All electrons of Ti, Zr, H, Li, Na, K, and Rb were considered explicitly. The bases for Ti, Zr, Na, K, and Rb were developed by Rappé and Goddard,[21] using the same methodology. In all cases a double-ζ contraction was used. A set of 5d primitives was employed on Ti.[22] The 4d primitives on K were replaced by a set of uncontracted 2d primitives ($\zeta = 0.2933$ and 0.05935).[23] The basis set for H was the unscaled triple-ζ contraction of the six gaussian basis of Huzinaga.[24] One set of p polarization functions was used ($\zeta = 1.0$).[25] An ECP was used to replace the $1s^2 2s^2 2p^6$ core electrons of Cl.[26a] The remaining five electrons, $3s^2 3p^5$, were treated explicitly, using a minimal basis with the contraction optimized for $TiCl_4$.[26b]

2.2 Wavefunctions

Ab initio generalized valence bond wavefunctions[27] (GVB) were used to describe all of the systems studied in this work. All metal−H bonds were correlated with the GVB-PP(1/2) wavefunction; each electron in the bond pair was given its own orbital and the one-electron orbitals within each pair were allowed to overlap. For the transition metal and thorium complexes with two metal-hydrogen bonds, both bonds were correlated in this way. (Section 2.2.1 in Part I has a much more detailed discussion of the GVB wavefunction.)

In order to examine purely covalent bonding, the initial wavefunctions were

constructed of the two optimized metal and hydrogen fragment orbitals at infinite separation. The geometries at the relaxed optimum bond distance were used for the Cl_2MH fragments. The orbital shapes were then frozen, i.e., not allowed to change except for orthogonality effects, at finite nuclear separation R. The bonding orbitals were orthogonalized to the core and to the other metal-ligand orbitals using the technique of Schmidt orthogonalization.[28] Thus, the other orbitals in the calculations were also left unchanged at finite R. The geometry of the other ligands in the Cl_2MH_2 complexes was frozen also.

Fully optimized (relaxed) wavefunctions were calculated at the theoretical equilibrium geometry for the Cl_2MH_2 species and over the entire energy surface for the alkali metals.

2.3 Anaylsis of Binding Energy

Both the frozen and relaxed binding energy surfaces can be easily broken down into their components and analyzed.[17] The exchange kinetic energy, T^x, at finite R is defined to be

$$T^x \equiv T - T^{Cl},$$ (1)

where T is the total kinetic energy of the molecule and T^{Cl} is the classical kinetic energy, which is just the sum of the kinetic energies of the two fragments at infinite separation. Similarly, the exchange potential energy is defined to be

$$V^x \equiv V - V^{Cl}.$$ (2)

The components of V^x include: 1) V^{nn}, nuclear repulsion; 2) V^{en}, electron-nuclear attraction; and 3) V^{ee}, electron-electron repulsion, all defined with re-

spect to the fragments. The exchange binding energy is simply

$$E^x = E - E^{Cl}. \qquad (3)$$

3. Results and Discussion

3.1 H_2^+ and H_2

The simplest covalently bound molecules that can be made are H_2 and H_2^+. Hence, it is instructive to first analyze the energy components of these molecules before proceeding with the more complicated systems. In Figs. 1 and 2 the frozen binding energy, E_f^x, the frozen exchange kinetic energy, T_f^x, and the frozen exchange potential energy, V_f^x, are shown for H_2^+ and H_2, respectively. The character of the frozen energy components is the same for both molecules. As found by Wilson and Goddard[17], the kinetic energy is attractive throughout the bonding region, whereas the potential energy is purely repulsive. The kinetic energy term was found to be dominated by the effect of contragradience, the smoothing of the slopes of the orbitals in the bonding region at finite R, which results in a larger box for the electrons to reside in and thus decreases the kinetic energy upon bond formation. This is illustrated pictorially in Fig. 3.

For H_2^+ the minimum energy points of the binding energy and kinetic energy curves are at essentially the same internuclear distance (R), ~1.3Å (see Table I). However, for H_2 the E_f^x minimum, 0.88Å, is shifted inside the T_f^x minimum, 1.07Å. The reason for the differences in minimum energy distances is the behavior of V_f^x between approximately 1.5Å, where it has a local maximum, and 0.75Å, where it has a local minimum. The relative decrease in potential energy in this region shifts the E_f^x minimum to a distance at which T_f^x is increasing. V_f^x for

H_2^+ is always increasing, but there is a region between $\approx 1.25\text{Å}-2.00\text{Å}$ where it is flat. In this region the nuclear repulsion, V^{nn}, is nearly balanced by the electron-nuclear attraction, V^{en}. If another electron is placed in the bonding region to make the neutral complex H_2, we would predict that V_f^z would be even more repulsive than for H_2^+ because of the additional force of electron-electron repulsion, V^{ee}.

Why then does the opposite effect occur for H_2? The reason is that there is a region of bonding where the one-electron bonding orbitals interpenetrate each other enough so as to have sufficient density at the opposing nucleus to decrease the repulsive two-electron energy and to increase the attractive electron-nuclear interaction energy. This behavior occurs as a result of the differences between the electron-electron screening of the nuclei at long R versus short R. The one electron bond does not have a dip in its V_f^z curve because there are no screening effects.

If we examine the Hartree-Fock (HF) frozen-energy curves for H_2 shown in Fig. 4, we also see a dip in V_f^z. Since HF presumes 50% covalent and 50% ionic character in the wavefunction at infinite R, it goes to the wrong dissociation limit, $H^- + H^+$, instead of to two H atoms. Thus, the potential energy starts out at a more positive value (that for H^-) than for the GVB wavefunction. As the atoms are brought closer together, though, the ionicity inherent in the HF description of the system better reflects the nature of the system and V_f^z starts to drop. The amount of ionicity in the wavefunction plays a strong role in determining the magnitude of this effect since it is a measure of the amount of character that both electrons have on the same nucleus.

Although our orbitals are frozen, the amount of bonding versus antibonding character mixed into the GVB wavefunction is not fixed but is allowed to optimize

variationally. At infinite R the wavefunction is composed of equal amounts of bonding and antibonding character. As the two fragments are moved toward each other, the amount of bonding character increases rapidly. In terms of one-electron orbitals, this means that each localized orbital is building up character on the other nucleus; i.e., the amount of ionic character in the wavefunction is optimized. Thus, compared to the HF wavefunction, the V_f^z component should be less repulsive at the equilibrium internuclear separation. This phenomenon is borne out upon comparison of Figs. 2 and 4.

We can correlate the local maximum of V_f^z with a calculatable property, the overlap of the GVB pair orbitals. Fig. 5 shows the overlap of the one-electron bonding orbitals (for the frozen wavefunction) versus internuclear distance. The inflection point of the overlap curve at approximately 1.5Å occurs just before the maximum in V_f^z for H_2. At this point the rate of change of overlap starts decreasing. Since the two-electron energy is basically proportional to the overlap of the one-electron GVB orbitals, the two-electron energy is not increasing at as fast a rate after this point, as the nuclei continue to move closer to each other. We can define this point as the "onset of bonding." We will see later that this correlation between overlap and V_f^z occurs for the alkali metal-hydrogen complexes also. Note, however, that for H_2, V_f^z is everywhere positive. Thus, there is a decrease in the potential energy that stems from bonding. However, it is not the cause of bonding.

What changes happen when we allow the wavefunction to relax? Figures 6 and 7 show us V^z, T^z, and E^z for the relaxed wavefunctions of H_2^+ and H_2, and Table II summarizes the plots. V^z adjusts dramatically to the orbital shape changes. The behavior is similar for both the one-electron and two-electron bonds with the salient modification, in comparison with the previous description, being

a large dropoff in V^x as one approaches r_e. T^x adjusts in the opposite fashion upon relaxation of the wavefunction. It is negative with respect to fragments at long R but then quickly becomes repulsive near r_e. In addition, r_e is shifted to smaller R ($r_e = 1.06$Å, $r_{ef} = 1.32$Å for H_2^+; $r_e = 0.76$Å, $r_{ef} = 0.88$Å for H_2). The qualitative changes in orbital shapes for the relaxed molecules are shown via line plots of orbital amplitude (along the internuclear axis at r_e and r_{ef}) in Figs. 8 and 9. For both H_2^+ and H_2, the orbitals of the relaxed wavefunction have contracted significantly with respect to their frozen counterparts. Tightening of electron density decreases the V^{en} and V^{ee} components of potential energy. This contraction in itself corresponds to a decrease in the kinetic energy by making the box in which the electrons have to move smaller. However, this readjustment of orbital shapes is a relaxation *effect* caused by bonding, but certainly *not* the actual cause of binding. The decrease in the kinetic energy is then offset by the relaxation as it moves electron density away from the internuclear region. The frozen orbital description, compared to the relaxed wavefunction, obtains 64% of the binding energy for H_2^+ and 79% for H_2 (see Tables I and II).

To summarize, the bonding in H_2^+ and H_2 is due to contragradience of the orbitals leading to lower exchange kinetic energy. The total potential energy component of the binding energy is always repulsive using the frozen orbital approach. Relaxation effects lead to a contraction of electron density away from the bond region towards the nuclei, lowering the potential energy and raising the kinetic energy; overall, the binding energy is lowered (36% for H_2^+, 21% for H_2).

3.2 Alkali-Hydrogen Bonds

Bond energies for alkali-hydrogen bonds steadily decrease down the column. This trend is documented in Table III.[30] The difference in bond energies among

the alkali cogeners also decreases slightly with increasing atomic number, and seems to hover near 40 kcal mol^{-1} for NaH, KH, RbH, and CsH. What causes these trends and can we explain this by using the T^z and V^z partitioning of the binding energy?

In Figs. 10a–e, the frozen energy partitions are plotted for Li, Na, K, Rb, and Cs, respectively. The individual quantities T^z_f, V^z_f, and E^z_f are plotted for all the molecules in Figs. 11a–c, respectively, and a synopsis of the relevant parameters for each curve is in Table IV. The shape of all the energy components is essentially the same for all the alkali molecules. V^z_f is repulsive at long R but attractive at small R, while the kinetic energy, T^z_f, is attractive for most of the bonding region but crosses over V^z_f and becomes repulsive at small R. The point at which the potential energy becomes attractive shifts to longer R as atomic size increases. The binding energy, E^z_f, is attractive at small R when the kinetic energy is less attractive than potential energy. In fact, for RbH, V^z_f is below T^z_f at the minimum energy distance of the binding energy curve. This is fundamentally different from the descriptions of H_2^+ and H_2, since for these molecules V^z_f was always repulsive and Tx_f was attractive from infinite separation to the equlibrium internuclear separation.

Does this mean that potential energy is somehow the cause of bonding energy at small R? There is a difference between the energy analysis for these bonds as opposed to that discussed above. The alkali metals, unlike H_2^+ and H_2, have core orbitals to which the incipient M−H bond must become orthogonal by the Pauli principle. Consequently, in order to effectively compare H_2^+ and H_2 to the M−H bonds, we must first remove the effects of orthogonality on the bond. Figure 12a shows the energy components for LiH$^+$, where we have removed the Li valence 2s electron and frozen the Li 1s and H 1s orbitals. Thus, this system represents the

interaction of the core electrons with the incoming hydrogen atom and should account for the core effects. As the doubly occupied 1s orbital approaches the singly occupied 1s H orbital, the potential energy drops because the 1s H orbital must build up density at Li to become orthgonal to the electrons localized on Li. This effectively decreases the electron-nuclear potential energy. The physics of this interaction is very similar to the relaxation effects that occurred for H_2. When the core kinetic and potential energy terms are subtracted from those of LiH, the T_f^z and V_f^z curves of Fig. 12b result. The potential energy is unchanged at long R up to the local maximum at ~2.5 Å but is much less attractive at small R. The potential energy function behaves in a manner similarly to that of V_f^z in Fig. 2 for H_2. It is interesting to note that, like frozen H_2, the potential energy has a region of decrease, and for LiH it is actually slightly attractive at fairly small R (ca. 1.0 to 1.4 Å). The attractive "dip" in the Cs−H potential curve (Fig. 10e), where all but the eight outer core electrons ($5s^2 5p^6$) are replaced with a RECP, indicates that this effect probably occurs for all alkali metals. In addition, the maximum in V_f^z (~2.5Å) for LiH occurs just after the inflection point in the overlap versus R plot (~2.6Å, see Fig. 13). Hence, as in H_2, the rate of increase of the two-electron repulsion energy slows with the change in the overlap, and V_f^z drops.

The frozen potential energy is attractive at small R for two reasons: 1) orthogonality effects with the core electrons decrease V^{en}, and 2) as with H_2, screening effects and a buildup of electron density at the nuclei at small R can lead to a decrease in potential energy. Both of these effects happen as a result of bonding but are not the forces creating the bond. Of course, potential energy does contribute to the total binding energy and in determining where r_e occurs.

The trends in Fig. 11a−c are that E_f^z and T_f^z decrease and V_f^z increases

(except for Rb) as atomic size grows. Since the binding energy tracks with the kinetic energy, this is further confirmation that kinetic energy is the most important factor in bonding. T_f^z decreases with increasing atomic number because the orbitals become larger and more diffuse. Hence, the amount of contragradience to be gained from overlap with the H 1s orbital is lessened, since the slope of the Ns metal orbital is becoming less steep. Note that this would *not* be true if the orbitals changed significantly in character from one alkali to the next. But from H to Cs, the basic description of the bond to H is an s—s bond with little or no hybridization.

Using the maximum potential energy and the minimum kinetic energy for each molecule, an estimate of the relative rates of increase and decrease of T_f^z and V_f^z can be made. The kinetic energy increases slightly faster than potential energy decreases from Li to Rb; see Table IV. For Cs, V_f^z has a higher rate of change than T_f^z, but this can be construed as an artifact of orthogonalization as Cs was treated with an RECP. Also, note that KH and RbH have essentialy the same potential energy at the maximum. The potential energy is basically a distance effect, $\frac{1}{R}$ potential; thus, the longer the internuclear separation, the less repulsive it will be. There will also be a dependence on the amount of contragradience, since this would increase two-electron repulsion by building up character in the bonding region. As the size of the alkali metals increases, the contragradience decreases and r_{ef} also decreases, leading to a smaller V_f^z. However, the value of R does not decrease linearly. In Table V a measure of the radial extent of the orbitals, $< \phi|r^2|\phi >^{1/2}$ (the square root of the sum of the second moments for an orbital), is tabulated for the valence atomic orbitals of the alkali metals and hydrogen atom. There is a larger difference between Na and K (2.443Å for Na as compared to 2.978Å for K) than for any other neighboring pair of alkali

atoms. This leads to a relatively longer r_{ef} (see Table IV) for KH, which should stabilize the potential energy comparatively more than for RbH.

The potential energy can be broken down into pieces involving only the electrons (V^{ee}), only the nuclei (V^{nn}), and both the electrons and the nuclei(V^{en}). The electronic repulsion of the two electrons in the bond pair, V^{ee}_{bf}, is shown in Fig. 14a. The repulsion decreases with atomic size owing to both the increasing distances between electrons and the contragradience decrease; i.e., the less attractive T^z_f is, the less repulsive V^z_f is. The repulsion is greatest for LiH, the system with the highest overlap, and least for CsH, the system with the least overlap. Note that the two-electron repulsion energy actually decreases at small R. The interpenetration of the orbitals, as discussed above for H_2, causes this to happen and leads to a dip in the V^z_f component of the exchange energy. The electron-nuclear attraction for the bonding electrons, V^{en}_{bf}, and the nuclear-nuclear repulsion are plotted in Fig. 14b. By virtue of the differences in nuclear charge, the absolute magnitudes of these quantities are not directly comparable from one system to the next. But the ratio of the two can be compared. At r_{ef}, the difference between V^{en}_{bf} and V^{nn} is essentially the same for all the alkali metal-hydrogen bonds. Hence, the trend in V^{ee} dominates and is the reason that the proportion of potential energy to kinetic energy decreases slightly, as noted above, with increasing atomic size.

Based upon analysis of the terms leading to bonding in the H_2 wavefunction, it has been shown[29] that the binding energy for a two-electron bond is proportional to

$$\frac{S^2}{R},\qquad(4)$$

where S is the overlap between the two GVB bonding orbitals (one-electron orbitals). From this has come the general assumption that the bond energy in

- 184-

all systems is proportional to the square of the overlap, given the same type of orbital character. Starting with the overlap at r_{ef} (S_{MH}) for each of the alkali species (Table V) and using the overlap (S_{H_2}) and binding energy (E_f^x) of H_2 as our base, a prediction can be made of the frozen bond energies in the the M−H systems (E_{MH}):

$$E_{MH} = \frac{S_{MH}}{S_{H_2}} E_{H_2}. \tag{5}$$

These bond energies are listed in Table V. All of the predicted E_{MH} values are too large compared to the actual energy. From Eq. 4 it is known that there also is a $\frac{1}{R}$ distance factor. The problem is that since the valence metal orbitals are of different principal quantum numbers, the choice of a value for R is unclear. What is needed is a scaled R value, R_s, that would reflect both the diffuseness of the orbital and the optimum bond length. This can be obtained by measuring the radial extent of the fragment orbitals (R_M and R_H) and comparing this to the final r_e. The R_s parameters for the alkali metal complexes are then given by

$$R_s^{MH} = \frac{r_e^{MH}}{(R_M + R_H)}. \tag{6}$$

The bond energy then becomes, based on H_2,

$$E_{MH} = \frac{R_s^{H_2}}{R_s^{MH}} \frac{S_{MH}}{S_{H_2}} E_{H_2}, \tag{7}$$

where

$$R_s^{H_2} = \frac{R_e^{H_2}}{(R_H + R_H)}. \tag{8}$$

The predicted bond energies in Table V are very close to the actual E_f^x for all the alkali-hydrogen bonds. Since R_s varies fairly linearly with increasing atomic number, it implies that the orbital shapes change little down the alkali column. If we base our bond energies on LiH instead of H_2, the agreement with the actual binding energies is even better. This is because H_2 has no core effects.

When the orbital shapes are allowed to relax (see Figs. 15a–e and Table VI for LiH through CsH), the changes that occur differ from those that occur in H_2. The potential energy and kinetic energy components have their maxima and minima pushed to longer R than for the frozen case. Compared to their frozen counterparts V^x decreases more rapidly and T^x increases very rapidly at small R. However, for the alkali metals, the potential energy maxima are more repulsive and the kinetic energy minima are more attractive for the relaxed wavefunctions than for the same descriptions of H_2. Since the alkali metals are considerably more electropositive than a hydrogen atom (0.7–1.0 for Cs-Li versus 2.1 for H using the Pauling scale of electronegativities), the relaxed wavefunction accounts for a large amount of charge transfer from metal to H. At long R, this results in an increase in potential energy (because of an increase in two electron repulsions); but at short R, the potential energy decreases rapidly because of the favorable coulombic interactions. Likewise, the pulling of charge off the metal to the H indirectly builds up electron density in the bonding region and decreases the kinetic energy at long R. This is illustrated by the amplitudes of the orbitals along a line connecting the nuclei at r_{ef} for Li–H through Cs–H, Figs. 16a–e. In general, there is an increase in electron density at the H nucleus and in the internuclear region with a concomitant decrease in density around the metal nuclei. Also, one can note that the largest increase and decrease in V^e and T^x occur for RbH probably because of a large core effect due to the introduction of filled d orbitals. The binding energy approximately doubles from the frozen wavefunction cases. This too is because of charge transfer.

In summary, the driving force for chemical bonding in the alkali molecules is the exchange kinetic energy, T^x. It is the only attractive part of the binding energy from long R to the equilibrium distance. Orthogonality and core effects

cause a sharp decrease in the potential energy and a sharp increase in the kinetic energy at small R, leading to the potential energy's being lower than the kinetic, but this is not a bonding effect. For the frozen orbitals, the binding energy tracks with the kinetic energy as atomic number increases; i.e., as the kinetic energy decreases down the column, the binding energy also decreases. In general, the potential energy, V_x, decreases with increasing bond length. However, it also dependent on the contragradience because the change in orbital shapes upon bonding indirectly increases electron density in the bonding region, which increases the two-electron repulsions. Since the atomic size does not necessarily increase linearly down the alkali group, it can change considerably from one member of the series to the next (as from KH to RbH). The frozen bond energies of H_2 and the entire series of alkali-hydrogen bonds are directly proportional to the square of the overlap at r_{ef} and are inversely proportional to a scaled internuclear separation. Since the principal quantum number of hydrogen atom and of the alkali metals increases down the column, a scaled bonding distance parameter can be obtained by using the sum of the radial extent, as measured by $< \phi | r^2 | \phi >^{1/2}$, of the fragment orbitals divided by the optimum bond length of the frozen molecule. Using H_2 as a base-binding energy, all the alkali metal-binding energies can then be related to each other through a proportionality relation. Relaxation effects occur as a result of bonding and cause the bonding orbitals to contract around their associated nuclei, lowering V^x and raising T^x.

The qualitative picture of binding between the alkali metals and hydrogen is an s—s bond which, since the principal quantum numbers are increasing down the column, becomes more and more diffuse as the atomic number of the alkali increases. This leads to higher kinetic energies with increasing size, because there is less contragradience; i.e., less smoothing of the orbital slopes, as the orbitals get

more diffuse. The potential energy decreases because both the contragradience is decreasing — V^{ee} is less because there is a smaller buildup of density in the bond region — and the distance between atoms is increasing. There is little or no hybridization involved and the orbital shapes are essentially the same for all the alkali cogeners. Hence, the increase (becoming less attractive) of T^x and the decrease (becoming less repulsive) of V^x occur at about the same rate leading to a lowering of the binding energy with increasing atomic size. As one goes to larger and larger principal quantum number there is less and less difference between the size of the valence orbitals (neglecting core effects), hence the binding energy decreases at a smaller rate from one alkali-hydrogen molecule to the next as size increases.

3.3 Ti, Zr, Hf, and Th Bonds with Hydrogen

The Group IVB transition metals Ti, Zr, and Hf, and the actinide Th all have the same valence electronic configuration, s^2d^2. Four bonds can be made with ligands. One of the simplest complexes that can be formed is L_2MH_2, where L is usually a cyclopentadienyl (Cp) or pentamethylcyclopentadienyl (Cp*) group.[31] By modeling the L group with a Cl ligand (see Part I, section 3.2), we have examined the M−H bonding in this sequence of molecules.

Experimental determinations of transition metal bond energies are very rare. Recently, the bond strengths of several thorium-ligand bonds have been measured by Tobin Marks and co-workers[32] using titration calorimetry. Their studies found that a Th−H bond is approximately 90 ± 10 kcal/mol strong in the gas phase. No experimental bond energies are available for Ti, Zr, or Hf bonds with hydrogen. Mean dissociation energies ($\bar{D}$) have been determined for M-CH$_2$CMe$_3$ in [MR$_4$], M = Ti, Zr, and Hf.[33] $\bar{D}_{Ti} = 44.9$, $\bar{D}_{Zr} = 54.3$, and $\bar{D}_{Hf} = 58.3$ (all in kcal

mol^{-1}. Thus this study will be able to add much to our knowledge about the differences in bonding from 1st to 2nd to 3rd row transition metals and from those to actinides.

The kinetic and potential energy components and the total binding energy from the frozen orbital wavefunction are plotted with respect to M$-$H distance for Ti, Zr, Hf, and Th in Figs. 17a–d, and each (T_f^z, V_f^z, and E_f^z) is plotted separately in Figs. 18a–c. A summary of the characteristics of T_f^z, V_f^z, and E_f^z are presented in Table VII. In contrast to the alkali-hydrogen compounds, the binding energy *increases* with increasing atomic number. The Ti complex is only slightly bound, 3.64 kcal/mol, with respect to Cl_2TiH and H atom. The Hf and Th systems have nearly the same E_f^z, 53.78 and 55.60 kcal/mol, respectively. Cl_2ZrH_2 is in between at 38.59 kcal/mol. This trend in bond energy occurs from long R to about 2.10Å where the E_f^z of Th$-$H crosses the Hf$-$H curve.

A glance at the figures shows that the trends in the component kinetic and potential energies are not as easy to characterize as they were for the alkali metals. At very long R (R > 4.00Å) T_f^z decreases (more attractive) from Ti to Th and V_f^z increases (more repulsive) from Ti to Th. At very large internuclear separation H atom encounters only the tail of the metal orbital's wavefunction, which will have the same slope for all the metals. Thus the contragradience should be greatest for the most diffuse orbital and least for the tightest orbitals and the potential energy should increase in response to the contragradience effect.

As R becomes smaller than four angstroms the H atom leaves the tail of the wavefunctions of Zr, Hf, and Th and both the potential and kinetic energy curves crossover each other. Ti has such tight orbitals that the crossover point does not occur until R is much smaller. Comparing the points at which T_f^z is at a minimum and V_f^z is at a maximum for all molecules, shows that there is a

trend of decreasing kinetic energy and increasing potential energy from Zr to Hf to Th. For Ti, the minimum T_f^z and maximum V_f^z are at values between Zr and Hf with the potential energy maximum being much closer in magnitude to the Zr V_f^z curve and kinetic energy minimum being closer in magnitude to the Hf T_f^z curve. Consequently, the binding energy of Ti is extremely small.

Considering only Zr, Hf, and Th, the trends in T_f^z and V_f^z are the same as that found for the alkali-hydrogen bonds. Yet the binding energy trend is just the opposite from the alkali metals. Since it is $T_f^z + V_f^z$ that make up E_f^z, this means that in order for the binding energy to increase with atomic size the value of V_f^z must become smaller with respect to kinetic energy from Zr to Th. Why does this occur?

The contragradience and hence, T_f^z, become smaller in magnitude (less attractive) with increasing size for the same reasons that it occured in the alkali metals. As the size of the metal atom increases, the orbitals get progressively more diffuse. As a result, the slopes of the orbitals become flatter and hence, less contragradience occurs upon overlap with the H atom 1s orbital.

Generally, the potential energy tracks opposite to the kinetic energy as the more contragradience the greater the buildup of electron density in the bonding region, which increases the electron-electron repulsion. For the alkali metals, V_{bf}^{ee} was larger for the bonds where there was more contragradience, i.e., LiH had the largest two electron repulsion energy and CsH had the smallest. While V_f^{en} was slightly lower than V^{nn} at r_{ef} for LiH through CsH. These effects lead to larger potential energies for the molecules with larger contragradience effects. On the other hand, for the transition metals and thorium, the two electron repulsion (see Fig. 19a) is greatest for the system with the least kinetic energy lowering, Cl_2ThH_2, and least for the complex with the most exchange kinetic

energy lowering. However, it is proportional to the overlap of the GVB orbitals. Even at fairly long R, 3.00Å, T_f^z of Zr is more negative than T_f^z of Th, and V_f^z of Zr is more repulsive than that of Th. Since the two-electron repulsion is greater for the Th complex at all distances, this indicates that the electron-nuclear attraction decrease with distance and the nuclear repulsion increase with distance must be less repulsive for Th versus Zr (and similarly for Hf versus Zr). That is,

$$\frac{|V_{Zr}^{nn}|}{V_{Zr}^{en}} \; > \; \frac{|V_{Th}^{nn}|}{V_{Th}^{en}}. \tag{9}$$

Fig. 19b illustrates this graphically. The nuclear repulsion increases at a faster rate for Cl_2ZrH_2 than the electron-nuclear attraction decreases. But for the Th analog, V^{ee} decreases at a faster rate than the nuclear repulsion increases. This more than makes up for the difference in V^{ee}.

The larger question is what in the bonding causes these effects to happen? This question can be answered by examining the orbital shapes (Fig. 20a-d). In Fig. 20b and Fig. 20d the amplitudes along the internuclear Zr−H and Th−H axes at their respective r_{ef}'s are plotted. The Zr−H bond looks like the "classic" contragradience effect. However, in the Th−H case the overlapping Th orbital (primarily 6d) is almost entirely under the H 1s orbital. The region of contragradience is small; hence, compared to Zr−H the kinetic energy is lowered less. The overlap is much higher for Th−H also because of this effect, leading to larger two electron repulsion. However, since the Th orbital has considerable density at the H's nucleus, the potential energy is much lower compared to the Zr case. Hence, the potential energy increases much more slowly with respect to the kinetic energy lowering for Th−H than for Zr−H. This leads to a stronger net binding energy for Th. The same effects hold true for Hf versus Zr. A comparison of the amplitude plots of the alkali metal-hydrogen bonds versus the transition

metals reveals that the greatest match (i.e., the best overlap) with the H atom

orbital is for Li and decreases down the column to Cs, while for the transition

metals the trend is just the opposite with Th having the best overlap with the

H atom and Ti the worst.

The first-row transition metal Ti has the tightest orbitals of all the Group

IVB metals. This occurs not only because of a lower principal quantum number

(3d) but also because the 1st row transition metals have no orthogonality con-

straints. The 3d orbitals are the first orbitals with angular momentum of L =

2; consequently, there is nothing to which they must orthogonalize. This results

in a much smaller radial extent for Ti's orbitals than for Zr's. In Table VIII,

the $< \phi | r^2 | \phi >^{1/2}$ radii indicate that the Ti 3d orbital's extent, 0.946Å, is only

slightly bigger than the H atom's 1s orbital, 0.917 Å! We might have expected, by

analogy with the alkalies, that Ti would have the greatest exchange kinetic en-

ergy lowering. In general, the tighter the orbital, the better the contragradience.

However, for Ti the orbital is so contracted that the minimum binding energy

occurs at a distance well before the kinetic energy minimum, while the potential

energy is still increasing. The potential energy increases rapidly because it is

inversely proportional to the distance between the nuclei and electrons. Thus,

the H atom is not able to approach close enough to Ti to obtain the maximal

benefits of contragradience before potential energy effects become dominating.

Hf is unique in some respects. Since it is a third-row element, it has a shell of

4f electrons (the first filled f orbitals) below the valence orbitals. The f electrons

are in very contracted orbitals. Since the valence electrons are well shielded from

the nucleus, the Hf bonding orbital is slightly larger ($\sim$0.15Å) than Zr's. But

because of the shielding by the f electrons, an incoming atom can approach the Hf

at a closer distance than it can for a Zr atom. (This is often termed the lanthanide

contraction because the f orbitals are filled during the lanthanide row.) However, the r_{ef}'s are essentialy identical. Thus Hf has a much better overlap with the H 1s orbital than Zr does, and Hf also has a much higher probability of lessening the potential energy with repect to the kinetic energy, since it is relatively closer to the H nucleus than is Zr.

As with the alkali metals, we can establish a proportionality relationship among bond energy, overlap, and distance for all four members of this series of metal-hydrogen bonds. Using the orbital radii and the overlap data in Table VIII, we have predicted the bond energies of Ti, Hf, and Zr from the bond energy of Th(see Table VIII). The E_f^z data obtained using just the square of the overlap are better than that with the scaled R parameter based on orbital radii for Zr and Hf, but not for Ti. Basing our bond energies on Hf, R_s gives a better fit than overlap alone. The Th—H bond energy is not fit well by the Hf-based series presumably because of hybridization differencs between Hf and Th.

What if the orbitals are allowed to relax? There are different answers to this question, depending on which metal is involved in the bond. Ti has essentially no bonding when the frozen orbitals are brought together. The repulsion of the potential energy term dominates. Once we let the orbital shapes change (see Fig. 20), the bonding orbital of Ti is modified to *decrease* the kinetic energy substantially while increasing the potential energy. The relaxed binding energy (diabatic) is 30.5 kcal/mol, whereas the frozen was only 3.6 kcal/mol (see Table IX). Hence, kinetic energy is the dominant force for bonding. For Hf and Zr, the relaxation effects are much smaller. From Table IX, the relaxed diabatic bond energies are 57.4 and 70.9 kcal/mol for Zr and Hf, but the frozen binding energies are 38.6 and 53.8 kcal/mol, respectively (ca. $\frac{2}{3}$ to $\frac{3}{4}$ of the relaxed values). There is a contraction of electron density around the nuclei, which

decreases the potential energy and increases the kinetic energy, resulting in a lowering of the binding energy. For Th, the relaxation effects are also small, but as in the alkali metals charge transfer plays a role leading to more contragradience in the bonding region and more electron density at the H nucleus, but the net effect at r_e is to increase the kinetic energy and to decrease the potenital energy.

The difference, then, between the transition metal cases and the alkali metals is the shape of the orbital that bonds to the H. The transition metals and thorium have an orbital that is mostly d in character to bind to the H 1s orbital. Since the d orbital has a directed shape as opposed to the spherical s valence orbitals of the alkalis', it can have a much better overlap with the H 1s orbital. This overlap actually improves as the d orbital gets more diffuse, since the d orbital can practically sit underneath the H atom. This effect decreases the potential energy relative to the contragradience lowering. Hence, the binding energy is lower for the atoms with larger atomic numbers. Hybridization can also help out the transition metals and thorium. The s and d orbitals in these systems are practically the same energy (and they become energetically more equivalent down the column,) and so they can mix in very strongly, giving even more directed bonds. The alkali metal atoms cannot do this.

The cause of bonding is the lowering in the exchange kinetic energy because of contragradience. The potential energy is purely repulsive except at small R, where effects of bonding and orthogonality can lead to attraction. The effect of the exchange potential energy is to oppose bonding as was seen in Cl_2TiH_2. However, the total binding energy is composed of both T^x and V^x. If the repulsion energy increases at a slower rate than the attractive kinetic energy, there will be a larger binding energy. This can occur for cases where there are diffuse orbitals that can make a good overlap with the ligand orbital. Thus, even though

the contragradience effects are not large, a strong bond can result if the repulsive potential energy effects are minimized.

If directed, diffuse orbitals can be better at bonding than tighter orbitals, why don't the bond strengths of p-bonds involving main group elements and hydrogen increase down the column? If we consider Group IVA, the bond strengths decrease down the column (see Table X) except from SiH to GeH ($^2\Pi$ state). Bonds using p orbitals are more directed than s bonds but apparently are still not directed enough. Also, hybridization occurs readily for the first-row atoms (like N) but less so down the column because of the widening energetic gap between the s and p orbitals. The opposite trend occurs for the transition metals. The increase in bond energy from SiH to GeH may well be due to the contraction effect of the d core orbitals; i.e., as in the Hf$-$H case above, the bond distance is much shorter for GeH than it should be because of the presence of very tight core orbtials. Thus, for the GeH case the "directed" nature of the p orbital does come into play because of the short internuclear separation. We would predict that the snap bond energies for the $^4\Sigma$ state would decrease from SiH to GeH since this state involves s bonding only. Hence, the unique shape of the d orbital and the unique hybridization characteristics of the transition metal and actinide elements allow for a reversal of the trends in bond energies from the main group elements, resulting in very different chemistry!

4. Summary

The process of bond formation can best be examined using a frozen wavefunction approach (orbital shapes are kept constant). The relaxed wavefunctions have too much information, which can make it very difficult to deconvolute the different bonding effects and thus can mask the true *cause* of bonding. For H_2^+, H_2, and all of the metal-hyrdogen bonds examined, the decrease in exchange kinetic energy, T^x, that is due to the contragradience of the bonding orbitals, is the only force responsible for chemical bonding. The exchange potential energy, V^x, is repulsive and thus opposes bond formation.

Even with our frozen wavefunctions, there are still some bonding effects that must be explained. At small internuclear separation, the potential energy does decrease and becomes attractive with respect to the separated fragments at infinity. This is caused by two effects: 1) orthogonalization to the core orbitals, 2) a delocalization of the orbital on one nucleus to buildup character on the other nucleus. The first consideration is easily separated out by examining just the interaction of the core electrons with the incoming bonding orbital. *The second effect is caused by bonding but is not in itself a cause of bonding.* Relaxation also decreases the potential energy while increasing the kinetic energy, but this too is a cause of bonding.

Since T^x plus V^x make up the total binding energy of the bond, not only are the magnitudes of these quantities important but also the relative ratio of one to the other. For the alkali metal-hydrogen bonds, the magnitude of T^x tracks with the binding energy as atomic size is increased. The proportion of V^x to T^x stays essentially constant. This leads to bond energies decreasing from Li to Cs. For the transition metal- and thorium-hydrogen bonds, the magnitude of T^x is

inversely related to the binding energy (for Zr, Hf, and Th). This occurs because the ratio of V^x to T^x is decreasing with increasing atomic size.

The qualitative difference between the alkali metals and the transition metals (including Th) is that the former just have s orbitals to bond with while the latter use hybridized d orbitals. Thus, the directed nature of the metal d orbitals enables them to decrease the repulsive interactions of potential energy with respect to the decrease in exchange kinetic energy that is due to contragradience. Even though the absolute magnitude of T^x for Zr is greater than that of Th, this lessening of the potential energy enables the Th—H bond to be stronger than the Zr—H bond. The alkali metals' bonding orbitals become more diffuse down the column with no directionality and do not have this effect.

The one quantity that tracks with bond energy within each series of molecules is the overlap of the GVB pairs. A scaled distance parameter can be obtained from the sum of the radii of the bonding orbitals at infinite internuclear separation divided by the final equilibrium distance. The binding energy (within each set of molecules) is then found to be proportional to the square of the overlap and inversely proportional to the scaled distance.

References

(1) L. Pauling, *The Nature of the Chemical Bond* (Cornell University Press, New York, 1960 [3rd Ed.]).

(2) *ibid.*, Proc. Nat. Acad. Sci. USA **14**, 359 (1928).

(3) *ibid.*, J. Am. Chem. Soc. **53**, 1367 (1931); *ibid.*, 3225 (1931).

(4) F. London, Z. Phys. **46**, 455 (1928).

(5) R. F. Bader, W. H. Henneker, and P. E. Cade, J. Chem. Phys. **46**, 3341 (1967).

(6) R. F. Bader and A. D. Bandrauk, J. Chem. Phys. **49**, 1653 (1968).

(7) P. R. Smith and J. W. Richardson, J. Phys. Chem. **71**, 924 (1967).

(8) R. F. Bader, I. Keaveny, and P. E. Cade, J. Chem. Phys. **47** (1967).

(9) R. F. Bader and A. D. Bandrauk, J. Chem. Phys. **49**, 1666 (1968).

(10 R. F. Bader and H. J. T. Preston, Int. J. Quant. Chem. **3**, 327 (1969).

(11) H. Hellman, Z. Phys. **85**, 180 (1973).

(12) K. Ruedenberg, Rev. Mod. Phys. **34**, 326 (1962).

(13) C. Edmiston and K. Ruedenberg, J. Phys. Chem. **68**, 1628 (1964).

(14) E. Layton and K. Ruedenberg, J. Phys. Chem. **68**, 1654 (1964).

(15) R. R. Rue and K. Ruedenberg, J. Phys. Chem. **68**, 1676 (1964).

(16) See for example, J. H. Van Vleck and A. Sherman, Rev. Mod. Phys. **7**, 167 (1935).

(17) C. W. Wilson and W. A. Goddard III, Theor. Chim. Acta (Berl.) **26**, 195-210 (1972); *ibid.* 211-230 (1972); *ibid.*, Chem. Phys. Lett. **5**, 45-49 (1970).

(18) W. J. Moore, *Physical Chemistry* (Prentice-Hall, Englewood Cliffs, NJ, 1972 [4th Ed.]), p. 670 ff; F. Daniels and R. A. Alberty, *Physical Chemistry* (John Wiley & Sons, New York, 1975 [4th Ed.]), p. 455 ff.

(19) P. W. Atkins, *Physical Chemistry* (W. H. Freeman, San Francisco, 1978), p. 448 ff; K. J. Laidler and J. H. Meiser, *Physical Chemistry* (Benjamin/Cummings, Menlo Park, CA, 1982), p. 514 ff.

(20) a) W. R. Wadt, J. Am. Chem. Soc. **103**, 6053-6057 (1981); b) P. J. Hay and W. R. Wadt, J. Chem. Phys. **82**, 299-310 (1985).

(21) A. K. Rappé and W. A. Goddard III, unpublished results.

(22) A. K. Rappé, T. A. Smedley, and W. A. Goddard III, J. Phys. Chem. **85**, 2607 (1981).

(23) M. J. Brusich and W. A. Goddard III, unpublished results.

(24) S. Huzinaga, J. Chem. Phys **42**, 1293 (1965).

(25) R. A. Bair and W. A. Goddard III, unpublished results.

(26) a) A. K. Rappé, T. A. Smedley, and W. A. Goddard III, J. Phys. Chem. **85**, 1662 (1981); b) A. K. Rappé and W. A. Goddard III, unpublished results.

(27) W. A. Goddard III, T. H. Dunning, W. J. Hunt, and P. J. Hay, Accts. Chem. Res. **6**, 368 (1973); W. A. Goddard III and L. B. Harding, Ann. Rev. Phys. Chem. **29**, 363 (1978).

(28) See, for example, G. Arfkin, *Mathematical Methods for Physicists* (Academic Press, New York, 1970 [2nd Ed.]), pp. 437-441.

(29) See, for example, W. A. Goddard III, *The Nature of the Chemical Bond* (California Institue of Technology, Pasadena, CA, 1983), p. 53 ff.

(30) K. P. Huber and G. Herzberg, *Molecular Spectra and Molecular Structure, IV. Constants of Diatomic Molecules* (Van Nostrand Reinhold, New York, 1979).

(31) Polymeric forms with bridging M−H bonds are formed for M = Zr and Hf. For L_2TiH_2 see, J. E. Bercaw and H. H. Brintzinger, J. Am. Chem. Soc. **93**, 2045 (1971); and J. E. Bercaw, R. H. Marvich, L. G. Bell, and H. H.

Brintzinger, J. Am. Chem. Soc. **94**, 1219 (1972). For L_2ZrH_2, see B. D. James, R. K. Nanda, and M. G. H. Wallbridge, Chem. Commun. p. 849 (1966); and P. C. Wailes and H. Weigold, J. Organomet. Chem. **24**, 405 (1970). For L_2HfH_2 see, S. Couturier, G. Tainturier, B. Gautheron, J. Organomet. Chem. **157**, C61 (1978). For L_2ThH_2 see, J. M. Manriquez, P. J. Fagan, T. J. Marks, J. Am. Chem. Soc. **100**, 3939-3941 (1978).

(32) J. W. Bruno, T. J. Marks, and L. R. Morss, J. Am. Chem. Soc. **105**, 6824-6832 (1983); D. C. Sonnenberger, L. R. Morss, and T. J. Marks, Organometallics 4, 352-355 (1985).

(33) M. F. Lappert, D. S. Patil, and J. B. Pedley, J. Chem. Soc. Chem. Commun. 836 (1975).

Table I. A Summary of the Global Minima of Kinetic Energy (T_f^x) and Binding Energy (E_f^x), and the Local Maxima and Minima of Potential Energy (V_f^x) for the Frozen GVB Wavefunctions of H_2^+ and H_2.

	H_2^+			H_2		
	T_f^x	V_f^x	E_f^x	T_f^x	V_f^x	E_f^x
min. R[b]	1.27	—	1.32	1.07	0.77	0.88
min. E[c]	-0.1174	—	-0.0649	-0.1921	0.0585	-0.1186
max. R[b]	—	—	—	—	1.37	—
max. E[c]	—	—	—	—	0.1019	—

a) Minima and maxima are shown only for the range of distances displayed in the plots (Fig. 1 for H_2^+ and Fig. 2 for H_2). A dash indicates that there are no minima and/or maxima for that curve. In all cases, the values of the distances and energies were obtained from a cubic spline fit to all the data points. b) R is the internuclear separation in Å. c) E is the energy in hartrees at the given R.

Table II. A Summary of the Global Minima of Kinetic Energy (T^x) and Binding Energy (E^x), and the Global Maxima of Potential Energy (V^x) for the Relaxed GVB Wavefunctions of H_2^+ and H_2.

	H_2^+			H_2		
	T^x	V^x	E^x	T^x	V^x	E^x
min. R^b	2.24	—	1.06	1.48	—	0.76
min. E^c	-0.0572	—	-0.1016	-0.1176	—	-0.1508
max. R^b	—	2.65	—	—	1.69	—
max. E^c	—	0.0300	—	—	0.0685	—

a) Minima and maxima are shown only for the range of distances displayed in the plots (Fig. 6 for H_2^+ and Fig. 7 for H_2). A dash indicates that there are no minima and/or maxima for that curve. In all cases, the values of the distances and energies were obtained from a cubic spline fit to all the data points. b) R is the internuclear separation in Å. c) E is the energy in hartrees at the given R.

Table III. The Experimental Binding Energies (D_0^0) and Equilibrium Internuclear Separations (r_e) of H_2^+, H_2, and the Alkali Metal-Hydrogen Systems, M-H, M = Li, Na, K, Rb, Cs.[a]

Molecule	D_0^0 (kcal/mol)	r_e (Å)
H_2^+	61.1	1.052
H_2	103.3	0.741
LiH	56.0	1.596
NaH	43.4	1.887
KH	42.9	2.243
RbH	—	2.367
CsH	41.7	2.494

a) Ref. 30.

Table IV. A Summary of the Global Mimina of Kinetic Energy (T_f^z) and Binding Energy (E_f^z), and the Local Maxima of Potential Energy (V_f^z) for the Frozen Wavefunctions of the Alkali Hydrides (M-H).[a]

Molecule	T_f^z			V_f^z			E_f^z	
	E[b]	E_{n-1}/E_n[c]	R[d]	E	E_{n-1}/E_n	R	E	R
LiH	−0.0651	—	2.28	+0.0394	—	2.47	−0.0337	1.88
NaH	−0.0549	1.186	2.58	+0.0353	1.116	2.77	−0.0276	2.10
KH	−0.0404	1.359	3.13	+0.0270	1.307	3.25	−0.0185	2.59
RbH	−0.0388	1.041	3.40	+0.0278	0.971	3.52	−0.0159	2.79
CsH	−0.0317	1.224	3.32	+0.0199	1.397	3.47	−0.0131	3.06

a) Maxima and minima are shown only for the range of distances displayed in the plots (Figs. 10a–e and Figs. 11a–c). In all cases, the values of the distances and energies were obtained from a cubic spline fit to all the data points. b) E is the energy in hartrees at the given R. c) Ratio of the energy of the previous alkali-H to this alkali-H. d) R is the internuclear separation in Å.

Table V. The Radial Extent of the Bonding Orbitals, as Measured By $< \phi | r^2 | \phi >^{1/2}$, Their Overlap, and Projected Bond Strengths Based on Overlap and Distance for H_2 and the Alkali Hydrides.

Molecule	$R_M + R_H$ [a]	R_s^{MH} [b]	S^c	$E_f^z \propto (S^2)_{H_2}^d$	$E_f^z \propto (\frac{S^2}{R_s})_{H_2}^e$	$E_f^z \propto (S^2)_{LiH}^f$	$E_f^z \propto (\frac{S^2}{R_s})_{LiH}^g$	E_f^z
H_2	1.832	0.482	0.759	—	—	47.9	59.4	74.4
LiH	3.144	0.598	0.504	32.8	26.4	—	—	21.1
NaH	3.359	0.625	0.467	28.2	21.7	18.1	17.3	17.3
KH	3.894	0.666	0.388	19.4	14.1	12.5	11.2	11.6
RbH	4.142	0.673	0.360	16.7	12.0	10.8	9.6	10.0
CsH	4.386	0.698	0.329	14.0	9.7	9.0	7.7	8.2

a) $R_M + R_H$ is the sum of the radii of the high spin fragment orbitals of the alkali metal and H atom in Å. The radii are measured using the expectation value $< \phi | r^2 | \phi >^{1/2}$. b) $R_s^{MH} = \frac{r_{ef}}{R_M + R_H}$. $R_H = 0.916$Å. r_{ef} is the equilibrium distance for the frozen binding energy. c) S is the overlap of the two bonding orbitals at r_{ef}. d) The projected bond energies for the alkali metals determined using the ratio of the square of the overlaps in MH and H_2 (see Eq. 5). e) The projected bond energies for the alkali metals computed using the ratio of the square of the overlaps in MH and H_2 and the inverse ratio of the scaled R parameters, R_s, for MH and H_2 (see Eqs. 6–8). f) Similar to d, only using the overlap of LiH as the proportionality base. g) Similar to e, only using the overlap and R_s of LiH as the proportionality base.

Table VI. A Summary of the Global Mimina of Kinetic Energy (T_f^x) and Binding Energy (E_f^x), and the Global Maxima of Potential Energy (V_f^x) for the Relaxed Wavefunctions of the Alkali Hydrides (M-H).[a]

Molecule	T_f^x		V_f^x		E_f^x	
	E^b	R^c	E	R	E	R
LiH	−0.0769	2.77	+0.0520	2.97	−0.0682	1.65
NaH	−0.0750	2.94	+0.0510	3.11	−0.0532	1.96
KH	−0.0819	3.54	+0.0610	3.76	−0.0487	2.38
RbH	−0.1438	3.47	+0.1178	3.70	−0.0434	2.58
CsH	−0.0287	4.14	+0.0148	4.75	−0.0389	2.85

a) Maxima and minima are shown only for the range of distances displayed in the plots (Figs. 15a–e). In all cases, the values of the distances and energies were obtained from a cubic spline fit to all the data points. b) E is the energy in hartrees at the given R. c) R is the internuclear separation in Å.

Table VII. A Summary of the Global Mimina of Kinetic Energy (T_f^x) and Binding Energy (E_f^x), and the Local Maxima of Potential Energy (V_f^x) for the M-H Bond in Cl_2MH_2, M = Ti, Zr, Hf, and Th, Using Frozen Wavefunctions.[a]

Molecule	T_f^x			V_f^x			E_f^x	
	E^b	E_{n-1}^c/E_n	R^d	E	E_{n-1}/E_n	R	E	R
Cl_2HTi-H	−0.2600	—	1.55	+0.2824	—	1.40	−0.0058	2.00
Cl_2HZr-H	−0.3629	0.716	2.23	+0.3121	0.905	2.28	−0.0615	1.93
Cl_2HHf-H	−0.2168	1.673	2.30	+0.1517	2.057	2.44	−0.0857	1.93
Cl_2HTh-H	−0.1525	1.422	2.70	+0.0913	1.662	2.96	−0.0886	2.27

a) Maxima and minima are shown only for the range of distances displayed in the plots (Figs. 17a–d and Figs. 18a–c). In all cases, the values of the distances and energies were obtained from a cubic spline fit to all the data points. b) E is the energy in hartrees at the given R. c) Ratio of the energy of the previous M-H to the current one. d) R is the internuclear separation in Å.

Table VIII. The Radial Extent of the Bonding Orbitals, as Measured By $<\phi|r^2|\phi>^{1/2}$, Their Overlap, and Projected Bond Strengths Based on Overlap and Distance for the Cl_2MH_2, M = Ti, Zr, Hf, and Th, complexes.

Molecule	$R_M + R_H$ [a]	R_s^{MH} [b]	S [c]	$E_f^x \propto (S^2)_{Th-H}$ [d]	$E_f^x \propto (\frac{S^2}{R_s})_{Th-H}$ [e]	$E_f^x \propto (S^2)_{Hf-H}$ [d]	$E_f^x \propto (\frac{S^2}{R_s})_{Hf-H}$ [e]	E_f^x
Cl_2TiH_2	1.858	1.092	0.252	5.5	3.9	6.4	4.6	3.6
Cl_2ZrH_2	2.318	0.832	0.647	36.5	34.0	42.3	39.8	38.6
Cl_2HfH_2	2.468	0.784	0.730	46.5	45.9	—	—	53.8
Cl_2ThH_2	2.928	0.774	0.798	—	—	64.3	65.1	55.6

a) $R_M + R_H$ is the sum of the radii of the high spin fragment orbitals of Cl_2MH and H atom in Å. The radii are measured using the expectation value $<\phi|r^2|\phi>^{1/2}$. $R_H = 0.916$Å. b) $R_s^{MH} = \frac{r_{ef}}{R_M+R_H}$. r_{ef} is the equlibrium distance for the frozen binding energy. c) S is the overlap of the two bonding orbitals at r_{ef}. d) The projected bond energies for Cl_2HM-H determined using the ratio of the square of the overlaps in M-H and Th-H (see Eq. 5). e) The projected bond energies for Cl_2HM-H computed using the ratio of the square of the overlaps in MH and H_2 and the inverse ratio of the scaled R parameters, R_s, for M-H and Th-H (see Eqs. 6–8). f) Similar to d, only using the overlap of Hf-H as the proportionality base. g) Similar to e, only using the overlap and R_s of Hf-H as the proportionality base.

Table IX. Diabatic (Snap) and Adiabatic Bond Energies[a] of M-H Bonds from the relaxed GVB(2/4) wavefunctions of Cl_2MH_2, M = Ti, Zr, Hf, and Th, complexes; and E_f^z of M-H bonds from the Frozen Wavefunctions of These Systems.

Molecule	D_e^{diab}	D_e^{adiab}	E_f^z
Cl_2TiH_2	30.5	29.6	3.6
Cl_2ZrH_2	57.4	54.5	38.6
Cl_2HfH_2	70.9	67.0	53.8
Cl_2ThH_2	70.6	67.2	55.6

a) All energies in kcal/mol.

Table X. The Experimental Binding Energies (D_0^0) and Equilibrium Internuclear Separations (r_e) of the Group IVA-Hydrogen Molecules.[a]

Molecule	D_0^0 (kcal/mol)	r_e (Å)
CH	79.9	1.120
SiH	70.6[b]	1.520
GeH	76.1[b]	1.588
SnH	63.0[b]	1.781
PbH	36.7[b]	1.838

a) Ref. 30. *b*) For SiH through PbH the true values of D_0^0 are stated to be less than or equal to these values.

**Figure 1.** The exchange kinetic (T_f^x), potential (V_f^x), and total binding (E_f^x) energies for the frozen GVB wavefunction of H_2^+.
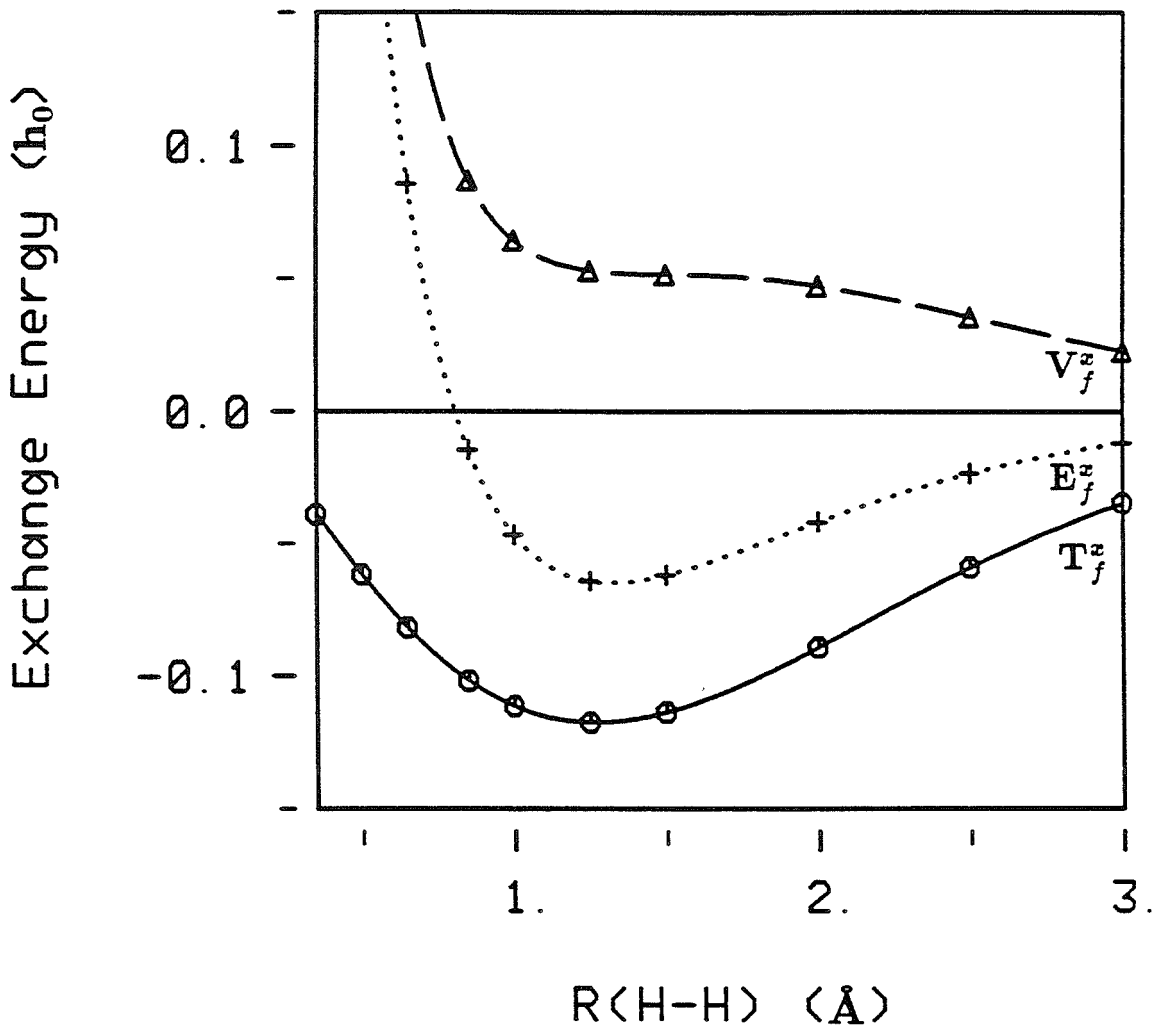
Figure 2. The exchange kinetic (T_f^x), potential (V_f^x), and total binding (E_f^x) energies for the frozen GVB wavefunction of H_2.
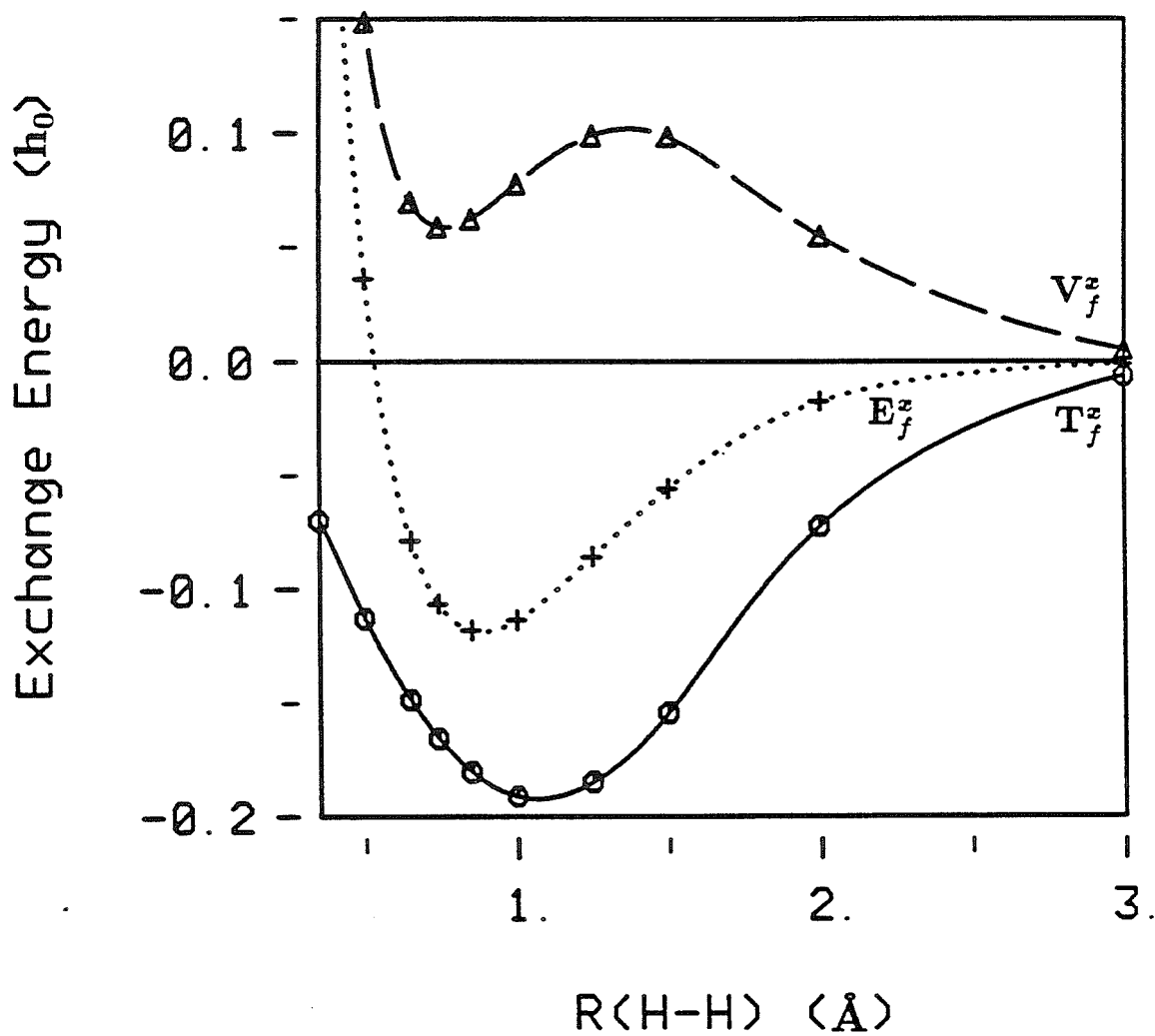
Figure 3. An illustration of contragradience. The over-
lapping solid lines are the amplitudes of the 1s orbitals of
two noninteracting H atoms, 0.88 Å apart, along a line con-
necting the nuclei. The dotted line is the resultant frozen
bonding orbital of H_2.
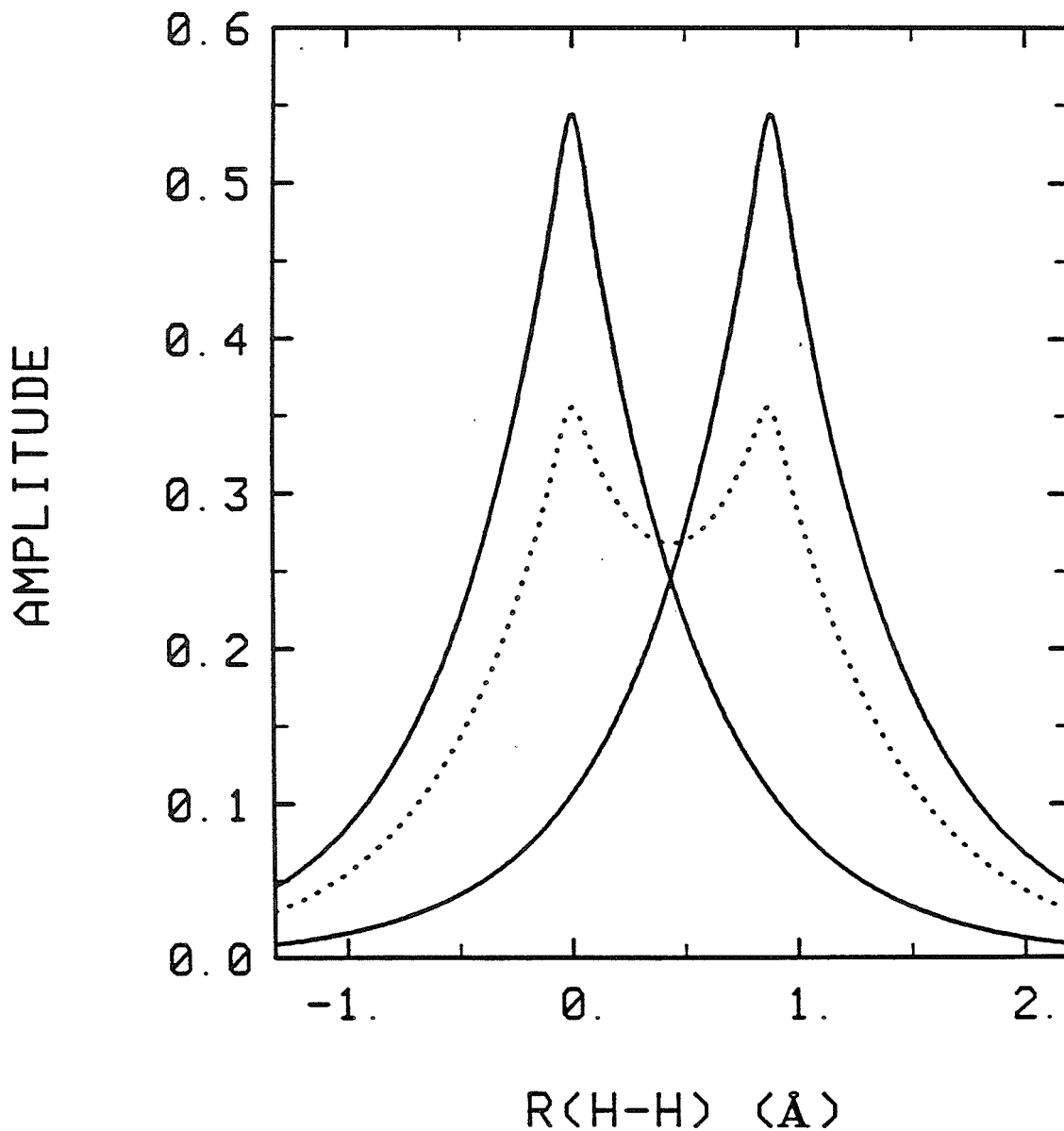
Figure 4. The exchange kinetic (T_f^x), potential (V_f^x), and total binding (E_f^x) energies for the frozen HF wavefunction of H_2.
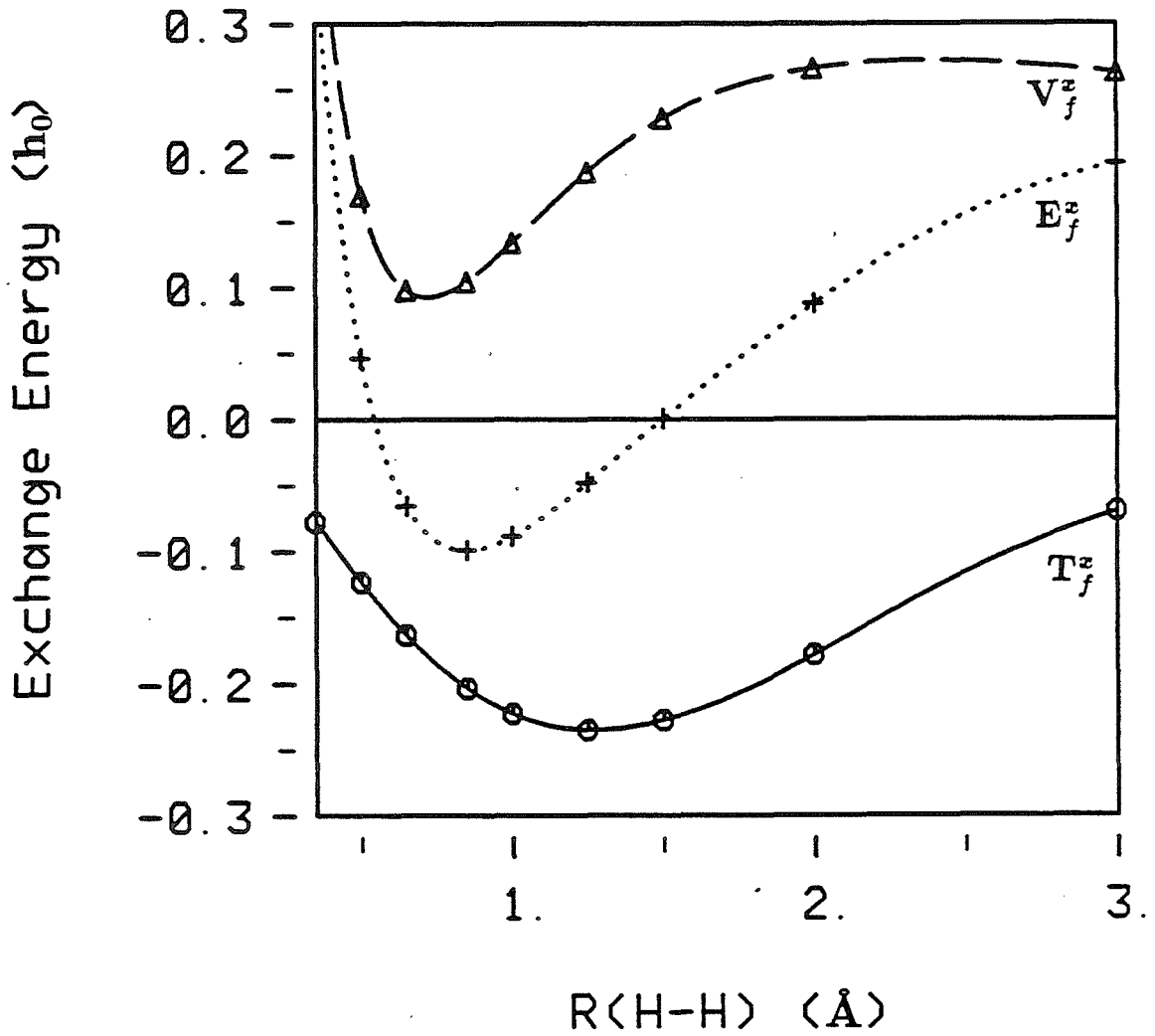
Figure 5. The overlap of the two GVB one-electron orbitals (bonding orbitals) versus internuclear separation, R, for H_2.
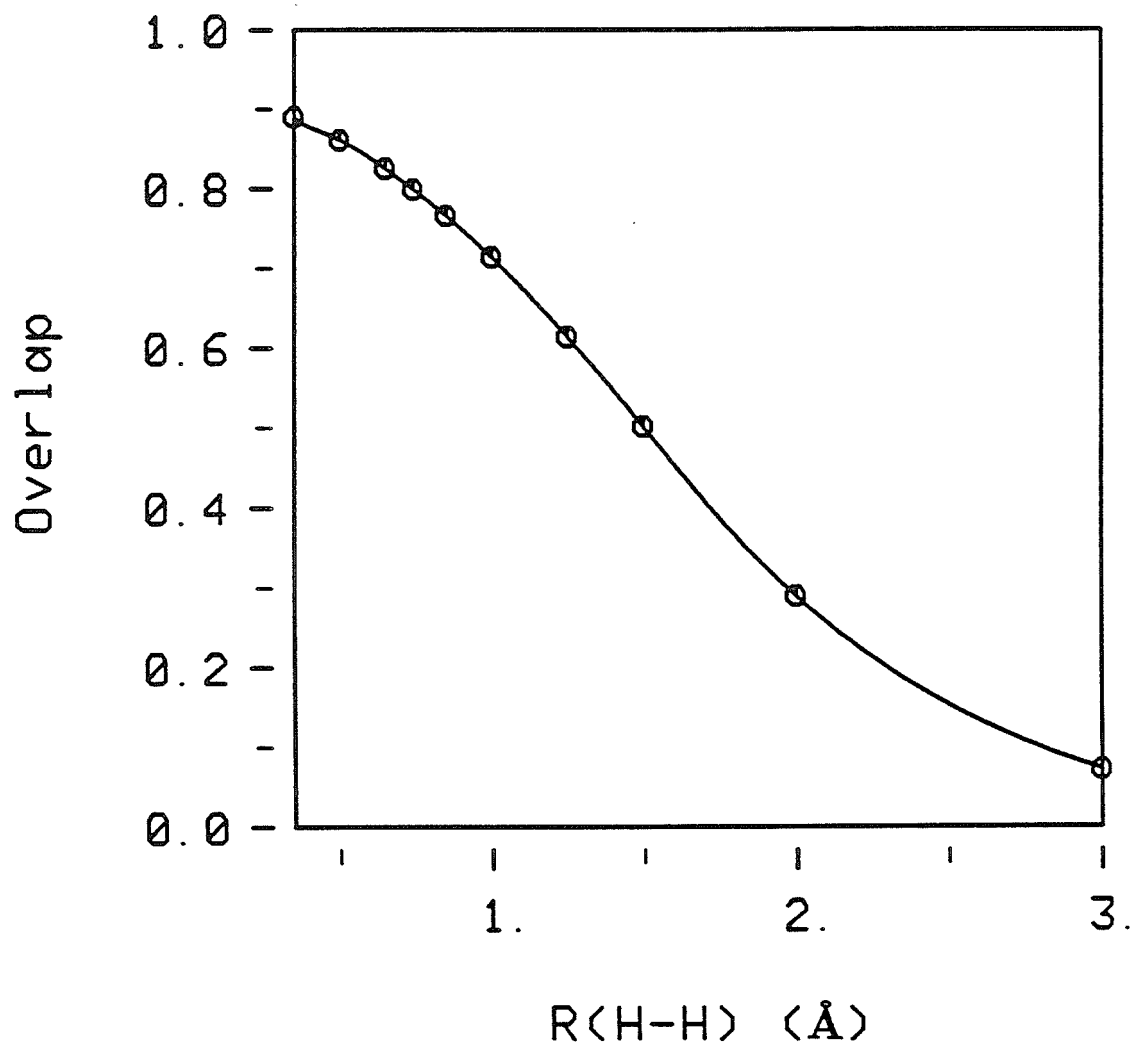
**Figure 6.** The exchange kinetic (T^z), potential (V^z), and total binding (E^z) energies for the relaxed GVB wavefunction of H_2^+.
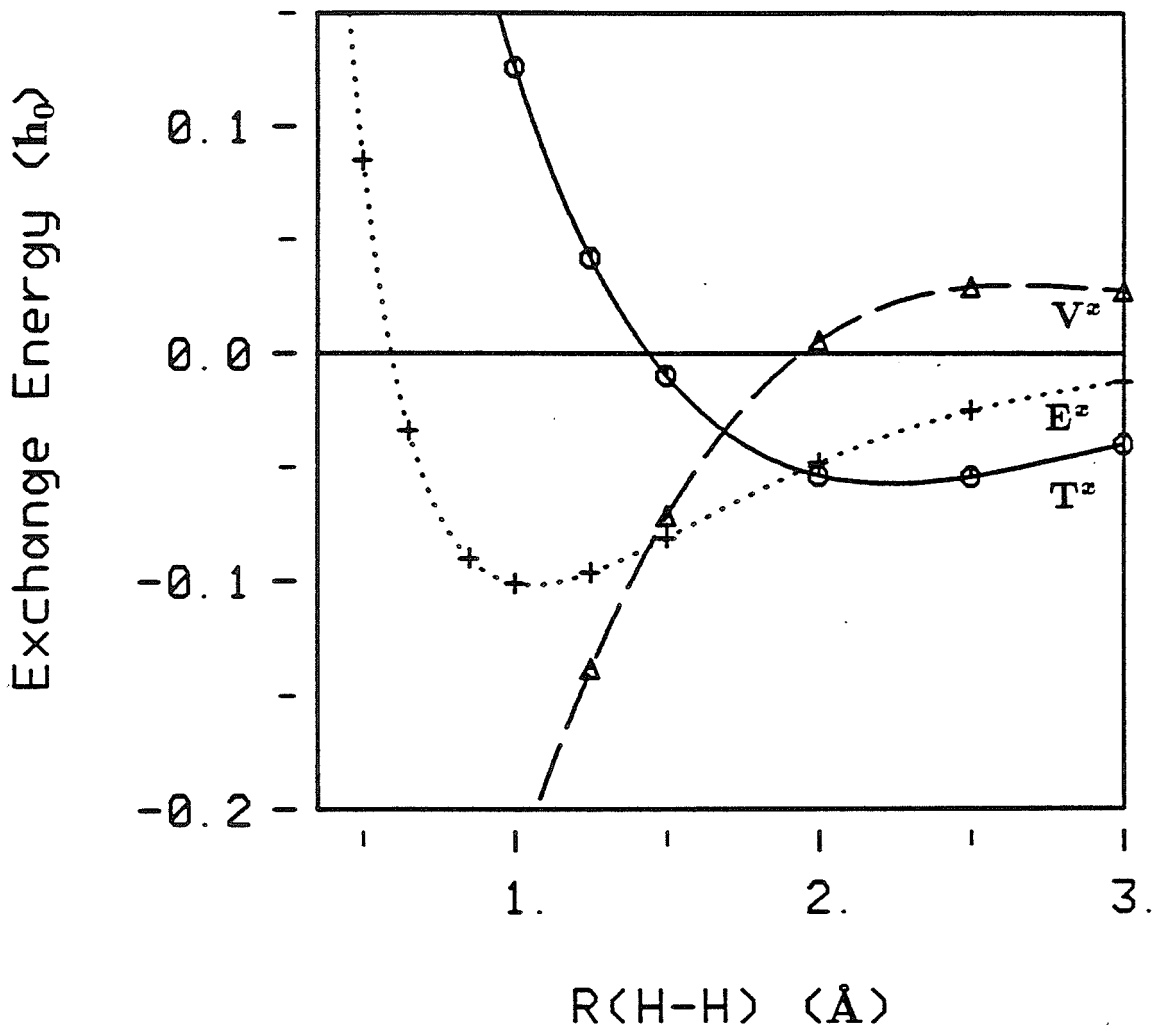
Figure 7. The exchange kinetic (T^x), potential (V^x), and total binding (E^x) energies for the relaxed GVB wavefunction of H_2.
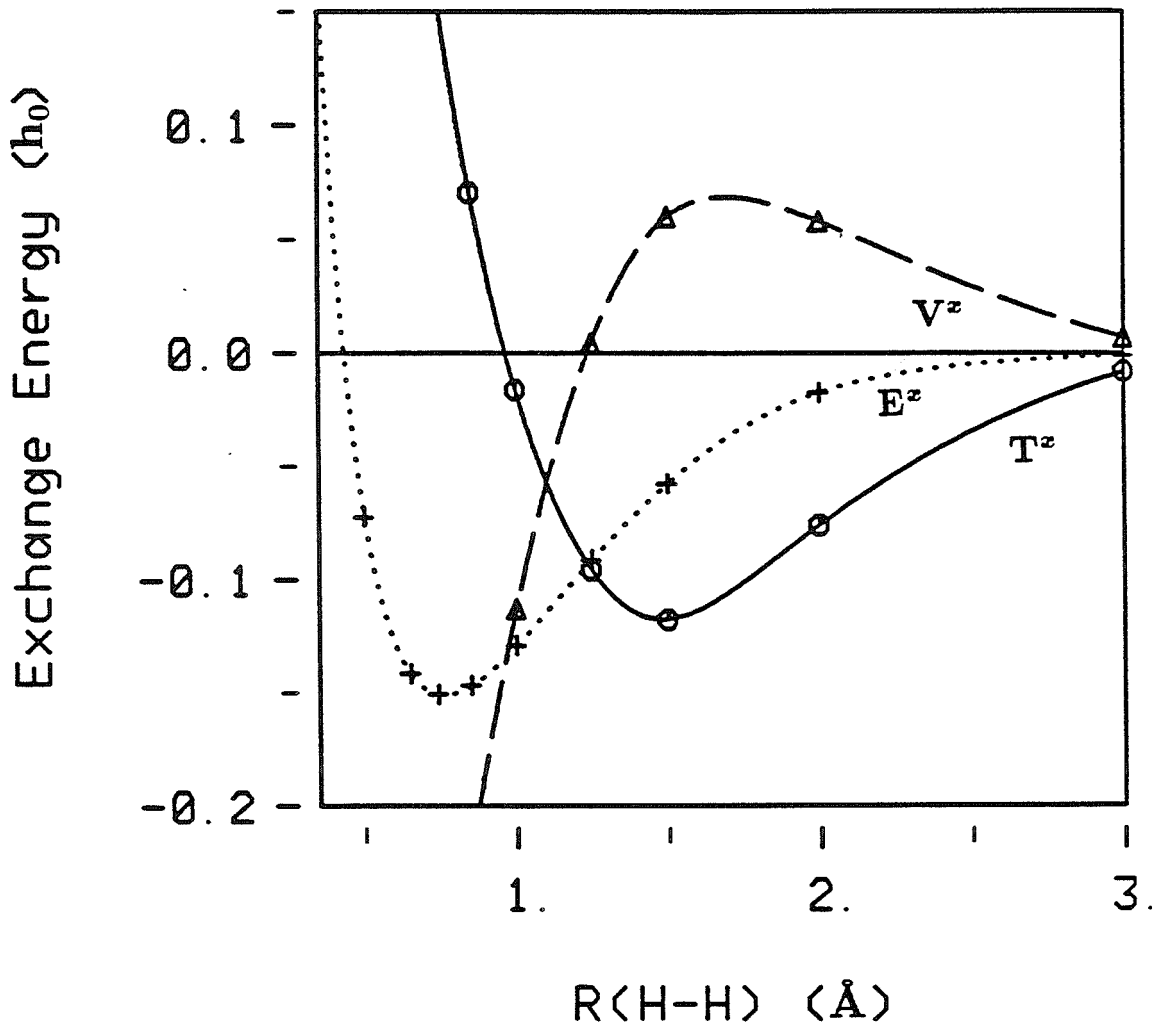
Figure 8. The amplitudes of the frozen (solid) and relaxed (dotted) bonding orbitals of H_2^+ plotted along a line connecting the two nuclei at r_{ef}.
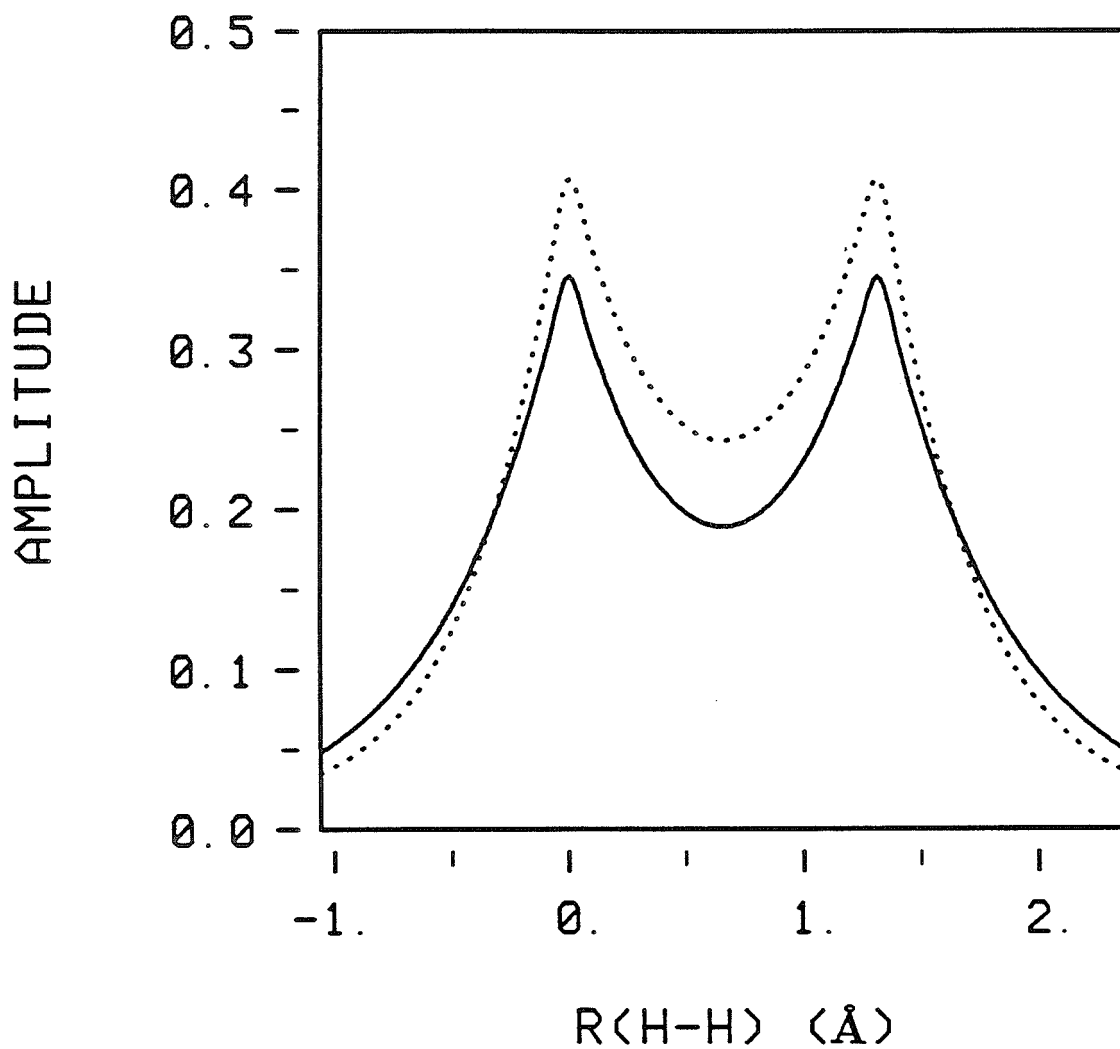
Figure 9. The amplitudes of the frozen (solid) and relaxed (dotted) bonding orbitals of H_2 plotted along a line connecting the two nuclei at r_{ef}.
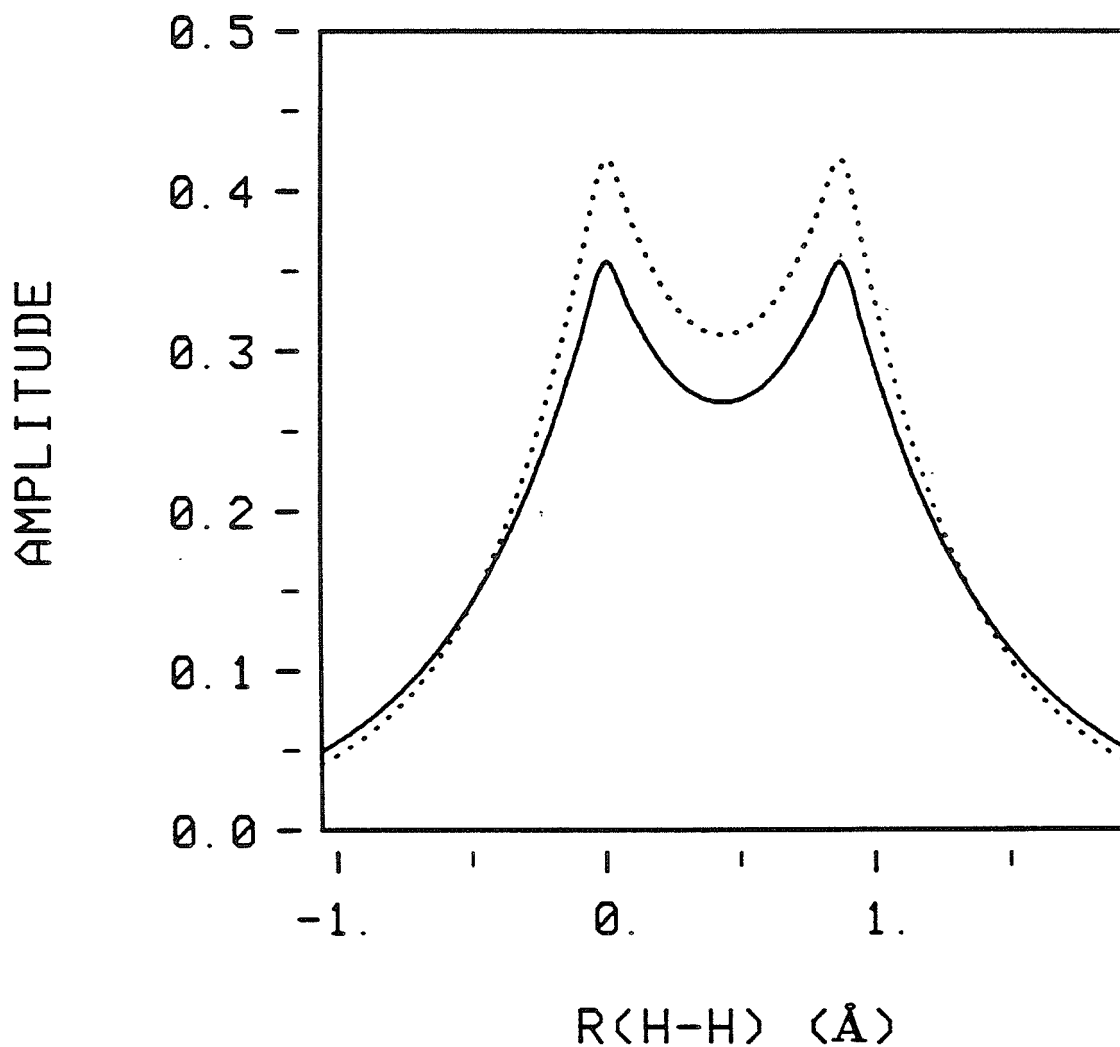
Figure 10a. The exchange kinetic (T_f^x), potential (V_f^x), and total binding (E_f^x) energies for the frozen GVB wavefunction of Li-H.
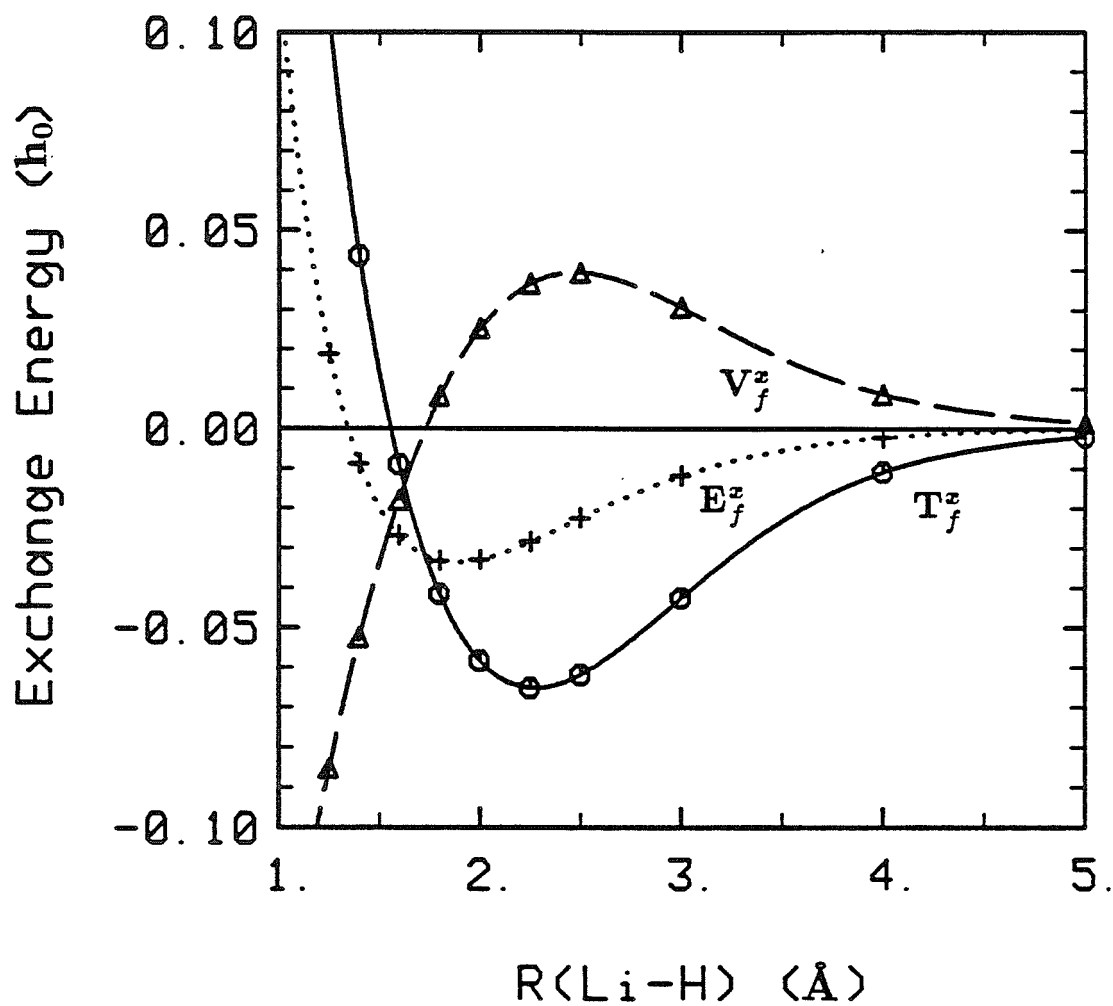
Figure 10b. The exchange kinetic (T_f^z), potential (V_f^z), and total binding (E_f^z) energies for the frozen GVB wave-function of Na-H.
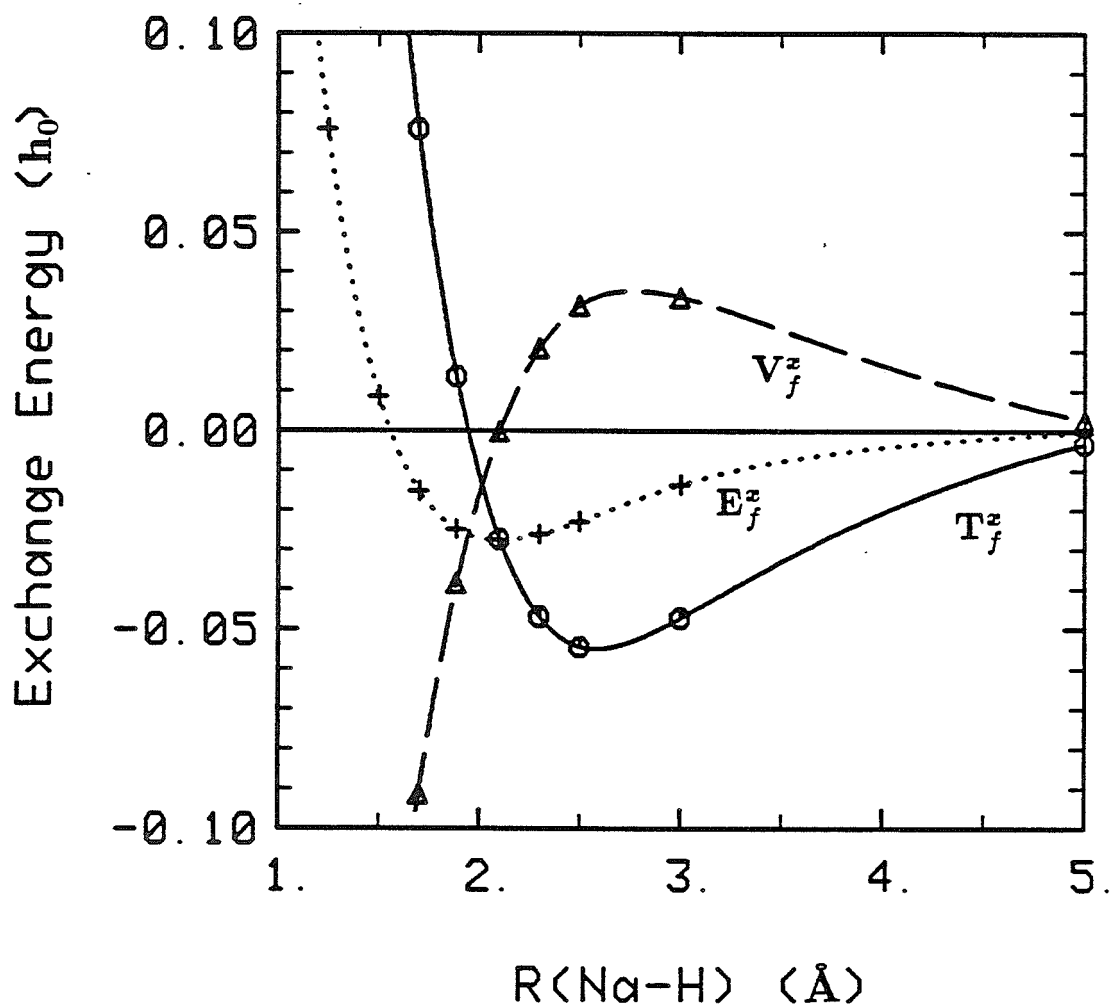
Figure 10c. The exchange kinetic (T_f^z), potential (V_f^z), and total binding (E_f^z) energies for the frozen GVB wavefunction of K-H.
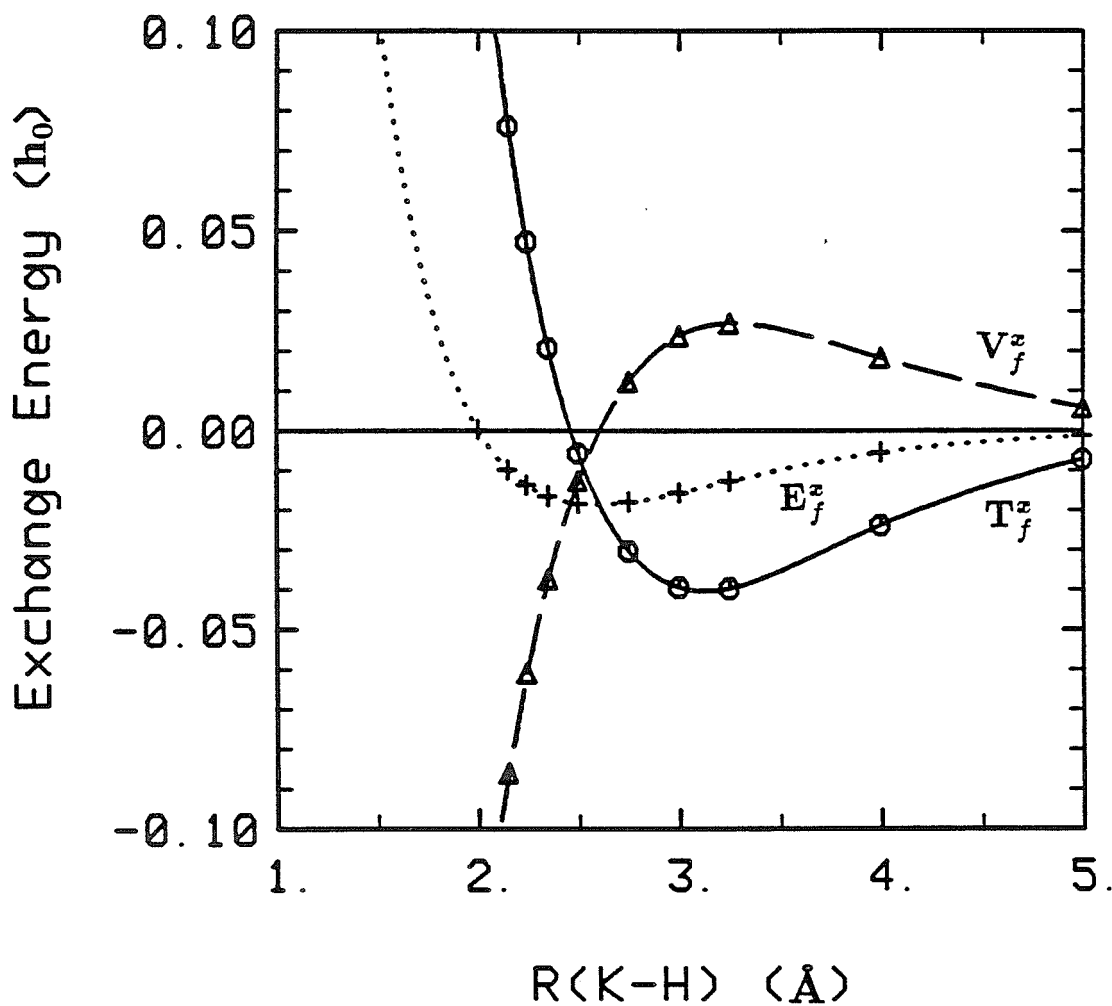
Figure 10d. The exchange kinetic (T_f^x), potential (V_f^x), and total binding (E_f^x) energies for the frozen GVB wave-function of Rb-H.
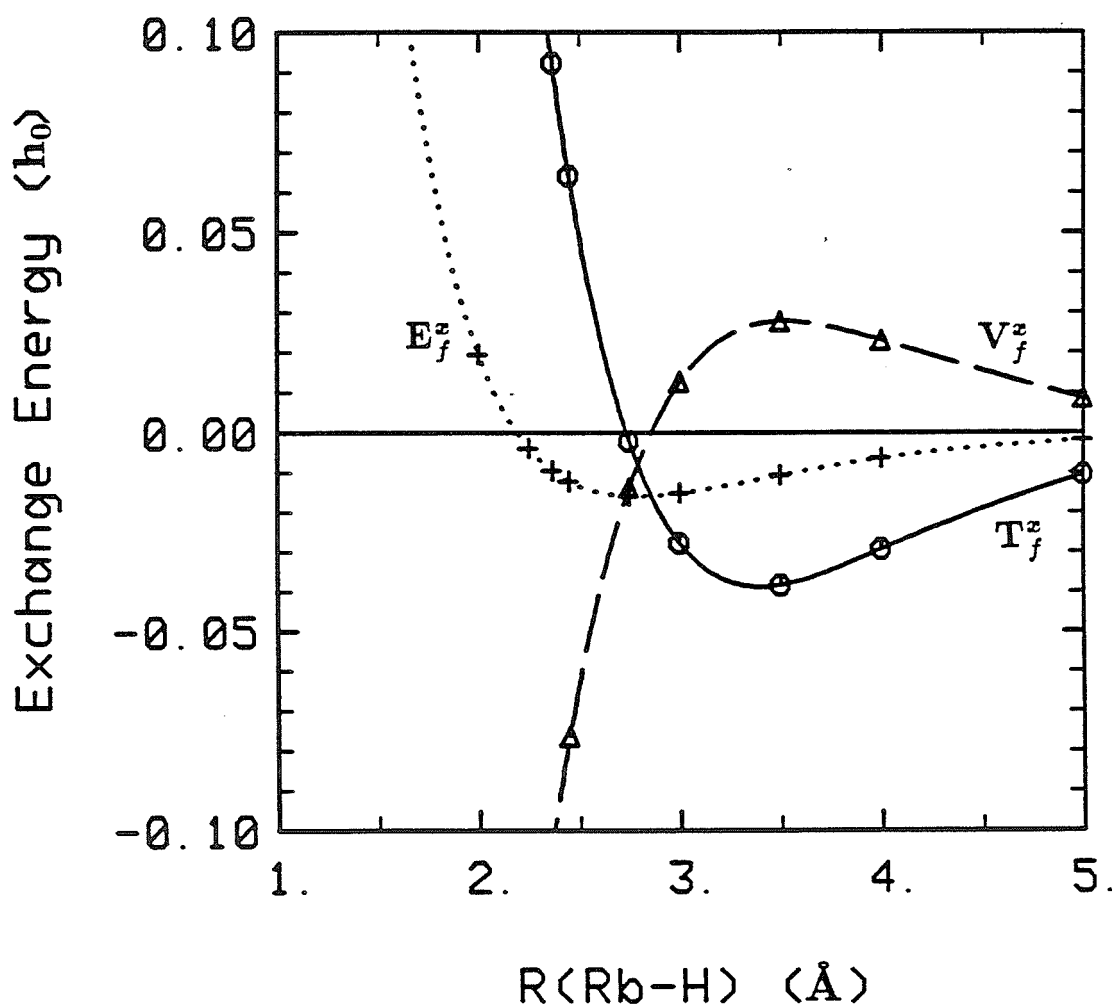
Figure 10e. The exchange kinetic (T_f^x), potential (V_f^x), and total binding (E_f^x) energies for the frozen GVB wavefunction of Cs-H.
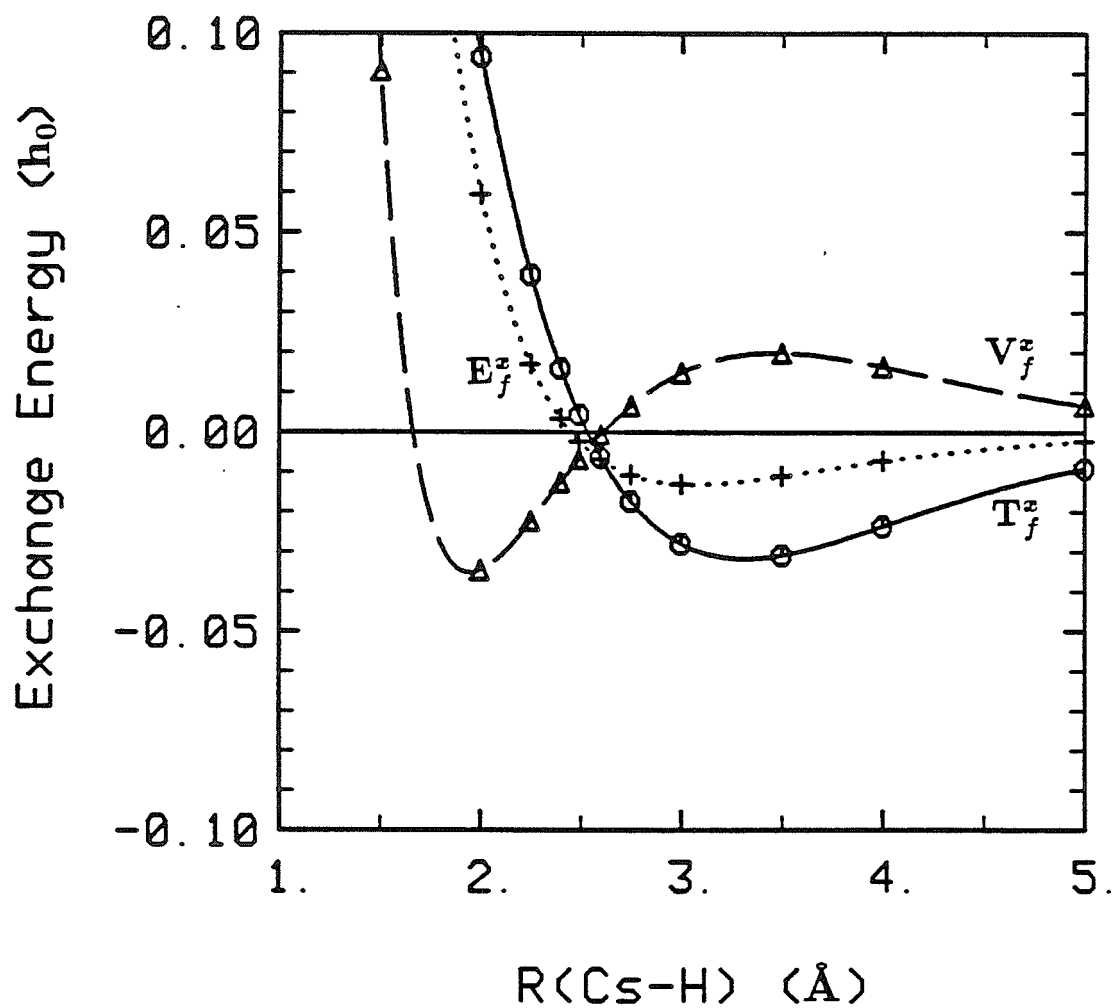
Figure 11a. The exchange kinetic energy (T_f^z) for the frozen GVB wavefunctions of the alkali metal hydrides (M-H). LiH, solid; NaH, large dashes; KH, dots; RbH, small dashes; and CsH, medium dashes.
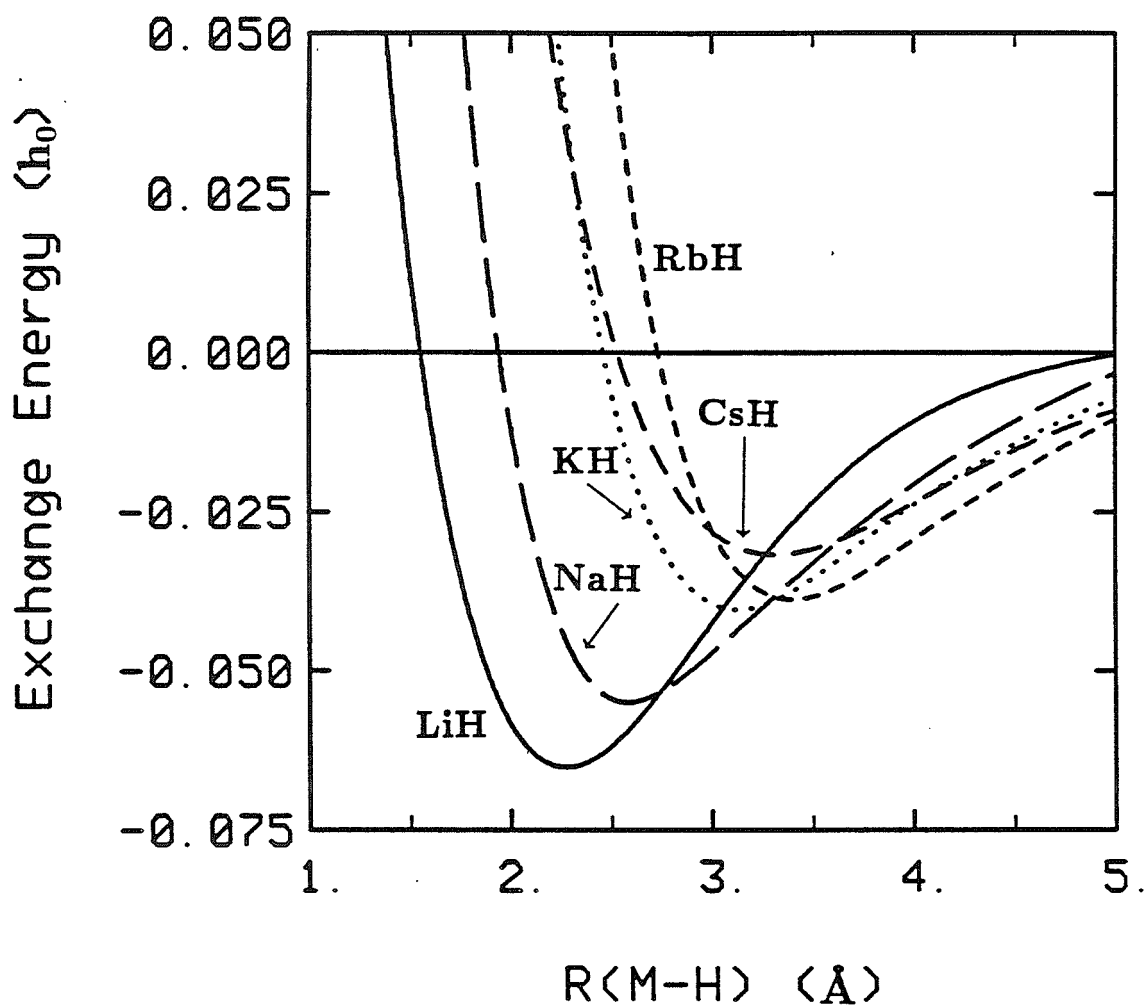
Figure 11b. The exchange potential energy (V_f^z) for the frozen GVB wavefunctions of the alkali metal hydrides (M-H). LiH, solid; NaH, large dashes; KH, dots; RbH, small dashes; and CsH, medium dashes.
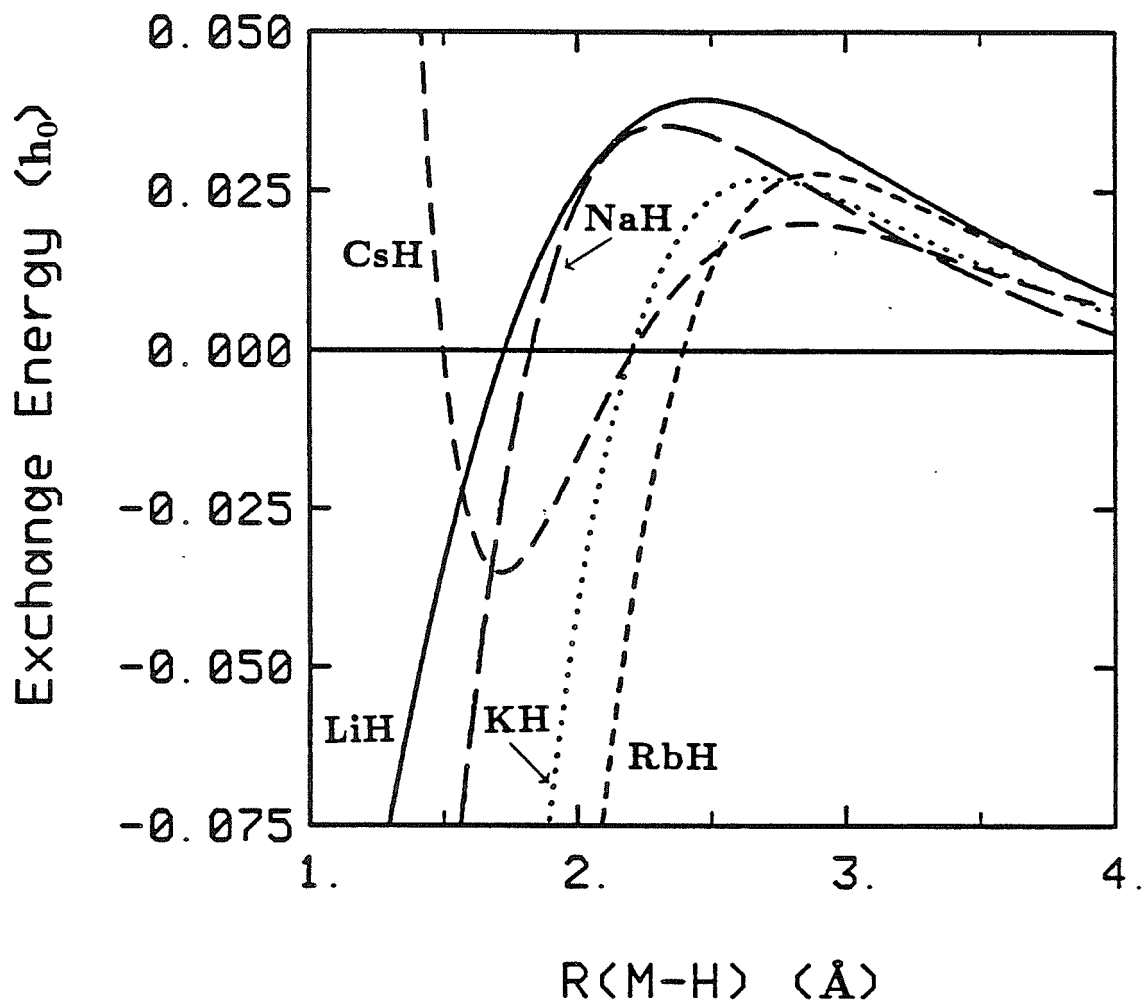
Figure 11c. The exchange total binding energy (E_f^z) for the frozen GVB wavefunctions of the alkali metal hydrides (M-H). LiH, solid; NaH, large dashes; KH, dots; RbH, small dashes; and CsH, medium dashes.
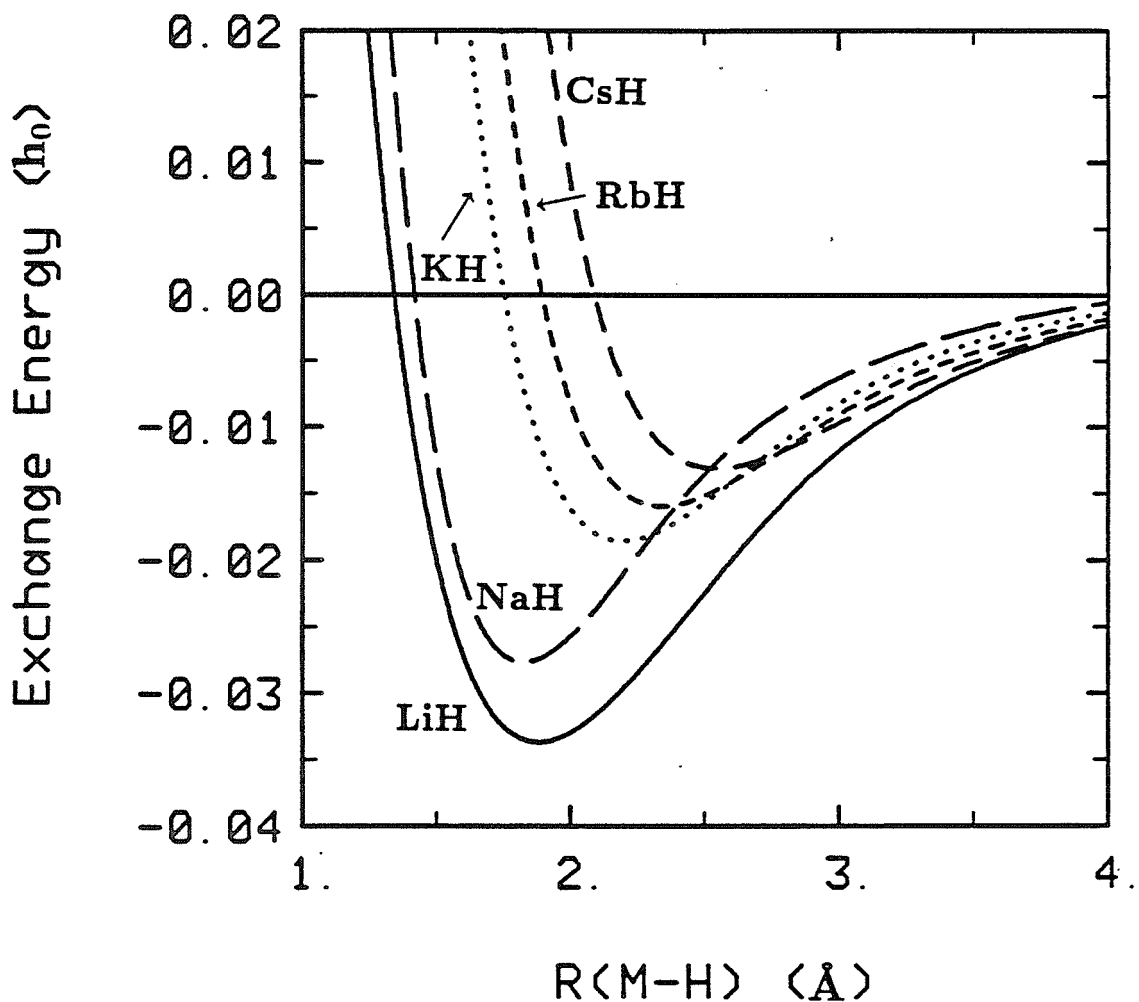
Figure 12a. The exchange kinetic (T_f^x), potential (V_f^x), and total binding (E_f^x) energies for the frozen GVB wavefunction of LiH^+. This represents the interaction of the Li 1s core electrons with the incoming H atom.
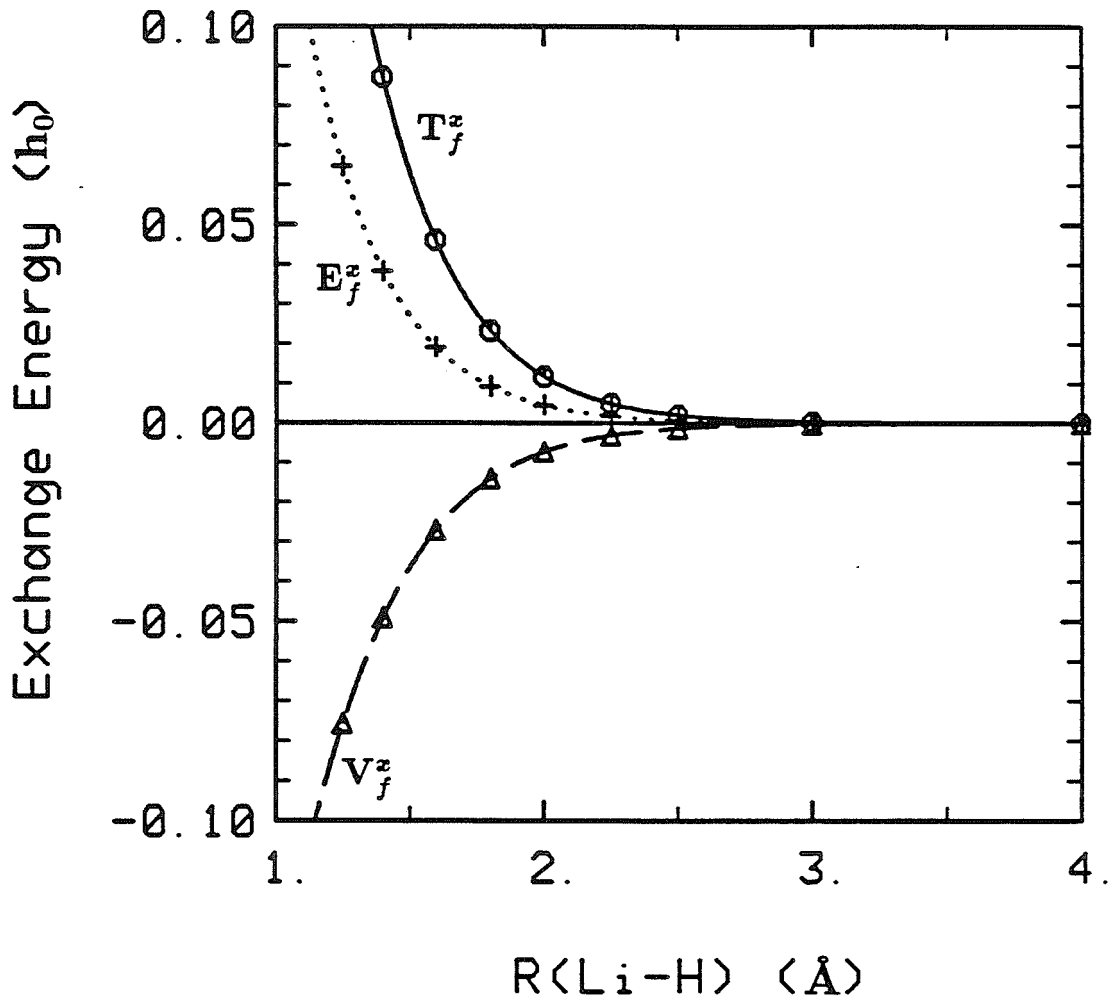
Figure 12b. The exchange kinetic (T_f^x), potential (V_f^x), and total binding (E_f^x) energies for the frozen GVB wavefunction of LiH without core effects. The energies from LiH^+ are subtracted from those of LiH to obtain this set of curves.
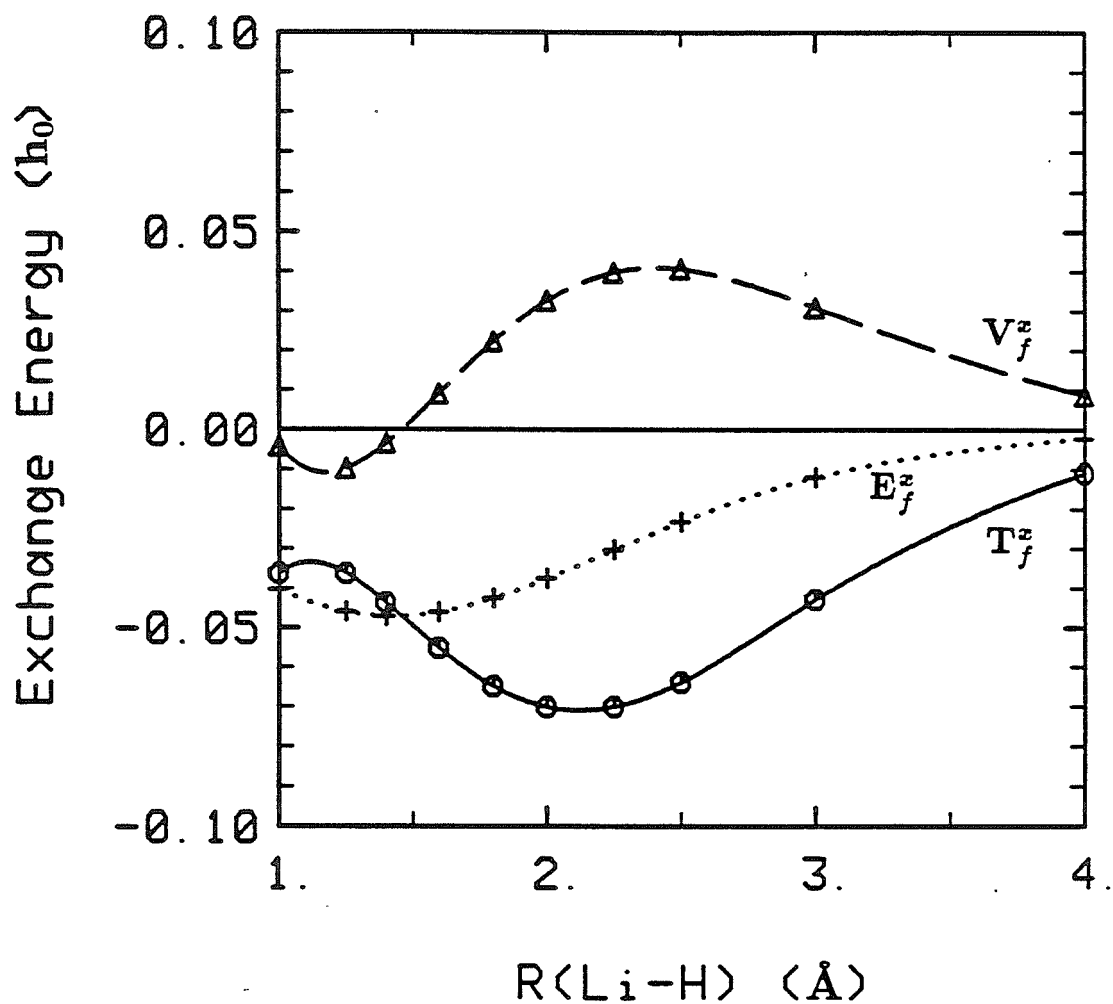
Figure 13. The overlap of the two GVB one-electron orbitals (bonding orbitals) versus internuclear separation, R, for LiH.
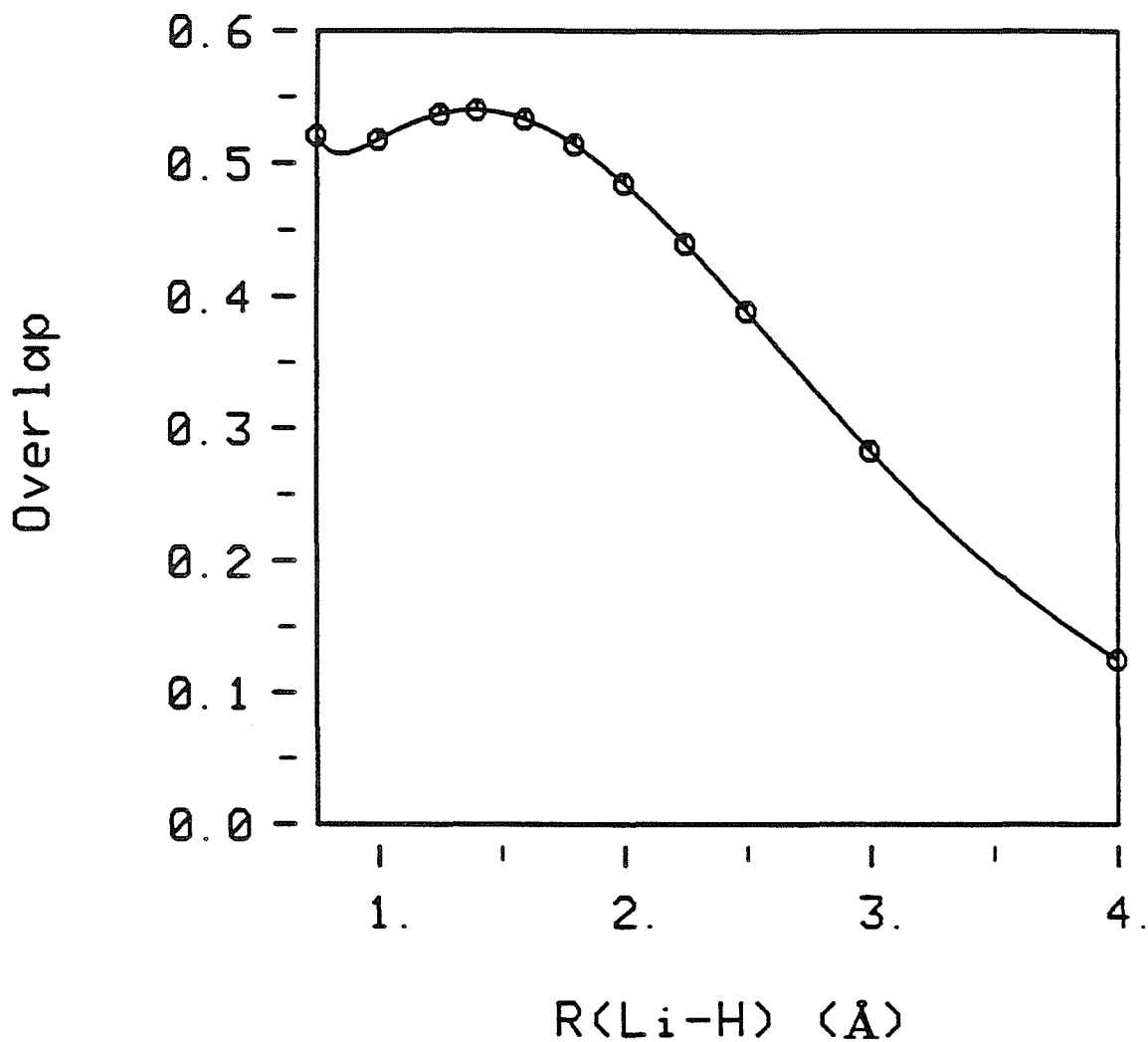
Figure 14a. The two-electron repulsion energy of the bond pair electrons, V_{bf}^{ee}, as a function of internuclear separation for the frozen GVB wavefunctions of the alkali metal hydrides (M-H). LiH, solid; NaH, large dashes; KH, dots; RbH, small dashes; and CsH, medium dashes.
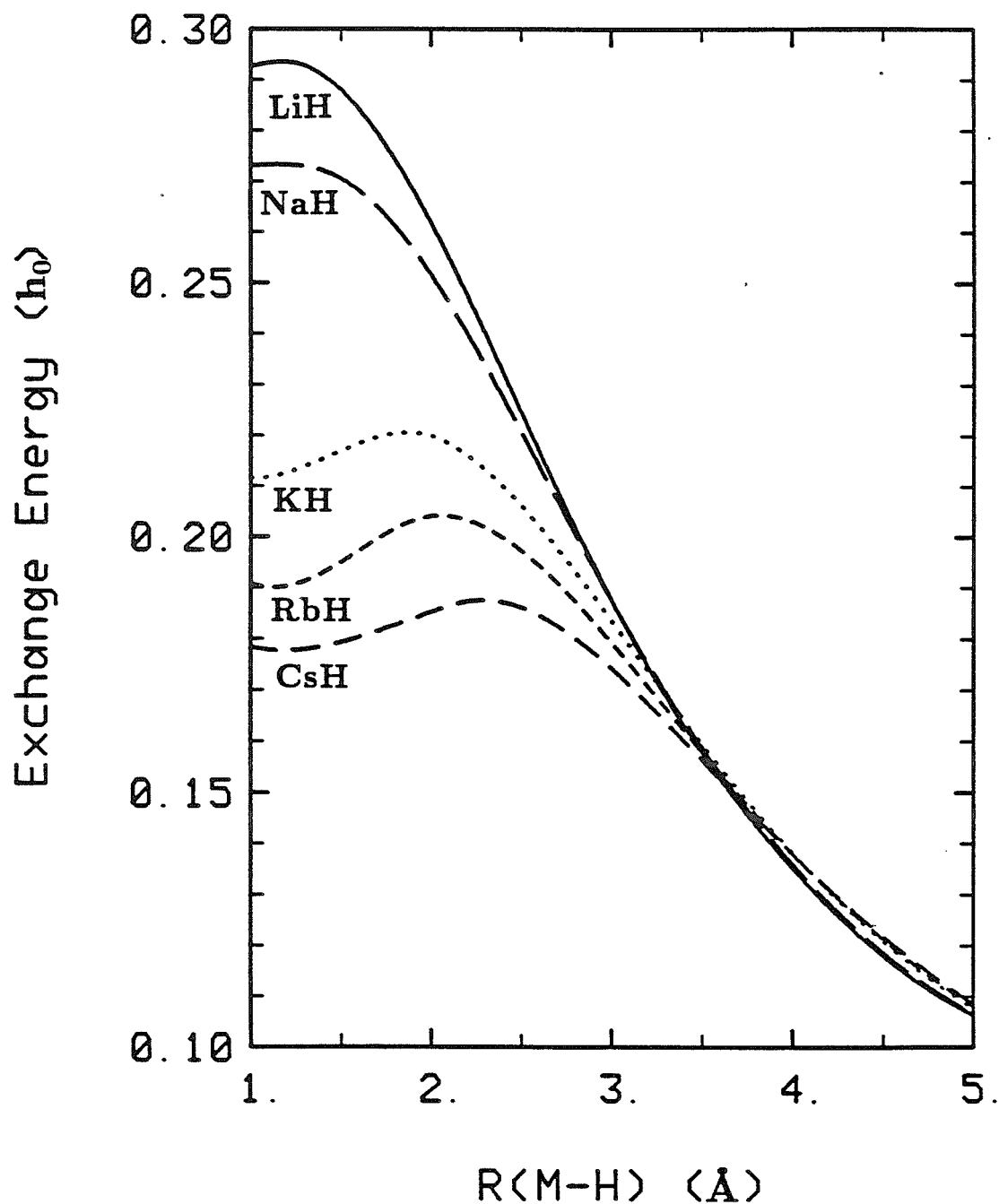
Figure 14b. The nuclear repulsion, V^{nn}, and the electron-nuclear attraction energy for the bond pair electrons, V^{en}_{bf}, as a function of internuclear separation for the frozen GVB wavefunctions of the alkali metal hydrides (M-H). The left scale is for V^{nn}; the right scale is for V^{en}_{bf}. LiH, solid; NaH, large dashes; KH, dots; RbH, small dashes; and CsH, medium dashes.
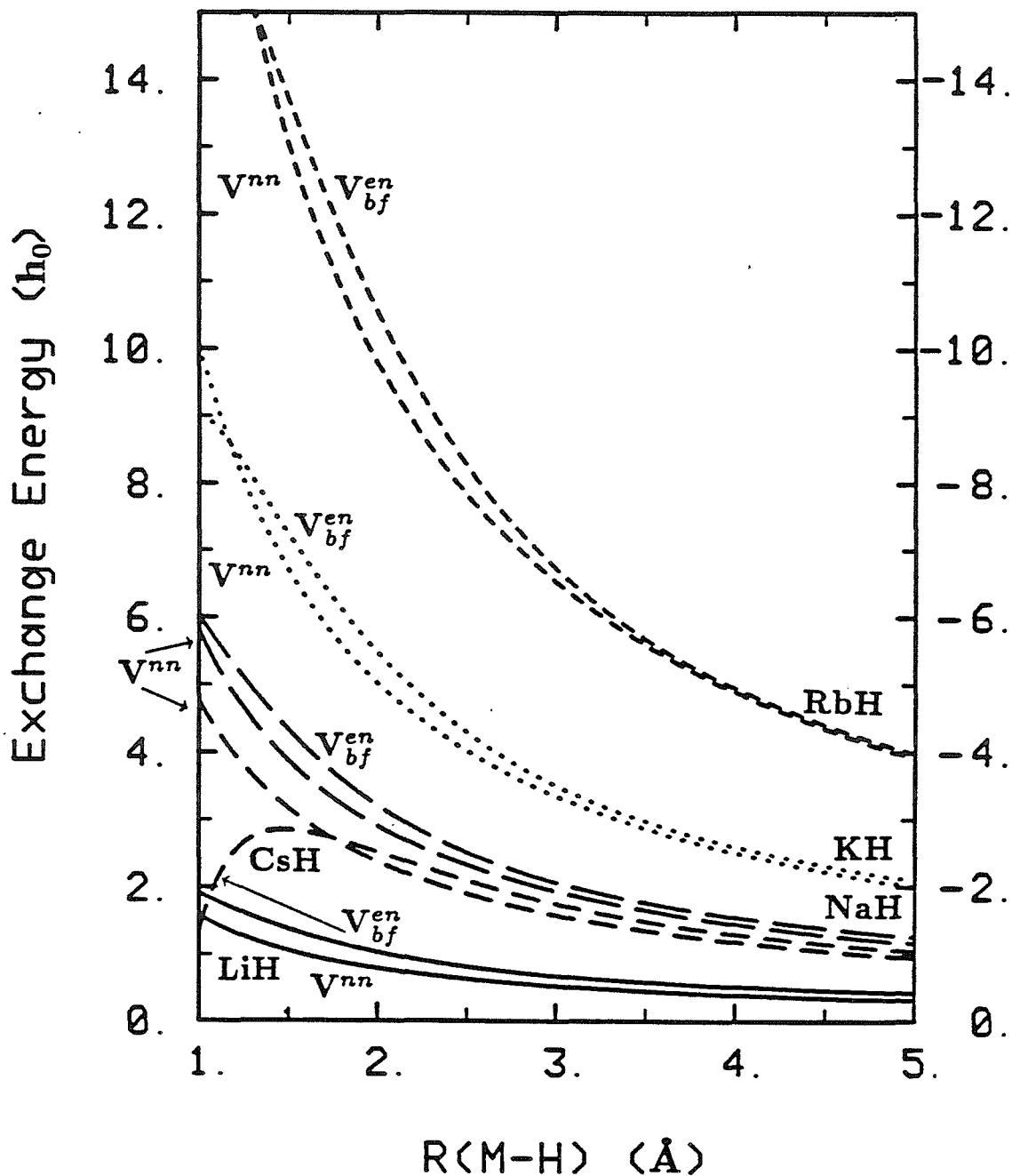
Figure 15a. The exchange kinetic (T^z), potential (V^z), and total binding (E^z) energies for the relaxed GVB wave-function of Li-H.
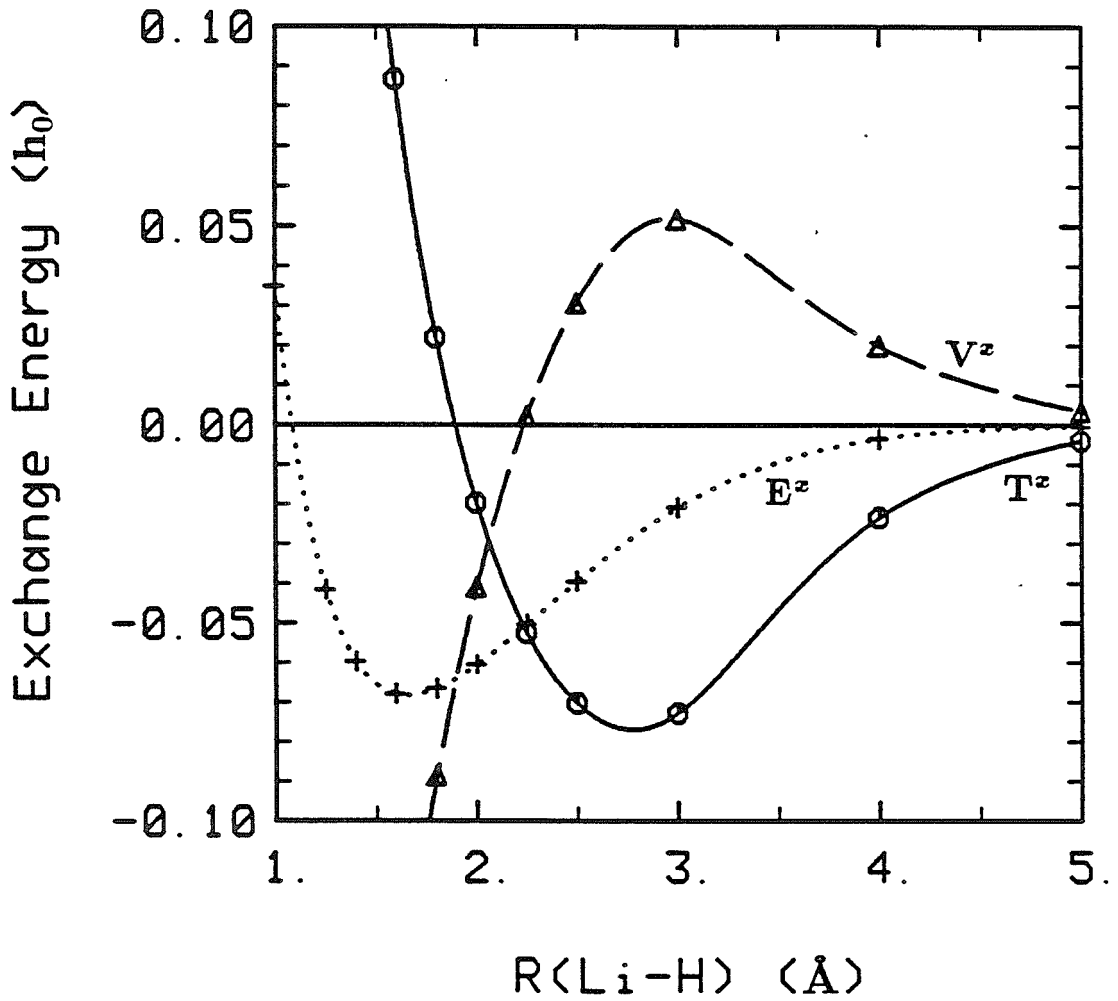
Figure 15b. The exchange kinetic (T^z), potential (V^z), and total binding (E^z) energies for the relaxed GVB wavefunction of Na-H.
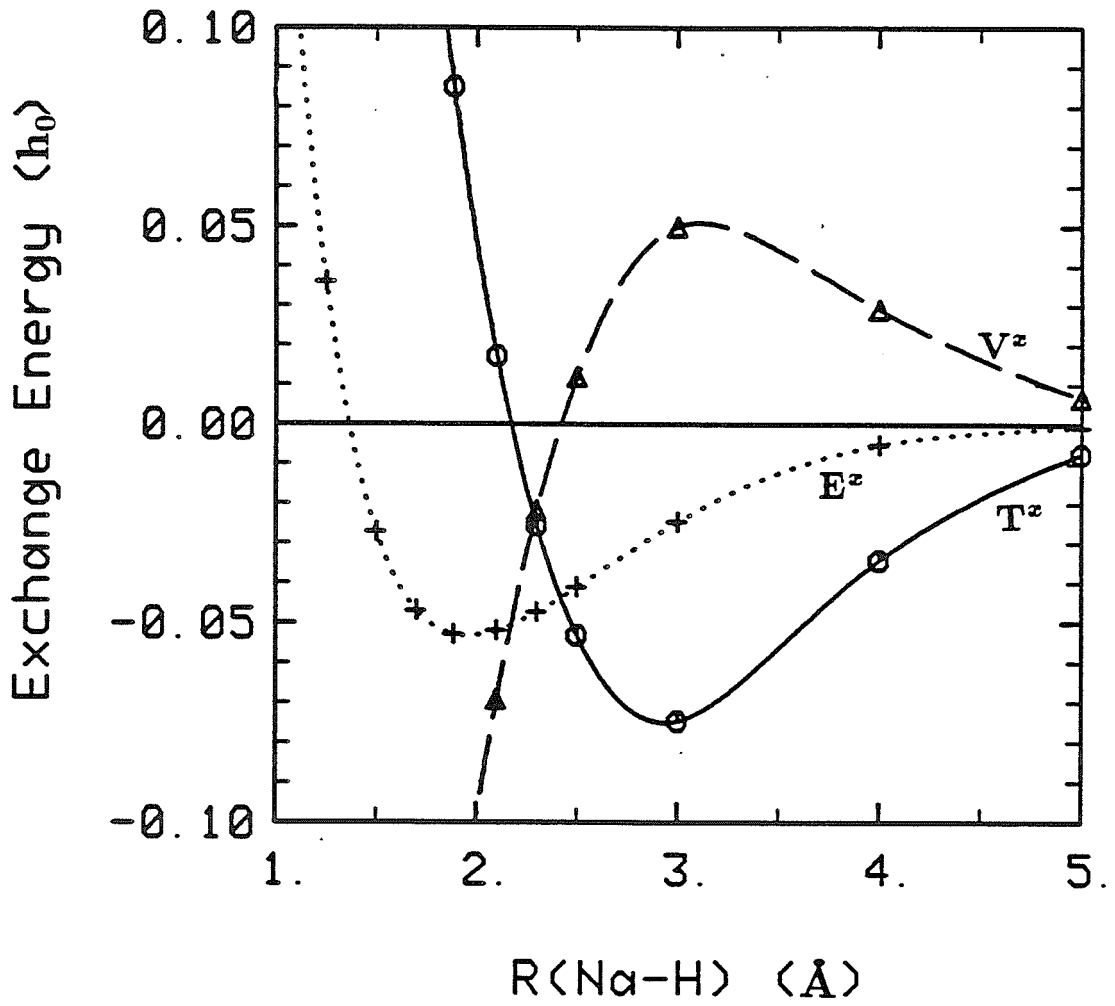
Figure 15c. The exchange kinetic (T^z), potential (V^z), and total binding (E^z) energies for the relaxed GVB wave-function of K-H.
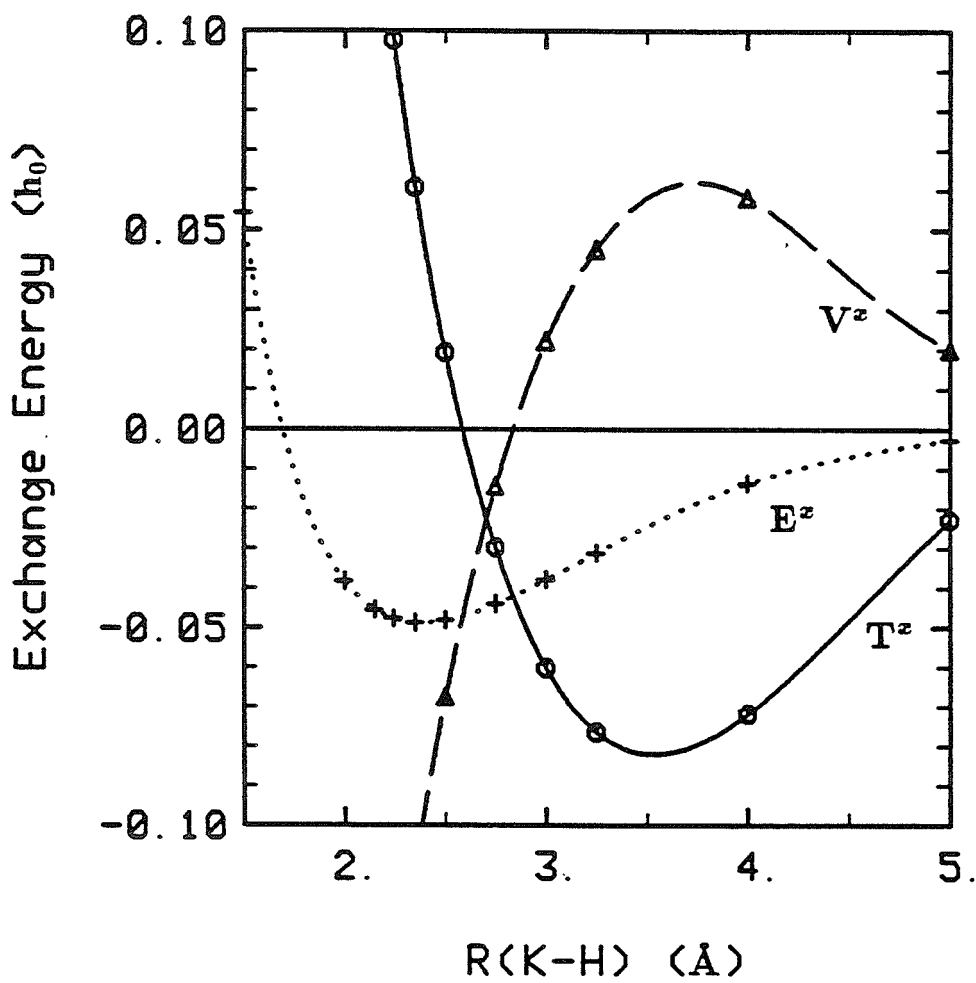
Figure 15d. The exchange kinetic (T^z), potential (V^z), and total binding (E^z) energies for the relaxed GVB wavefunction of Rb-H.
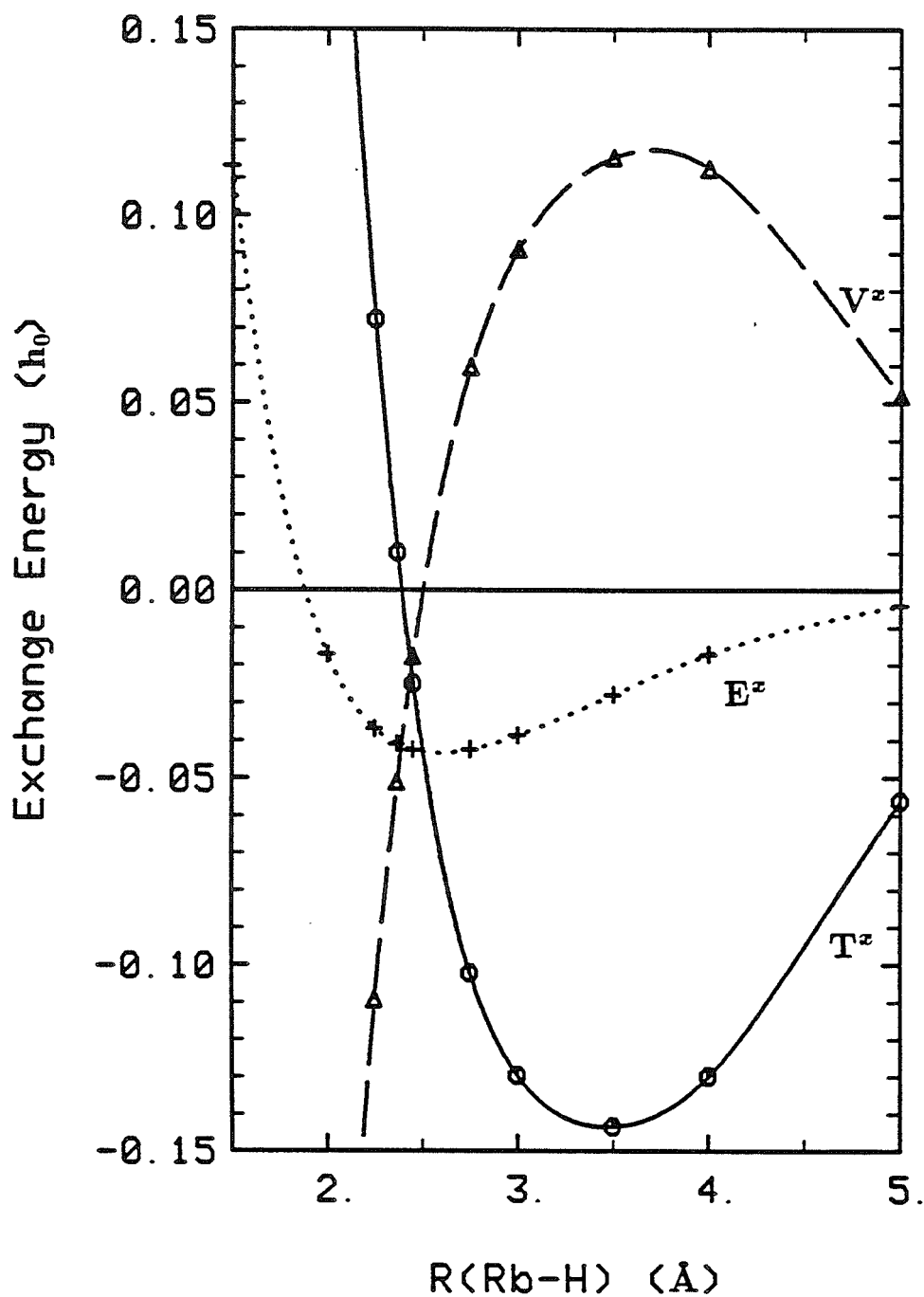
Figure 15e. The exchange kinetic (T^z), potential (V^z), and total binding (E^z) energies for the relaxed GVB wavefunction of Cs-H.
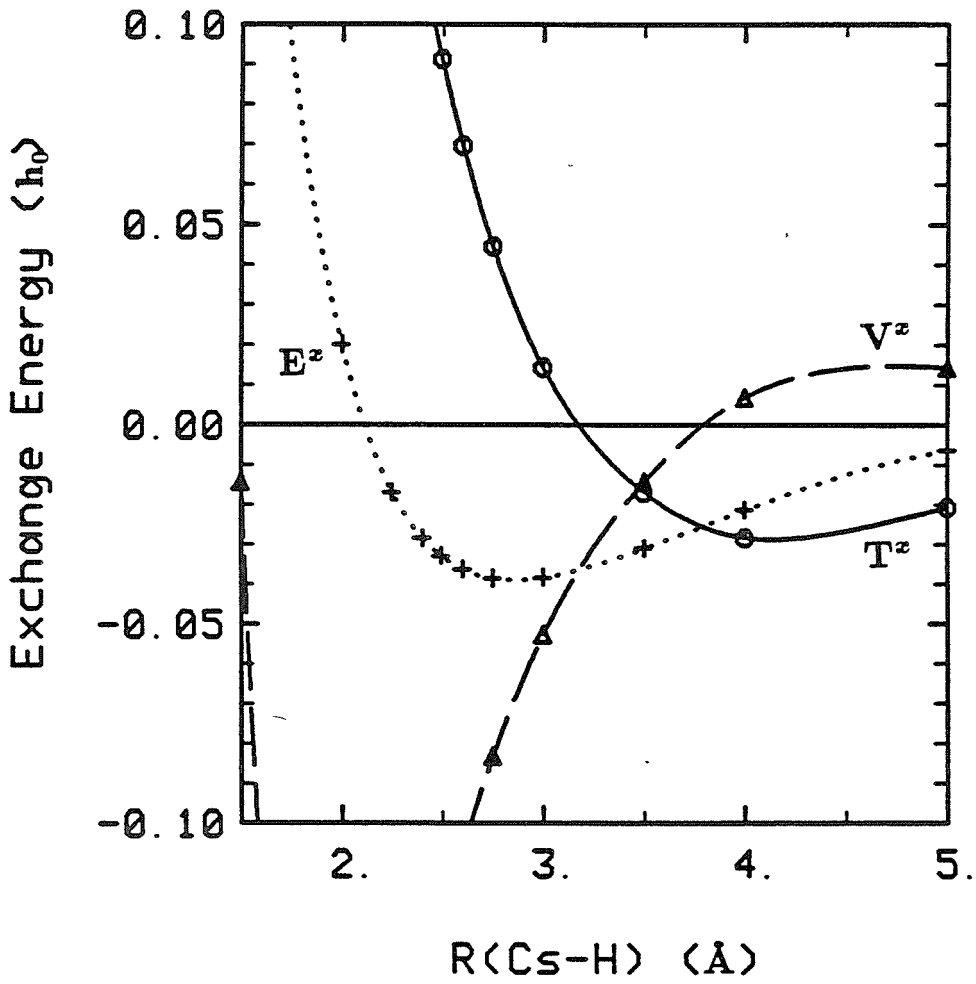
Figure 16a. The amplitudes of the frozen (solid) and relaxed (dotted) bonding orbitals of LiH plotted along a line connecting the two nuclei at r_{ef}.
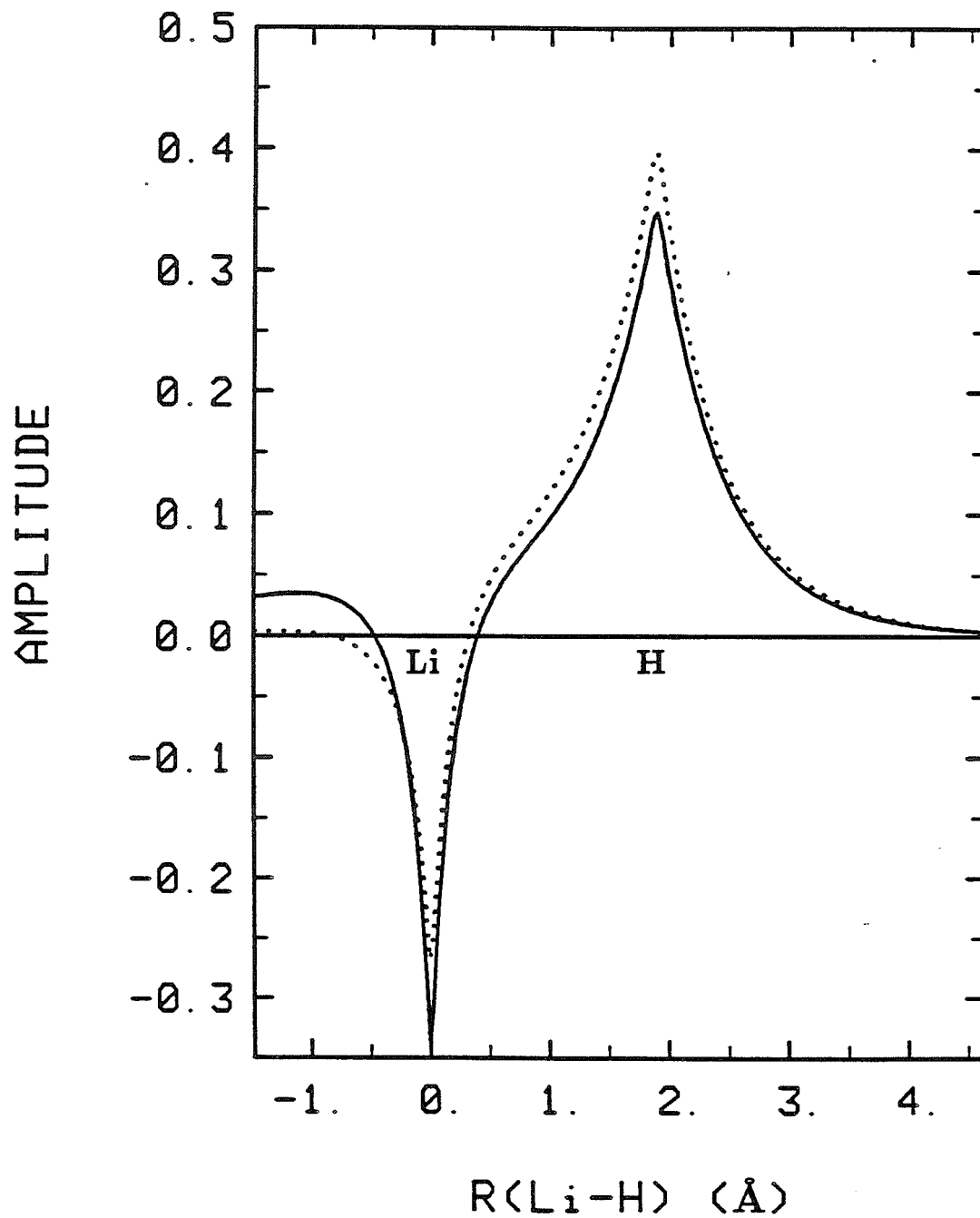
Figure 16b. The amplitudes of the frozen (solid) and relaxed (dotted) bonding orbitals of NaH plotted along a line connecting the two nuclei at r_{ef}.
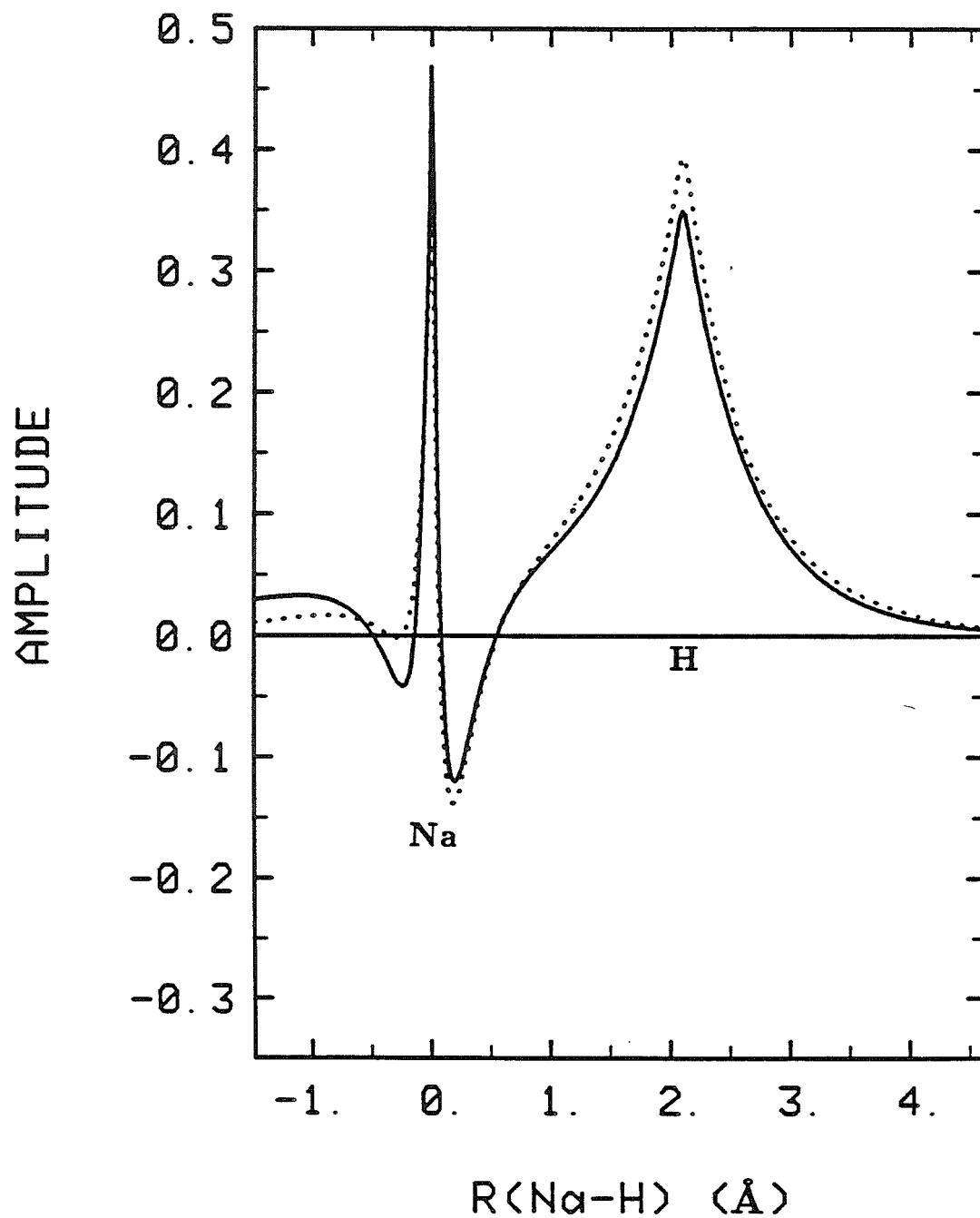
Figure 16c. The amplitudes of the frozen (solid) and relaxed (dotted) bonding orbitals of KH plotted along a line connecting the two nuclei at r_{ef}.
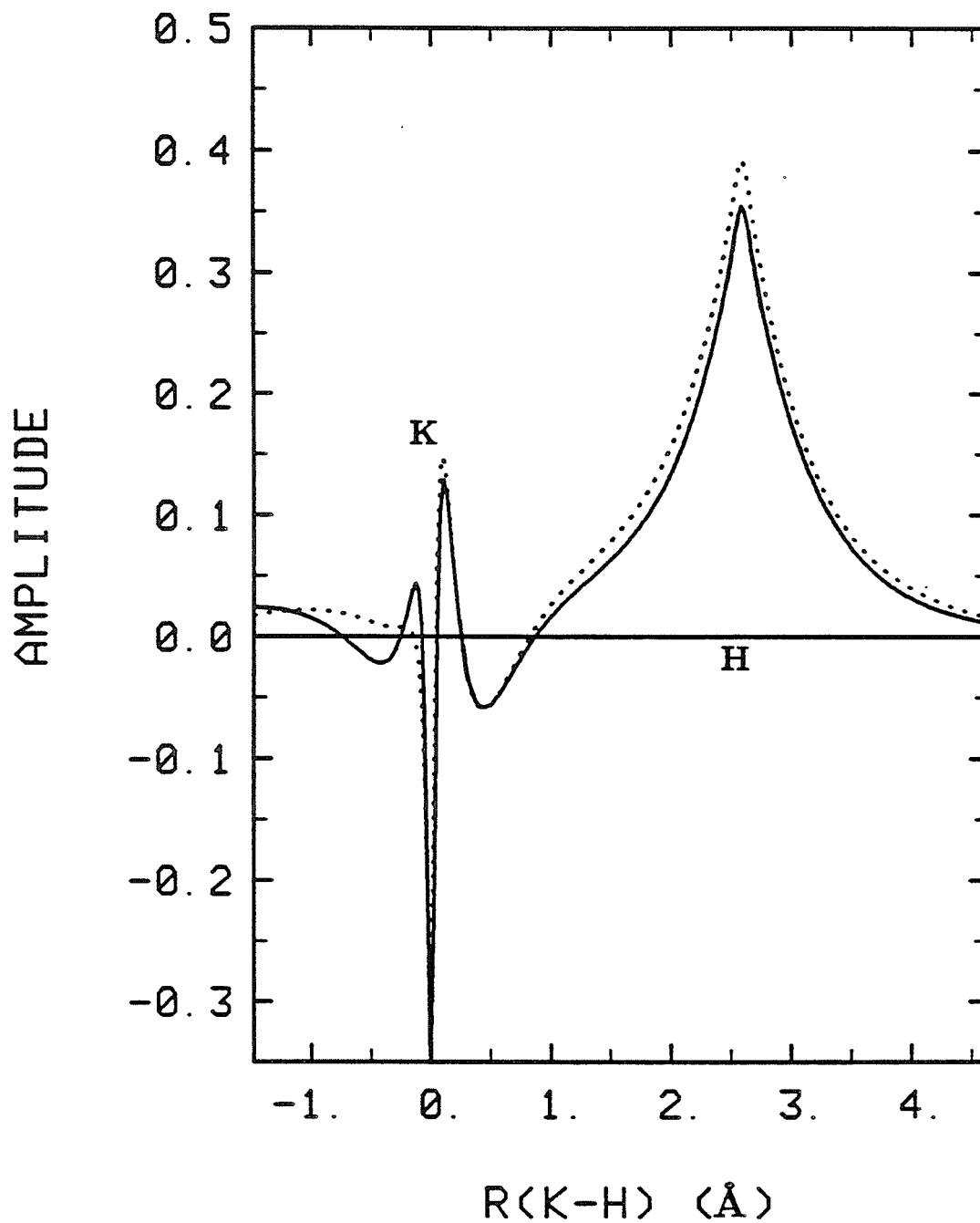
Figure 16d. The amplitudes of the frozen (solid) and relaxed (dotted) bonding orbitals of RbH plotted along a line connecting the two nuclei at r_{ef}.
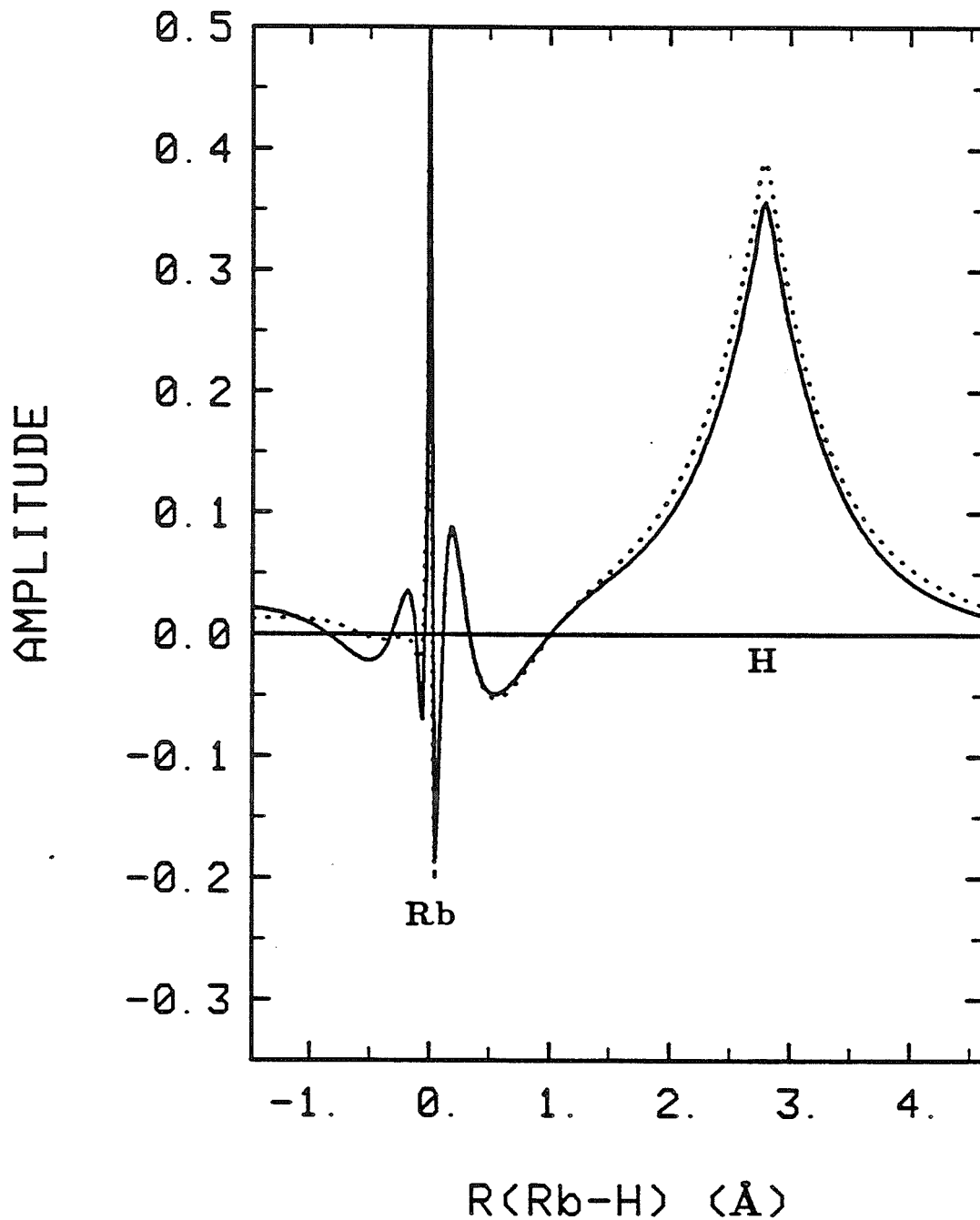
Figure 16e. The amplitudes of the frozen (solid) and relaxed (dotted) bonding orbitals of CsH plotted along a line connecting the two nuclei at r_{ef}.
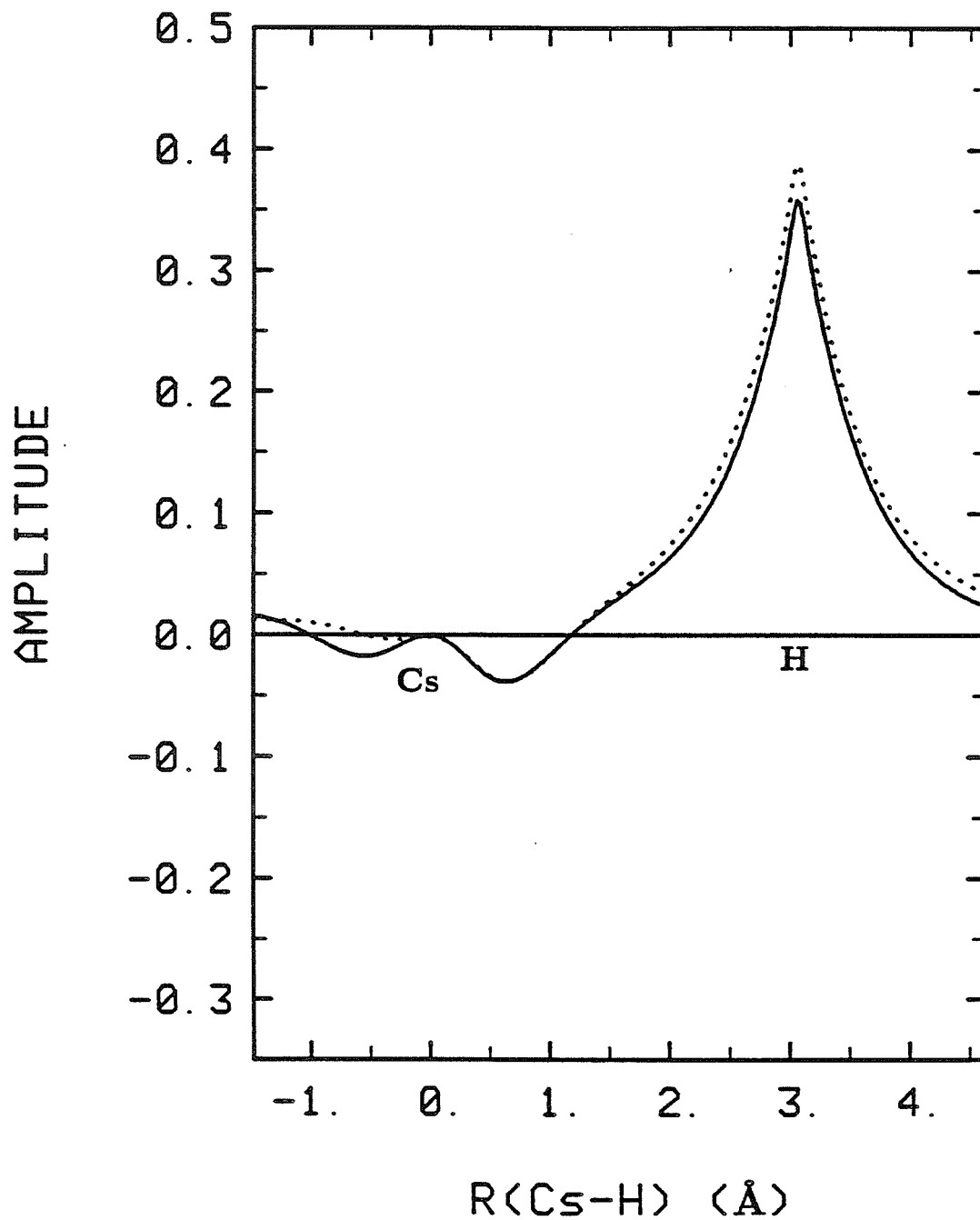
Figure 17a. The exchange kinetic (T_f^x), potential (V_f^x), and total binding (E_f^x) energies for the frozen GVB wavefunction of Cl_2HTi-H.
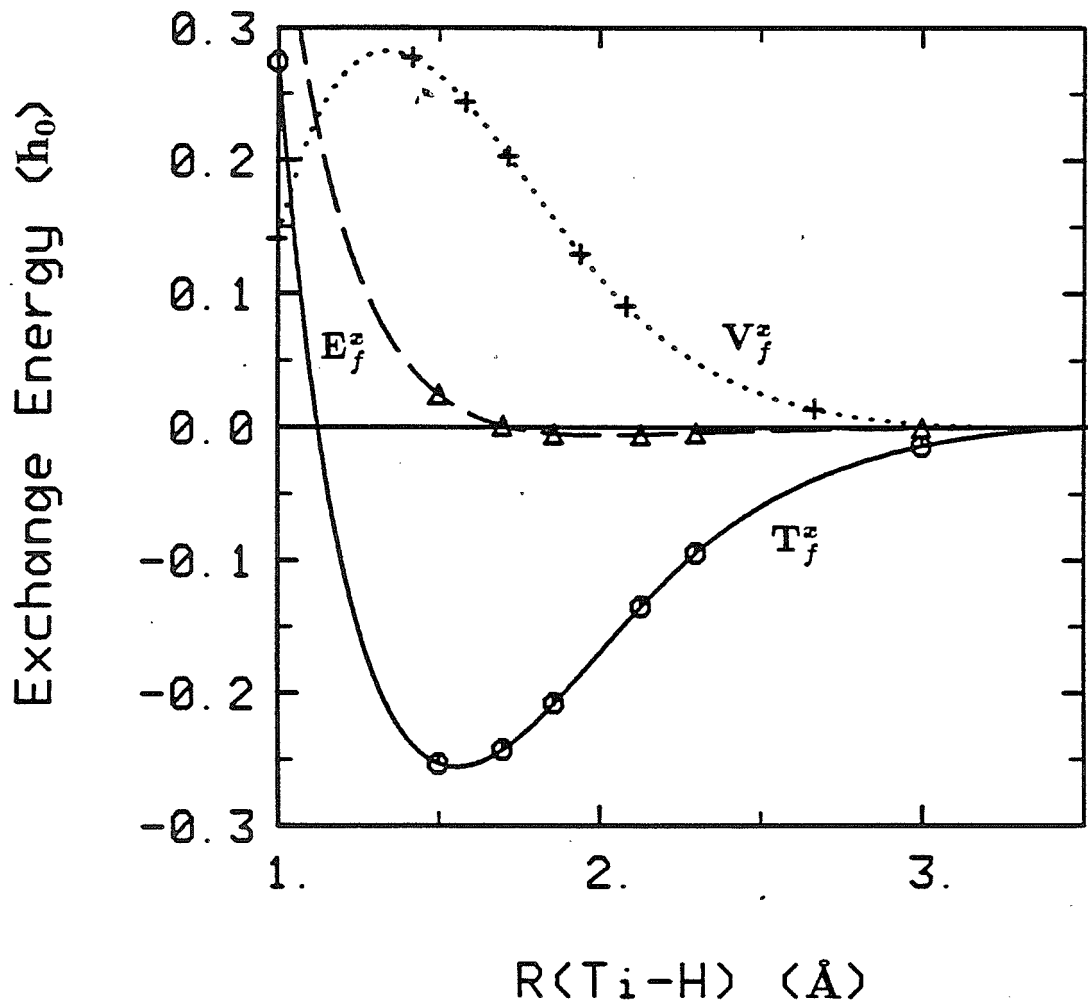
Figure 17b. The exchange kinetic (T_f^x), potential (V_f^x), and total binding (E_f^x) energies for the frozen GVB wavefunction of Cl_2HZr-H.
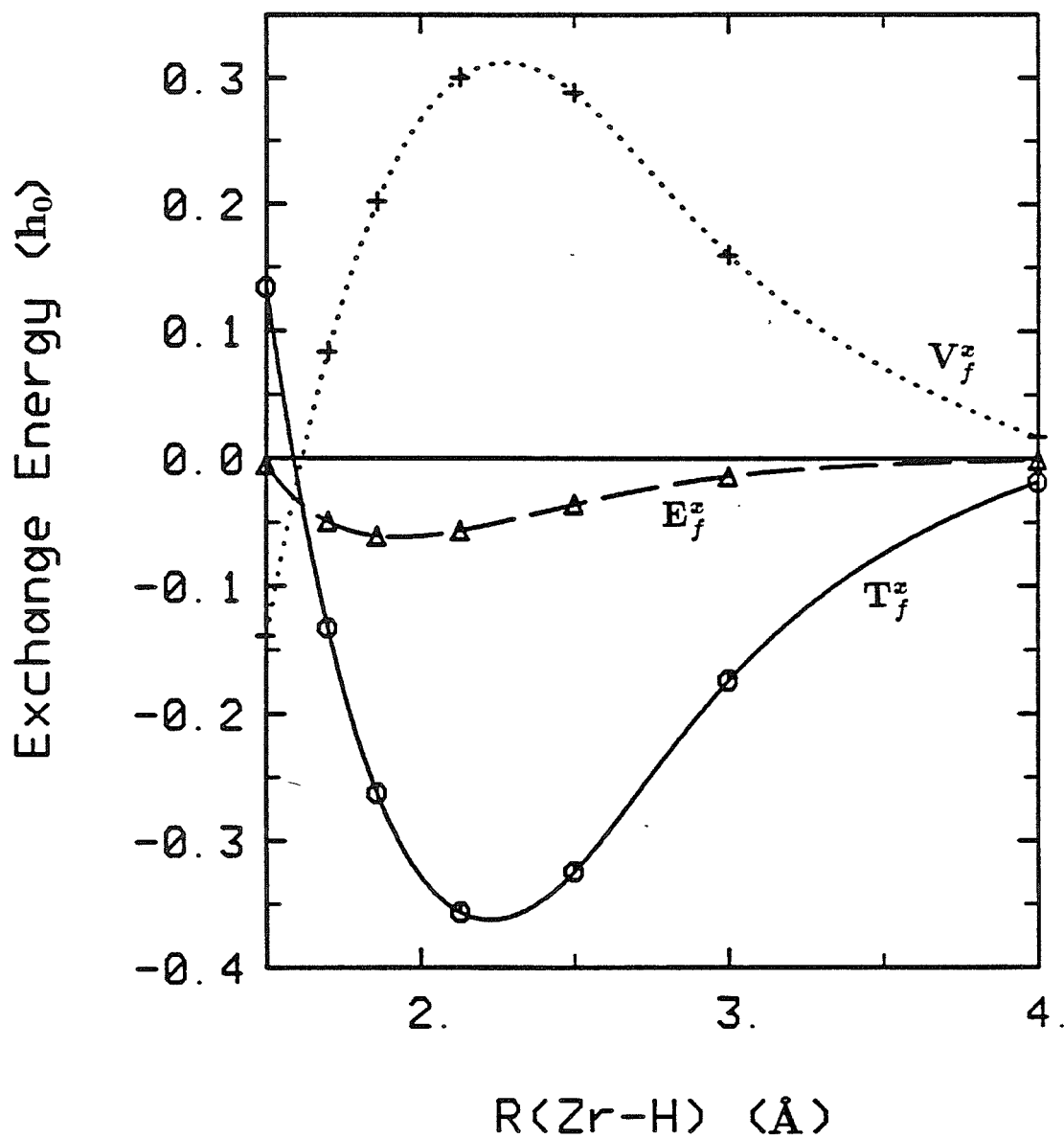
Figure 17c. The exchange kinetic (T_f^x), potential (V_f^x), and total binding (E_f^x) energies for the frozen GVB wavefunction of $Cl_2HHf\text{-}H$.
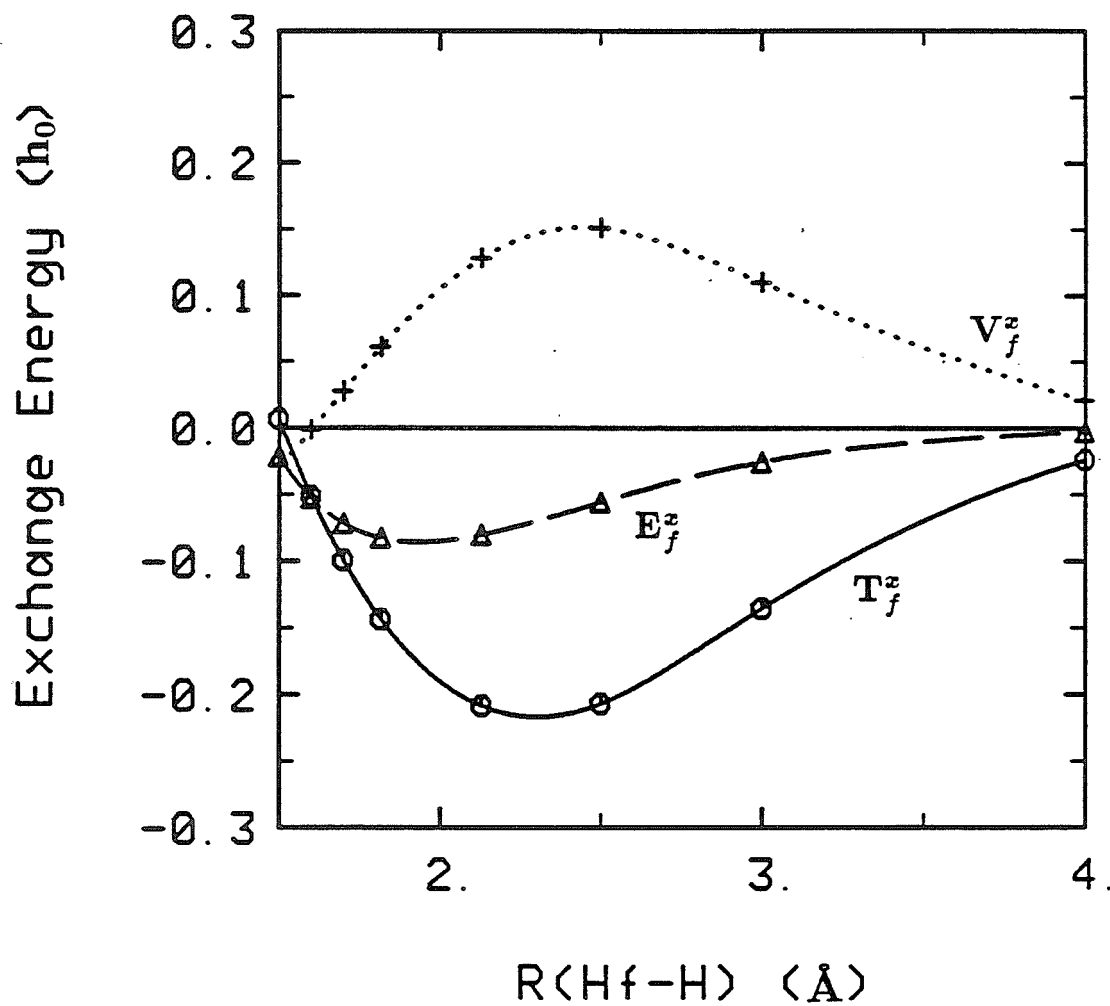
Figure 17d. The exchange kinetic (T_f^z), potential (V_f^z), and total binding (E_f^z) energies for the frozen GVB wavefunction of Cl_2HTh-H.
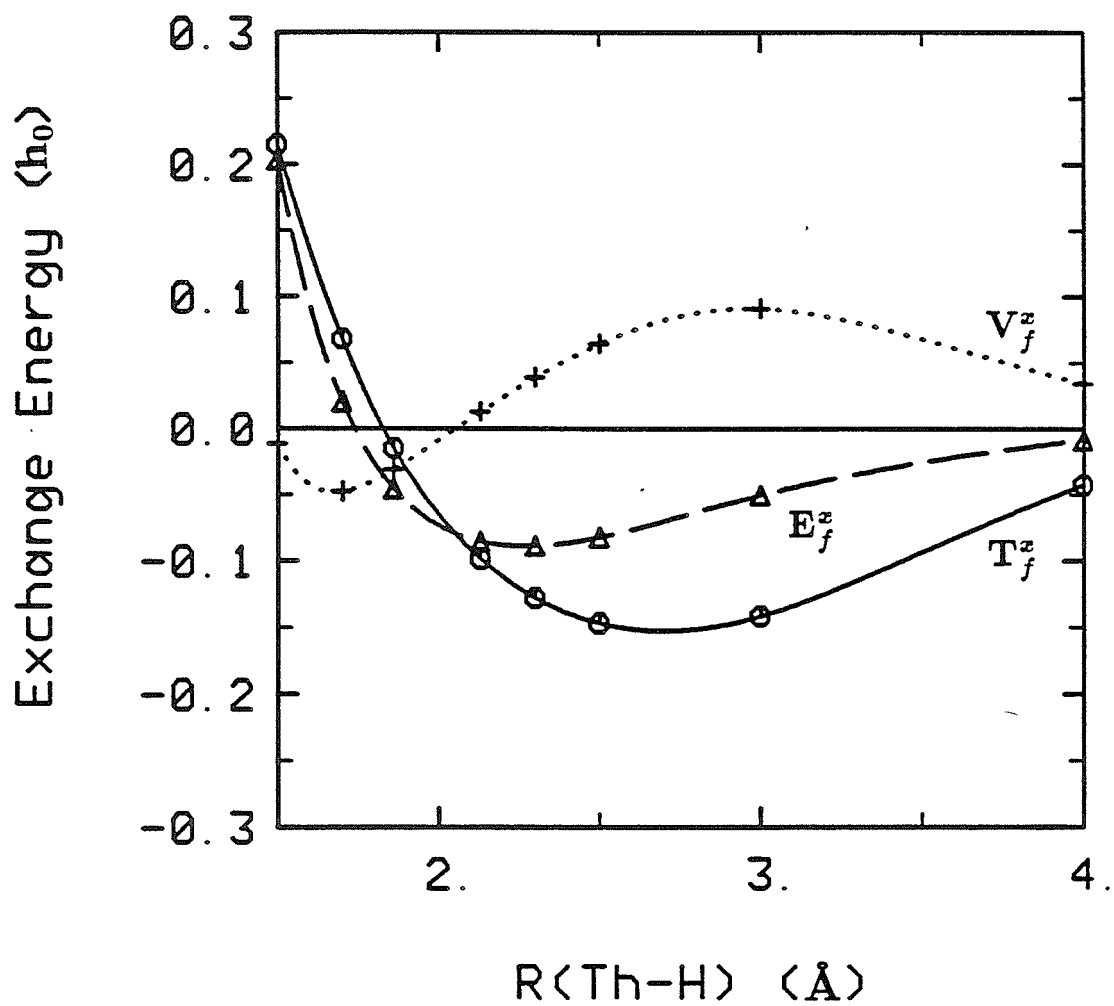
Figure 18a. The exchange kinetic energy (T_f^z) for the frozen GVB wavefunctions of the Group IVb and Th hydrides ($Cl_2HM\text{-}H$). Ti-H, solid; Zr-H, large dashes; Hf-H, dots; Th-H, small dashes.
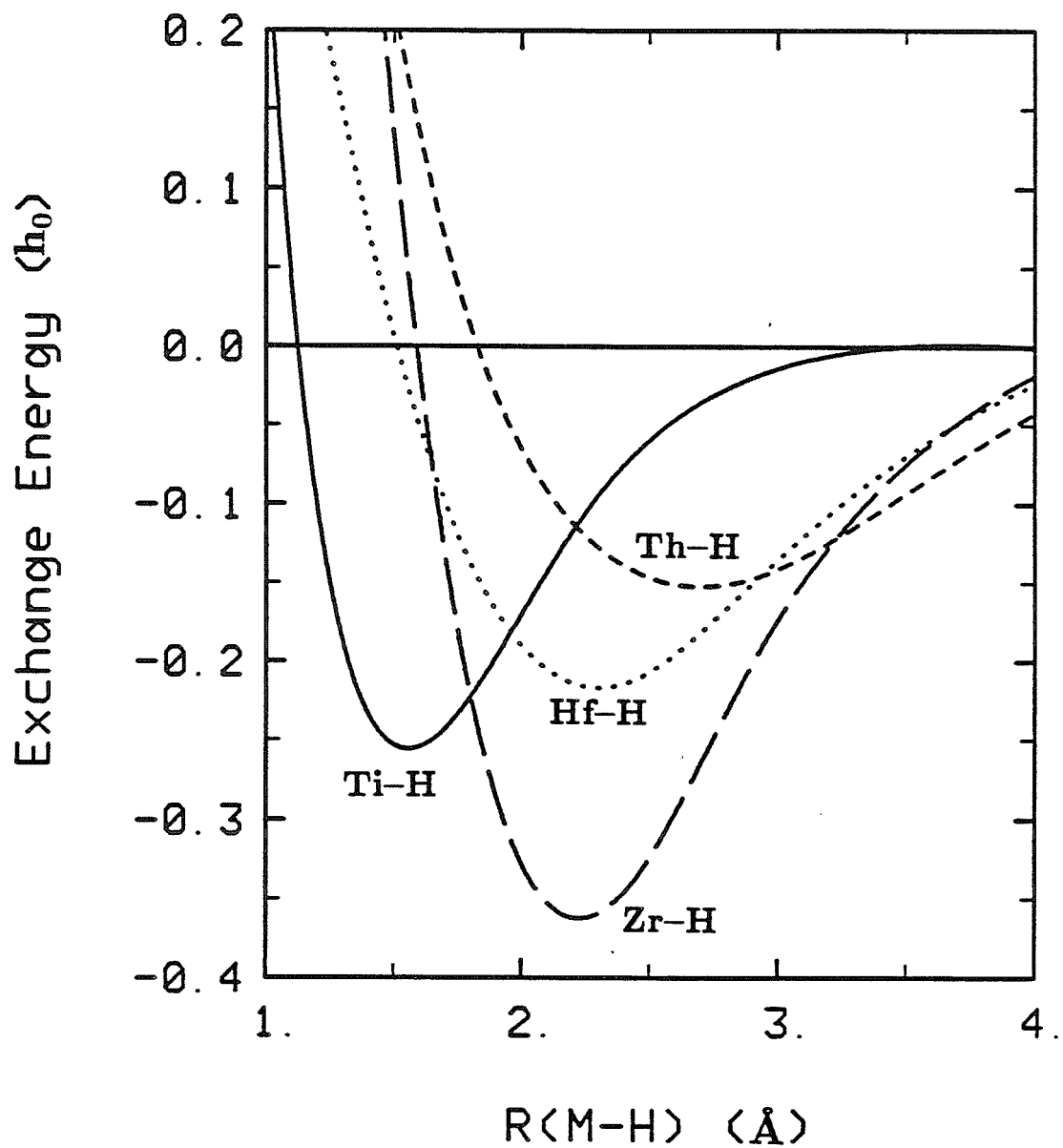
Figure 18b. The exchange potential energy (V_f^z) for the frozen GVB wavefunctions of the Group IVb and Th hydrides (Cl_2HM-H). Ti-H, solid; Zr-H, large dashes; Hf-H, dots; Th-H, small dashes.
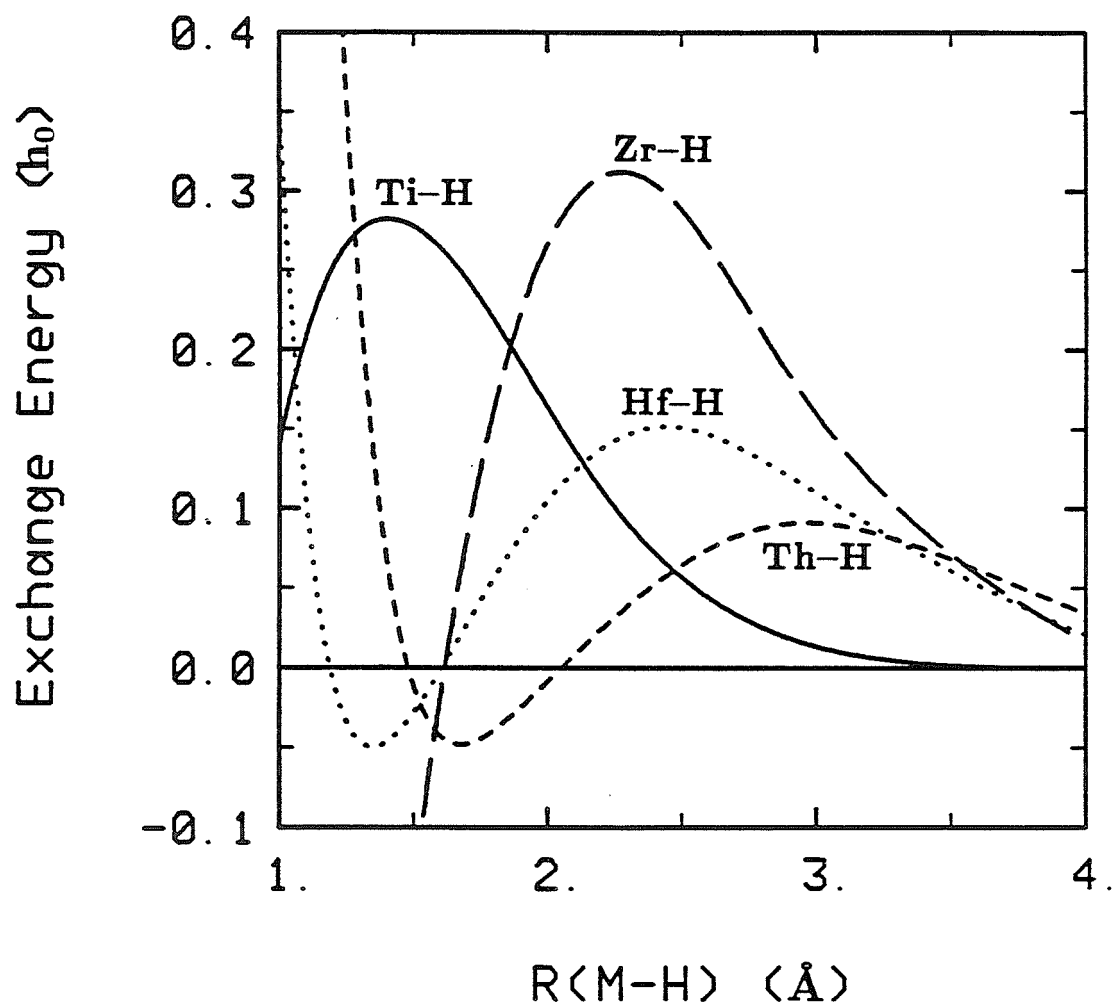
Figure 18c. The exchange total binding energy (E_f^z) for the frozen GVB wavefunctions of the Group IVb and Th hydrides (Cl_2HM-H). Ti-H, solid; Zr-H, large dashes; Hf-H, dots; Th-H, small dashes.
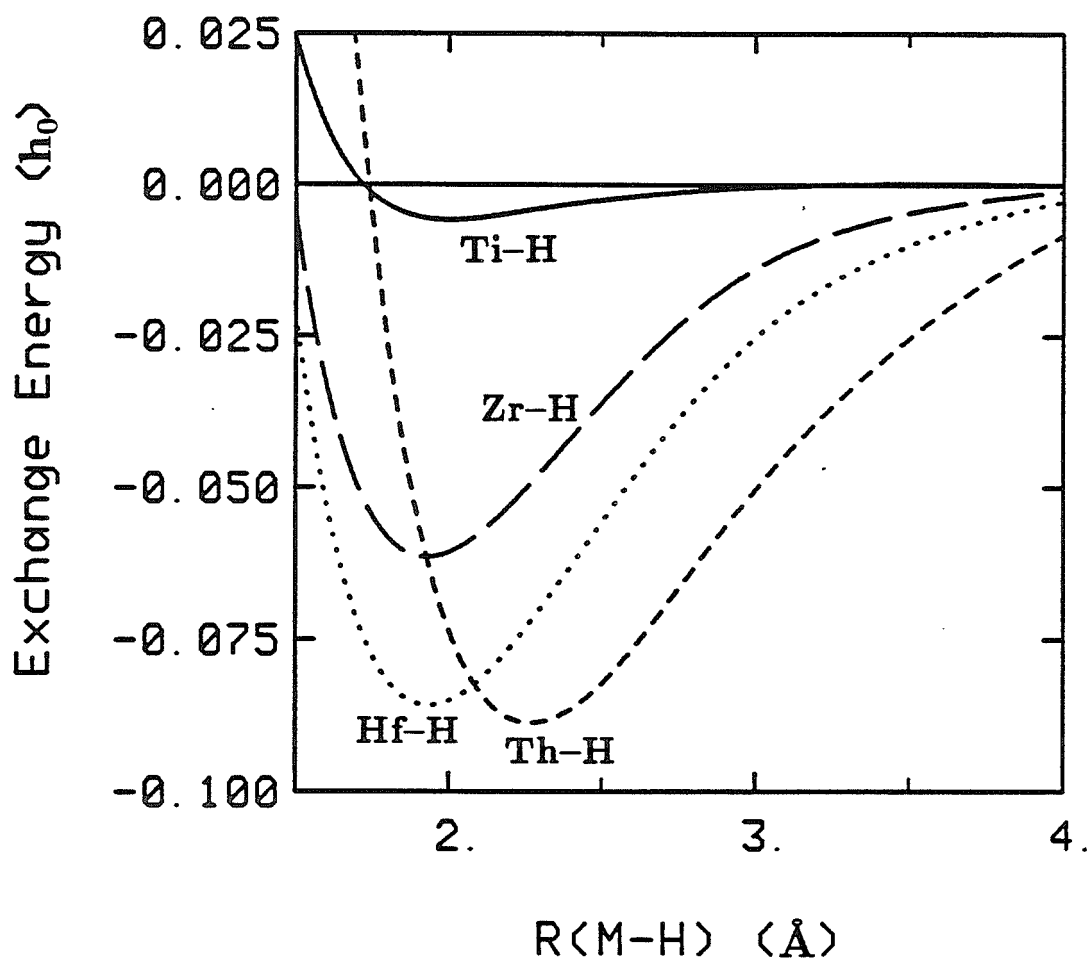
Figure 19a. The two electron repulsion energy of the bond pair electrons, V_{bf}^{ee}, as a function of internuclear separation for the frozen GVB wavefunctions of the Group IVb and Th hydrides (Cl_2HM-H). Ti-H, solid; Zr-H, large dashes; Hf-H, dots; Th-H, small dashes.
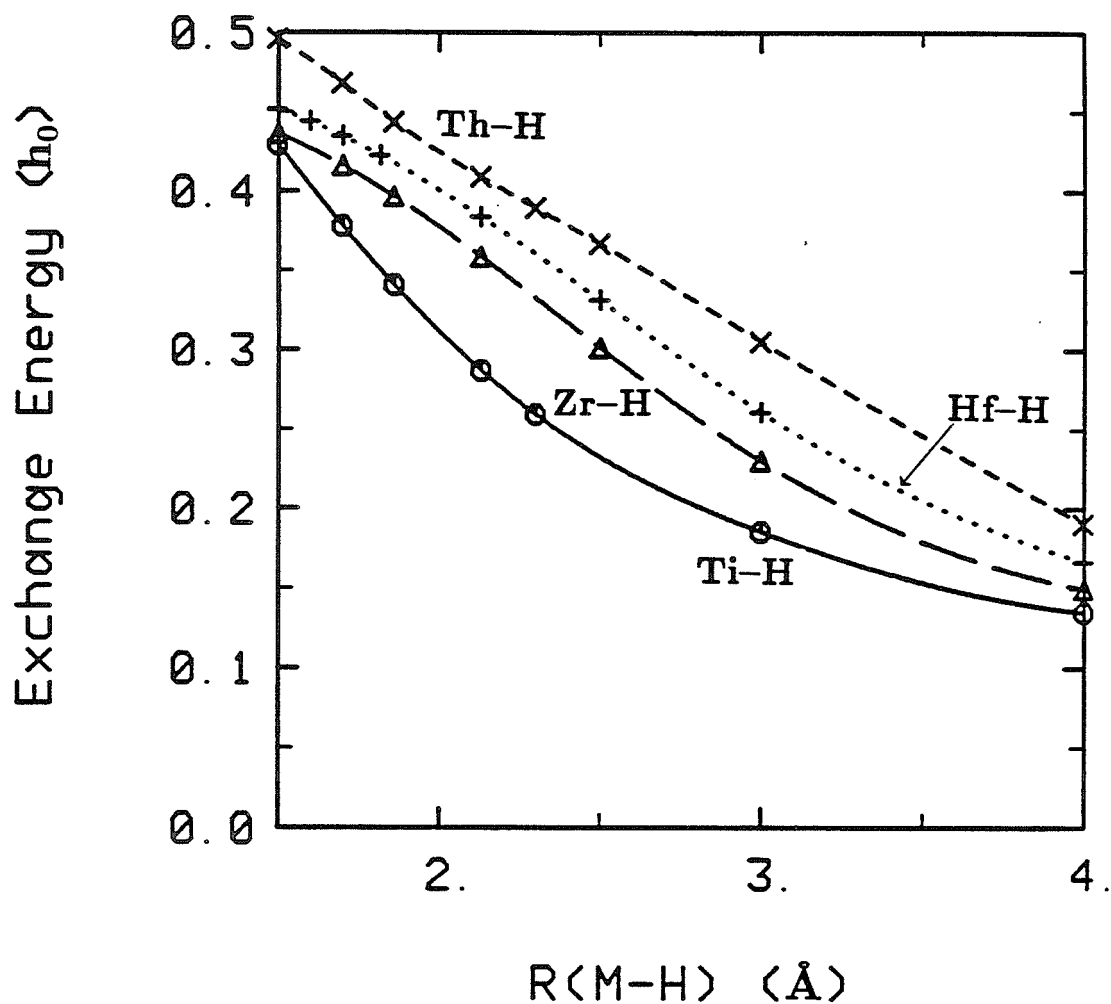
Figure 19b. The nuclear repulsion, V^{nn}, and the electron-nuclear attraction energy for the bond pair electrons, V_{bf}^{en}, as a function of internuclear separation for the frozen GVB wavefunctions of the Group IVb and Th hydrides (Cl_2HM-H). The left scale is for V^{nn}; the right scale is for V_{bf}^{en}. Ti-H, solid; Zr-H, large dashes; Hf-H, dots; Th-H, small dashes.
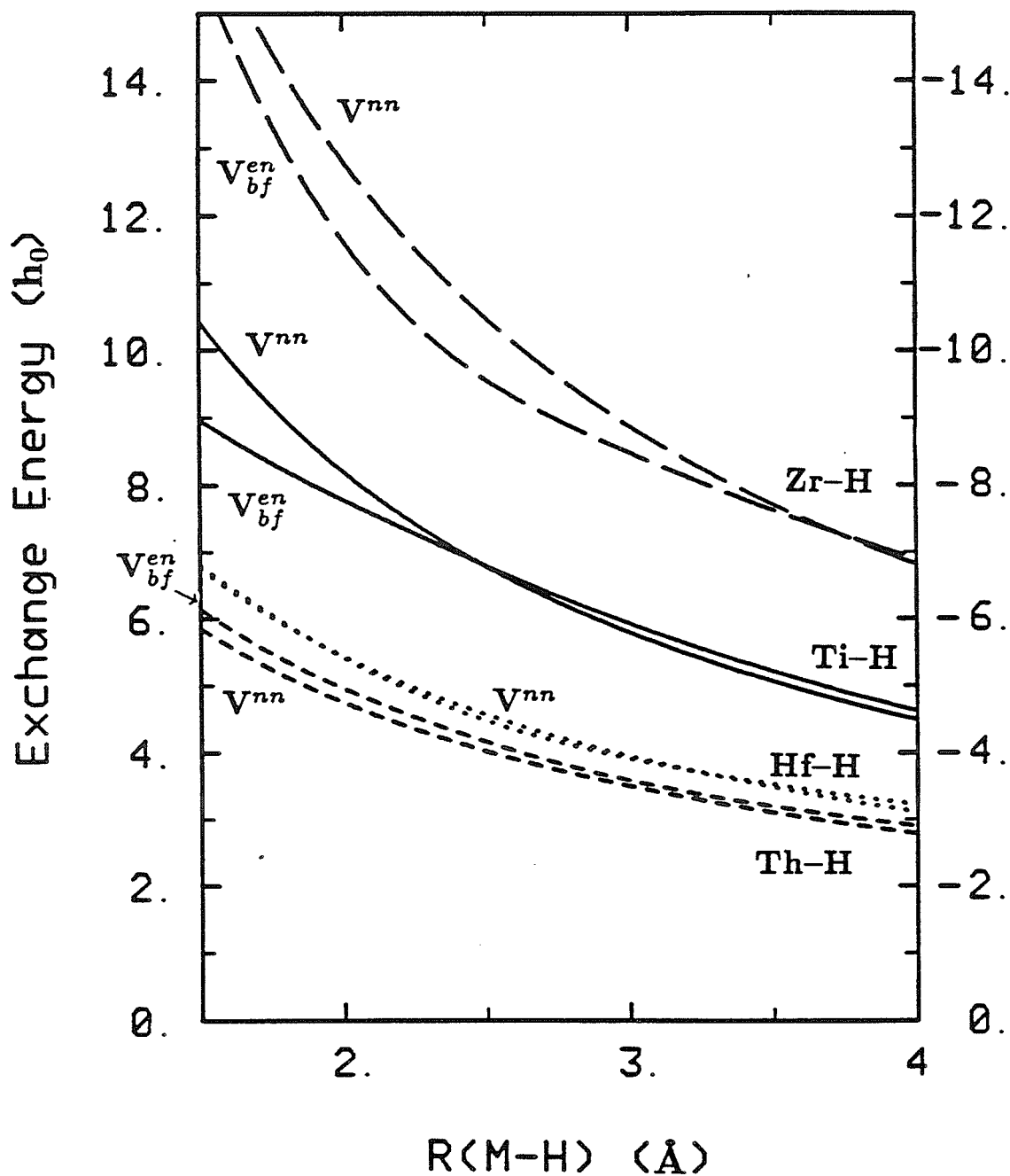
Figure 20a. The amplitudes of the frozen (solid) and relaxed (dotted) bonding orbitals of Cl_2HTi-H plotted along a line connecting the two nuclei at r_e .
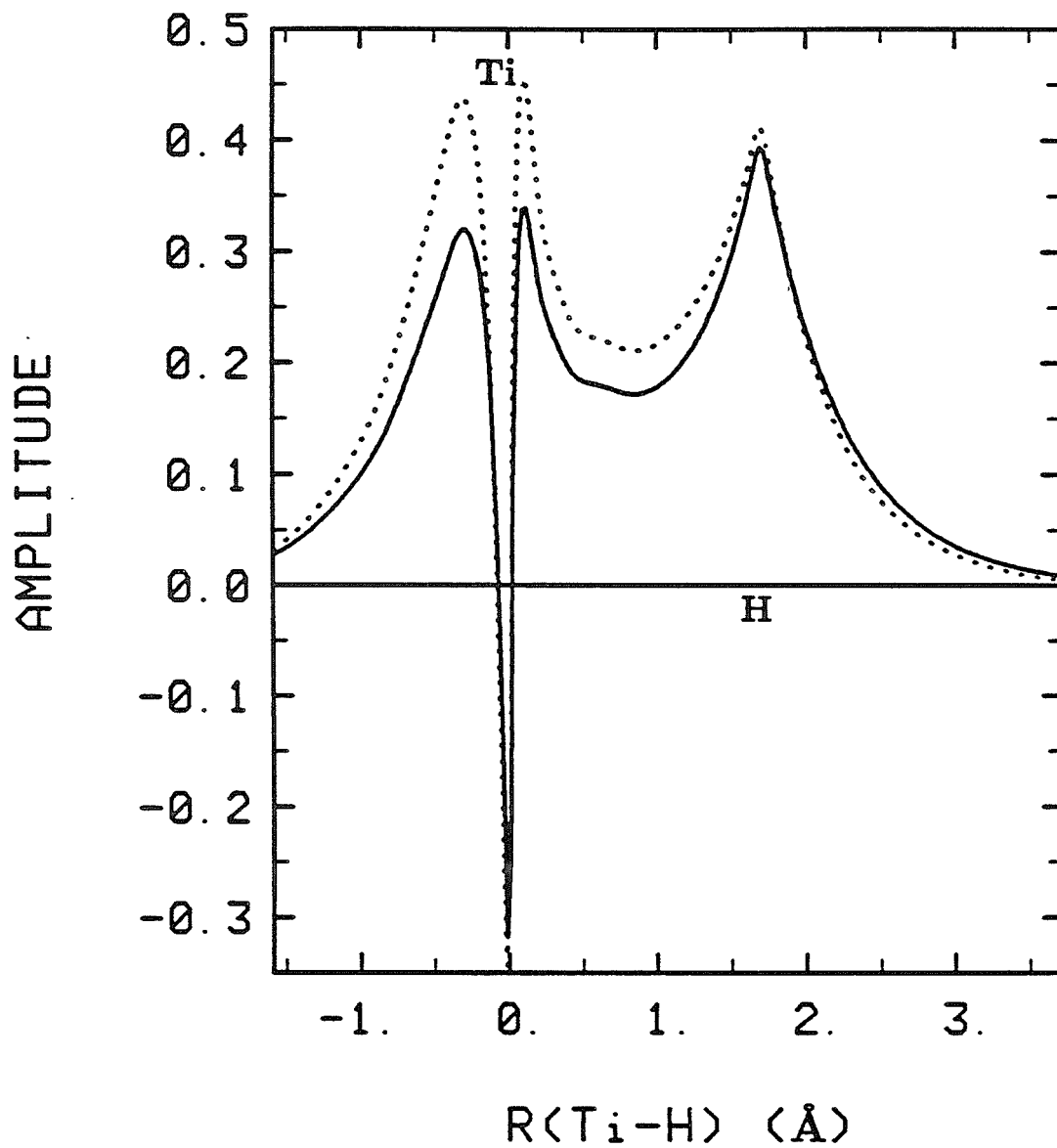
Figure 20b. The amplitudes of the frozen (solid) and relaxed (dotted) bonding orbitals of Cl_2HZr-H plotted along a line connecting the two nuclei at r_e .
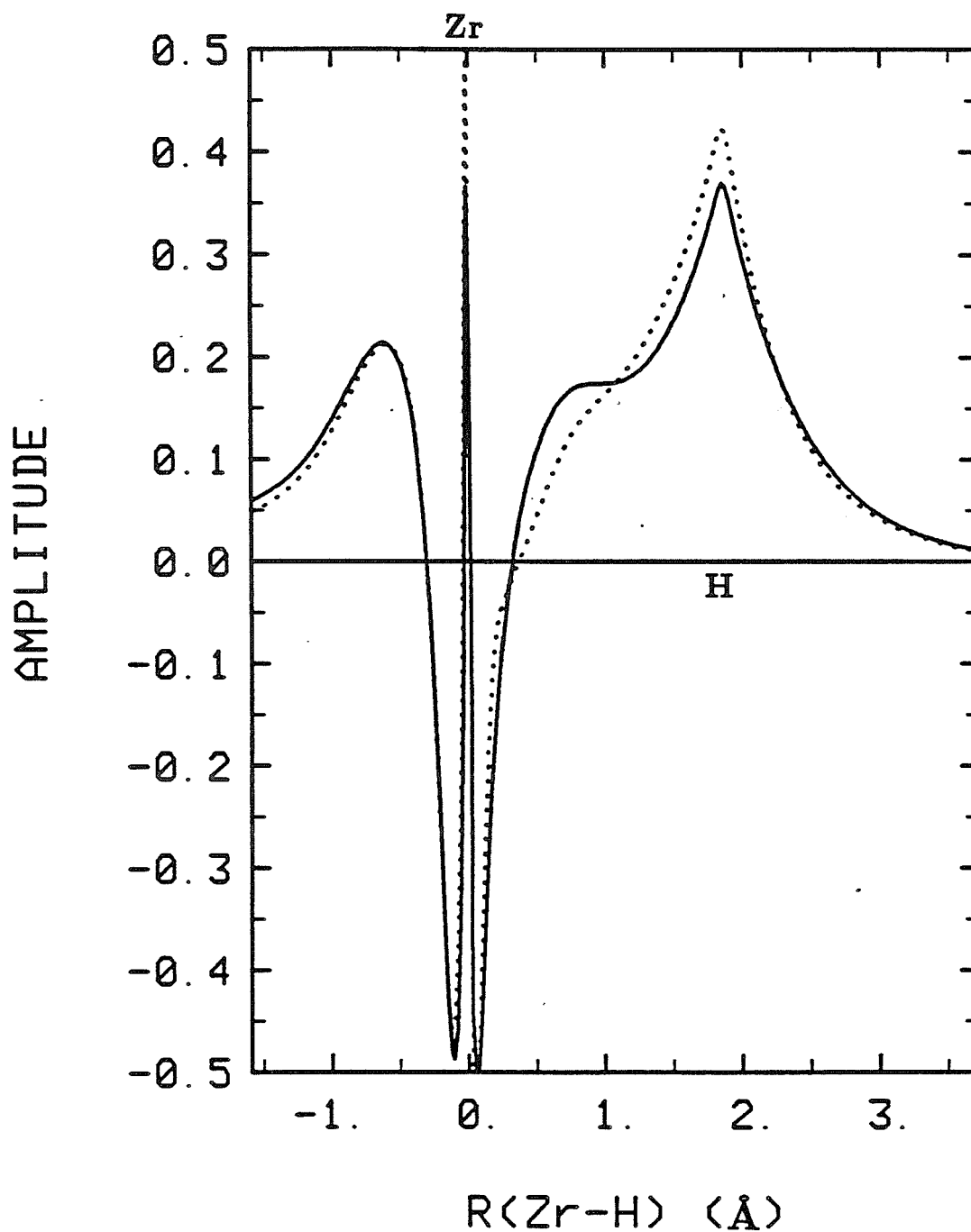
Figure 20c. The amplitudes of the frozen (solid) and re-
laxed (dotted) bonding orbitals of Cl_2HHf-H plotted along
a line connecting the two nuclei at r_e
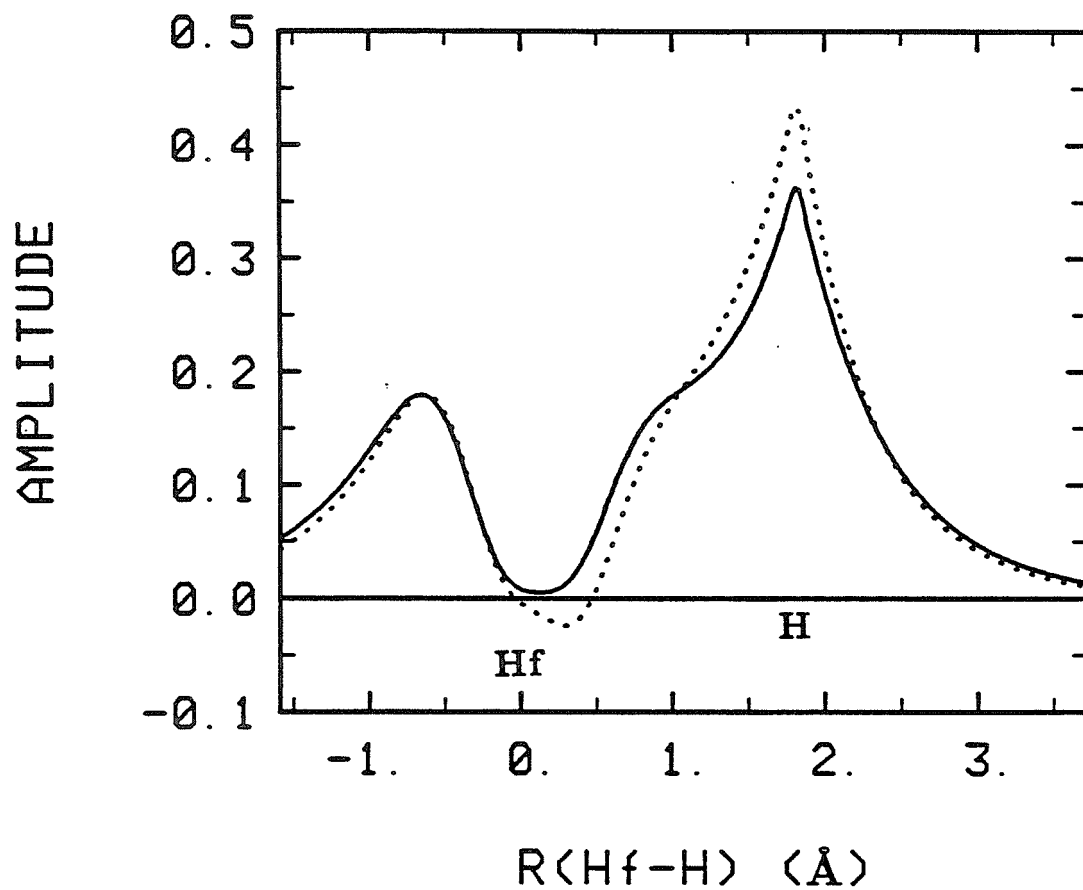
Figure 20d. The amplitudes of the frozen (solid) and re-
laxed (dotted) bonding orbitals of Cl_2HTh-H plotted along
a line connecting the two nuclei at $r_{e,.}$.
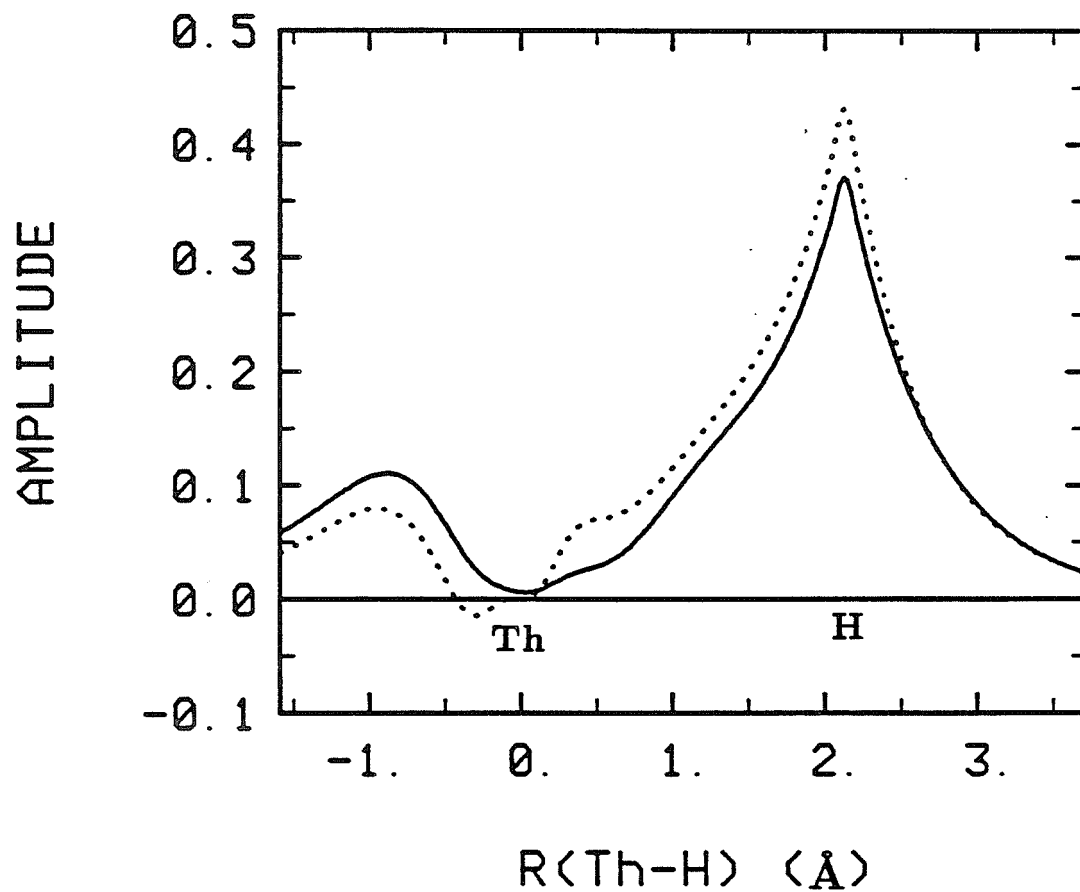
Appendix A

Metallacyclobutadiene
Versus
Metallatetrahedrane
Structures for $Cl_3MoC_3H_3$ Complexes

The text of this section is an Article coauthored with Eric V. Anslyn and William A. Goddard III which appeared in *Organometallics*.

METALLACYCLOBUTADIENE

VERSUS

METALLATETRAHEDRANE

STRUCTURES FOR $Cl_3MoC_3H_3$ COMPLEXES

Eric V. Anslyn, Mark J. Brusich, and William A. Goddard III

Contribution No. 7586 from the Arthur Amos Noyes Laboratory

of Chemical Physics, California Institute of Technology,

Pasadena, California 91125

ABSTRACT: The bonding and energetics in the $Cl_3MoC_3H_3$ metallacyclobutadiene are contrasted with those in the metallatetrahedrane. The complexes are found to be within 20 kcal/mol of one another, with the metallatetrahedrane being the lower in energy. The Mo-C bonds are essentially covalent in both structures and the metallacyclobutadiene possesses resonance stabilization. Charge distribution in the carbon fragments reveals no cyclopropenium character in the C_3H_3 ring of the metallatetrahedrane. Bonding, energetics, and charge distributions are all discussed with an emphasis on structure and reactivity.

I. INTRODUCTION

Metallacyclobutadienes **A** are believed to play the same role in acetylene metathesis[1] [eq (1)] as metallacyclobutanes **B** play in olefin metathesis,[2] [eq (2)]. Strong evidence for the role of **A** in acetylene metathesis is provided by the isolation and crystal structures of the following complexes: **1.** $W[C(CMe_3)(CMe)_2]Cl_3$,[3] **2.** $W(C_3Et_3)[O-2,6-C_6H_3(iPr)_2]_3$,[4] and **3.** $W(C_3Et_3)[OCH(CF_3)_2]_3$.[5] Unfortunately, not all of the metallacyclobutadienes isolated are active catalysts.[5-7] Species **2** and **3** are, however, isolated as end products from catalytically active systems.[4,5] Despite the experimental observation of these species, there remain a number of questions concerning the bonding in these complexes. Are the complexes best viewed as metallacyclobutadienes, and, if so, is there resonance stabilization or destabilization in the π system? The x-ray structures of **1**, **2**, and **3** reveal a particularly short W-βC distance ranging from 2.093 to 2.159 Å—only about 0.2 Å longer than the W-αC bond.[3-5] This naturally led to speculation that there might be a bonding interaction between W and the β carbon, and that **1**, **2**, and **3** might be structurally or electronically different from the metallacycles presumed to form in the catalytically active systems. Further studies of dialkylacetylene metathesis involved varying the steric bulk of the alkyl groups on the metallacycle carbons and of the axial-equatorial ligands. The conclusion reached was that sterics are the overriding factor influencing the rate of metathesis and thus the stability of the metallacycle.[4-7]

The fate of **1** in the presence of excess diethylacetylene is not that of metathesis but of cyclopentadienyl formation. Surprisingly, two cyclopentadienyl complexes (**4** and **5**) are formed.[7] The simplest mechanism which would give rise to a cyclopentadienyl complex is one in which the alkyne coordinates and then inserts into a W-alpha C bond to yield a tungstenabenzene intermediate, which

$$LnM \equiv CR + RC \equiv CR \rightleftharpoons \underset{A}{\left[\begin{array}{c} LnM = CR \\ | \quad \| \\ RC = CR \end{array} \right]} \rightleftharpoons \underset{RC}{\overset{LnM}{\|}} + \underset{CR}{\overset{CR}{\|}} \qquad 1$$

$$LnM = CR + RC = CR \rightleftharpoons \underset{B}{\left[\begin{array}{c} LnM - CR \\ | \quad | \\ RC - CR \end{array} \right]} \rightleftharpoons \underset{RC}{\overset{LnM}{\|}} + \underset{CR}{\overset{CR}{\|}} \qquad 2$$

Cl_3W — (structure) **1**

$[C_6H_3(i\text{-}Pr)_2\text{-}O\text{-}]_3W$ — (structure) **2**

$[(CF_3)_2CHO]W$ — (structure) **3**

WCl₃ — (structure) **4**

WCl₃ — (structure) **5**

6
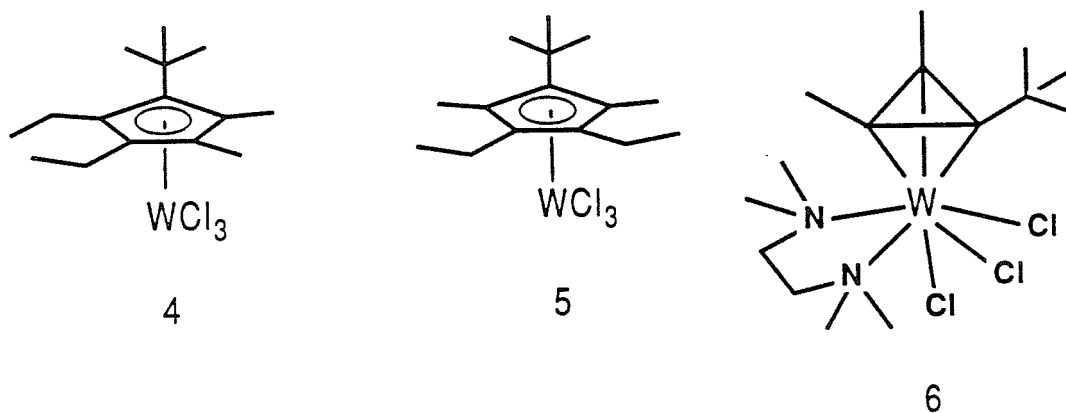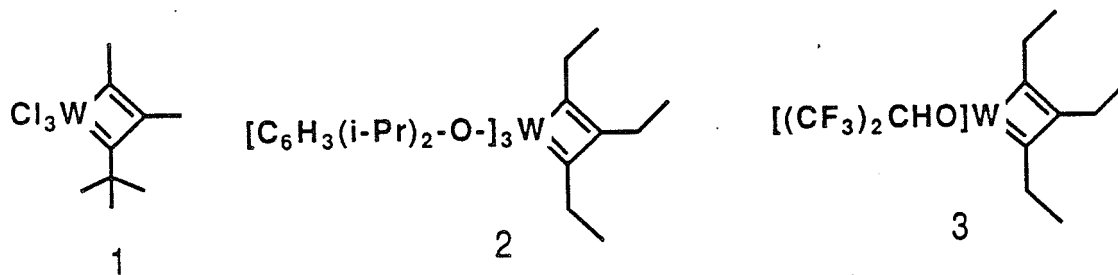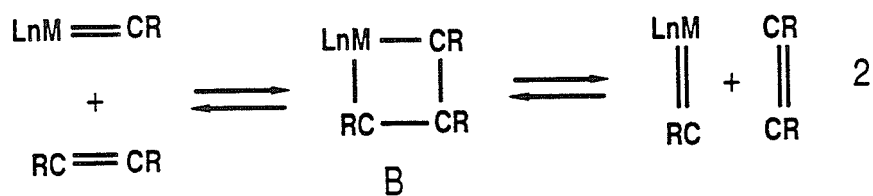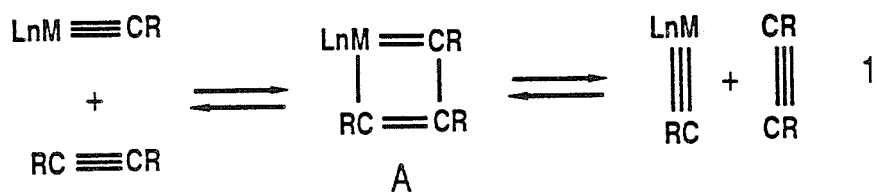
then collapses to a cyclopentadienyl complex. Such a route should yield only
4. A possible answer to this problem[7] was suggested following the isolation of
6 $W[C_3Me_2(CMe_3)][TMEDA]Cl_3$ from the reaction of 1 and TMEDA (tetram-
ethylethylenediamine). The complex is pseudo-octahedral and contains a *symmet-
rically bound* η_3-cyclopropenyl ligand. This interconversion between a metallacy-
clobutadiene and a metallatetrahedrane allows for the formation of the two cy-
clopentadienyl complexes by rotation of the η_3 ring, and thus isomerization of the
alkyl groups in the metallacyclobutadiene.

The structure of 6 revealed that the ring substitutents all bend up out of the
plane of the carbon ring.[7] The original investigators[7] explain this in terms of steric
interactions between the ring groups and the W ligands. The origin of this interac-
tion is presumably due to the carbon ring being drawn close to the metal due to the
latter's electron deficiency. These investigators[7] proposed W(IV) and $(C_3R_3)^-$ but
did not rule out that the tungstenatetrahedrane is W(VI) with a $(C_3R_3)^{3-}$ ligand.
They suggested that $(C_3R_3)^+$ with W (II) seemed least satisfactory.

The interconversion between metallatetrahedrane and metallacyclobutadiene
has been treated theoretically for the general case where an ML_n fragment cleaves a
C-C bond of the metallatetrahedrane to give a metallacyclobutadiene.[8] Equilbrium
geometries for several ML_n and C_3R_3 fragments were predicted, but detailed analy-
ses of bonding and energetics were not presented. Therefore we undertook to study
in detail a specific system of considerable current experimental interest.

The experimental studies suggest several questions which lend themselves to
detailed theoretical analysis. What is the nature of the W-C bonding interaction
in the metallacyclobutadiene and the metallatetrahedrane; is it mostly covalent or
ionic? Is there resonance stabilization or destabilization in the metallacyclobutadi-
ene? What are the charges on the carbon fragments and how large is the electron

deficiency of each species? Is there any W-βC bonding interaction in the metallacyclobutadiene? What are the relative energetics between the two structures and why do they interconvert so readily? Is there any barrier to rotation of the C_3R_3 ring in the metallatetrahedrane species? What role do the electron-withdrawing ligands play in the energetics of the species?

II. CALCULATIONAL DETAILS

A. *Basis Sets and Effective Potentials*

All electrons were considered explicitly for C and H but effective potentials were used to replace core electrons of Cl and Mo. For Cl, the Ne core was replaced with the SHC effective potential[9] (treating neutral Cl with seven explicit electrons) and for Mo, a relativistic effective potential[10] was used for the Zn core (treating neutral Mo with 12 explicit electrons). All calculations used Cartesian Gaussian basis sets. For carbon,[9] the (9s5p) primitive Gaussian basis was contracted to valence double zeta [3s, 2p].[11] For hydrogen,[9] the (3s) primitive basis was scaled ($\zeta = 1.2$) and contracted to (2s).[11] For Mo,[10] the basis set was contracted to [3s, 4p, 2d] from the primitive (3s, 5p, 3d). For Cl,[9] the (3s, 2p) primitive basis was contracted to [1s, 1p] based on $TiCl_4$.

B. *Wavefunctions*

Wavefunctions were calculated at the Hartree-Fock (HF), generalized valence bond (GVB) and generalized valence bond configuration interaction (GVB-CI) levels. For HF, the singlet state has all orbitals doubly-occupied,

$$\Phi^{HF} = \phi(1)\phi(2)(\alpha\beta - \beta\alpha) \tag{3}$$

but optimized self-consistently. This leads to a good description of bonds constructed from highly overlapping orbitals but a poor description of bonds involving low overlap (e.g., M-C pi bonds). The GVB wavefunction introduces electron correlation effects by allowing each electron to have its own orbital, which is then optimized self-consistently. For a typical two-electron bond, the GVB wavefunction has the form

$$\Phi^{GVB} = [\phi_\ell(1)\phi_r(2) + \phi_r(1)\phi_\ell(2)](\alpha\beta - \beta\alpha), \tag{4}$$

where ϕ_r and ϕ_ℓ are, in general, fairly localized on opposite atoms in the bond.

Because some electron pairs are well treated in HF [as in (1)], while others require correlation [as in (3)], GVB calculations often correlate only a portion of the bond pairs.[12] Generally, we correlated the pairs that change significantly during a reaction sequence and those that have large correlation errors. To indicate the level of correlation, the GVB wavefunction is denoted as GVB (n/m), where n is the number of electron pairs being correlated and m is the number of orbitals used for the correlated pairs (generally 2n). In the various $Cl_3Mo(C_3H_3)$ complexes, the 12 electrons involved in Mo-C and C-C bonding are correlated since these electrons change dramatically as the structure is changed from **7** to **8**. Thus we carry out GVB (6/12) level calculations. The shape of the self-consistent GVB orbitals is used to interpret the bonding characteristics of the wavefunction. We find that these six bond pairs have the following character: the metallacyclobutadiene **7** has two metallacycle π bonds, two Mo-C σ bonds, and two C-C σ bonds (leaving the other orbitals as self-consistent doubly-occupied orbitals). The metallatetratrahedrane involves three Mo-C bonds and three C-C bonds.

The self-consistent GVB calculations were restricted (perfect pairing) such that each correlated pair is constrained to have the form in Eq. (4). This leads to an excellent description of systems that are well described in term of one bonding structure (e.g., **8**) but not of systems involving strong resonance effects (as in **7**).

7a   **7b**   **8**
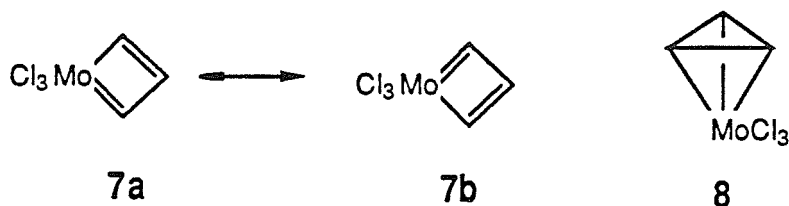
One approach to handling resonance in the GVB description is to optimize the orbitals for the resonating structures (**7a** and **7b**) self-consistently, while allowing different orbitals for the two structures.[13] This is termed GRVB (generalized resonating

valence bond) and has been applied to similar systems (e.g., cyclobutadiene).[14] An alternative approach is to start with the GVB orbitals for one bonding structure, say (7a), and then to carry out a configuration interaction calculation in which the occupation of the orbitals is allowed to change, permitting the orbitals to describe other resonance structures (e.g., 7b). For the metallacyclobutadiene, we used the latter approach. Thus for (a), the Mo-C and C-C sigma bonds were allowed to have all spin pairings within each set of natural orbitals in a given bond pair [not just the one in (4)]; this is termed GVB-RCI. We allowed all excitations within the four natural orbitals representing the GVB π bonds (GVB-CI). In addition, to allow readjustments in the shapes of the various orbitals in the presence of resonance, we allowed all excitations out of the dominant configurations into the entire valence space (GVB-RCI-S) for the Mo-C bonds in order to allow resonance. For the metal-latetrahedrane, the C-C bonds were described with GVB-RCI and the Mo-C bonds with GVB-CI.

III. RESULTS AND DISCUSSION

First, we will examine the GVB description of the bonding in both the metallacyclobutadiene and the metallatetrahedrane with an emphasis on qualitative aspects. Next, we examine charge distribution, and finally we will compare relative energetics between the two complexes. This will all be done with an emphasis on reactivity.

A. Geometries

The structures for the two geometries are presented schematically in Figure 1. Mo was used in place of W for calculational convenience. It is felt that because of the close correspondence of reactivity and structures for W and Mo, that this substitution will not significantly affect the trends calculated. In fact, similar alkylidyne,[15] metallatetrahedrane[16] and metallacyclobutadiene[15d] chemistry for Mo is already emerging and exhibits acetylene metathesis and polymerization activity. In addition, several acetylene metathesis systems based on Mo are known.[17] Furthermore, the covalent and ionic radii for Mo and W are similar,[18] so that no adjustment of the bond lengths and angles from the W crystal structure are expected.

In support of this assumption, a recent crystal structure of a less oxidized metallatetrahedrane, $CpMo(CO)_2(C_3Ph_3)$ showed bond lengths of approximately 0.1 Å longer than used in our calculation. This is as would be expected for a less oxidized species where the electron-rich C_3R_3 fragment is not held as close to the metal.

The goal of this study is to extract a conceptual understanding of 7 and 8 and of the relative bonding characteristics and relative energetics. Consequently, we based the geometries solely on crystal structure information. In cases where the crystal structure information could not be used to place the atoms, several geometries were calculated. For complex 8, we constrained the system to have equal Mo-C distances

and equal C-C distances, leading to C_{2v} symmetry in the Cl_3Mo (C_3H_3) complex. In complex **8**, however, the chlorines are not totally placed from crystal structure information and the TMEDA ligand was omitted. The Mo-Cl bond distances were derived from the crystal structure but the Cl positions relative to the cyclopropenyl fragment were placed in several arrangements, always retaining C_{3v} symmetry. The TMEDA ligand was deleted so that the two complexes have the same number of ligands and electrons, allowing a fair comparison of the relative energetics for these bonding types.

B. Orbitals

The contour plots of the GVB orbitals for the metallacyclobutadiene are presented in Figure 2, and the GVB orbitals for a metallatetrahedrane in Figure 3. As discussed in Section II.B, each GVB orbital has **one** electron, but the two orbitals of a bond pair are allowed to overlap, forming a wavefunction as presented in Eq. (2).

1. Bonding in the Metallacyclobutadiene

As indicated in Figure 2, the metallacyclobutadiene has covalent Mo-C_1, $C_1 - C_2$, $C_2 - C_3$, and Mo-C_3 σ bonds and covalent $C_1 - C_2$ and Mo-C_3 π bonds. Thus, the name metallacyclobutadiene is appropriate. Considering both resonance structures (**7a** and **7b**), the bond order is $1\frac{1}{2}$ for each (Mo-C) and (C-C) bond. The result is that three d orbitals on the Mo are involved in the bond to the C_3H_3 fragment. The other three valence electrons initially on Mo are involved in partially ionic bonds to the three Cl atoms.

The C_3H_3 framework has a central bond angle of 118.1°, and the C-C bond pairs are well directed along the bond axes (unstrained). However, Figures 2a and 2b show that the Mo-C single bonds are strained. The center of the C lobe of the GVB bond is at an angle of 120° with respect to the $C_1 - C_2$ axis (as if it were

going to point at the H of planar allyl), leading to an angle of 42° off the line joining Mo and C_1. Similarly, the d-like bonding orbital on the Mo points about 22° off of the Mo-C_1 vector, leading to a bent bond. The net result is that the two Mo d-like orbitals form Mo-C bonds lying at an angle of 129° with each other. This is quite consistent with the prediction of Rappé and Goddard[19] who showed that in order for two pure d orbitals to each be symmetric about their respective bond axes, the angle must be 125.3°.

The C-C π bond (Figure 2h) is conventional, involving px orbitals on each carbon. The Mo-C π bond (Figure 2g) is quite covalent, involving one orbital that is Mo d-like ($d_{xy} + d_{ys}$) and one that is Cp_x. A cross section through these π bonds in a plane parallel to the MoC_3H_3 plane (xz) but displaced 0.5 Å (in the y direction) reveals some bonding delocalization of the C-C π bond onto the Mo-C π bond (in Figures 2e and 2f) and some delocalization of the Mo-C π bond onto the C-C π bond. In fact, this delocalization from the Mo-C π bond to the C-C π bond is about equal on each carbon. In addition, the delocalization of the C-C π bond to the Mo-C π bond is about equal on both the C and the Mo. Thus, *neither of these bonds has any significant interaction between Mo and the β C* but only delocalization stemming from a resonance contribution. The contour plots (Figure 2) show that there is no significant bonding interaction between the Mo and the βC. The C-C σ framework is sp^2 (Figures 2c and 2d) with a C-C-C and H-C-C bond angle of ~120°. The combination of a C-C-C bond angle of 118° with bent Mo-C single bond leads to a short Mo-beta-C distance. The geometry thus is a balance struck between the small C-Mo-C angle and the restraint of forming two good C-C bonds with a bond order of 1.5. There is no a Mo-βC bonding interaction.

A contrasting view is presented by Bursten,[20] who performed Fenske-Hall[21] molecular orbital calculations and found a significant W-β carbon interaction in

the butadienoid core $[WC_3H_3]^{3+}$. Bursten's results are best portrayed by using perturbational molecular orbital theory (PMOT). The interaction of the two occupied orbitals (A_2, B_2) of allyl radical with the two $d\pi$ orbitals on W produce the two bonding orbitals presented below.

b_2 a_2
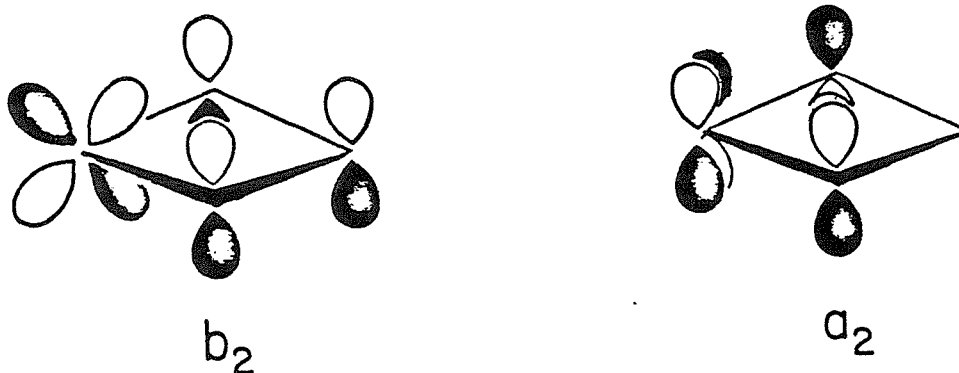
As is seen in the b_2 orbital, there is considerable W-β carbon bonding. Linear combinations of these orbitals do not produce localized π bonds as described in our GVB calculations.

The results from ab initio calculations are quite different. The $d\pi$ bonds that were used to build molecular orbitals in the PMOT approach are instead used to make localized π bonds which are then allowed to resonate (7a and 7b). This approach allows for a full 1.5 bond order between the carbons and also includes electron correlation in the bond pairs. This metalloaromatic system is thus stable because of the two $d\pi$ symmetry orbitals that allow the metal to form two π bonds simultaneously (by resonance) with bond orders each less than 1. In contrast, cyclobutadiene, uses a *single* carbon p orbital to form the π interaction with *both* adjacent carbon p orbitals.[14]

There is also an additional resonance structure which could arise from the PMOT approach by second-order mixing of the antibonding allyl orbital and the b_2 orbital. This would yield the valence bond structure shown below.

$$Cl_3Mo \diamondslash$$
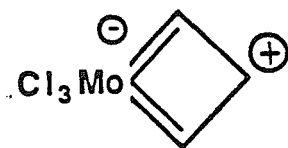
There is no significant mixing of this state in our ab initio calculations, as indicated by the positive charge of 0.86 found on the Mo and the small charge (-0.03) on the βC (see Section C and Figure 4).

To form the two Mo-αC bonds and two resonating π bonds, the Mo uses four of its five available d orbitals. The empty orbital is of d_{x^2} character and leads to a coordination of a ligand along the x axis. An acetylene coordinated along this axis could then insert into an Mo-αC bond to form a metallacyclohexatriene complex. In forming this insertion product, resonance is initially lost from the metallacyclobutadiene but is reintroduced in a hypothetical planar metallacyclohexatriene complex.

While the C-Mo-C angle prefers to be 125° to form the optimum directional dσ bonds, the axial Cl-Mo-Cl angle is expected to be large (166° in this case) due to high sp character (180° is optimal for two such bonds). Due to the high electronegativity of Cl, the Mo-Cl bonds are highly polarized toward Cl. These polar Mo-Cl bonds use Mo s orbitals since the ionization potential of the 5s electrons is less than for the 4d electrons. As a result of the charge transfer to the chlorines, the metal is positive, leading to covalent bonds to the carbons that are 4d-like and highly directed. This is the case in both the metallacyclobutadiene and the metallatetrahedrane.

2. Bonding in the Metallatetrahedrane

For the metallatetrahedrane, all GVB wavefunctions led to three covalent Mo-C bonds. All attempts to force another description such as a π allyl complex only resulted in reversion to the three covalent bond description. A typical Mo-C σ bond is in Figure 3a.

Each Mo-C bond involves a Mo d σ orbital pointing at an sp^3-like orbital of the C$_3$H$_3$ fragment to form a σ bond. The metallatetrahedrane Mo-C σ bonds are less directional (more spatially diffuse) than in the metallacyclobutadiene because the metal now is forced to make three σ bonds rather than two. The bond is slightly bent ($\sim$12°) from the bond axis, leading to an angle of 63° between ends of the Mo-d orbitals involved in each Mo-C bond. This small angle is created by the short C-C distance compared with the Mo-C distance. Rappé and Goddard[22] showed that the equivalent orthogonal d orbitals, each rotationally symmetric about its bond axis, must be at an angle of 54.7°, in reasonable agreement with the calculated results. A contour map of the C-C bond is shown in Figure 3b. It involves typical sp^3 orbitals localized on each carbon with no interaction with the metal.

C. Charges

Reactivity in transition metal complexes is controlled by the charge distributions between the metal and its ligands and by the nature of the metal-ligand bonds. The proposed reactivity of the metallacyclobutadiene in coordinating an acetylene requires that the metal center have an empty orbital and be electrophilic. The metallacyclobutadiene is a 12-electron species and therefore has empty orbitals. It is also calculated to be electrophilic, with the metal having a high positive charge of 0.86. In this complex, each chlorine takes approximately 0.34 electrons (see Figure 4 for all Mulliken populations). The alpha carbons are slightly negative and the beta carbon is neutral. This charge distribution of the organic ligand is basically covalent, with no large charge polarization between the Mo and the C's. This is also apparent by viewing the contour maps 2a and 2b. Each one-electron orbital is essentially centered on the individual atoms.

The chlorine-to-molybdenum bonds behave the same in both complexes. The chlorines serve to remove s electron density from the metal. In each case, the

chlorines take about 1.1 electrons and leave the positive charge to be dispersed among the Mo and the organic fragment.

The metallatetrahedrane has a similar charge distribution as the metallacyclobutadiene. Each chlorine takes about 0.36 of an electron and leaves the Mo with a positive 0.74 charge and the ring with a positive 0.34 charge (0.34 for the tetrahedrane, 0.19 for the butadiene). Again, the carbons have a slight negative charge, reflecting a higher electronegativity than Mo or H. This is as expected for a covalent Mo-C interaction.

In order to explore how charge transfer is affected by geometry of the C_3H_3 ring, we recalculated the wavefunction with a flat C_3H_3 ring (the original geometry had the H's bent back by 44°). Since $C_3H_3^-$ is "anti-aromatic", this might lead to a propensity for $C_3H_3^+$ and hence charge transfer to the metal. Indeed, the carbons lose 0.18 electrons to obtain a net charge of +0.52, while the metal gains 0.12 electrons to obtain a net charge of 0.86. Basically, the strong tendency for the Mo and the C's to form covalent Mo-C bonds prevents charge flow from the ring in either the flat or bent up hydrogen geometry. Furthermore, metallatetrahedrane with the flat C_3H_3 geometry is 6 kcal/mol [GVB (6/12)] above the system with a nonplaner C_3H_3 geometry. Although this bent back geometry is favored by steric interactions with the metal ligands, we believe that the dominant factor is the covalent metal-carbon bonding. Hence, the "bend-back angle" is a guide to the true metallatetrahedrane character in the bonding. Every metallatetrahedrane may have different bend-back angles depending on the charge distribution between the metal and the carbon ring, the oxidation state of the metal, and the steric requirements of the ligands on the metal and the alkyl groups on the carbon ring. In summary, the charge transfer is dominated by the nature of the M-C bonds. Because of the greater polarity in its Mo-C σ bond, the Mo in the metallacycle is more electrophilic

than in the metallatetrahedrane.

D. Geometries and Energies

A dominant factor in the interconversion of the metallacyclobutadiene and metallatetrahedrane is the difference in ground state energies. In Figures 5 and 6, the energy separations between the metallacycle and the metallatetrahedrane are shown for various levels of theoretical treatments.

The metallacycle has four σ bonds, two of which are Mo-C and two are C-C. It also has one Mo-C π bond and one C-C π bond. The metallatetrahedrane also has six covalent bonds, three of which are Mo-C and three are C-C. Taking GVB overlaps as a rough guide to relative bond strengths, the total bond strength would be approximately the same since the sums of the overlaps are approximately the same (Table I). This neglects strain effects and resonance which favors the metallacycle and also neglects the energetics associated with the chlorine ligand geometries.

The placement of the chlorine ligands in the metallatetrahedrane was calculated in several geometries. Calculations were done at both 109° and 90° for the angle between the Cl's (the Cl-Mo-Cl angle). The 109° geometry is lower in energy by 44.0 kcal (for $MoCl_3$ high spin quartet, the 109° geometry is favored by 24.8 kcal). These energy differences are due to the decreased steric interaction between the chlorines in the 109° geometry.

The second geometry change was to stagger or eclipse the Cl's with the carbons of the C_3H_3 ring. The various geometries and their relative energies are presented in Figures 5 and 6. From calculations of the staggered and eclipsed geometries of the metallatetrahedrane with respect to the Cl's, we found that the *eclipsed* conformation is significantly lower than the staggered (by 18 to 45 kcal). In order to investigate the origin of this effect, we calculated the quartet state of free $MoCl_3$,

arriving at the localized orbitals for the $MoCl_3$ fragment presented in Figure 7. These orbitals are the ones used to bond the C_3H_3 fragments and are linear combinations of the orbitals in Figure 8. These localized high spin orbitals are *eclipsed* with respect to the chlorines. Thus, the origin of the eclipsed preference for the tetrahedrane is in the $MoCl_3$ fragment. Since the free $MoCl_3$ quartet state prefers to have an eclipsed set of d orbitals, the metallatetrahedrane bonds to the C_3H_3 fragment and leads to the eclipsed geometry. The staggered geometry requires rehybridization of $MoCl_3$ orbitals in order to bond to the C_3H_3 fragment.

The high spin orbitals for the $MoCl_3$ fragment are presented in Figure 8. Mixing these frontier orbitals with the frontier orbitals of the cyclopropenium quartet state lead to the orbital interaction diagram of Figure 9 (no energy scale intended). The 1e and $1a_1$ orbitals on the metal are of the correct symmetry to mix with the equivalent symmetry orbitals of the cyclopropenium fragment *only* in an eclipsed geometry. Thus, covalent three-coordinate early transition metal systems (where the $1a_1$ and 1e set of orbitals is only singly-filled) prefer to make covalent bonds to three other substituents in an eclipsed geometry. As these orbitals fill, the preference for a staggered (octahedral) geometry becomes stronger. Steric interactions could also lead to a preference for staggered and are probably the dominant interactions in most experimental systems. Thus, in Group VIII metal systems where these orbitals are filled (e.g., $Cl_3Fe^{\ominus}Me_3$,[23]), the geometry would be staggered due to the symmetry of the high lying 2e and $2a_1$ orbitals.[23]

Literature structures related to these conclusions are limited to the trigonal prism complexes of early transition metals with dithiolato bidentate ligands.[24] It has been suggested that these complexes are eclipsed due to S-S bonding interactions.[25] Since this suggestion, dithiolato complexes have been isolated with S-S distances greater than the sum of the covalent radii.[26] We propose that the eclipsed preference

is instead due to the electronic effects presented above.

The preference for eclipsed geometries derives from the high-spin $MoCl_3$ fragment. This fragment has been calculated previously, and our calculations confirm the past results.[27,28] The $1e_1$ orbitals are tilted from the axis due to mixing of d_{xy} with d_{xz} and $d_{x^2-y^2}$ with d_{yz}. The question of bonding then reduces to why the $1e_1$ orbitals mix in such a fashion so as to prefer eclipsing. Calculations on $MoCl_3$ at several Cl-Mo-Cl angles reveal the preference for the high-spin orbitals to lie in the nodal planes of the Mo-Cl bonds. This allows for the least repulsion due to orthogonality between various occupied orbitals. It can be seen in Figure 8 that the $d_{x^2-y^2}$ and d_{yz} combination lies with the positive lobe directly between two Mo-Cl bonds. Conversely, the d_{xy} and d_{xz} combination has an angular node placed directly along an Mo-Cl bond. In this manner the high-spin orbitals prefer to make bonds directly over the Mo-Cl bonds.

E. Electron Correlation

The above calculations used the simple GVB-PP wavefunction where the orbitals are optimized for a single bonding structure (for spin coupling). Thus these calculations are biased *against* this fully delocalized metallacycle, which requires two configurations.

In order to elucidate further the energetic differences between the metallatetrahedrane and the metallacyclobutadiene, we undertook several calculations designed to allow resonance in the metallacyclobutadiene.

An Mo atom with three unpaired d orbitals prefers the high spin state (Hund's rule) in which all three d electrons have the same spin, say α. However, bonding these electrons to ligands requires that the two electrons in the bond have opposite spins and that each electron has both α and β.
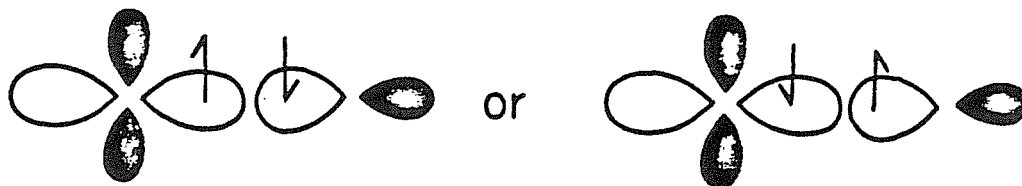
As a result, the d electrons on the metal can no longer all have the same spin. Thus the high spin coupling of the metal tends to inhibit full bonding to the ligands and vice versa. A proper description of these spin coupling effects requires bonding structures in which the two electrons of a given pair are allowed to be coupled either low spin (bonding) or high spin (antibonding). Such configurations are included in the GVB-RCI wavefunction, and we find that the metallacycle energy drops 6.28 kcal/mol more in the RCI than does the tetrahedrane. The contribution from such excitations within each GVB π bond pair resulted in a 19.8 kcal/mol lowering (half the total RCI lowering). Comparison to the analogous excitations from the C-C σ bonds of the metallatetrahedrane shows only a 7.63 kcal/mol lowering.

In order to allow resonance to build into the metallacycle, a full GVB-CI in the π space was allowed, with simultaneous σ relaxations (single excitations out of the σ bonds). This gave a further lowering of 9.86 kcal/mol. The tetrahedrane was then subjected to a comparable calculation. It consisted of a full GVB-CI in the Mo-C space while leaving the RCI in the C-C space. This gave a further lowering of 6.56 kcal/mol. The final separation between the two geometries is 8 kcal/mol, favoring the metallatetrahedrane structure 2a. Due to the incorporation of resonance into the π system, these final CI's introduced a greater lowering for the metallacyclobutadiene than for the metallatetrahedrane.

The long Mo-C bond distances (in comparison to C-C bond distances) places the π bonds much further from one another than in cyclobutadiene.[14] This means that the repulsion from orthogonality that is so destabilizing in cyclobutadiene is much less evident in the metallacyclobutadiene and therefore the metallacycle takes

advantage of some resonance stabilization.[14] Analysis of the resonance configurations shows a resonance stabilization of 8.68 kcal/mol.

F. Implications for Chemistry

This study allows us to speculate about the mechanism of metathesis performed by metallacyclobutadienes. It is viewed as decomposition of the metallacycle to an acetylene-alkylidyne adduct which then loses the initial acetylene before or after coordinating a second acetylene. This reaction thus involves the slipping of an acetylene from a metallacycle to pi-coordination at the metal. The initial metallacyclobutadiene is a 12-electron species whereas the acetylene-alkylidyne complex is a 14-electron species. The movement of the acetylene thus increases the electron richness of the metal. A strong π electron donor ligand should slow this reaction. This is a direct consequence of filling the orbitals the acetylene is moving into, and thus making them less accessable. This logic is supported by the calculation of Rappé and Upton[29] for titanium metallacyclobutane olefin metathesis. In the titanium case, electron donating substituents on the titanium slow the metathesis reaction.[30] This is in direct contrast to the tungsten acetylene metathesis reaction where electron withdrawing groups are indicated by Schrock *et al.* to slow the metathesis reaction.[5] Thus, there is a contradiction and it would seem that the major effect operating in the tungsten metathesis systems is the steric environment imposed by the axial-equatorial ligands.

IV. SUMMARY

The Mo-C bonding in both the metallacyclobutadiene and the metallatetrahe-drane is covalent with no large polarization toward either Mo or C. The Cl's remove 5s electron density from the Mo, leaving the d electrons to form hybrids that bond to the carbon fragments. The positive charge induced by the large electronegative chlorines is dispersed among the metal and the organic fragments. The metalla-cyclobutadiene is more electrophilic than the metallatetrahedrane. This supports the notion that the metallacycle can coordinate an acetylene. The electrophilicity of the Mo in the metallacycle argues in favor of accepting electron density from the axial-equatorial ligands. However, in contrast to the proposal by the original investigators,[5] this acceptance would (on an electronic basis) slow the metallacy-cle decomposition to an acetylene-alkylidyne. The energy difference between the metallacycle and metallatetrahedrane shows that the two geometries are very close in energy (within 20 kcal/mol by all calculational procedures). This is due to covalent bonds in the metallatetrahedrane that make up for the increased strain energy. In contrast to cyclobutadiene, the metallacyclobutadiene shows resonance stabilization. There is no bonding interaction between the Mo and the β carbon in the metallacycle ring. The bending of the ring substituents out of the plane of the carbons in the metallatetrahedrane is due to bonding effects (hybridization at the carbons forming covalent bonds to the Mo) not steric interactions with the axial-equatorial ligands. There is a considerable barrier to rotation of the C_3H_3 ring in the metallatetrahedranae due to strong electronic preference for the eclipsed geometry.

References and Notes

(1) (a) Wengrovious, J. H.; Sancho, J.; Schrock, R. R. *J. Am. Chem. Soc.* **1981,** *103*, 3932; (b) Sancho, J.; Schrock, R. R. J. Mol. Catal. **1982,** *15*, 75.

(2) (a) Dragutan, V.; Balaban, A. T.; Dimone, M. "Olefin Metathesis and Ring Operning Polymerizations of Cyclo-Olefins"; Wiley-Interscience: Chichester, 1985; (b) Ivin, K. J. "Olefin Metathesis"; Academic Press: London, 1983; (c) Mol, J. C. *Chemtech* **1983,** *13*, 250; (d) Grubbs, R. H. in "Comprehensive Organometallic Chemistry"; Wilkinson, G., Ed.; Pergamon Press, Ltd.: Oxford, 1982; Vol. 8, pp 499-551; (e) Banks, R. L. *Catalysis* **1981,** *4*, 100.

(3) Pedersen, S. F.; Schrock, R. R.; Churchill, M. R.; Wasserman, H. J. *J. Am. Chem. Soc.* **1982,** *104*, 6808.

(4) Churchill, M. R.; Ziller, J. W.; Freudenberger, J. H.; Schrock, R. R. *Organometallics* **1984,** *3*, 1554.

(5) Freudenberger, J. H.; Schrock, R. R.; Churchill, R. M.; Rheingold, A. L.; Ziller J. W. *Organometallics* **1984,** *3*, 1563.

(6) (a) Schrock, R. R.; Clark, D. N.; Sancho, J.; Wengrovious, J. H.; Rocklage, S. M.; Pedersen, S. F. *Organometallics* **1982,** *1*, 1645; (b) Schrock, R. R.; Listermann, M. L.; Sturgeoff, L. G. *J. Am. Chem. Soc.* **1982,** *104*, 4291.

(7) Schrock, R. R.; Pedersen, S. F.; Churchill, M. R.; Ziller J. S. *Organometallics* **1984,** *3*, 1574.

(8) Jemmis, E. D.; Hoffmann, R. *J. Am. Chem. Soc.* **1980,** *102*, 2570.

(9) Huzinaga, S. *J. Chem. Phys.* **1965,** *42*, 1293.

(10) Hay, P. J., personal communication to Goddard, W. A. III.

(11) Dunning, Jr., T. H. *J. Chem. Phys.* **1970,** *53*, 2823.

(12) Bobrowicz, F. W.; Goddard III, W. A. in "Modern Theoretical Chemistry, Methods of Electronic Structure Theory"; Schaefer,H. F., III, Ed.; Plenum

Press: New York, 1977; Vol. 3, Chapter 4, pp 79-127.

(13) Voter, A. F.; Goddard, W. A., III *Chem. Phys.* **57**, *3*, 253.

(14) Voter, A. F.; Goddard, W. A., III *J. Am. Chem. Soc.* **1986**, *108*, 2830.

(15) (a) Fischer, E. O.; Kreis, G.; Kreiter, C. G.; Müller, J.; Huttner, G.; Lorentz, H. *Angew. Chem., Int. Ed. Engl.* **1973**, *12*, 564; (b) Clark, D. N.; Schrock, R. R. *J. Am. Chem. Soc.* **1978**, *100*, 6774; (c) Schrock, R. R.; Clark, D. N.; Sancho, J.; Wengrovious, J. H.; Rocklage, S. M.; Pedersen, S. F. *Organometallics* **1982**, *1*, 1645; (d) McCullough, L. G.; Schrock, R. R.; Dewan, J. C.; Murdyck, J. C. *J. Am. Chem. Soc.* **1985**, *107*, 5987.

(16) Drew, M. G. B.; Bresdon, B. J.; Day, A. J. *J. Chem. Soc., Dalton Trans.* **1981**, 1310, and references therein.

(17) (a) Mortreux, A.; Delgrange, J. C.; Blanchard, M.; Lubochinsky, B. *J. Mol. Catal.* **1977**, *2*, 73; (b) Devarajan, S.; Wlaton, O. R. M.; Leigh, G. J. *J. Organomet. Chem.* **1979**, *181*, 99; (c) Bencheick, A.; Petit, M.; Mortreux, A.; Petit, F. *J. Mol. Catal.* **1982**, *15*, 93; (d) Villemin, D.; Cachiot, P. *Tetrahedron Lett.* **1982**, 5139; (e) Petit, M.; Mortreux, A.; Petit, F. *J. Chem. Soc., Chem. Commun.* **1982**, 1385.

(18) Weast, R. C. "CRC Handbook of Chemistry and Physics"; CRC Press: Boca Raton, 1980.

(19) Rappé, A. K.; Goddard, W. A., III *J. Am. Chem. Soc.* **1982**, *104*, 297.

(20) Bursten, B. E. *J. Am. Chem. Soc.* **1983**, *105*, 121.

(21) Hall, M. B.; Fenske, R. F. *Inorg. Chem.* **1972**, *11*, 768.

(22) Rappé, A. K.; Goddard, W. A., III, unpublished results.

(23) Albright, T. A.; Hofmann, P.; Hoffmann, R. *J. Am. Chem. Soc.* **1977**, *99*, 7546.

(24) (a) Brown, G. F.; Stiefel, E. I. *Chem. Commun.* **1970**, 728; (b) Brown, G. F.;

Stiefel, E. I. *Inorg. Chem.* **1973**, *12*, 2140; (c) Eisenberg, R.; Ibers, J. A. *J. Am. Chem. Soc.* **1965**, *87*, 3776; (d) Smith, A. E.; Schranger, G. N.; Mayweg, V. P.; Heinrich, W. *J. Am. Chem. Soc.* **1965**, *87*, 5798.

(25) Gray, H. B.; Eisenberg, R.; Stiefel, E. I. *Advances in Chemistry Series* **1966**, *62*, 641.

(26) (a) Bennett, M. J.; Cowie, M.; Martin, J. L.; Takats, J. *J. Am. Chem. Soc.* **1973**, *95*, 7504; (b) Cowie, M.; Bennett, M. J. *Inorg. Chem.* **1976**, *15*, 1584, 1589.

(27) (a) Elian, M.; Hoffmann, R. *Inorg. Chem.* **1975**, *14*, 1058; (b) Elian, M.; Chen, M. M. L.; Minges, D. M. P.; Hoffmann, R. *Inorg. Chem.* **1976**, *15*, 1148; (c) Burdett, J. K. *Inorg. Chem.* **1975**, *14*, 375.

(28) Orgel, L. E. "An Introduction to Transition Metal Chemistry"; Wiley: New York, 1960; p 174.

(29) Upton, T. H.; Rappé, A. K. *J. Am. Chem. Soc.* **1981**, *103*, 5582.

(30) Finch, W. C.; Anslyn, E. V.; Grubbs, R. H., unpublished results.

Table I. Orbital overlaps for the GVB pair orbitals.

Metallacyclobutadiene		Metallatetrahedrane	
Bond	Overlap	Bond	Overlap
Mo-Cα	0.74	Mo-C	0.67
Mo-Cα	0.74	Mo-C	0.67
Mo-Cπ	0.53	Mo-C	0.67
C-Cπ	0.71	C-C	0.83
C-Cσ	0.87	C-C	0.83
C-Cσ	0.87	C-C	0.83
	--		--
Total	4.46	Total	4.50

FIGURE CAPTIONS

Figure 1. Calculated structures for the metallatetrahedrane and the metallacyclobutadiene.

Figure 2. Contour plots for the GVB-PP orbital of metallacyclobutadiene. Spacing between contours is 0.05 a,u.; solid lines are positive and dashed lines are negative.

Figure 3. Contour plots for the metallatetrahedrane.

Figure 4. Mullikan populations for each atom in the metallatetrahedrane and metallacyclobutadiene.

Figure 5. Ground state energy difference of several metallatetrahedranes and the metallacyclobutadiene at the GVB(6/12) level.

Figure 6. Ground state energy differences of the metallatetrahedrane and the metallacyclobutadiene at the CI level.

Figure 7. Singly-occupied orbitals localized over the Cl's of the quartet state of $MoCl_3$.

Figure 8. Singly-occupied orbitals of the quartet state of $MoCl_3$.

Figure 9. Orbital interaction diagram showing the preference for the eclipsed geometry arises from the ground state high-spin orbitals of $MoCl_3$.
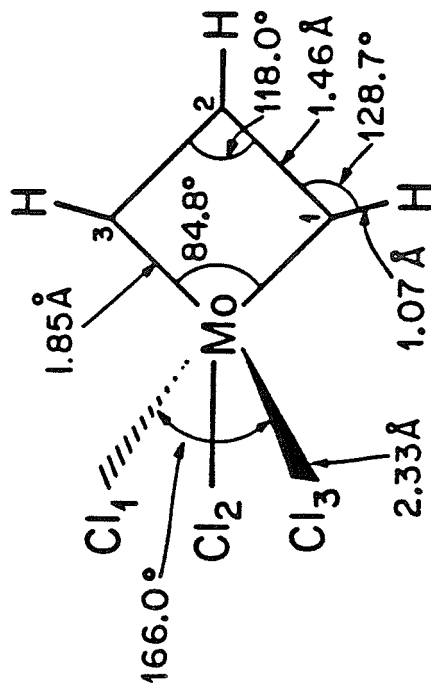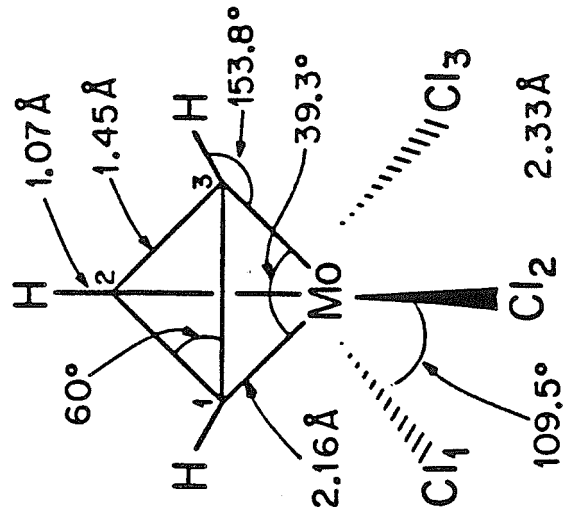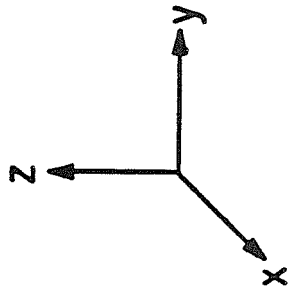
Figure 1.
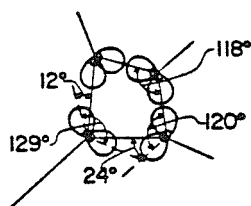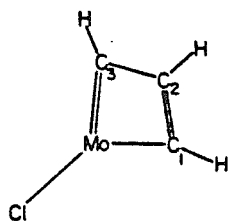
(a) Mo-C$_1$ Sigma Bond Pair
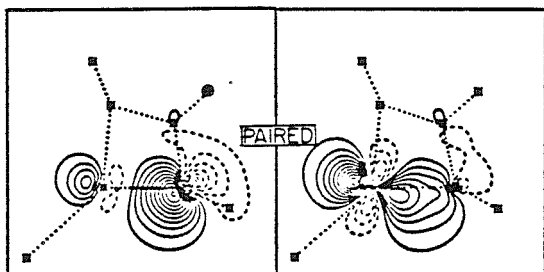
(b) Mo-C$_3$ Sigma Bond Pair
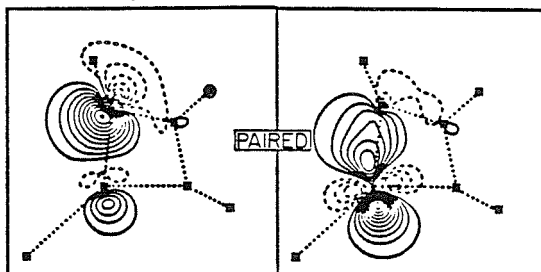
(c) C$_1$-C$_2$ Sigma Bond Pair
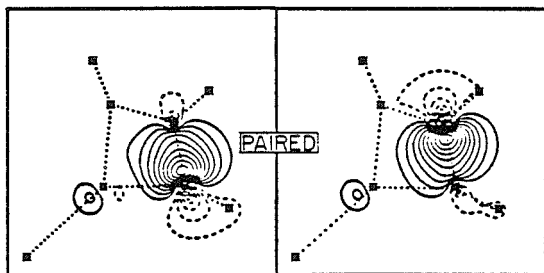
(d) C$_2$-C$_3$ Sigma Bond Pair
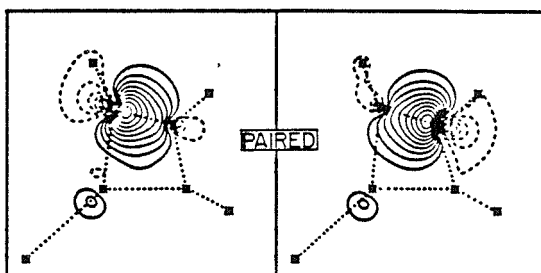
(e) Mo-C$_3$ Pi Bond Pair
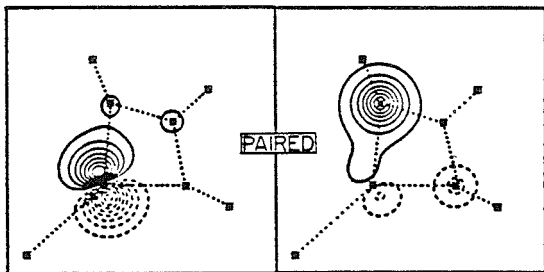
(f) C$_1$-C$_2$ Pi Bond Pair
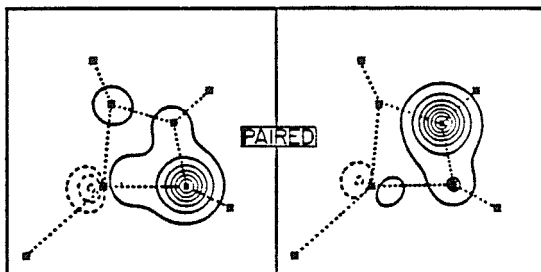
(g) Mo-C$_3$ Pi Bond Pair
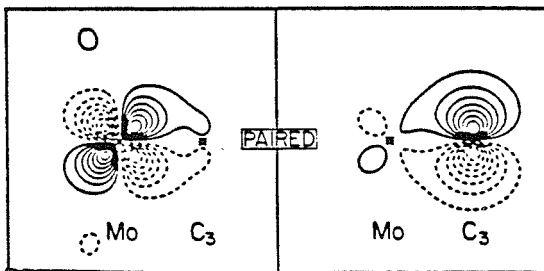
(h) C$_1$-C$_2$ Pi Bond Pair

Figure 2.

(a) Mo-C Bond Pair

(b) C-C Bond Pair

PAIRED
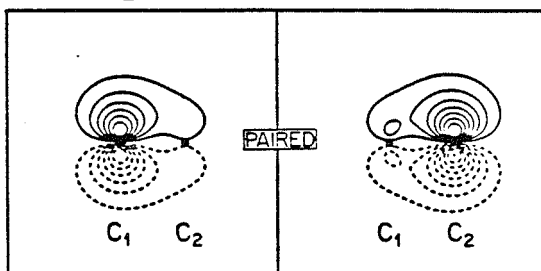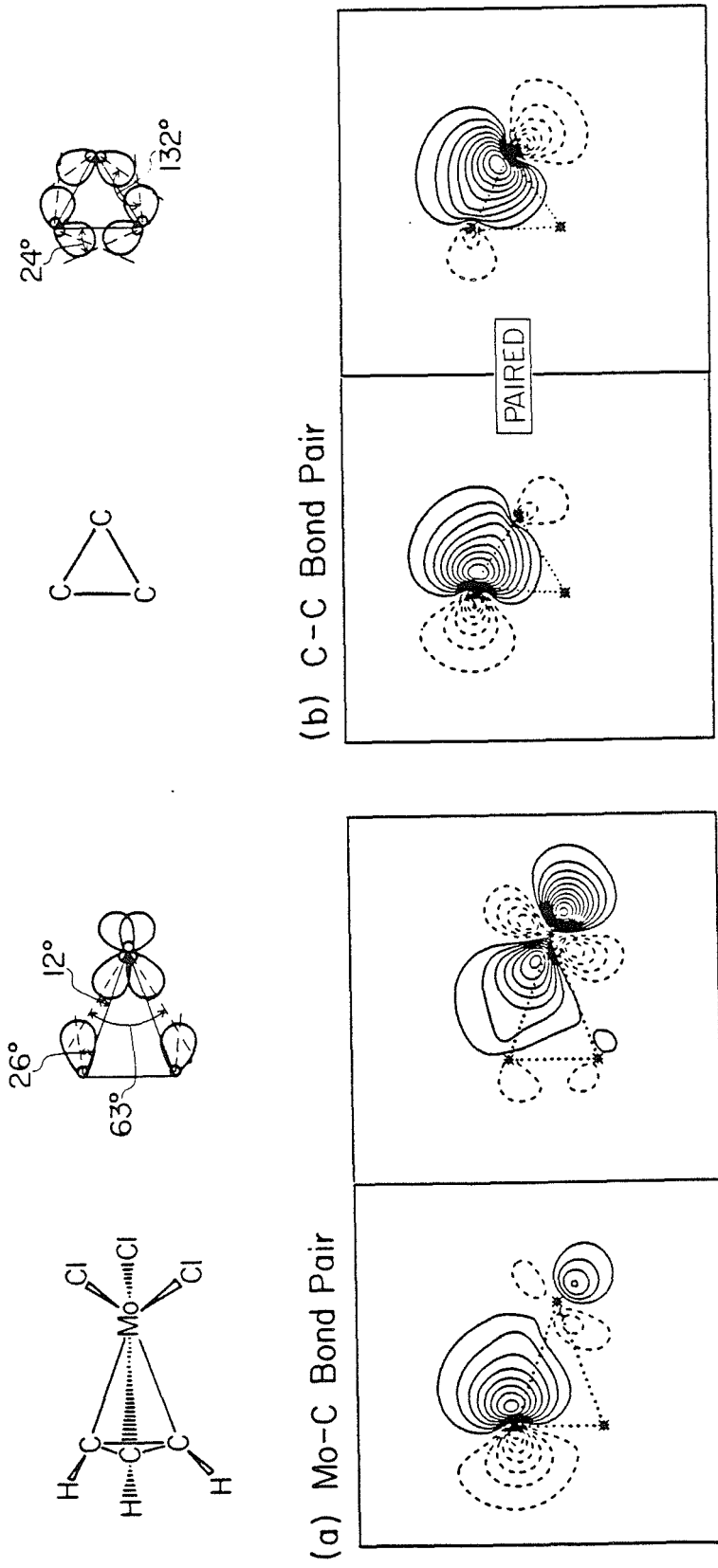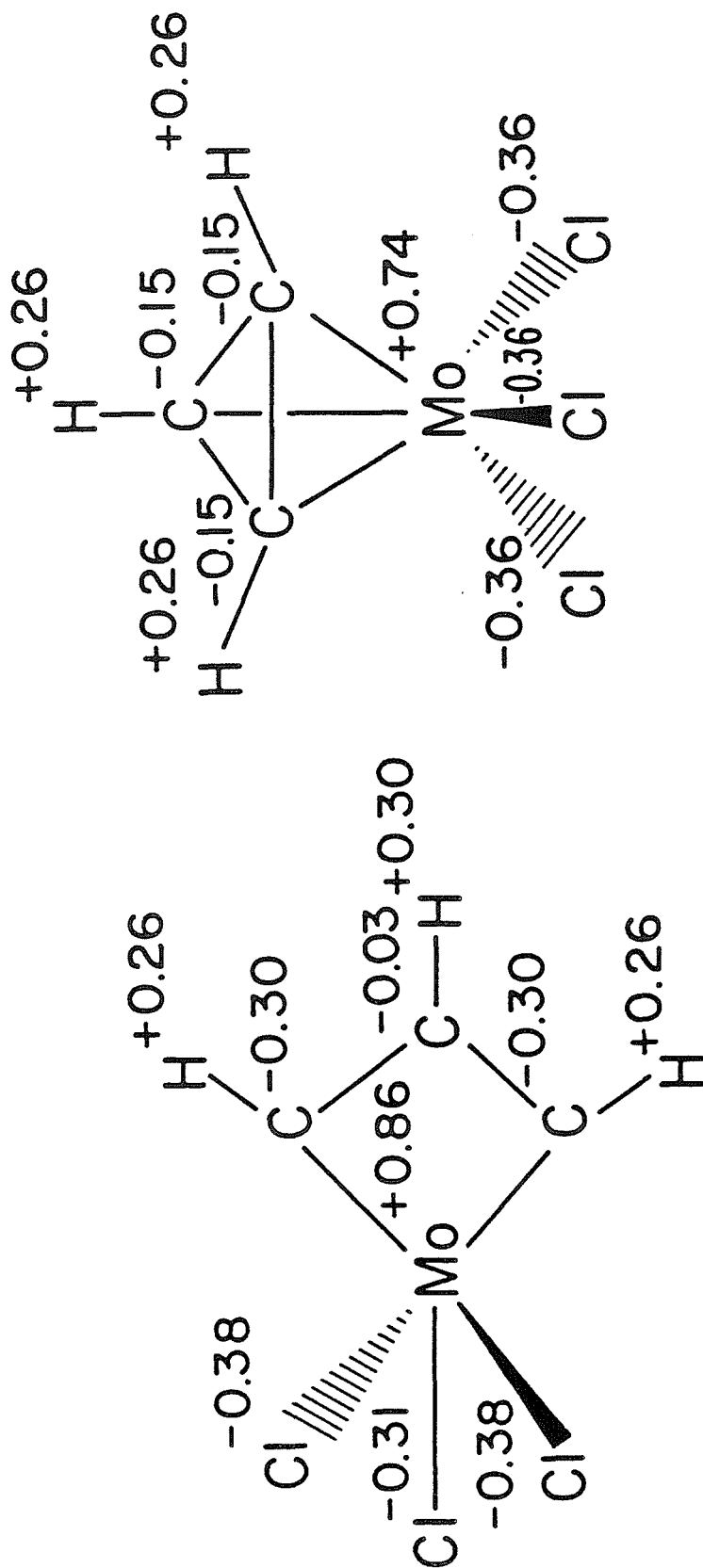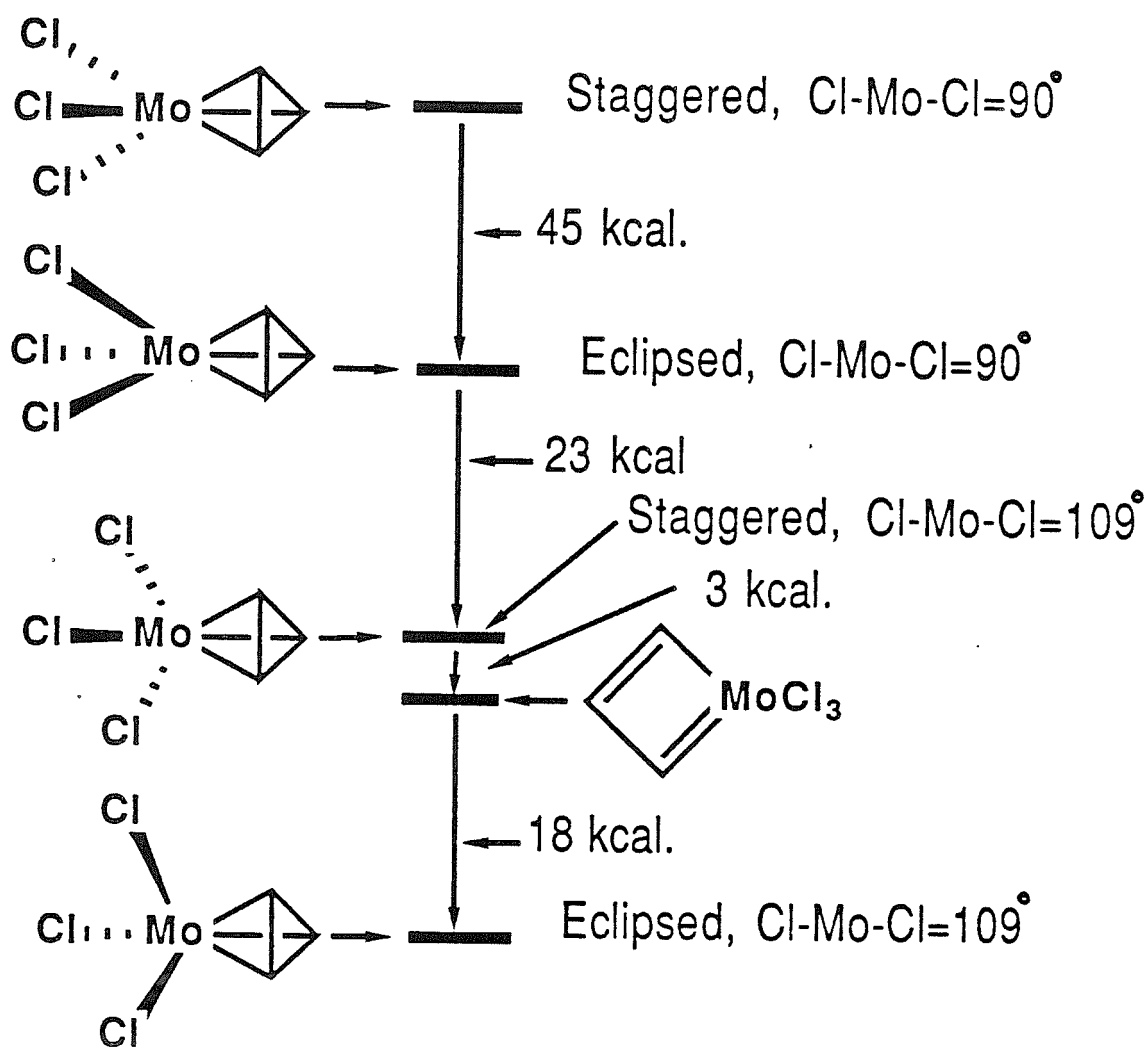
Figure 3.

Figure 4.

Figure 5.
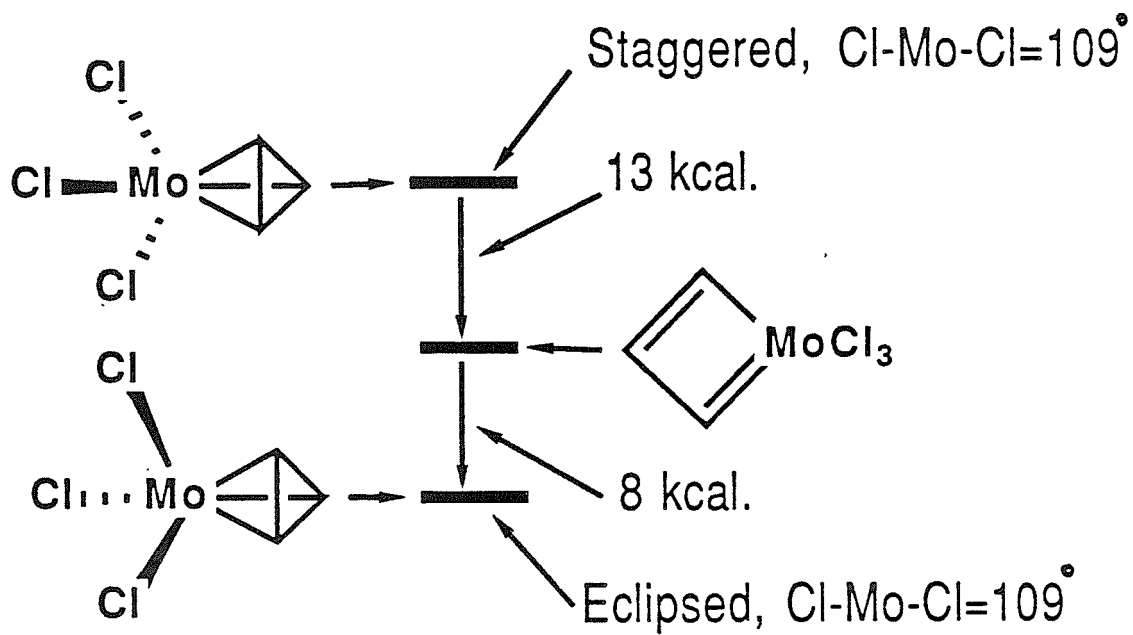
Figure 6.
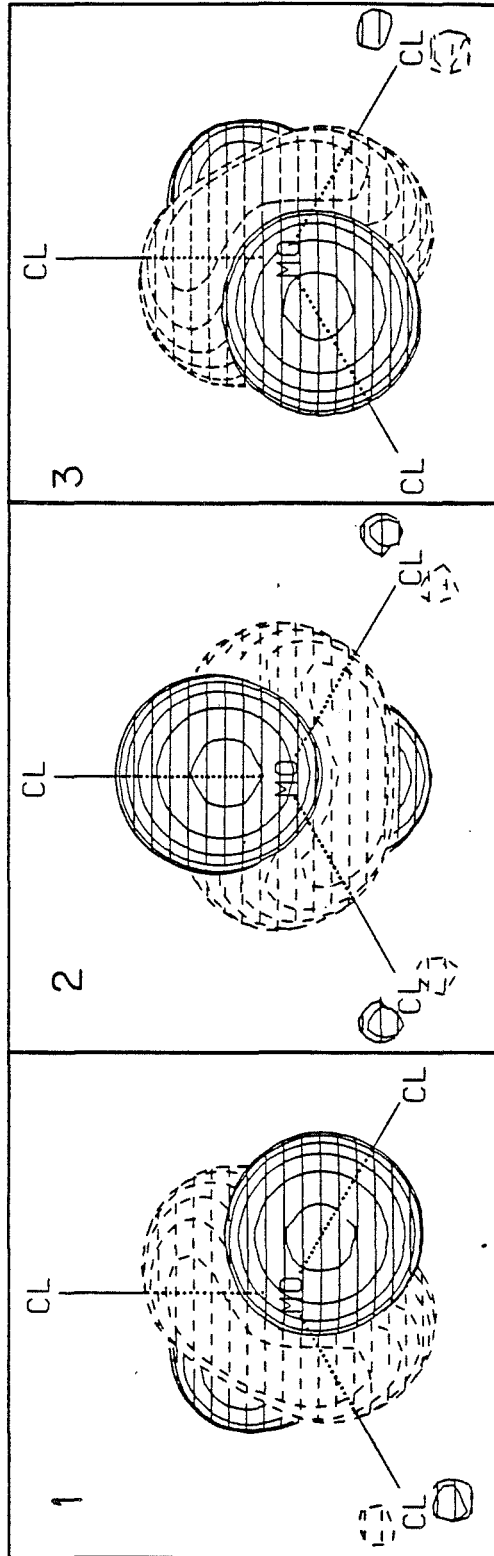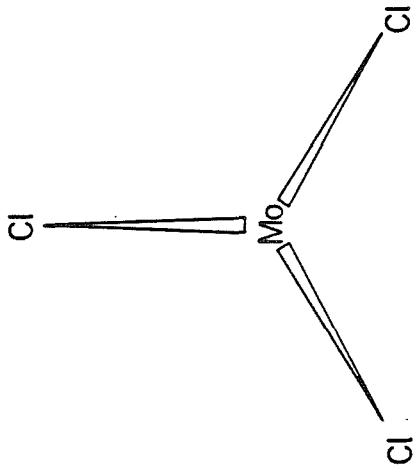
Figure 7.
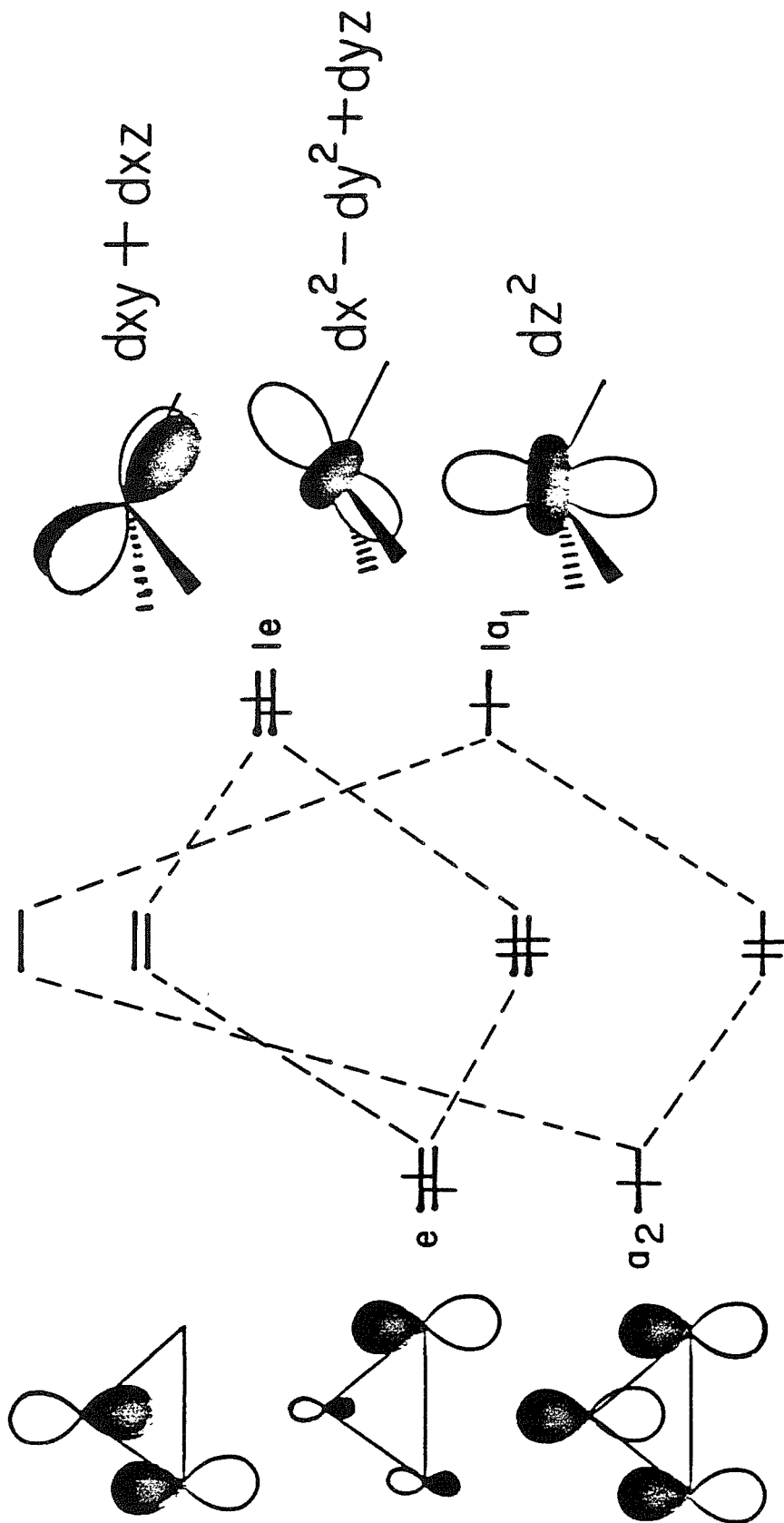
Figure 8.

Figure 9.

Appendix B

Fully Ab Initio Prediction of Crystal Structures: Cooperative Ordering in KCuF₃ Perovskite Induced by Jahn-Teller Distortions

The text of this section is an Article coauthored with Sergei Yu. Shashkin, William A. Goddard III, and A. E. Nikiforov which has been submitted to *Phys. Rev. B.*

FULLY AB INITIO PREDICTION OF CRYSTAL STRUCTURES:

COOPERATIVE ORDERING IN KCuF$_3$ PEROVSKITE

INDUCED BY JAHN-TELLER DISTORTIONS

Sergei Yu. Shashkin,[a] Mark J. Brusich, and William A. Goddard III

Contribution No. 7312 from the

Arthur Amos Noyes Laboratory of Chemical Physics,

California Institute of Technology, Pasadena, California 91125

and

Anatolii E. Nikiforov

Physics Department, A. M. Gorkii Urals State University,

Sverdlovsk, 620083, USSR

Received

With the goal of developing procedures for purly *ab initio* predictions of crystal structures, we have examined the distorted perovskite structures exhibited by KCuF$_3$. Using the Landau symmetry theory, we consider all possible types of structural phase transitions for perovskites associated with condensation of crystal modes (at the R, M, or X points of the Brillouin zone) that provide a nonzero e_g distortion of the CuF$_6$ octahedron around each Jahn-Teller ion Cu^{++}(d^9). This symmetry analysis leads to 21 low symmetry phases, five of which have tetragonal symmetry with a doubled primitive unit cell volume (namely, D$_{4h}^{18}$, D$_{4h}^{17}$, D$_{4h}^5$, and two different cases of D$_{4h}^1$). From *ab initio* calculations (involving

[a] Permanent address: Physics Department, A. M. Gorkii Ural State University, Sverdlovsk, 620083, U.S.S.R.

electron correlation) on a number of clusters ($[CuF_6]^{4-}$, $[Cu_2F_3]^{+}$, $[Cu_2F]^{3+}$, CuF_2, $F^- - F^-$, KF), we extracted analytical potentials and used them to predict the energies and structural parameters of the five tetragonal phases. The result is that the two optimal structures, $D_{4h}^{18}(R_{12})$ and $D_{4h}^{5}(M_3)$, correspond to the two observed structures (with lattice parameters correct to 0.7% for a and 3.3% for c). Of the other three structures, $D_{4h}^{17}(R_{12})$ is predicted to be 30 cm^{-1} higher (per formula unit) and is predicted to be the stable phase for external hydrostatic pressure above 132 kbar. The other two structures, $D_{4h}^{1}(X_1)$ and $D_{4h}^{1}(M_1)$, we predict to be unstable by 226 cm^{-1}, and the cubic (perovskite) form is predicted to be unstable by 802 cm^{-1} (explaining why the crystal melts before the phase transition to cubic is observed).

PACS numbers: 71.70E, 34.15, 61.60, 31.20G

I. Introduction

Although cubic(O_h^1) at high temperatures, most perovskite ABX_3 compounds exhibit a low temperature transition to lower symmetry[1,2] involving systematic atomic displacements. These displacive structural phase transitions can be analyzed in terms of a softening and condensation of a finite set of normal vibrational modes. For example, the phase transitions in $SrTiO_3$[3] and in a number of fluoride perovskites[4,5] are connected with rotations of the fluorine octahedra and generated by instability of the vibrational modes at the R and M points of the Brillouin zone. Such analyses explain these transitions in terms of the possible crystal structures resulting from various combinations of distortions and mode softening. However, they do not provide an understanding of the microscopic forces *underlying* these distortions and mode softening. Our goal is to gain such understanding by developing a completely first-principles methodolgy for predicting such structural distortions from the fundamental forces. Thus (i) we extract *a priori* analytic energy functions (two-body and multi-body) directly from extensive quantum mechanical calculations of clusters, (ii) we enumerate the various possible structural transitions using Landau theory, and (iii) we use these atomic forces to predict the energies and other properties of distorted crystal structures. In this way it should be possible to extract the underlying microscopic origin of the structural transformations. With such a microscopic understanding, one should be able to design new compounds with desirable specific properties.

In the current study, we restrict our consideration to perovskite crystals, ABX_3, that possess a B ion sublattice having a doubly degenerate orbital ground state [e.g., B = Cu^{2+} (d^9), Cr^{2+} (high-spin d^4), Mn^{3+} (high-

spin d^4), and Ni^{3+} (low-spin d^7)].

Perovskites were chosen because of the large number of low-symmetry phases with interesting properties (ferroelectrics, piezoelectrics, non-linear optical materials). In this paper, we examine specifically the case of $KCuF_3$ because two different low symmetry phases of this crystal have been observed.[6]

In the undistorted perovskite form of $KCuF_3$, each Cu would be at the center of a $[CuF_6]^{4-}$ octahedron. Such a $Cu^{++}(d^9)$ site leads to ^2E_g ground state, and hence the $[CuF_6]^{4-}$ octahedron is expected to undergo an e_g Jahn-Teller (JT) distortion. Previous studies[7] have established that this distortion lowers the energy about 1000 cm^{-1} per Cu, a very strong driving force.

As a first step, we have carried out *ab initio electronic structure calculations* [Hartree-Fock (HF), configuration interaction (CI), and generalized valence bond (GVB)] of various clusters $\{[CuF_6]^{4-}, CuF_2, [Cu_2F_3]^+, ([Cu_2F]^{3+} + 10$ point charges), $(F^-)_2$, and KF\}. From these *ab initio* energy surfaces we determined $[CuF_6]^{4-}$ many-body terms (JT coupling constants) and various pair potentials that were then parameterized so as to be suitable for predicting the structural parameters and energies for the various structures of $KCuF_3$.

Using the Landau theory of phase transitions, we analyzed the possible low-symmetry distortions of the cubic perovskite (ABX_3) structure due to e_g-like JT displacements at each B ion. This group theoretical analysis predicts 21 different types of permissible low-symmetry phases possessing primitive unit cells with two, four, or eight formula units. Of these, five correspond to a doubled unit cell with tetragonal symmetry (D_{4h}).

To determine which of these permitted structures is most stable requires the actual calculation of the crystal energy for the various permitted phases. Using the *ab initio* two-body and multi-body terms, we calculated the energies and structural parameters for the five tetragonally disorted structures having doubled unit cells and find that the optimum structures of all five D_{4h} space groups are at least 576 cm^{-1} (per formula unit) lower than cubic. The predicted ground structure $D_{4h}^{18}(R_{12})$ has been observed in numerous experiments, and the structure $D_{4h}^5(X_1)$, predicted 1.5 cm^{-1} higher, has also been observed. The other three structures, $D_{4h}^{17}(R_{12})$, $D_{4h}^1(M_1)$, and $D_{4h}^1(X_1)$, are all predicted much higher and have not been observed.

In the two observed structures, the calculated lattice constants a and c are larger than experiment by 0.7% and 3.3%, respectively. The predicted JT distortion angles of $\pm 108°$ (for D_{4h}^{18} and D_{4h}^5) are within 1° of experiment, while the magnitudes of flourine shifts are about half of experiment. Such predictions of distorted crystal structures from purely first principles indicate the utility of this approach. Since the two-body potentials are true two-body terms (rather than the effective two-body terms that would be obained by fitting to experimental structures), the use of these potentials for prediction of other low symmetry configurations (surfaces, defects, grain boundaries) should be of equal reliability.

II. Group Theoretical Analysis of Possible Types of Structural Phase Transitions Induced by Cooperative JT Effect

The Landau symmetry theory of phase transitions[8] starts with the high symmetry space group G and considers the crystal distortion ΔR (a 3N-dimensional atomic shift vector) relating a particular low-symmetry phase with space group G_D to the high symmetry phase with space group G. Assuming G_D to be a subgroup of G, ΔR is expanded in terms of the basis vectors φ_μ^Γ of a particular irreducible representation Γ of G

$$\Delta R = \sum_\mu C_\mu \varphi_\mu^\Gamma , \qquad (1)$$

where the sum on μ runs over all components of representation Γ. For the perovskite structure considered herein, $G = O_h^1$, and all possible phase transitions from crystals with space group O_h^1 to other low symmetry crystalline modifications have been enumerated by Vinberg et al.[9] Analysis of experimental crystallographic data[1,2] shows that the crystals under consideration undergo phase transitions that are always accompained by an enlargement of the primitive unit cell volume (by factors of two, four, and eight). Thus we shall take into account only the irreducible representations associated with the wave-vectors at the R, X, and M points of the Brillouin zone (these correspond to the $\{k_{13}\}$, $\{k_{10}\}$, and $\{k_{11}\}$ wave-vector stars, respectively, in the Kovalev[10] notation for the O_h^1 space group).

For each wave-vector star, Table I (modified from Ref. 9) expresses the elementary translations d_1, d_2, and d_3 of the Bravais lattice for the low-symmetry phases in terms of the elementary translations a_1, a_2, and a_3 of the high-symmetry perovskite phase. This table also indicates the ratio of the primitive unit cell volumes in the low- and high-symmetry

phases, $p = V_D/V$. The different Bravais lattices associated with the same wave-vector star are denoted in Table I by symbols a, b, and c.

The origin of the low symmetry cooperative crystal distortion in the the ABX_3 perovskites to be considered herein is the JT instability connected with the twofold orbital degeneracy of the E_g electronic state of the B-ion situated in the octahedral environment in the ideal structure. Therefore we need to select among all crystal modes only those that provide e_g distortions of the X-ion octahedron surrounding each B-ion. We shall refer to these crystal modes as *JT active modes*.

In order to consider all possible such JT active modes, we constructed the basis vectors φ_μ^Γ for all irreducible representations of O_h^1 space group associated with the R, X, and M points (i.e., the $\{k_{13}\}$, $\{k_{10}\}$, and $\{k_{11}\}$ stars) following the technique suggested in Ref. 11. We find that the only JT active irreducible representations are the R_{12}, M_1, M_3, and X_1 irreducible representations of the O_h^1 space group (in the Bouckaert, Smoluchwski, and Wigner notation[12]) or equivalently the $\{k_{13}\}\tau_5$, $\{k_{11}\}\tau_1$, $\{k_{11}\}\tau_5$, and $\{k_{10}\}\tau_1$ irreducible representations (in the Kovalev notation[10]). Table II gives the basis vectors of these representations. Only the ion shifts in the zero unit cell (presented in Figure 1) are shown in Table II since the shifts in an abitrary unit cell (n_1, n_2, n_3) are related to the shifts in the zero unit cell by the phase factor $\exp[ik(n_1 a_1 + n_2 a + n_3 a_3)]$. The two-dimensional representation R_{12} (or $\{k_{13}\}\tau_5$) is connected with a single-armed star R (or $\{k_{13}\}$) and the two-dimensional small representation e_g (or τ_5). Thus we denote the components of this representation as θ and ε. The M_1 (or $\{k_{11}\}\tau_1$), M_3 (or $\{k_{11}\}\tau_5$), and X_1 (or $\{k_{10}\}\tau_1$) representations are connected with three-armed stars and one-dimensional small representations, so we denote

their components by the wave-vectors from each star (the components of these wave-vectors are given in the units of $2\pi/a_0$, where a_0 is the perovskite lattice constant).

Tables III and IV (modified from Ref. 9) give the possible low-symmetry crystal structures associated with different combinations of expansion coefficients C_μ in (1) for all JT active representations. The ratio of unit cell volumes (p) and the particular type of low symmetry elementary translations (denoted as a, b, c in Table I) are also given in Tables III and IV.

A particularly interesting example of cooperative JT distortion is exhibited by $KCuF_3$, which has two stable phases with different crystal structures.[6] Both phases have a doubled primitive unit cell, belonging to the D_{4h}^{18} (I4/mcm) and D_{4h}^{5} (P4/mbm) space groups, respectively. According to Tables III and IV, this means that the phase transitions in $KCuF_3$ can follow either R_{12} or M_3 representations.

The symmetry analysis suggested above allows us to *classify* the observed JT distorted crystal structures; however, it is not able to *predict which* low symmetry structure takes place for the specific crystal under consideration. The most stable (at low temperature) low-symmetry phase can be chosen only on the basis of microscopic calculations of the crystal energy that account for the specific electronic-lattice interactions. The point of this paper will be to illustrate the procedure for doing this using $KCuF_3$ as a prototype. As mentioned above, $KCuF_3$ exhibits two tetragonal phases (D_{4h}^{18} and D_{4h}^{5}), both corresponding to a distorted perovskite with doubled unit cell. According to symmetry analysis, there are five possible tetragonal phases with doubled unit cells (see Tables III and IV):

$$D_{4h}^{18}(R_{12}) = I4/mcm$$
$$D_{4h}^{5}(M_3) = P4/mbm$$
$$D_{4h}^{17}(R_{12}) = I4/mmm$$
$$D_{4h}^{1}(X_1) = P4/mmm$$
$$D_{4h}^{1}(M_1) = P4/mmm \, ,$$

two of which are the observed structures. To designate the different tetragonal phases, we indicate the space group and the soft crystal mode leading to this low-symmetry phase.

The fluorine nuclear shifts (designated as δ_1, δ_2,..., δ_6) corresponding to the allowed nonuniform crystal deformations induced by the phase transition are shown in Figure 2 (with four perovskite unit cells). Each particular type of phase transition has particular relations between the various fluorine shifts, as demanded by the corresponding irreducible representation. Table V presents these relations where we see that for each low-symmetry phase the nonuniform deformation of the crystal structure is defined by just one parameter δ. The five distorted crystal structures are displayed in Figure 3.

III. Evaluation of the Ab Initio Interaction Potentials

The interaction potentials were extracted from the results of first-principles calculations of $F^- - F^-$, $K^+ - F^-$ and a variety of clusters composed of Cu^{2+} and F^- ions ($[CuF_6]^{4-}$, $[Cu_2F_3]^+$, $[Cu_2F]^{3+}$, and CuF_2). In this section, we present the physical ideas underlying the procedure of deriving the interaction potentials and describe the results obtained for $F^- - F^-$, $K^+ - F^-$, and $Cu^{2+} - F^-$. The general expression for the pair potential and some mathematical details are given in Appendix I.

A. $F^- - F^-$ *Interaction Potential*

In order to determine the $F^- - F^-$ pairwise potentials, we carried out HF and CI calculations as described below. We started with the Huzinaga and Sakai (11s,7p) basis[13] contracted to (6s,3p), supplemented this basis with additional diffuse s and p functions (with scaled exponents of 0.0892 and 0.0657, respectively) and added two sets of d functions (with exponents of 0.45 and 0.20). We calculated fully self-consistent HF molecular orbitals at each distance, localized these orbitals onto the separate centers, and carried out CI calculations allowing all single excitations from the left F^- to all virtuals *simultaneously* with all single excitations from the right F^- to all virtuals (excitations were not allowed out of the 1s orbitals). This CI is designed to account for the *interatomic* electron correlation dominating the van der Waals (or dispersion) attraction.

Analogous calculations for Ne_2 lead to a bond distance within 0.05 Å of the experimental value and a bond energy within 0.0006 eV of experiment. (These calculations are described in more detail in Ref. 14.)

We obtained analytic fits to these theoretical $F^- - F^-$ curves in the following way. The long-range interaction between ions with charges Q

and Q' separated by a distance r is QQ'/r; however, at the typical chemical bond distances, significant corrections for shielding are required. Thus we calculated the electrostatic interaction resulting from superimposing charge densities of two F^- ions at various distances. We found that the total electrostatic interaction is quite accurately described by the form

$$\frac{QQ'}{r} - \frac{A}{r} e^{-Br} , \qquad (2)$$

where the A and B are determined from a best fit to the computed electrostatic interactions.

The actual interaction energies at small internuclear distances are dominated by the repulsive interactions arising from orthogonalizing the doubly occupied atomic orbitals, as demanded by the Pauli principle (hereafter denoted simply as Pauli replusion). These terms can be accurately described by the term

$$C e^{-DR} . \qquad (3)$$

The electrostatic interaction energy (2) and Pauli repulsion (3) must be corrected by adding the dispersion terms associated with instantaneous correlation between the electrons on different centers. The dominant term here (for $F^- - F^-$) involves a p-to-d transition on each F^-, leading to an energy expression of the form

$$-\frac{C_6}{R^6} . \qquad (4)$$

The Pauli repulsion interactions described by (3) and electrostatic interactions (2) lead to a polarization of each F^- so as to decrease the overlap of the doubly-occupied orbitals. These polarization effects are very important for various $F^- - F^-$, $K^+ - F^-$, and $Cu^{++} - F^-$ clusters, and

we find that these polarizations must be included explicitly in order to simultaneously fit the results for all clusters. In order to keep the calculations as simple as possible, we describe this polarizability of the fluorine ions through use of the Dick and Overhauser shell model.[15] Here we assume that the polarization can be described by shifting the valence 2p shell of F^- (with six electrons) as a unit and that the increase in atomic energy corresponding to a shift by a distance l from the nucleus is described by

$$\frac{1}{2} K_F \cdot l^2 \ . \tag{5}$$

The core-shell spring constant, K_F, can be related to the atomic polarizability α_F,

$$\alpha_F = Y_F^2 / K_F \ , \tag{6}$$

where we assume the shell charge to be $Y_F = -6$.

Since the terms in (3) and (4) are dominated by the distance between the valence electrons, we use the distance $(r + 2\,l)$ for R in these terms (where r is the internuclear distance), leading to

$$C\,e^{-D(r\,+\,2\,l)} \tag{7}$$

in place of (3) and

$$V_{VDW} = -\frac{C_6}{(r + 2\,l)^6} \tag{8}$$

in place of (4).

Keeping the constants A_{FF} and B_{FF} fixed, we obtained the parameters C_{FF}, D_{FF}, C_6, and K_F given in Table VI from a fit to the *ab initio* CI calculations at seven different internuclear distances within the interval 1.5 - 5.0 Å. These calculations yield a value of $\alpha_F = 8.6$ a.u., which compares well

with the exact HF value of $\alpha_F = 10.7$ a.u.[16] In these fits the constant term in the $F^- - F^-$ pairwise potential (corresponding to the infinite separation limit) was taken as twice the value of separated F^- ions $V_{FF}^{(0)} = 2E(F^-) = -198.913118$ a.u.[14] (instead of considering the $V_{FF}^{(0)}$ as an extra fit parameter as in Ref. 17).

We also tested the variation of the shell charge, Y_F, and found a strong correlation between Y_F and K_F, as expected, since the only combination of these parameters with physical significance is (6).

In the fits to the various Cu-F clusters described below, it was necessary to subtract out the $F^- - F^-$ interactions in order to obtain explicit Cu-F pairwise interactions. These calculations used a valence double zeta F^- basis sets[18] and did not include the $F^- - F^-$ dispersion terms. Consequently, we carried out HF calculations for $F^- - F^-$ (using the same basis as for the various Cu-F clusters) at six distances within the interval 2.55 - 4.5 Å. Again we extracted the A and B parameters for shielding from superimposing fixed F^- densities. The residue was then fitted to obtain C_{FF}, D_{FF}, and K_F for this restricted calculation. The C_6 term was not included since HF would not account for dispersion terms. The K_F obtained here leads to $\alpha_F = 5.9$ a.u., a value much less than the value (8.6 a.u.) obtained with the large basis (the HF limit is 10.7 a.u.).

B. $K^+ - F^-$ *Interaction Potential*

We performed HF calculations for the system $K^+ - F^-$ at six internuclear distances within 2.2 - 3.5 Å. Here the valence double zeta basis[18] was used for F^- and the Huzinaga minimum basis set (Ref. 19, p.405) was used for K^+. The fluorine shell model parameters K_F and Y_F were taken from the $F^- - F^-$ calculations with the same basis but the potassium ion

was treated as unpolarizable. The infinite limit energy $V_{KF}^{(0)}$ = $E(K^+)$ + $E(F^-)$ = -598.374385 a.u. was taken from separate F^- and K^+ calculations. The fitted electrostatic correction and short-range parameters are given in Table VI.

C. $Cu^{2+} - F^-$ Interaction Potentials

1. Pairwise Interactions

The results from a number of *ab initio* calculations on Cu-F clusters were used to extract the $Cu^{2+} - F^-$ interaction potential parameters. In each case the appropriate $F^- - F^-$ terms were subtracted to obtain a residual cluster energy to be fitted by a superposition of $Cu^{2+} - F^-$ terms. We included the following clusters:

(i) CI calculations were carried out on three octahedral and five tetragonally distorted configurations of $[CuF_6]^{4-}$ (as reported recently.[7]) For the tetragonally distorted configurations, the average energy $\frac{1}{2}[E(^2A_{1g}) + E(^2B_{1g})]$, corresponding to the unsplit ^2E_g ground state, was used in obtaining the pair potentials.

(ii) CI calculations were carried out on seven linear configurations of CuF_2. The results for four symmetric configurations (with R_{Cu-F} = 1.73, 1.76, 1.79, and 2.22 Å) and for one antisymmetric configuration (with R_{Cu-F} = 1.7508 and 1.8108 Å) were reported recently.[18] To these we added CI calculations for R_{Cu-F} = 1.72 and 1.97 Å (using the average-of-configuration CI-SD(2) MVS approach developed in Ref. 18).

(iii) GVB calculations[20] were carried out for three symmetric linear configurations of $[Cu_2F_3]^+$ with R_{Cu-F} = 2.00, 2.03, and 2.06 Å. Here we solved for the $^1A_{1g}$ ground state with a GVB pair describing the

correlation of z^2-like electrons providing the σ-bond. (The singlet-triplet splitting is 22 cm^{-1} at R_{Cu-F} = 2.03 Å and was neglected in the potential fits.)

(iv) GVB calculations [with one σ GVB pair as in (iii)] were carried out for the cluster composed of two Cu^{2+} ions separated by an F^- ion and supplemented with ten point charges of Q = -1. This cluster models two $[CuF_6]^{4-}$ clusters sharing a mutual fluorine ion as in the $KCuF_3$ crystal structure. We solved for the ground state wavefunction Ψ of the total system $\{[Cu_2F]^{3+} + 10$ point charges$\}$, but then we calculated the energy $E(Cu_2F) = \langle\Psi|H_0|\Psi\rangle$ where H_0 is the hamiltonian of the free $[Cu_2F]^{3+}$ cluster. $E(Cu_2F)$ was the energy that was matched with the model pair potential expression for $[Cu_2F]^{3+}$. The calculations were performed for three symmetric configurations with $R_{Cu-F} = R_{Cu-point\ charge}$ = 2.00, 2.03, and 2.06 Å and one antisymmetric configuration obtained from the symmetric one with $R_{Cu-F} = R_{Cu-point\ charge}$ = 2.03 Å by shifting the F^- 0.06 Å towards one of the Cu^{2+} ions.

In all fits, we matched the *relative* calculated cluster energies with the *relative* cluster energies for the pair potential model. The energies of the symmetric configurations with R_{Cu-F} = 2.03 Å for $[CuF_6]^{4-}$, $[Cu_2F_3]^+$, and $[Cu_2F]^{3+}$ clusters and with R_{Cu-F} = 1.79 Å for CuF_2 were chosen as the reference energies. The valence double zeta Cu^{2+} and F^- basis sets developed in Ref. 18 were used for all calculations (i)-(iv). The $F^- - F^-$ interaction potentials from fits to corresponding $F^- - F^-$ calculations were subtracted (allowing fluorines to polarize) and the Cu^{2+} ions were considered unpolarizable during the fit.

The results of calculations (iii) and (iv) allow the analysis of possible short-range interactions between two Cu^{2+} ions shared by an F^- ion [as in (2) and (3)]; however, the exponents $B_{Cu-Cu} \approx D_{Cu-Cu} \approx 8.0$ a.u. obtained from fitting these cases indicate that $Cu^{2+} - Cu^{2+}$ short-range interactions are negligible, and no such terms were included in the final fit. The results of the final fit for the $Cu^{2+} - F^-$ parameters are given in Table VI.

2. Jahn- Teller Coupling Constants

The results of the *ab initio* HF and CI calculations of the JT coupling (JTC) constants V_e, N_e, P and anharmonicity constant A for octahedral clusters $[CuF_6]^{4-}$ have been reported recently.[7] Table VII presents the values for these constants (from CI studies) which we used for the $KCuF_3$ energy optimization. Note that for an isolated cluster, the optimum distortion is elongation with an energy lowering of 1075 cm^{-1}.[7]

IV. The Model for Crystal Energy Calculations

In order to study the stability of the five tetragonal phases relative to that of the ideal cubic perovskite structure, it is necessary to compute the energy of each low-symmetry phase (and the cubic phase) as a function of the various free parameters.

The high-symmetry phase of $KCuF_3$ has not been observed experimentally; thus we started with the hypothetical perovskite $KCuF_3$ structure with a cubic unit cell and lattice constant of $a_0 = 4.06$ Å (the average distance between the nearest Cu^{2+} ions in real $KCuF_3$ crystals[6]).

We allow the symmetry transformation to be accompaned by a tetragonal uniform deformation of the crystal, and hence the unit cells in Figures 2 and 3 are taken to have the dimensions $a\sqrt{2}$, $a\sqrt{2}$, and $2c$, where

$$c = a_0 + \eta_1 ,$$

$$a = a_0 + \eta_2 ,$$

$$(9)$$

and the parameters η_1, η_2 describe uniform crystal deformations. The numbers and the coordinates of atoms within the tetragonal unit cell (in units of $a\sqrt{2}$, $a\sqrt{2}$, and $2c$) are given in Table VIII. In addition, there is a single distortion parameter δ for each structure. Thus a full optimization of these structures involves optimization of η_1, η_2, and δ.

Since we utilize the shell model to take into account the F^- polarizability, we must also calculate the shell shifts for each phase. From symmetry, the fluorine shells and fluorine cores must shift along the same axes for each of the JT phase transitions, but the magnitudes of the shifts will be different. The magnitudes of the i-th shell and core shifts are denoted as δ_{is} and δ_i, respectively. The pattern for the shifts in δ_{is} of

different fluorines is the same as for δ_i as given in Table V. Therefore, the crystal energy is a particular function of four parameters η_1, η_2, δ, and δ_s for any of the five D_{4h} phases.

We describe the crystal energy per tetragonal unit cell (Figure 2) in terms of the elastic and JT energies, as follows

$$E = U_{el} + U_{JT} , \tag{10}$$

$$U_{el} = \frac{1}{2} \sum_{i=1}^{20} \sum_{j(\neq i)} V_{ij} , \tag{11}$$

$$U_{JT} = \sum_{k=1}^{4} U_{JT}(k) , \tag{12}$$

where the V_{ij} are pair interaction potentials and U_{JT} arises from JT interactions within each $[CuF_6]^{4-}$ unit. In (11), i runs over all ions within the unit cell while j runs over all ions in the crystal, and in (12) k runs over copper ions withinthe unit cell. The JT contributions (12) are expressed in terms of the $e_g(Q_\theta, Q_\epsilon)$ and $a_{1g}(Q_a)$ symmetrized displacements of the fluorine octahedron around each Cu ion with respect to the perfect octahedron with $R_{Cu-F} = a_0/2$, as follows

$$U_{JT}(k) = - [(V_e + PQ_a^{(k)})^2 \rho_k^2 - 2(V_e + PQ_a^{(k)})N_e\rho_k^3 \cos 3\Phi_k + N_e^2\rho_k^4]^{\frac{1}{2}} , \tag{13}$$

where V_e, N_e, and P are the JTC constants for the $[CuF_6]^{4-}$ cluster (defined and calculated in Ref. 7). In (13) the polar coordinates ρ_k, Φ_k are used in place of the e_g-coordinates Q_θ, Q_ϵ

$$Q_\theta^{(k)} = \rho_k\cos\Phi_k ,$$
$$\tag{14}$$
$$Q_\epsilon^{(k)} = \rho_k\sin\Phi_k .$$

The expressions of $Q_a^{(k)}$, $Q_\theta^{(k)}$, $Q_\epsilon^{(k)}$ in terms of fluorine nuclear shifts and uniform deformation parameters η_1, η_2 are given in Table IX.

For small values of distortion, the elastic crystal energy U_{el} can be expanded in a power series involving η and δ. Keeping only linear and quadratic terms in this expansion and omitting constant terms, we obtain

$$U_{el}^h = \alpha(\eta_1 + 2\eta_2) + \beta_1\eta_1^2 + \beta_2\eta_2^2 + \beta_{12}\eta_1\eta_2$$

$$+ R\delta^2 + R_s\delta_s^2 + R_{ns}\delta\delta_s + K(\delta - \delta_s)^2 \tag{15}$$

for the harmonic part of the elastic energy, where each coefficient α, β, R is a sum of the long-range coulombic (α^C, β^C, R^C) and the short-range (α^{sr}, β^{sr}, R^{sr}) contributions (except for the R_{ns} term which contains no short-range contribution). The most important terms contributing to the anharmonic part of the elastic energy U_{el}^{anh} will be introduced below [Eq. (26)]. The coulombic contributions are evaluated from calculation of the appropriate lattice sums (see Appendix II). For the short-range contributions, we take into account the interactions between the nearest neighbors $K^+ - F^-$, $Cu^{2+} - F^-$, $F^- - F^-$ and between the second neighbors $F^- - F^-$, for each of which we used the interaction potential parameters as described in Section III. In calculating the lattice energy, we expanded the coefficients for (15) in terms of the first and second derivatives of the short-range contributions f_{ij}, g_{ij} (see Appendix I)

$$A_m = \left[\frac{\partial^2 g_{ij}(x)}{\partial x^2}\right]_{x_0}; \quad B_m = \left[\frac{1}{x}\frac{\partial g_{ij}(x)}{\partial x}\right]_{x_0}; \tag{16}$$

$$H_m = \left[\frac{\partial^2 f_{ij}(x)}{\partial x^2}\right]_{x_0}; \quad G_m = \left[\frac{1}{x}\frac{\partial f_{ij}(x)}{\partial x}\right]_{x_0}. \tag{17}$$

The subscript m in (16) and (17) refers to a particular pair of ions and the corresponding value of x_0, namely, $m = 1$ corresponds to $i = K^+$, $j = F^-$ with $x_0 = a_0/\sqrt{2}$; $m = 2$ corresponds to $i = Cu^{2+}$, $j = F^-$ with $x_0 = a_0/2$; $m = 3$ corresponds to $i = j = F^-$ with $x_0 = a_0/\sqrt{2}$; $m = 31$ corresponds to $i = j$

F^- with $x_0 = a_0$.

The data presented in Table VI lead to a straightforward evaluation of all necessary force constants (16) and (17).

In (15), only two of the three coefficients β_1, β_{12}, and β_2 describing uniform deformation of the *cubic* crystal are independent; they are connected with the elastic constants c_{ij} (defined for the lattice constant a_0) as follows,

$$\beta_1 = 2a_0 \cdot c_{11},$$
$$\beta_2 = 4a_0 \cdot (c_{11} + c_{12}),$$
$$\beta_{12} = 8a_0 \cdot c_{12}$$

and obey the relation

$$\beta_2 = \frac{1}{2}(\beta_{12} + 4\beta_1). \tag{18}$$

The short-range contributions to the coefficients α, β of the elastic energy expression (11) are given by the following equations,

$$\alpha^{sr} = 2a_0[4(B_1 + B_3 + G_1 + G_3) + B_2 + G_2 + 6(B_{31} + G_{31})] \tag{19}$$

$$\beta_1^{sr} = 2(A_1 + B_1 + A_3 + B_3 + H_1 + G_1 + H_3 + G_3) + A_2 + H_2 \\ + 6(B_{31} + G_{31}) \tag{20}$$

$$\beta_{12}^{sr} = 4(A_1 - B_1 + A_3 - B_3 + H_1 - G_1 + H_3 - G_3). \tag{21}$$

The coefficients R, R_s, R_{ns}, and K depend on the particular type of *nonuniform* crystal deformation responsible for the low-symmetry distortion. The expressions for K and the short-range contributions to R and R_s are presented in Table X, where the abbreviated notations

$$\gamma = 2[2(G_1 + H_3 + G_3 + H_{13}) + H_2 + 3G_{31}], \tag{22}$$

$$\gamma_s = 2[2(B_1 + A_3 + B_3 + A_{13}) + A_2 + 3B_{31}], \tag{23}$$

$$\kappa = 2(G_3 - H_3) \,, \tag{24}$$

$$\kappa_s = 2(B_3 - A_3) \,, \tag{25}$$

are used.

The positions of the adiabatic potential minima for the JT interaction of an E electronic state with e-vibrations are strongly affected by the anharmonic term $A(Q_\vartheta^3 - 3Q_\theta Q_\varepsilon^2) = A\rho^3 \cos 3\Phi$ of the potential energy.[21] Indeed, this anharmonic term can be of the same importance for the cooperative JT effect in the crystal[22,23] as the second-order JT term $(\sim N_e \rho^2)$ included in (13). The corresponding contribution to the anharmonic part of the crystal elastic energy is

$$U_{el}^{anh} = \sum_{k=1}^{4} A\rho_k^3 \cos 3\Phi_k \,, \tag{26}$$

where A is the anharmonicity constant for $[CuF_6]^{4-}$ cluster. This contribution (26) is the only anharmonic contribution to the crystal elastic energy that we take into account (the same approximation was used in the previous studies[22-24]).

Thus the final expression for the $KCuF_3$ crystal energy (per four formula units) has the form

$$E(\eta_1, \eta_2, \delta, \delta_s) = U_{el}^h + U_{JT} + U_{el}^{anh} \tag{27}$$

with the right-hand side terms defined by (15), (12), and (26). Of course, the explicit form of each contribution in (27) differs for each tetragonal phase. Minimization of function (27) with respect to the η_1, η_2, δ, and δ_s leads to relative energies of the different tetragonal phases allowing us to determine the most stable low-symmetry crystal modification.

V. Results of Energy Optimization for the Tetragonal Phases of $KCuF_3$

A. *Full Optimization*

The results of full energy optimization are shown in Table XI and Figure 3. We find that the ground state is $D_{4h}^{18}(R_{12})$ but that $D_{4h}^{5}(M_3)$ is only 1.5 cm^{-1} higher (per formula unit). The other tetragonal phases are all predicted to be much higher. Thus, $D_{4h}^{17}(R_{12})$ is 30 cm^{-1} above the ground state, while $D_{4h}^{1}(X_1)$ and $D_{4h}^{1}(M_1)$ are 226 cm^{-1} above the ground state. The high symmetry cubic (perovskite) phase is predicted to be 802 cm^{-1} above $D_{4h}^{18}(R_{12})$.

These results are in excellent agreement with experiment. The D_{4h}^{18} phase is found in all studies of $KCuF_3$, whereas D_{4h}^{5} is found only in some cases. This is consistent with D_{4h}^{18} having the lowest energy but D_{4h}^{5} being very close. The transition to cubic perovskite has not been observed (the crystal melts first), consistent with the predicted high energy of the cubic phase. The other tetragonal phases have not been observed, consistent with the predicted higher energies of these phases. As discussed in the next section, the theory predicts that D_{4h}^{17} will become stable for high pressure, providing a means for an experimental test of these results.

The total energy stabilization of D_{4h}^{18} with respect to O_h^1 is 802 cm^{-1}. This is only slightly smaller than the optimum JT stabilization of isolated $[CuF_6]^{4-}$ clusters (1075 cm^{-1}). *These results prove that the origin of the lower symmetry perovskite phase for $KCuF_3$ is the JT distortion at each Cu.*

The JT distorted crystal structures can be expressed in terms of three independent parameters, η_1, η_2 (or a and $f = a/c$), and δ, but it is

suitable to analyize them in terms of local distortions ρ, Φ, and Q_a. The value of ρ gives the *magnitude* of the JT distortion, while the angle Φ gives the particular type of JT distortion around each copper ion (e.g., $\Phi = 0$ corresponds to the elongation of the fluorine octahedron along the z axis, while $\Phi = 180°$ corresponds to compression). The above mentioned parameters are given in Table XI for all the phases.

From Table XI we see that the calculated angles $\Phi = \pm 180°$ are in full agreement with the experimentally observed values of $\Phi = \pm 109°$ and $108°$ for phases D_{4h}^{18} and D_{4h}^{5}, respectively. The angle Φ is most sensitive to the magnitudes of the A and N_e constants, and this agreement provides evidence for the efficacy of our model. Using the calculated value of $\rho = 0.220$ Å, we obtain $A\rho^3 = -142$ cm^{-1} and $N_e\rho^2 = -22$ cm^{-1}; thus the anharmonicity term is most important for the stabilization of the particular crystal distortions (note that $A = N_e = 0$ would lead to $\Phi = \pm 90°$ for phases D_{4h}^{18} and D_{4h}^{5}).

Our model predicts the correct sign of the uniform tetragonal deformation for the phases D_{4h}^{18} and D_{4h}^{5} (a/c > 1), and the predicted lattice constants a and c are 0.7% and 3.3%, respectively, greater than experimental values. However, the calculated values of fluorine shift δ and JT distortion ρ are about half of experiment. Comparing the second and the third groups of results in Table XI, we see that the use of more reliable $F^- - F^-$ interaction potentials provides more distinct stabilization of the phases D_{4h}^{18} and D_{4h}^{5} and makes the calculated lattice constants, δ, and ρ values slightly closer to the experimental ones.

The fluorine polarizability seems not very important for the quantitative explanation of the low-symmetry distortion in KCuF$_3$ (the neglect of F^- polarizability leads to a 13% increase in the crystal energy for the

phases D_{4h}^{18}, D_{4h}^{17}, and D_{4h}^{5} having $\delta \neq 0$, reduction of the ρ and δ values by about 15% for these phases, and a small increase of the angle Φ up to $\pm 110°$ for the phases D_{4h}^{18} and D_{4h}^{5}), but it is highly important for the correct determination of the interaction potentials from the cluster calculations because of significant F^- polarization in the finite size clusters.

B. Partial Optimization

In order to provide some insight into what parts of the potentials are important in the transformations, we have also carried out various restricted optimizations as follows.

Neglecting the JT and anharmonicity contributions to the lattice energy (27), we find that the energy minimum for each of the tetragonal phases corresponds to the ideal perovskite structure ($\delta = \delta_s = 0$) with the lattice constant $a^{(0)} = a_0 + \eta_1 = a_0 + \eta_2 = 4.142$ Å. This is 2% longer than our estimated experimental value of 4.06 Å (obtained by averaging the distances in distorted $KCuF_3$[6]).

Evaluation of the elastic constants for this hypothetical cubic perovskite structure gives $c_{11} = 198.4$, $c_{12} = 63.2$ GPa. This can be compared with the experimental elastic constants for similar materials ($c_{11} = 114.6$, $c_{12} = 40.5$ GPa for $KMnF_3$;[25] $c_{11} = 130$, $c_{12} = 51$ GPa for $KCoF_3$;[26] $c_{11} = 158$, $c_{12} = 48.5$ GPa for $KNiF_3$[27]). Based on these comparisons, we conclude that our model interaction potentials provide a rather realistic description of the crystal.

At the next step, the linear JT contributions were taken into account but the second order JT terms (N_e, P) and anharmonicity term (26) were neglected. For all tetragonal phases this model leads to the existence of two equivalent minima (with the energy -667 cm^{-1} with respect to the O_h^1

phase) corresponding to pure uniform deformation of the crystal with either unit cell elongation ($\Phi = 0°$) or compression ($\Phi = 180°$) along the c-axis. In addition, each of the phases possesses a third minimum corresponding to nonuniform deformation alone (i.e., a/c = 1 and $\delta \neq 0$). For phases D_{4h}^{18}, D_{4h}^{17}, and D_{4h}^{5}, this latter case leads to absolute minimum energies of -922, -922, and -920 cm^{-1}, respectively. Thus, in the absence of anharmonicity and second-order JT terms, our model predicts that the D_{4h}^{18}, D_{4h}^{17}, and D_{4h}^{5} crystal modifications without uniform deformation would have the lowest energies. This contradicts experimental data, showing that the high order terms are quite important.

Including all JT terms and lattice anharmonicity, but allowing only pure uniform tetragonal deformation, we obtain noncubic minima for all phases (see Table XI), but elongation of the unit cell along the four-fold axis leads to the lower minimum (-576 cm^{-1} against -520 cm^{-1} for compression). These energies are less negative due mainly to the cross term $e_g \times a_{1g}$ in the JT energy (13) (since $V_e < 0$, P > 0 and the optimum crystal structures possess $Q_a^{(k)} > 0$). In this case, local minima with $\delta \neq 0$ were not found for both D_{4h}^{1} phases, but there are deeper minima (corresponding to full optimization) with $\delta \neq 0$ and a/c $\neq 1$ for phases D_{4h}^{18}, D_{4h}^{17}, and D_{4h}^{5} (with energies -802, -772, and -800 cm^{-1}, respectively).

Allowing full optimization, we find that the energy of phase D_{4h}^{17} is 30 cm^{-1} higher than the energy of phase D_{4h}^{18}. Thus the lattice anharmonicity and second-order JT interactions provide *coexistence of the uniform tetragonal deformation (a/c $\neq$ 1) and nonuniform deformation ($\delta \neq 0$)*, leaving only two nearly equally stable (within 1.5 cm^{-1}) tetragonal phases with space groups D_{4h}^{18} and D_{4h}^{5}. Both these phases have been observed experimentally.[6]

Optimizing the energy with respect to the δ and δ_s for several fixed lattice constants near their optimum values a and c, we evaluated some of the elastic constants for the D_{4h}^{18} modification of $KCuF_3$. We obtain $(c_{11} + c_{12}) = 248.8$, $c_{33} = 134.9$, and $c_{13} = 82.5$ GPa. The experimental elastic constants for $KCuF_3$ are not available, so that no comparison with experiment can be made.

C. The Effect of External Hydrostatic Pressure

In the presence of external forces, the equilibrium parameters describing the crystal are determined by the equation

$$P_\xi = -\left\{\frac{\partial F(\xi,T)}{\partial \xi}\right\}_T , \tag{28}$$

where $F(\xi,T)$ is the crystal free energy, T is the temperature, and P_ξ is the external thermodynamic force conjugate to the parameter ξ. Introducing the unit cell volume

$$v = 4(a_0 + \eta_1)\cdot(a_0 + \eta_2)^2 \tag{29}$$

and the ratio

$$f = (a_0 + \eta_2)/(a_0 + \eta_1) \tag{30}$$

as new variables (instead of η_1 and η_2), we obtain from (28) for T = 0 and external hydrostatic pressure P

$$\frac{\partial E}{\partial v} = -P ;$$

$$\tag{31}$$

$$\frac{\partial E}{\partial \xi} = 0 , \quad \xi = f, \delta, \delta_s$$

where E is the crystal energy (27) expressed in terms of the v, f, δ, and δ_s. Equations (31) are equivalent to the conditions for minimizing the

function $W = E + P \cdot v$; therefore, minimization of W leads to the optimum crystal structure at zero temperature and fixed value of P.

We investigated the influence of the external hydrostatic pressure on all five tetragonal $KCuF_3$ phases and on the ideal perovskite cubic phase (which is optimum if $V_e = N_e = P = A = 0$). The main results are presented in Table XII and in Figure 4 (we use the $F^- - F^-$ interaction potential obtained in the CI calculations). For all phases, the hydrostatic pressure causes an *increase* of the e_g distortion near each copper ion and thus leads to a decrease in the JT part of the crystal energy. But the elastic energy grows with pressure so that the total energy increases for all phases. Therefore the pressure *destabilizes* the low-symmetry phases and one can expect *a decrease* in the transition temperature to the JT phase with pressure. This situation is in contradiction to the conclusions of Samara *et al.*[28] that the transition temperature should increase for phase transitions associated with soft zone-boundary phonons. The experimental data for a series of crystals analysed in Ref. 28 and the calculations of Boyer and Hardy [4] for $RbCaF_3$ prove that the transition temperature does indeed increase for zone-boundary rotations of some structural units in the crystal. However, JT distortions in $KCuF_3$ correspond to zone-boundary stretches in $[CuF_6]^{4-}$ clusters, and an opposite trend is predicted.

An interesting result is the prediction of a phase change in $KCuF_3$ for $P > 132$ kbar. From Figure 4, we see that the energies of the two phases (D_{4h}^{18} and D_{4h}^5) experimentally observed at zero pressure increase more rapidly with pressure than the energy of phase D_{4h}^{17}, with the result that D_{4h}^{17} becomes the most stable phase at high pressure. Thus it may be possible to transform the tetragonally compressed crystal (phases D_{4h}^{18}, D_{4h}^5)

into the tetragonally elongated one (phase D_{4h}^{17}) through application of hydrostatic pressure.

VI. Discussion

Two mechanisms have been previously suggested to rationalize the crystallographic and magnetic ordering in $KCuF_3$.

Kugel and Khomskii[29] concluded that the exchange interaction of magnetic ions is responsible for the low symmetry distortion and they were able to provide a qualitative description of the observed crystal and magnetic structures of $KCuF_3$. However, this model did not take into account the crystal elastic energy that increases with the ion shifts from positions corresponding to the ideal perovskite lattice. Kanamori[22] suggested another model in which the JT interaction dominates the low-symmetry distortion of the perovskite structure. This model has been used and developed in a series of phenomenological studies of the cooperative JT effect in perovskites.[24,30] On the basis of semi-empirical calculations of the JTC constants for $[CuF_6]^{4-}$, Nikiforov et al.[23] showed that considering *only* the JT mechanism leads to a prediction of the existence of both experimentally observed crystallographic modifications[6] of $KCuF_3$ and gives a correct explanation of the magnetic ordering[31] in this crystal. They also showed that the exchange mechanism of ordering is ineffective for the crystals having strong JT interaction.

The weak point in these previous analyses is that the physical constants (exchange integrals, JTC constants) are to some extent treated as adjustable parameters, leaving open the question of whether the explanation is actually valid. Our results, which correctly predict the space group and are derived entirely from first principles, prove that the JT distortions originate the low symmetry transformations in $KCuF_3$.

Our analysis of possible JT structures (Tables III and IV) should also be applicable to perovskite systems involving d^9 (Cu^{++}), low-spin d^7 (Ni^{3+}),

and high-spin d^4 (Cr^{2+}, Mn^{3+}) metals at the B site. Thus the crystals $RbCuF_3$, $TlCuF_3$,[32] and $(NH_4)CuF_3$[33] possess the D_{4h}^{18} space group and, therefore, the phase transition in these crystals is expected to follow the R_{12} (or $\{k_{13}\}\tau_5$) representation. The tetragonal unit cell with the edges of $a = b = \sqrt{2}\,a_0$, $c = 2a_0$ was found for $KCrF_3$[34-36] and for $RbCrF_3$, $(NH_4)CrF_3$, and $TlCrF_3$.[36] Thus these crystals must belong to either the D_{4h}^{17} or D_{4h}^{18} space groups (with doubled primitive unit cell) and the phase transformations must be associated with R_{12} (or $\{k_{13}\}\tau_5$).

On the other hand, the crystals $NdMnO_3$, $SmMnO_3$, $GdMnO_3$,[37,38] $EuMnO_3$, and $DyMnO_3$[38] possess the D_{2h}^{16} space group; $LaNiO_3$[39] has the D_{3d}^5 space group; and $BiNiO_3$[40] has the ideal perovskite structure. Thus, for these oxide pseudo-perovskite systems, we can conclude that the cooperative JT interaction considered in this paper is not the dominant factor responsible for the low symmetry distortion.

The major limitation in our approach is that we did not calculate the lattice modes and hence cannot predict the phase diagrams. The procedure for doing this would be straightforward to implement and is planned.

The calculations to determine the energy functions can also be extended. We did not include dispersion (van der Waals attraction) interactions for $K^+ - F^-$ and $Cu^{++} - F^-$ pairwise potentials and we did not include polarization of the K^+ and Cu^{++} ions. Such extensions would be straightforward. In addition, we did not include three-body terms involving $F^- - F^- - F^-$, $F^- - K^+ - F^-$ etc. These terms could easily be included within the methods used here and are planned. In calculating the crystal energies, we used an expansion approach valid only for small values of η_1, η_2 and δ. A program is being developed for a more generalized analysis of

the crystal energies that would allow these restrictions to be lifted and would simplify consideration of the cases with large unit cells.

There is obviously much to do in obtaining more complete and more accurate predictions; however, we believe that the current success justifies the effort to develop more general and more automatic procedures.

VII. Summary and Conclusions

We have presented the symmetry analysis of the possible displacive phase transitions associated with cooperative JT distortions in perovskites possessing a sublattice of ions having an E_g ground state. This analysis allows the permissible crystal structures to be classified so as to identify the low-symmetry distortions to be considered in the explicit calculation of the energy.

The computation of crystal energy for various structures of $KCuF_3$ was based on pair interaction potentials, shell model parameters, and JT coupling constants derived from the *ab initio* calculations of different clusters. *No empirical adjustments have been made in any of the parameters*. Thus, these results are truly first-principles predictions of the displacive phase transitions. We find that the D_{4h}^{18} crystal structure has the lowest energy, and the energy of D_{4h}^5 structure is only 1.5 cm^{-1} higher (per formula unit), while D_{4h}^{17} is at +30 cm^{-1} and both D_{4h}^1 structures have the energies of +226 cm^{-1}. The fact that only D_{4h}^{18} and D_{4h}^5 have been observed experimentally is strong support for the efficacy of the theoretical approach. Indeed, the calculated lattice constants and the magnitude of JT distortion for D_{4h}^{18} and D_{4h}^5 structures also agree reasonably well with the experimental data[6] for $KCuF_3$.

Since all parameters are derived from *ab initio* wavefunctions, we can be certain that the origin of the distorted structures of $KCuF_3$ is indeed the JT distortion of the $[CuF_6]^{4-}$ octahedron.

We find that anharmonicity plays a fundamental role in determining the type of distorted structure exhibited by $KCuF_3$. The anharmonic term is responsible for the coexistance of both uniform and nonuniform crystal deformation, and this term is the basic reason for stabilization of

the phases D_{4h}^{18} and D_{4h}^5 with respect to the phase D_{4h}^{17}.

Our study predicts the lowering of transition temperature with hydrostatic pressure for the phase transitions associated with the JT active zone-boundary crystal modes (which is in contrast with the zone-boundary rotational instabilities considered in Ref. 4 and 28). We also predict the stability of a new $KCuF_3$ low-symmetry phase for large external hydrostatic pressure.

Acknowledgments

Appendix I

The general form for the pairwise interaction potential V_{ij} is

$$V_{ij} = V_{ij}^{(0)} + \frac{Z_i Z_j}{r} + \frac{Y_i Z_j}{|r - l_i|} + \frac{Y_j Z_i}{|r + l_j|} + \frac{Y_i Y_j}{|r - l_i + l_j|}$$

$$+ f_{ij}(r) + g_{ij}(|r - l_i + l_j|) + \frac{1}{2}K_i l_i^2 + \frac{1}{2}K_j l_j^2 , \qquad (32)$$

where

$$f_{ij}(r) = -\frac{A_{ij}}{r}\exp(-B_{ij}r) \qquad (33)$$

and

$$g_{ij}(|r - l_i + l_j|) = C_{ij}\exp(-D_{ij}|r - l_i + l_j|) - \frac{C_6}{|r - l_i + l_j|^6} . \qquad (34)$$

Here $V_{ij}^{(0)}$ is a constant; Z_i, Y_i are the charges of the i-th core and shell, respectively (the formal charge of the i-th ion is $Q_i = Z_i + Y_i$); r is the distance between the cores (r directed from i-th to j-th ion); l_i is the shift of the i-th shell with respect to the i-th core, K_i is the shell-core spring constant; and $l_i = |l_i|$.

For any fixed nuclei positions and any set of the model parameters A_{ij}, B_{ij}, C_{ij}, D_{ij}, Y_i and K_i, we allow the fluorine shells to adjust so as to minimize the energy for the total system. Thus, for each cluster the fluorine shell shifts l_i are functions of both the model parameters and nuclear configuration. The optimal shell shifts are obtained from the energy minimum condition

$$\frac{\partial}{\partial l_{it}}\left[\frac{1}{2}\sum_{j\neq k}V_{jk}\right] = 0 , \quad t = x,y,z , \qquad (35)$$

where j and k run over all ions in the cluster.

Since the shell shifts are small in comparison with the internuclear distances, it is convenient to obtain approximate solutions of (35) using the following truncated expansions of (32)

$$V_{ij} \approx V_{ij}^{(0)} + \frac{Q_iQ_j}{r} + f_{ij}(r)$$

$$+ Q_iY_j\left[-\frac{(r l_j)}{r^3} + \frac{3(r l_j)^2 - r^2 l_j^2}{2r^5} \right] + Q_jY_i\left[-\frac{(r l_i)}{r^3} + \frac{3(r l_i)^2 - r^2 l_i^2}{2r^5} \right]$$

$$+ Y_iY_j\frac{r^2(l_i l_j) - 3(r l_i)(r l_j)}{r^5} + g_{ij}(|r - l_i + l_j|) + \frac{1}{2}(K_i l_i^2 + K_j l_j^2) , \quad (36)$$

where f_{ij} is defined in (33) and

$$g_{ij}(|r - l_i + l_j|) \approx C_{ij}\exp(-D_{ij}r) \times \left\{ 1 \right.$$

$$\left. -\frac{D_{ij}r(l_j - l_i)}{r} - \frac{D_{ij}}{2r}(l_j - l_i)^2 + \frac{D_{ij}(1 + D_{ij}r)}{2r^3}[r(l_j - l_i)]^2 \right\}$$

$$-\frac{C_6}{r^6} \times \left\{ 1 -\frac{12}{r}|l_j - l_i| + \frac{84}{r^2}(l_j - l_i)^2 \right\} . \quad (37)$$

Due to the high symmetry of the clusters under consideration, the general expressions (36) and (37) lead to a rather simple formulas [and simple solutions of (35)]. Indeed the interaction potentials and fluorine shell model parameters were obtained using Eqs. (36) and (37) rather than (32) and (34).

Appendix II

The long-range coulombic contributions to the energy of the perovskite crystal under uniform tetragonal deformation were evaluated by Boyer and Hardy.[4] Using Eq. (7) from Ref. 4 (with $\delta = 0$) and $a_0 = 4.06$ Å, we obtain (in atomic units)

$$\alpha^C = 0.280363, \quad \beta_1^C = -0.054586, \quad \beta_{12}^C = 0.036087 \ . \tag{38}$$

The β_2^C coefficient is determined by (18) from β_1^C and β_{12}^C. In order to obtain the long-range contributions R^C, R_s^C, and R_{ns}^C to the coefficients of (15) describing *pure nonuniform* deformation, we performed a direct computation of the lattice sums

$$\Delta E^C(\delta, \delta_s) = \frac{1}{2} \sum_n \sum_{i,j=1}^{32} {}' q_i q_j \times$$

$$\left\{ |R_{0i}(\delta, \delta_s) - R_{nj}(\delta, \delta_s)|^{-1} - |R_{0i}(0,0) - R_{nj}(0,0)|^{-1} \right\} , \tag{39}$$

where $R_{nj}(\delta, \delta_s)$ is the radius-vector of the j-th ion in the n-th unit cell (containing four $KCuF_3$ formula units). We consider the cores and shells of fluorines as separate ions in (39); therefore, $q_i = Q_i$ for $1 \le i \le 8$ ($Q_{Cu} = +2$, $Q_K = +1$), $q_i = Z_F = +5$ for $9 \le i \le 20$, and $q_i = Y_F = -6$ for $21 \le i \le 32$. The prime in the sum (39) indicates that all self-terms (with i = j within the zero unit cell) and the core-shell terms within the *same* fluorine ion are excluded from the summation. Due to the small values of δ and δ_s (and in the absence of uniform crystal deformation), each contribution to (39) with the fixed index i is a sum of potentials produced by a lattice of nearly point dipoles; thus the sums (39) converge rapidly.

Neglecting high-order terms and fixing $\eta_1 = \eta_2 = 0$ leads to

$$\Delta E^C(\delta, \delta_s) = R^C \delta^2 + R_s^C \delta_s^2 + R_{ns}^C \delta \, \delta_s \ . \tag{40}$$

Calculating the lattice sums (39) with $\delta = 0.01$, $\delta_s = 0$; $\delta = 0$, $\delta_s = 0.01$; and $\delta = \delta_s = 0.01$ (in atomic units) for each low-symmetry phase we evaluated all necessary coefficients R^C, R_s^C and R_{ns}^C. These results are given in Table XIII.

References

1. J. B. Goodenough and J. M. Longo, Landolt-Bornstein Numerical Data and Functional Relationships in Science and Technology, New Series, III/4a, p.126, Springer, 1970.

2. S. Nomura, Landolt-Bornstein Numerical Data and Functional Relationships in Science and Technology, New Series, III/12a, p.368, Springer, 1978.

3. R. A. Cowley, Phys. Rev. **134**, A981 (1964).

4. L. L. Boyer and J. R. Hardy, Phys. Rev. B **24**, 2577 (1981).

5. N. Lehner, H. Rauh, K. Strobel, R. Geick, G. Heger, J. Bouillot, D. Renker, M. Rousseau, and W. G. Stirling, J. Phys. C **15**, 6545 (1982).

6. A. Okazaki and Y. Suemune, J. Phys. Soc. Jpn. **16**, 176 (1961); A. Okazaki, ibid. **26**, 870 (1969); N. Tsukuda and A. Okazaki, ibid. **33**, 1088 (1972).

7. S. Yu. Shashkin and W. A. Goddard III, Phys. Rev. B, in press.

8. L. D. Landau and E. M. Lifshitz, Statisticheskaya fizika (Statistical Physics), Part 1, Nauka, M., 1976 (Engl. Translation of 2nd edn., Addison-Wesley, Reading, Mass., 1969).

9. E. B. Vinberg, Yu. M. Gufan, V. P. Sakhnenko, and Yu. I. Sirotin, Kristallografiya **19**, 21 (1974); [Sov. Phys. - Crystallogr. **19**, 10 (1974)].

10. O. V. Kovalev, Neprivodimye predstavleniya prostranstvennykh grupp (Irreducible representations of the space groups), Izd-vo AN UkrSSR, Kiev, 1961 (Engl. translation., Gordon and Breach, New York, 1965).

11. Yu. A. Izyumov, Usp. Fiz. Nauk **131**, 387 (1980); [Sov. Phys. Usp. **23**, 356 (1980)].

12. L. Bouckaert, R. Smoluchwski, and E. Wigner, Phys. Rev. **50**, 58 (1936).

13. S. Huzinaga and Y. Sakai, J. Chem. Phys. **50**, 1371 (1969).

14. M. J. Brusich, S. Yu. Shashkin, and W. A. Goddard III, manuscript in preparation.

15. B. G. Dick and A. W. Overhauser, Phys. Rev. **112**, 90 (1958).

16. G. H. F. Diercksen and A. J. Sadley, Mol. Phys. **47**, 33 (1982).

17. J. H. Harding and A. H. Harker, Philos. Mag. B **51**, 119 (1985).

18. S. Yu. Shashkin and W. A. Goddard III, J. Phys. Chem., in press.

19. S. Huzinaga, Gaussian Basis Sets for Molecular Calculations, Elsevier, N.Y., 1984.

20. F. W. Bobrowicz and W. A. Goddard III, in Methods of Electronic Structure Theory (Plenum Press, New York, 1977), p. 79.

21. U. Opik and M. H. L. Pryce, P. R. Soc. London, Ser. A **238**, 425 (1957).

22. J. Kanamori, J. Appl. Phys. **31**, 14S (1960).

23. A. E. Nikiforov, S. Yu. Shashkin, M. L. Levitan, and T. H. Agamalyan, Phys. Status Solidi B **118**, 419 (1983).

24. B. Halperin and R. Englman, Phys. Rev. B **3**, 1698 (1971).

25. Yu. A. Popkov, V. A. Fomin, and L. T. Kharchenko, Fiz. Tverd. Tela (Leningrad) **13**, 1626 (1971); [Sov. Phys. - Solid State **13**, 1360 (1971)].

26. M. Aleksiejuk and D. Kraska, Phys. Status Solidi A **31**, K65 (1975).

27. M. Rousseau, J. Nouet, and A. Zarembowitch, J. Phys. Chem. Solids **35**, 921 (1974).

28. G. A. Samara, T. Sakudo, and K. Yoshimitsu, Phys. Rev. Lett. **35**, 1767 (1975).

29. K. I. Kugel and D. I. Khomskii, Zh. Eks. Teor. Fiz. **64**, 1429 (1973); [Sov. Phys. - JETP **37**, 725 (1973)].

30. P. Novak, J. Phys. Chem. Solids **31**, 125 (1970).

31. K. Hirakava and Y. Kurogi, Prog. Theor. Phys. (Suppl.) **46**, 147 (1970).

32. W. Rudorf, G. Lincke, and D. Babel, Z. Anorg. Allg. Chem. **320**, 150 (1963).

33. D. S. Crocket and H. M. Haendler, J. Am. Chem. Soc. **82**, 4158 (1960).

34. V. Scatturin, L. Corliss, N. Elliot, and J. Hastings, Acta Cryst. **14**, 19 (1961).

35. J. C. Cousseins and A. de Kozak, C. R. Acad. Sci. **263**, 1533 (1966).

36. G. Vollmer, Ph.D. Thesis, University of Tubingen, Germany (1966).

37. P. F. Bertaut and F. Forrat, J. Phys. Rad. **17**, 129 (1956).

38. G. J. McCarthy, P. V. Gallagher, and C. Sipe, Mater. Res. Bull. **8**, 1277 (1973).

39. A. Wold, B. Post, and E. Banks, J. Am. Chem. Soc. **79**, 4911 (1957).

40. Yu. Ya. Tomashpol'skii, E. V. Zubova, K. P. Burdina, and Yu. N. Venevtsev, Kristallografiya **13**, 987 (1968); [Sov. Phys. - Crystallogr. **13**, 859 (1969)].

Table I. Bravais lattices for low-symmetry phases in terms of the elementary translations a_1, a_2, and a_3 of the cubic perovskite phase (from Ref. 9).

Brillouin zone symmetry point, wave-vector star	Type of lattice	d_1	d_2	d_3	$p=V_D/V$
R,[a] $\{k_{13}\}$[b]		a_2+a_3	a_3+a_1	a_1+a_2	2
X,[a] $\{k_{10}\}$[b]	a	$2a_1$	$2a_2$	$2a_3$	8
	b	$2a_1$	$2a_2$	a_3	4
	c	a_1	a_2	$2a_3$	2
M,[a] $\{k_{11}\}$[b]	a	$-a_1+a_2+a_3$	$a_1-a_2+a_3$	$a_1+a_2-a_3$	4
	b	a_1-a_2	a_1+a_2	a_3	2

[a] Ref. 12.

[b] Ref. 10.

-331-

TABLE II. BASIS VECTORS OF THE JT ACTIVE IRREDUCIBLE REPRESENTATIONS.

ION	R'_{12} [a] (or $\{k_{13}\}\tau'_5$) [b]		M_1 [a] (or $\{k_{11}\}\tau'_1$) [b]			M'_3 [a] (or $\{k_{11}\}\tau_5$) [b]			X_1 [a] (or $\{k_{10}\}\tau_1$) [b]		
	θ	ϵ	$(\tfrac{1}{2},\tfrac{1}{2},0)$	$(\tfrac{1}{2},0,\tfrac{1}{2})$	$(0,\tfrac{1}{2},\tfrac{1}{2})$	$(\tfrac{1}{2},\tfrac{1}{2},0)$	$(\tfrac{1}{2},0,\tfrac{1}{2})$	$(0,\tfrac{1}{2},\tfrac{1}{2})$	$(0,0,\tfrac{1}{2})$	$(0,\tfrac{1}{2},0)$	$(\tfrac{1}{2},0,0)$
X_1	$(\bar{1}00)$	(100)	(100)	(100)	(000)	(100)	$(\bar{1}00)$	(000)	(000)	(000)	(100)
X_2	$(0\bar{1}0)$	$(0\bar{1}0)$	(010)	(000)	(010)	$(0\bar{1}0)$	(000)	(010)	(000)	(010)	(000)
X_3	(002)	(000)	(000)	(001)	(001)	(000)	(001)	$(00\bar{1})$	(001)	(000)	(000)

[a] Ref. 12.

[b] Ref. 10.

Table III. The crystal structures arising due to the phase transition following the two-dimensional irreducible representation R_{12} ($\{k_{13}\}\tau_5$).

Γ	$C = (C_\theta, C_\varepsilon)$					
	(C_1, C_2)		$(C, 0)$		$(0, C)$	
	G_D	p	G_D	p	G_D	p
R_{12} $(\{k_{13}\}\tau_5)$	D_{2h}^{25}	2	D_{4h}^{17}	2	D_{4h}^{18}	2

TABLE IV. THE CRYSTAL STRUCTURES ARISING DUE TO THE PHASE TRANSITION FOLLOWING

THREE-DIMENSIONAL IRREDUCIBLE REPRESENTATIONS

	$\hat{C} = (C_1, C_2, C_3)$					
	(C_1, C_2, C_3)	$(C_1, C_2, 0)$	(C_1, C_1, C_3)	$(C_1, C_1, 0)$	$(0, 0, C_3)$	(C_1, C_1, C_1)
	G_D lattice^a p	G_D lattice^a p	G_D lattice^a p	G_D lattice^a p	G_D lattice^a p	G_D lattice^a p
M_1 ($[k_{11}]\tau_1$)	D_{2h}^{25} a 4	D_{2h}^{25} a 4	D_{4h}^{17} a 4	D_{4h}^{17} a 4	D_{4h}^{1} b 2	O_h^{9} a 4
M_3 ($[k_{11}]\tau_5$)	D_{2h}^{25} a 4	D_{2h}^{25} a 4	D_{2h}^{25} a 4	D_{4h}^{17} a 4	D_{4h}^{5} b 2	T_h^{5} a 4
X_1 ($[k_{10}]\tau_1$)	D_{2h}^{1} a 8	D_{2h}^{1} b 4	D_{4h}^{1} a 8	D_{4h}^{1} b 4	D_{4h}^{1} c 2	O_h^{1} a 8

a) Type of Bravais lattice as denoted in Table I.

Table V. Fluorine shifts for possible tetragonal phases of $KCuF_3$ having doubled primitive unit cell volume.

Γ	G_D	Fluorine shifts (see Figure 2)					
		δ_1	δ_2	δ_3	δ_4	δ_5	δ_6
R_{12} $(\{k_{13}\}\tau_5)$	D_{4h}^{18}	δ	δ	0	0	$-\delta$	$-\delta$
R_{12} $(\{k_{13}\}\tau_5)$	D_{4h}^{17}	δ	$-\delta$	2δ	2δ	$-\delta$	δ
X_1 $(\{k_{10}\}\tau_1)$	D_{4h}^1	0	0	δ	$-\delta$	0	0
M_1 $(\{k_{11}\}\tau_1)$	D_{4h}^1	δ	$-\delta$	0	0	δ	$-\delta$
M_3 $(\{k_{11}\}\tau_5)$	D_{4h}^5	δ	δ	0	0	δ	δ

Table VI. The parameters of the pair interaction potentials and fluorine core-shell spring constant (in atomic units).

Ions	A	B	C	D	K_F	C_6
$(F^- - F^-)^a$	17.7368	1.20622	108.022	1.86248	6.11428	-
$F^- - F^-$	36.4562	1.37783	157.083	1.89265	4.17966	69.5469
$K^+ - F^-$	-2.6090	0.86279	95.732	1.90762		
$Cu^{2+} - F^-$	18.8136	1.07338	64.509	1.70780		

[a] Restricted basis set for F^- from Ref. 18.

Table VII. The adiabatic potential constants for the ^2E_g state of $[CuF_6]^{4-}$ (CI results from Ref. 7; atomic units).

V_e (10^{-9} N)	N_e (N/m)	P (N/m)	A (10^{11} N/m^2)
-0.020908	-0.000579	0.011152	-0.008990

Table VIII. Coordinates of ions in the $KCuF_3$ tetragonal unit cell given in Figure 2. The x and y coordinates are in units of $\sqrt{2}a$ and z coordinates in units of 2c; $u_i = (\delta_i/\sqrt{2})/(a\sqrt{2})$, $w_i = \delta_i/2c$.

Ion	Ion number	Coordinates		
		x	y	z
Cu	1	0	0	0
Cu	2	0	0	1/2
Cu	3	1/2	1/2	0
Cu	4	1/2	1/2	1/2
K	5	1/2	0	1/4
K	6	1/2	0	3/4
K	7	0	1/2	1/4
K	8	0	1/2	3/4
F	9	0	0	$(1/4+w_4)$
F	10	0	0	$(3/4-w_4)$
F	11	1/2	1/2	$(1/4-w_3)$
F	12	1/2	1/2	$(3/4+w_3)$
F	13	$(1/4+u_2)$	$(1/4+u_2)$	0
F	14	$(3/4-u_2)$	$(3/4-u_2)$	0
F	15	$(3/4+u_1)$	$(1/4-u_1)$	0
F	16	$(1/4-u_1)$	$(3/4+u_1)$	0
F	17	$(1/4+u_6)$	$(1/4+u_6)$	1/2
F	18	$(3/4-u_6)$	$(3/4-u_6)$	1/2
F	19	$(3/4+u_5)$	$(1/4-u_5)$	1/2
F	20	$(1/4-u_5)$	$(3/4+u_5)$	1/2

Table IX. The symmetrized displacements of fluorine octahedra about each copper ion.

Number of copper ion	$\sqrt{6}Q_a$	$\sqrt{3}Q_\theta$	Q_ε
1	$\eta_1+2\eta_2-2\delta_1+2\delta_2+2\delta_4$	$\eta_1-\eta_2+2\delta_4+\delta_1-\delta_2$	$-\delta_1-\delta_2$
2	$\eta_1+2\eta_2-2\delta_5+2\delta_6-2\delta_4$	$\eta_1-\eta_2-2\delta_4+\delta_5-\delta_6$	$-\delta_5-\delta_6$
3	$\eta_1+2\eta_2+2\delta_1-2\delta_2-2\delta_3$	$\eta_1-\eta_2-2\delta_3-\delta_1+\delta_2$	$\delta_1+\delta_2$
4	$\eta_1+2\eta_2+2\delta_5-2\delta_6+2\delta_3$	$\eta_1-\eta_2+2\delta_3-\delta_5+\delta_6$	$\delta_5+\delta_6$

Table X Short range contributions to the coefficients for the elastic energy expansion (15). The γ, γ_s, κ, and κ_s are defined in (22)-(25); K_F is the fluorine core-shell spring constant.

Low-symmetry phase	R^{sr}	R_s^{sr}	K
$D_{4h}^{18}(R_{12})$	$4(\gamma+\kappa)+8G_{31}$	$4(\gamma_s+\kappa_s)+8B_{31}$	$4K_F$
$D_{4h}^{17}(R_{12})$ [a]	$12(\gamma+\kappa)+24G_{31}$	$12(\gamma_s+\kappa_s)+24B_{31}$	$12K_F$
$D_{4h}^{1}(X_1)$	$2\gamma-12G_{31}$	$2\gamma_s-12B_{31}$	$2K_F$
$D_{4h}^{1}(M_1)$	$4(\gamma-\kappa)-8G_{31}$	$4(\gamma_s-\kappa_s)-8B_{31}$	$4K_F$
$D_{4h}^{5}(M_3)$	$4(\gamma+\kappa)-8G_{31}$	$4(\gamma_s+\kappa_s)-8B_{31}$	$4K_F$

[a] Since cases $D_{4h}^{18}(R_{12})$ and $D_{4h}^{17}(R_{12})$ correspond to different components φ_z and φ_θ of the same irreducible representation R_{12} (or $\{\kappa_{13}\}\tau_5$), one expects the R, R_s, and K values to be the same for these cases. However, the normalized crystal modes are $\varphi_z \sim \delta$ for case $D_{4h}^{18}(R_{12})$ and $\varphi_\theta \sim \sqrt{3}\delta$ for case $D_{4h}^{17}(R_{12})$; therefore, the ratio of the coefficients presented here for cases $D_{4h}^{18}(R_{12})$ and $D_{4h}^{17}(R_{12})$ is 1:3.

TABLE XI. RESULTS OF ENERGY OPTIMIZATION FOR DIFFERENT TETRAGONAL PHASES OF KCuF$_3$.

Comments	Low-Symmetry Phase	Relative Energy (cm^{-1})	a (Å)	a/c	δ (Å)	δ_s (Å)	Local e_g - Distortion ρ^b (Å)	ϕ_1 (in degrees)	ϕ_2	ϕ_3	ϕ_4
$N_e=P=A=0$; (F$^-$-F$^-$)	All Phases	-667	4.052	0.938	0.0	0.0	0.154	0	0	0	0
		-667	4.230	1.067	0.0	0.0	0.154	180	180	180	180
potentials from extensive basis CI calculations	D_{4h}^{18}	-922	4.142	1.000	0.106	0.113	0.213	-90	90	90	-90
	D_{4h}^{17}	-922	4.142	1.000	0.061	0.066	0.213	0	180	180	0
	D_{4h}^1 (X$_1$)	-356	4.142	1.000	0.071	0.069	0.082	180	0	180	0
	D_{4h}^5 (M$_1$)	-158	4.142	1.000	0.032	0.030	0.037	0	0	180	180
	D_{4h}	-920	4.412	1.000	0.106	0.113	0.212	-90	-90	90	90
All terms; (F$^-$-F$^-$)	All Phases	-562	4.054	0.939	0.0	0.0	0.152	0	0	0	0
		-508	4.219	1.056	0.0	0.0	0.128	180	180	180	180
potentials from simple basis HF calculations	D_{4h}^{18}	-744	4.176	1.027	0.098	0.102	0.205	-108	108	108	-108
	D_{4h}^{17}	-718	4.125	0.990	0.055	0.057	0.214, 0.168^a	0	180	180	0
	D_{4h}^5	-743	4.177	1.027	0.097	0.101	0.205	-108	-108	108	108
All terms; (F$^-$-F$^-$)	All Phases	-576	4.045	0.938	0.0	0.0	0.154	0	0	0	0
		-520	4.210	1.056	0.0	0.0	0.130	180	180	180	180
potentials from extensive basis CI calculations	D_{4h}^{18}	-802	4.169	1.028	0.105	0.112	0.220	-108	108	108	-108
	D_{4h}^{17}	-772	4.116	0.989	0.059	0.063	0.231, 0.177^c	0	180	180	0
	D_{4h}^5	-800	4.169	1.028	0.105	0.112	0.220	-108	-108	108	108
Exper.^{d}	D_{4h}^{18}		4.141	1.055	0.186		0.393	-109	109	109	-109
	D_{4h}^5		4.140	1.053	0.190		0.398	-108	-108	108	108

a) Per formula unit.
b) The value of ρ is the same for all Cu^{2+} ions except for Phase II. In the presence of uniform tetragonal deformation.
c) First number for 1st and 4th copper ions, second number for 2nd and 3rd copper ions.
d) Ref. 6.

Table XII. The influence of external hydrostatic pressure on the parameters of the low-symmetry $KCuF_3$ phases.

Pressure (kbar)[a]	Phase	Relative energy (cm^{-1})	v (Å^3)	a/c	δ (Å)
0	Ideal perovskite	0	284.236	1.000	0.0
	$D_{4h}^{18}(R_{12})$	-802	281.779	1.028	0.105
	$D_{4h}^{17}(R_{12})$	-772	282.018	0.989	0.059
	$D_{4h}^1(X_1),D_{4h}^1(M_1)$	-576	282.180	0.938	0.0
	$D_{4h}^5(M_3)$	-800	281.784	1.028	0.105
100	Ideal perovskite	0[b]	260.196	1.000	0.0
	$D_{4h}^{18}(R_{12})$	-776	257.338	1.047	0.130
	$D_{4h}^{17}(R_{12})$	-762	257.804	0.982	0.071
	$D_{4h}^1(X_1),D_{4h}^1(M_1)$	-542	257.612	0.917	0.0
	$D_{4h}^5(M_3)$	-774	257.346	1.046	0.129
200	Ideal perovskite	0[b]	239.876	1.000	0.0
	$D_{4h}^{18}(R_{12})$	-665	236.445	1.072	0.160
	$D_{4h}^{17}(R_{12})$	-722	237.280	0.970	0.084
	$D_{4h}^1(X_1),D_{4h}^1(M_1)$	-405	236.580	0.891	0.0
	$D_{4h}^5(M_3)$	-664	236.459	1.071	0.160

[a] 1 kbar = 3.3989·10^{-6} a.u.

[b] The energy of the cubic phase with respect to that at zero pressure: 5874 cm^{-1} (100 kbar), 21081 cm^{-1} (200 kbar).

Table XIII. Long range Coulombic contributions to the elastic energy expansion coefficients describing nonuniform deformation (in atomic units).

Low-symmetry phase	R^C	R_s^C	R_{ns}^C
$D_{4h}^{18}(R_{12})$	-1.3049	-6.8867	7.6842
$D_{4h}^{18}(R_{12})$ [a]	-3.9147	-20.6601	23.0526
$D_{4h}^{1}(X_1)$	2.0202	0.4053	-2.5724
$D_{4h}^{1}(M_1)$	6.2680	4.0183	-10.4908
$D_{4h}^{18}(M_3)$	-1.2876	-6.8618	7.6427

[a] See footnote for the Table X.

Figure Captions

Figure 1. The perovskite unit cell for ABX_3 compound (A at body center, B at corners, and X at edges).

Figure 2. Tetragonal unit cell used for $KCuF_3$ (containing four formula units). The coordinates of ions are given in Table VI; K^+ ions are not shown.

Figure 3. Tetragonal phases of $KCuF_3$ having a doubled primitive unit cell volume (four formula units are shown). The fluorine shifts are indicated by arrows; potassium ions are not shown.

Figure 4. The energy dependence of $KCuF_3$ tetragonal phases on the external hydrostatic pressure (relative to the energy of the perovskite cubic phase at the same pressure).
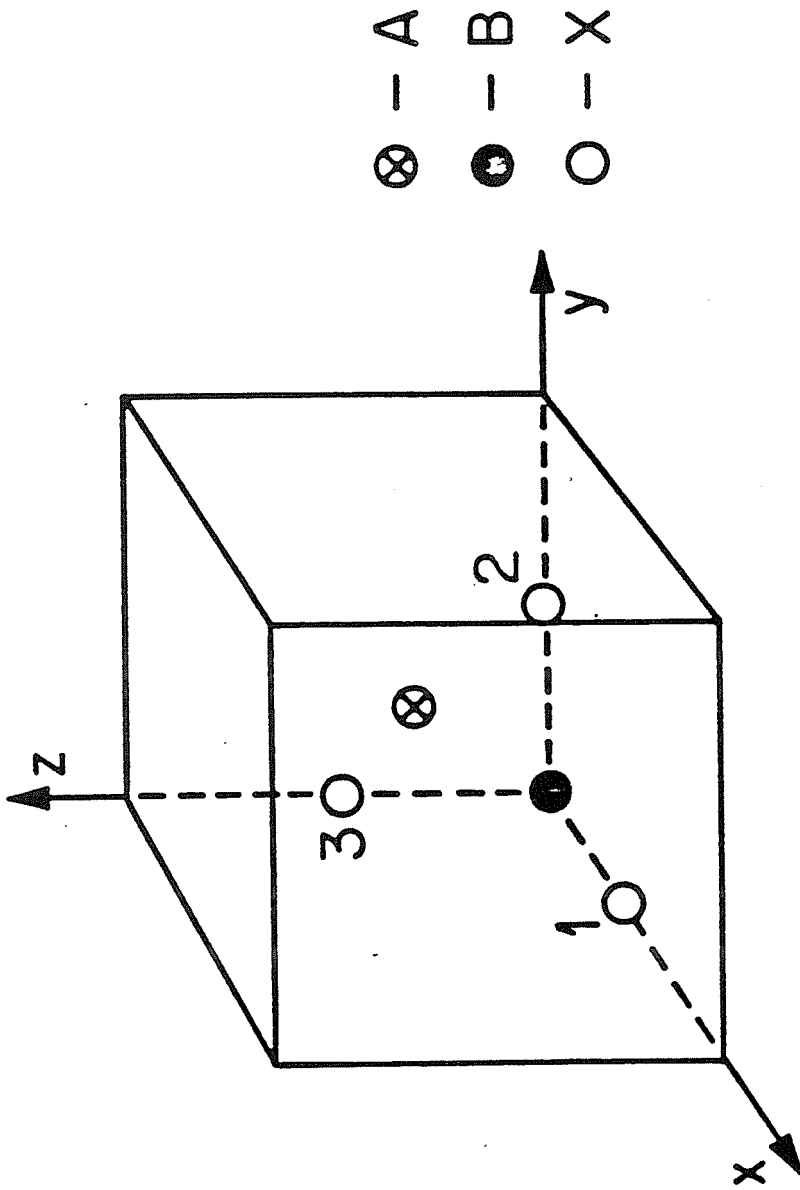
Figure 1.
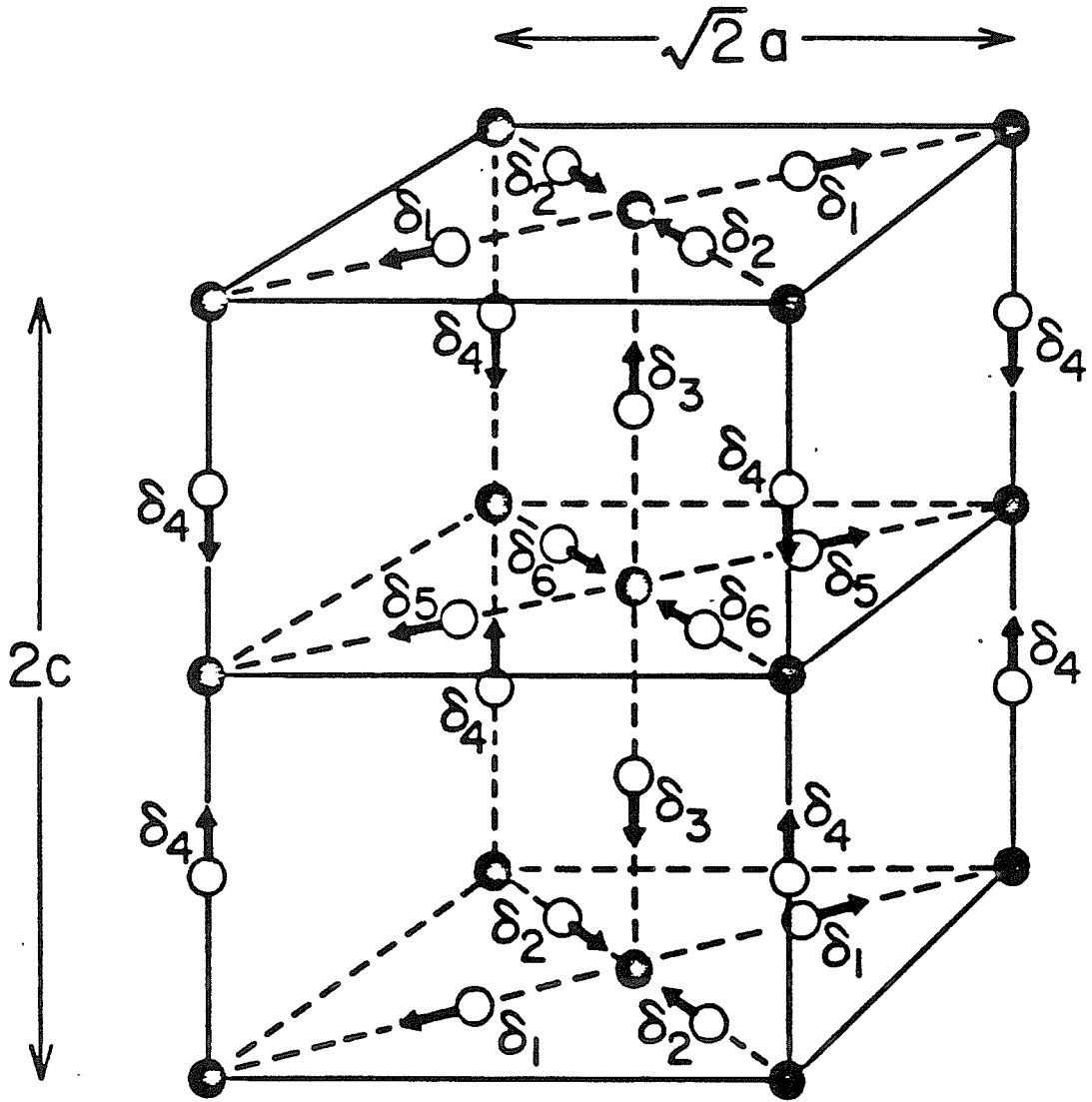
Figure 2.
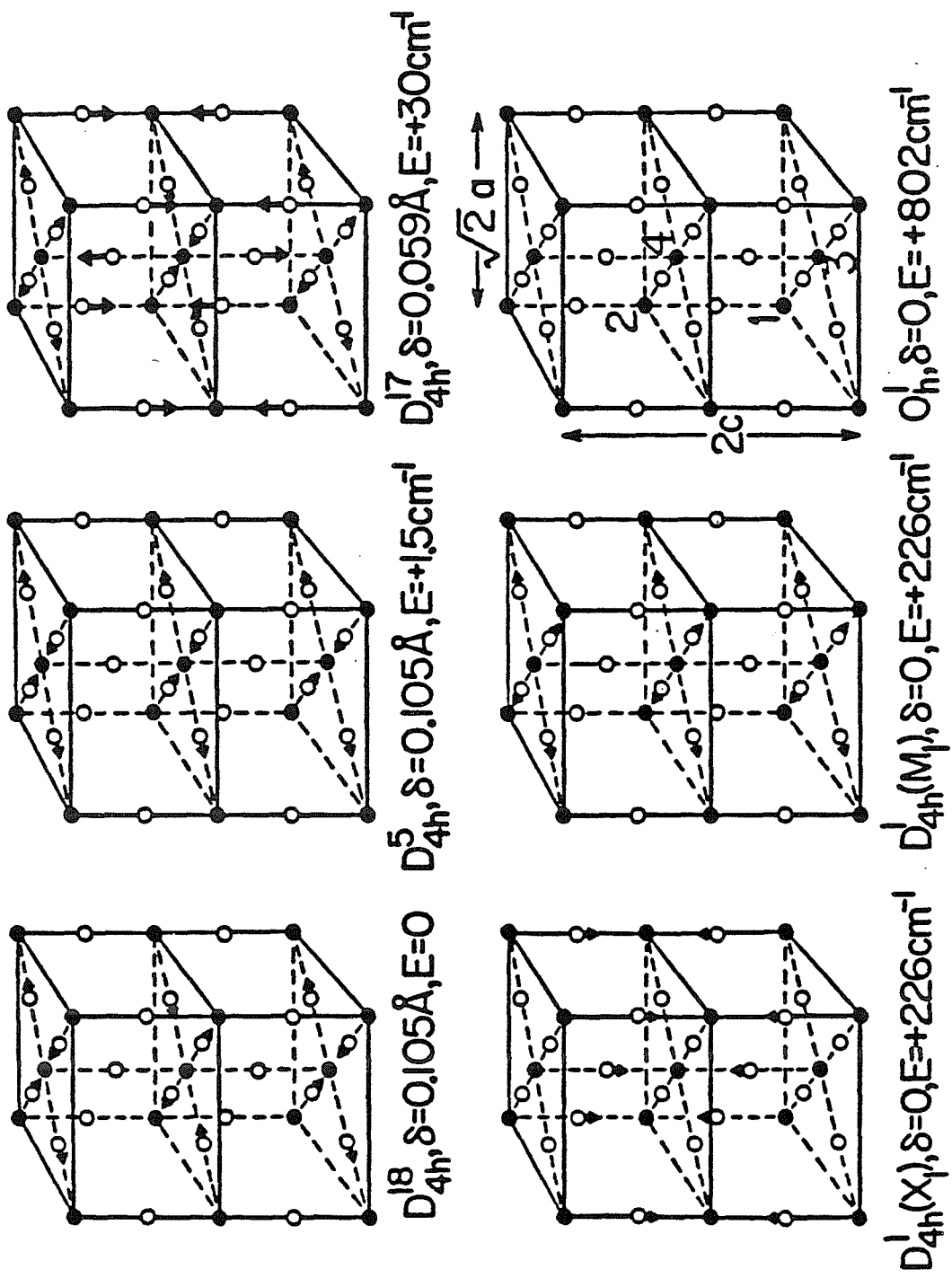
Figure 3.
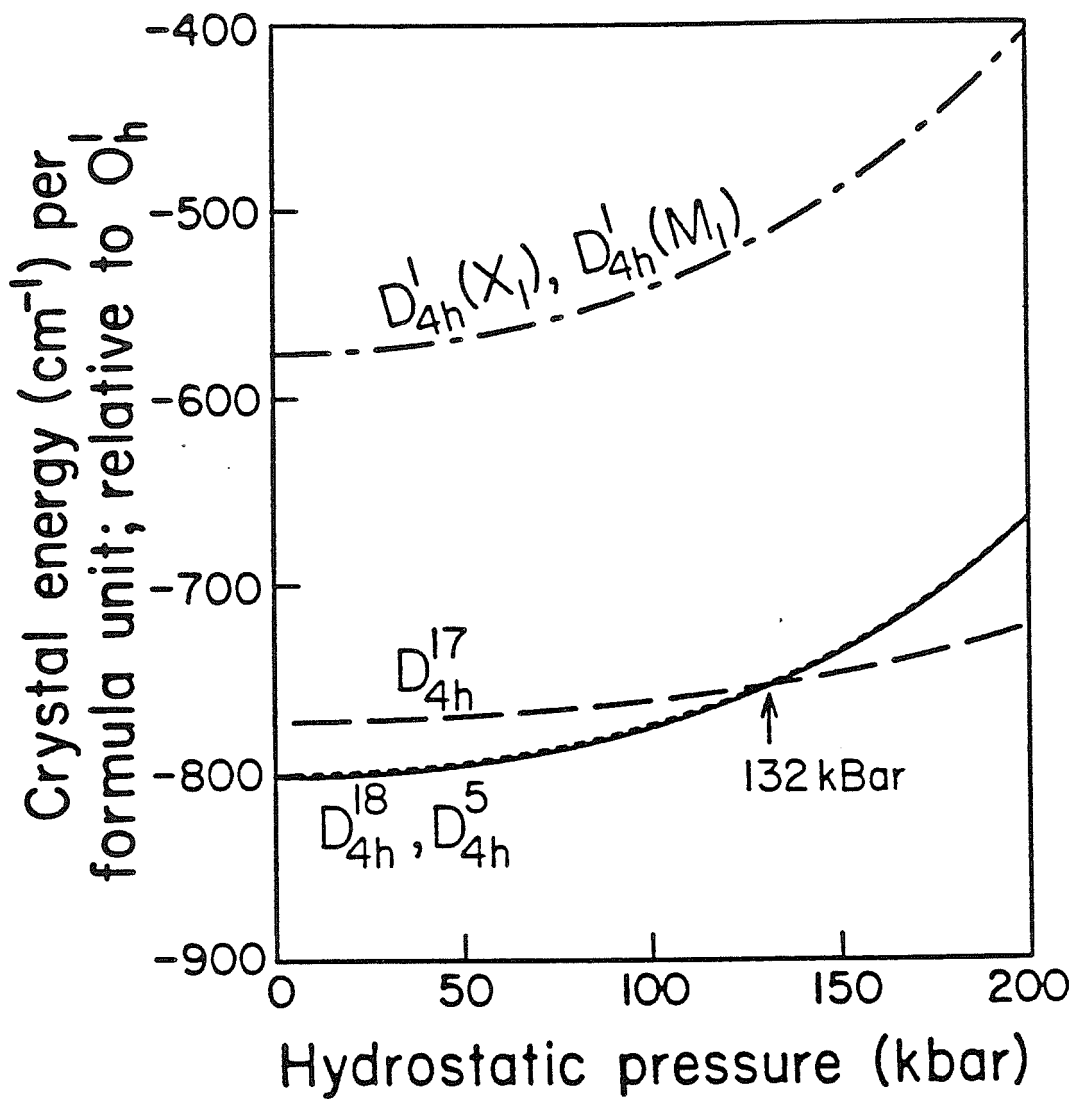
Figure 4.

Have compassion on your fellow man.
When you succeed, give thanks to God
for his loving kindness and mercy.
When you fail, remember that before
you take your neighbors to task for
their faults.
Never lose heart for recall that the
"failure" of the Cross led to the
salvation of the world.